DISSERTATION

ADDITIVE MANUFACTURING OF AN INTERVERTEBRAL DISC REPAIR PATCH TO TREAT SPINAL HERNIATION

Submitted by

Mitchell Ian Page

Department of Mechanical Engineering

In partial fulfillment of the requirements

For the Degree of Doctor of Philosophy

Colorado State University

Fort Collins, Colorado

Summer 2021

Doctoral Committee:

Advisor: Christian Puttlitz

Paul Heyliger
Susan James
Kirk McGilvray

ABSTRACT

ADDITIVE MANUFACTURING OF AN INTERVERTEBRAL DISC REPAIR PATCH TO TREAT SPINAL HERNIATION

Chronic low back pain is ubiquitous throughout society. The consequences of this disease are extensive and lead to physical, mental, and financial suffering in the affected population. Herniation of the intervertebral disc (IVD) is the primary cause of chronic low back pain due to the essential mechanical role of the IVD in the spinal column. Degenerative changes to the IVD tissues, in particular the annulus fibrosus (AF), lead to a pronounced vulnerability to herniation. Although numerous treatments for intervertebral disc herniation currently exist, these treatments are typically palliative and prone to hernia recurrence. Accordingly, there is a distinct need for an IVD hernia therapy that can provide long-term pain relief and recovery of spinal function.

One novel strategy to repair the intervertebral disc is to tissue-engineer a construct that facilitates regeneration of the healthy and functional IVD tissue. Advances in additive manufacturing technology offer the fabrication of complex tissue-engineered structures that augment biological content and biocompatible materials. Therefore, this work sought to engineer an additive manufactured repair patch for IVD herniation towards an improved treatment for chronic low back pain. Specifically, the aims of this work were to leverage experimental and computational methods to: (1) to characterize the mechanics of additive manufactured angle-ply scaffolds, (2) evaluate the tissue response of cell-laden scaffolds cultured with dynamic biaxial mechanical stimuli, and (3) to design and implement an annulus fibrosus repair patch.

The mechanics of additive manufactured scaffolds for AF repair were experimentally characterized in a physiologically-relevant, biaxial loading modality. To assess sensitivity of the scaffold mechanics to additive manufacturing parameters, a broad scope of scaffold designs were evaluated with a parameterized finite element model. A custom incubator was developed, cell-laden scaffolds were cultured with a prescribed, multi-axial mechanical loading protocol, and ECM production within the scaffold was evaluated. A finite element model was developed to aid in understanding the relationship between global scaffold loading and the local, inhomogeneous cellular micromechanical environment within the scaffold. The developed TE material was translated into an implant and was implemented in a large animal model. The efficacy of the AF repair strategy was also evaluated in finite element model of the human lumbar spine. This work formed a multi-scale approach to consolidate biological and mechanical efficacy of a novel AF repair strategy. Ultimately, this approach may facilitate regeneration of the AF and represent a revolutionary treatment for chronic low back pain.

ACKNOWLEDGMENTS

This work was only possible because of the guidance and support of many people. First, I am especially grateful for the mentorship of Christian Puttlitz, who has been an incredible advisor and friend. Thank you for stoking my ambition and coaching me through this journey. I would also like to express my gratitude for the members of my doctoral committee: Kirk McGilvray, Paul Heyliger, and Susan James. In particular, Kirk McGilvray has been an outstanding friend and mentor through the last five years.

I also appreciate the help of all past and present OBRL team. Ben Gadomski is another friend and mentor that I have been extremely lucky to work with. Peter Linde made instrumental contributions to the presented cell culture work and to developing my acumen in practical biology. I am thankful for Cecily Broomfield and Lauren Berens, without whom I could have never navigated the world of histology. The PSRL crew, in particular Jeremiah Easley, Katie Bisazza, and Andres Bonilla, provided critical contributions to the animal model work. I would also like to acknowledge the following people in particular for their amazing support and friendship: Kevin Labus, Heather Troyer, Lucas Nakamura, Jake Wolynski, Jason Kuiper, Erik Brodin, Jimmy Johnson, Devin von Stade, Nicole Ramo, Conor Sutherland, Michael Poland, and Megan English.

Finally, I am grateful for all of my friends and family that have supported me on this journey. Above all, I am overwhelmingly thankful for my parents, Sheryll and Daryl, and my Grandparents, Des, Mary, Val, and Bill, for their endless love and support. Thank you for providing me with every opportunity to succeed and for instilling in me the ambition and perseverance that made all of this possible.

TABLE OF CONTENTS

ABSTRACT ii
ACKNOWLEDGMENTS iv
1. BACKGROUND 1
1.1. Epidemiology and Clinical Significance 1
1.2. Functional Anatomy of the Intervertebral Disc 3
1.3. Intervertebral Disc Disease 9
1.4. Treatment of Intervertebral Disc Disease 12
1.5. Tissue Engineering 14
1.6. Additive Manufacturing 16
1.7. Computational Methods in Tissue Engineering 21
1.8. Summary 24
1.9. Specific Aims 25
2. MECHANICAL CHARACTERIZATION OF ADDITIVE MANUFACTURED ANGLE-PLY SCAFFOLDS 28
2.1. Experimental Approach 28
2.1.1. Introduction 28
2.1.2. Materials and Methods 29
2.1.3. Results 33
2.1.4. Discussion 45
2.1.5. Conclusions 52
2.2. Computational Approach 54
2.2.1. Introduction 54
2.2.2. Materials and Methods 54
2.2.3. Results 62
2.2.4. Discussion 72
2.2.5. Conclusion 80
3. THE REGENERATIVE RESPONSE OF CELL-LADEN TISSUE ENGINEERED SCAFFOLDS UNDER MECHANICAL STIMULUS 81

3.1. Experimental Approach 81
3.1.1. Introduction 81
3.1.2. Methods 81
3.1.3. Results 91
3.1.4. Discussion 99
3.1.5. Conclusions 111
3.2. Computational Approach 112
3.2.1. Introduction 112
3.2.2. Materials and methods 116
3.2.3. Results 123
3.2.4. Discussion 135
3.2.5. Conclusion 145
4. DESIGN AND IMPLEMENTATION OF AN ANNULUS FIBROSUS REPAIR PATCH 147
4.1. Experimental Approach 147
4.1.1. Introduction 147
4.1.2. Methods 148
4.1.3. Results 160
4.1.4. Discussion 186
4.1.5. Conclusions 196
4.2. Computational Approach 198
4.2.1. Introduction 198
4.2.2. Methods 198
4.2.3. Results 207
4.2.4. Discussion 222
4.2.5. Conclusions 231
5. CONCLUSIONS 232
5.1. Summary of Findings 232
5.2. Future Work 234
REFERENCES 237
APPENDIX A 263

APPENDIX B **266**
APPENDIX C **272**
APPENDIX D **275**
APPENDIX E **283**
APPENDIX F **299**
APPENDIX G **304**

CHAPTER 1 – BACKGROUND

The objective of the current research is to develop an additive manufacturing (AM) technique towards the repair of diseased IVD and, ultimately, treat chronic low back pain (CLBP). Sections 1.1 to 1.5 outline:

(1) the epidemiology of CLBP and the clinical significance of IVD disease treatment,

(2) the functional anatomy and structure of the IVD,

(3) the etiology and symptoms of IVD disease,

(4) the current treatment strategies for IVD disease,

(5) the relevant tissue engineering (TE) strategies for IVD repair,

(6) the relevant additive manufacturing (AM) techniques for IVD repair, and

(7) The role of computational methods in TE.

1.1. Epidemiology and Clinical Significance

Low back pain is ubiquitous in society. Up to 85% of people will experience low back pain at some time in their life and up to 45% of people are affected annually[1]. Of the individuals who experience low back pain, 5-10% suffer from severe morbidity due to their condition, incurring substantial healthcare costs, limitation of physical activity, and decreased quality of life[2,3]. Consequently, low back pain is consistently among the leading reasons for physician visits, hospitalizations, and surgeries in the United States[4,5], generating a substantial burden on the healthcare system. Further, physical limitation from low back pain is the most common cause of

work absence in people aged under 45[6] and is the leading cause of years lived with disability in the United States[7]. These widespread impairments to the population induce an immense economic impact. Each year, 2% of the US workforce are financially compensated for low back injuries[1]. Overall, the total costs associated with low back pain is typically 1-2% of the gross domestic product of a country[8–10] and is over $100 billion annually in the United States[11].

Hernia of the IVD is a major cause of low back pain, and is often associated with IVD degeneration, another leading cause of low back pain[12]. Disc herniation is a commonly diagnosed disorder, with a prevalence of approximately 3% of adults[13]. Additionally, men are more likely to be affected by disc herniation; the prevalence of disc herniation has been reported as approximately 4.8% in men over the age of 35 as compared to approximately 2.5% among females over the same age range[13]. Whilst the incidence of disc hernia diagnoses are relatively high, this prevalence is continually increasing due to the aging population[14] and it is frequently undiagnosed when no symptoms are presented. Following lumbar spine imaging, annular fissures have been observed in 19% of asymptomatic 20 year-old individuals and 29% of asymptomatic 80 year-old individuals[15].

Current therapies for IVD hernia facilitate initial recovery from the symptomatic pain in approximately 90% of individuals within one year from the onset of symptoms[16]. However, despite this high rate of initial recovery from pain, it appears that the underlying pathology often remains. Recurrence of disc herniation symptoms has been reported in as many as 80% of people[16]. These individuals with recurrent IVD herniation require additional medical treatment and continued work absence, financial burden, and physical suffering. There is a need for advanced treatments to improve the quality of IVD hernia treatment to improve the rate of initial recovery and, in particular, the long-term recovery to reduce the high rate of symptomatic reherniation.

1.2. Functional Anatomy of the Intervertebral Disc

The IVD is a critical component of the vertebral column to support the body and facilitate upper body motion. In the human spine, 23 IVDs form fibrocartilaginous joints between each of the articulating vertebrae (Figure 1a). Overall, there are six IVDs in the cervical spine, twelve in the thoracic spine, and five in the lumbar spine. The size of IVDs generally increases in the caudal direction[17,18]. Therefore, IVDs in the lumbar spine are larger as compared to the thoracic spine, and IVDs in the thoracic spine are larger as compared to the cervical spine. Lumbar discs have a height of approximately 7-10 mm and have a diameter of approximately 40 mm[19].

1.2.1. Structure of the Intervertebral Disc

The IVD consists of three main components: the cartilaginous endplates (CEP), nucleus pulposus (NP), and annulus fibrosus (AF) (Figure 1b). Collectively, the CEP, NP, and AF function to transmit vertebral loads and facilitate spinal motion. The CEPs are two thin hyaline cartilage layers on the cranial and caudal aspects of the IVD and attached to the vertebral bodies (Figure 1b)[20]. These CEPs have three primary functions: (1) containing the NP and AF craniocaudally, (2) as a load bearing surface on the vertebral body, and (3) to permeate fluid allowing the exchange of nutrients between the vascularized vertebral bodies and the avascular NP/AF. The NP is a gelatinous tissue located centrally in the IVD (Figure 1b) that generates large swelling pressures. This pressure arises from the composition of the NP: a collagen and elastin fiber network with high glycosaminoglycan (GAG) content, which results in approximately 80% water content in healthy NP[21]. Healthy NP has chondrocytic cells with a spherical morphology and reported cell populations of 5000 cells/mm^3 [22].

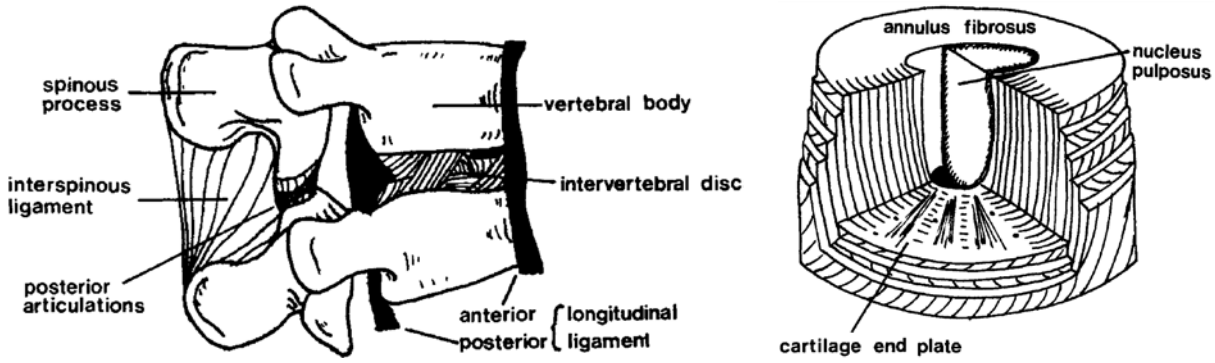

(a) (b)

Figure 1. Diagrams of the IVD: **(a)** the IVD and adjacent vertebrae in situ indicating important anatomical features, and **(b)** the structure of the intervertebral disc depicting the the main anatomical regions. Figure adopted from Humzah & Soames[23] with permission from John Wiley and Sons, Inc.

1.2.2. The Annulus Fibrosus

The NP is peripherally contained by the AF, a highly collagenous fibrocartilage with multiple concentric lamellae (Figure 1b)[23]. The AF is composed of 15-25 lamellae[24], increasing in thickness radially from approximately 200 µm at the inner AF to 400 µm at the outer AF[25]. Fibril bundles measuring 10-50 µm in diameter within the AF are composed of collagen types I, II, and III[23]. These fiber bundles are crimped and aligned parallel within each lamellae. Between each lamellae, the alignment of collagen alternates, forming an angle-ply architecture (Figure 2). Interlamellar fibers of collagen and elastin also span between lamellae, and Sharpey's fibers anchor the AF through the CEP into the adjacent vertebral bodies[26].

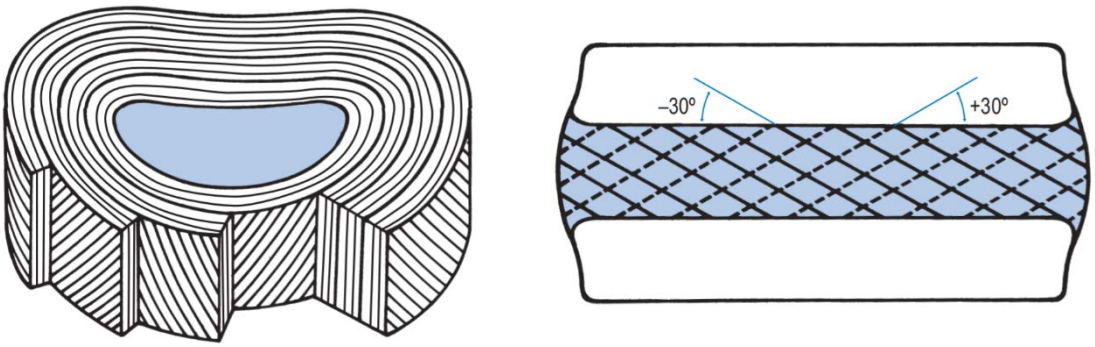

Figure 2. Angle-ply laminate collagen structure of the AF depicting the highly-organized, alternating fiber orientation. Collagen fiber in the outer lamellae are oriented approximately ±30° from the circumferential direction. Figure adopted from Ombregt[27] with permission from Elsevier.

Lamellae of the AF are not homogenous and exhibit distinct structural and phenotypical differences in the radial direction. There is no well-defined boundary between AF and NP but, instead, a gradual change in cell phenotype and tissue structure between these regions. On the peripheral wall of the IVD, the outer lamellae have a higher collagen type I fiber content which are aligned in two distinct directions approximately ±30° from the circumferential direction (Figure 2)[28]. Fibroblast cells in the outer lamellae are elongated and oriented to the dominant fiber directions. Lamellae closer to the center of the IVD have an increasing collagen-II fiber content that gradually orient to approximately 45° in the lamellar plane[28]. The inner lamellae exhibit increasing similarity to NP. As compared to the outer lamellae, inner lamellae contain a higher proteoglycan content, cells are more sparsely distributed with a more rounded morphology, and gene expression is more alike NP. These structural and phenotypical differences in AF lamellae partially derive from their variations in mechanical role. Inner lamellae have a transverse isotropic architecture with large hydrostatic support, facilitating the mechanical transition from NP to outer AF. Conversely, the structure of the outer annulus is developed to prevent annular bulging.

1.2.3. Mechanics of the Annulus Fibrosus

Mechanically, the AF experiences relatively large and coincident circumferential and axial stresses and strains *in vivo*[28]. This mechanical loading drives the highly-structured architecture of the AF. Accordingly, the AF exhibits anisotropic, inhomogeneous, and nonlinear elastic behavior[28–30]. It has been reported that the healthy human AF exhibits a range of elastic moduli, and that these material coefficients are highly dependent upon the loading modality (i.e. compressive, tensile, shear, etc.) and due to the simultaneous stresses (uniaxial, biaxial, etc.) imposed on the tissue[29,31–42]. Therefore, multiaxial testing and, in particular, biaxial testing is essential to characterize the physiologically-relevant mechanics of the AF (and AF replacements) by reproducing the major *in vivo* loads and constraints experienced by the AF[43]. Specifically, AF has no free boundaries, is continuous in the circumferential direction, and is constrained axially by the CEPs[43].

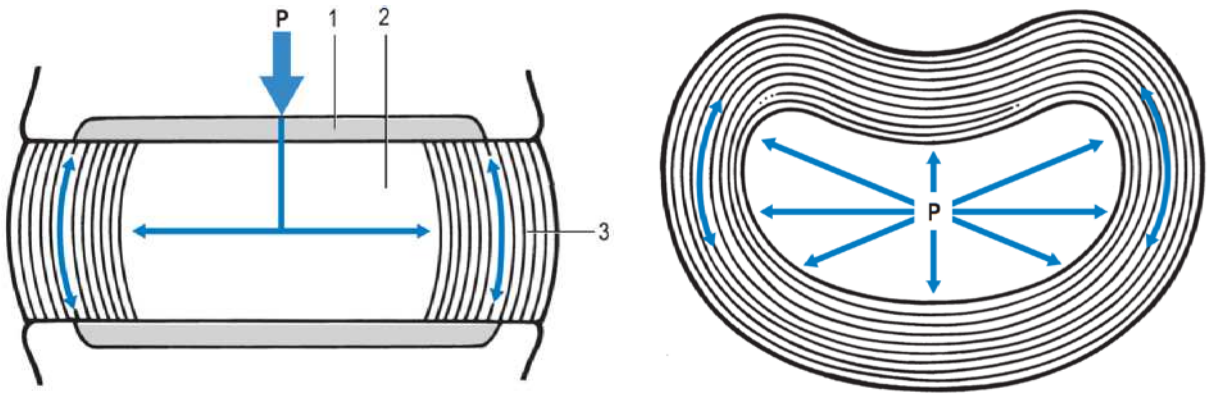

Figure 3. Loading of the AF *in vivo*. **(a)** Coronal plane view showing the bodyweight load (large blue arrow, labelled "P") delivered via the CEPs (labelled "1"), supported by the pressurized NP (labelled "2), and distributed as axial tension in the AF (labelled "3"). **(b)** Transverse plane view of nucleus pressurization under the same bodyweight load, P, generating circumferential tension (hoop stress) in the AF. Figure adopted from Ombregt[27] with permission from Elsevier.

Previously reported moduli of human AF subject to local equibiaxial, local transverse-constrained uniaxial, and unconstrained uniaxial tension are shown in Table 1. These moduli demonstrate the range of stiffnesses of AF tissue in various loading modes and the relative stiffnesses between loading modes. However, these mechanical properties may also vary dramatically due to the rate and magnitude of loading, anatomical location, inherent variation within the population, and interpretation of the nonlinear mechanical response. The AF experiences *in vivo* disc pressures up to 2.3 MPa[44] and biaxial tensile strains between 4% and 6% in magnitude during typical functional loading (flexion and extension)[45]. Compressive and tensile *in vivo* AF strains have been reported up to 28% and 65%, respectively[46,47]. However, higher strains have been linked to catabolic responses in isolated AF cells[48–50].

Table 1. Linear-region elastic moduli, E, and axial-to-circumferential elastic moduli ratio, E_r, of AF tissue in biaxial and uniaxial loading modes.

Load Condition	Measure	Min.	Max.	Reference
Equibiaxial	E (MPa)	27	87	[31]
	E_r	0.55	0.62	[31]
Constrained Uniaxial	E (MPa)	13	27	[33]
Unconstrained Uniaxial	E (MPa)	0.42	45	[29,34–40]

1.2.4. Cellular Micromechanical Environment in the Annulus Fibrosus

The biological and mechanical integrity of the AF is contingent on the production and maintenance of ECM by AF cells[21,51], and diseased states of the IVD have been associated with a loss of tissue cellularity and dramatic changes to the organization and regeneration of the ECM[52–54]. A major regulator of cell viability, differentiation, and extracellular matrix (ECM) deposition is mechanical loading[55–58]. As compared to other anatomical systems, the musculoskeletal system experiences a broad magnitude of mechanical loads. Consequently, cell fates in muscle, bone, articular cartilage, fibrocartilage, tendon, and ligament are all driven largely by mechanical cues. For example, studies on mesenchymal stem cells and bone fracture healing have used hydrostatic stress history and maximum principal strain history as mechanical measures to model tissue regeneration[59,60]. In these models, the cellular micromechanical environment to generate and maintain fibrocartilaginous tissue is congruent with the *in vivo* loads experienced by the AF. Specifically, fibrocartilage has been shown to develop where the local three-dimensional mechanical state has a tensile strain history with simultaneous compressive hydrostatic loading.

To generate fibrocartilage, studies have demonstrated that mechanical loading is critical to stimulate cell activity and gene expression[61,62]. Cyclic loading at a physiological frequency (1 Hz) has been shown to be essential for AF cells to maintain matrix production and prevent catabolic reponses[49,50,63]. AF cells isolated from rabbits have demonstrated anabolic responses at maximum principal strains (ϵ_1) of 3% to 18%, and this response was maximized at 6% strain[64]. At 1% strain, rabbit AF cells have demonstrated no significant changes in proteoglycan production, cell death, MMP-1 expression, or MMP-3 expression as compared to static loading[65]. This remodeling window is supported in studies of human AF cells. Upregulation of catabolic factors associated with disc degeneration has been demonstrated at 20% strain[48]. Decreased catabolic gene expression has been shown for human AF cells at 10% strain[66], and increased cell proliferation, collagen production, and glycosaminoglycan production has been reported at this strain magnitude[67]. Similarly, AF cells have exhibited anabolic responses for compressive hydrostatic strains ($\epsilon_h < 0$)[68–72] and an upper limit of 1 MPa compressive hydrostatic stress ($\sigma_h > -1$ MPa) has been proposed for eliciting catabolic responses[69,73]. Accordingly, these maximum principal strain and hydrostatic stress remodeling windows may be utilized as targets for cell-level loading to drive AF regeneration.

1.3. Intervertebral Disc Disease

Pathologies of the IVD which lead to impaired function of the spine and severe pain are extremely common in society[53,74]. These pathologies cause the disc to fail by a complex combination of physical overloading and physiological changes. The most prevalent pathology of the IVD is degenerative disc disease, or IVD degeneration (IVDD), which causes significant morphological, biochemical, and functional transformation of the IVD[75]. Though the etiology of IVD degeneration is not well understood[76], it is generally considered to be a multifactorial

pathology due to a combination of deficient nutrient supply, excessive mechanical loading and injury, and genetic factors[77]. Chronic low back pain and IVDD are intimately related; over 40% of patients experiencing chronic low back pain have signs of disc degeneration evident in medical images[12].

During degeneration, the distinct functional regions of the IVD (CE, NP, and AF) become less defined and the tissue structures become less organized. The normally gelatinous NP transforms into a more fibrotic tissue and fissures develop throughout the IVD[53,78]. Increased vascularization and innervation are observed throughout the disc with degeneration[79]. IVD cells proliferate during degeneration and are increasingly necrotic and apoptotic[75]. From a biochemical perspective, the major attributes of IVD degeneration are a loss of proteoglycan content in the NP [80] and an alteration to the type and distribution of collagen fibers throughout the IVD[21]. Respectively, these biochemical changes reduce the hydrostatic pressure generated by the NP and structurally weaken the AF tissue. Accordingly, the disc experiences a diminished load bearing capacity, reduced disc height, and bulging of the peripheral AF wall. These degenerative transformations of the IVD also have adverse effects on spinal column mechanics which frequently lead to spinal stenosis, facet joints arthritis, and alteration of the adjacent spinal ligaments[75].

The mechanical changes incurred with degeneration frequently lead to herniation of the IVD. Consequently, herniation is the most common symptomatic disorder of the IVD[75]. IVD herniation is characterized by a rupture in the AF that allows the NP to protrude radially (Figure 4a and Figure 4b). Due to the higher loads experienced by the lower spine, 95% of herniated discs occur at the L4L5 and L5S1 levels[81]. With aging and degeneration, the NP shifts posteriorly within the IVD[78] and disc herniation typically occurs at the posterior and posterolateral aspects of the IVD (Figure 4c)[82]. This posterior location of herniation frequently results in the protruding tissue

applying pressure to the spinal cord or nerve roots and inducing a subsequent inflammatory response, resulting in low back pain. Because the primary mechanical role of the AF is to contain the NP and prevent IVD herniation, a healthy and functional AF is critical in preventing spinal herniation. Functional repair of the AF or total replacement of the whole disc function are necessary to treat the underlying pathology and relieve the associated pain.

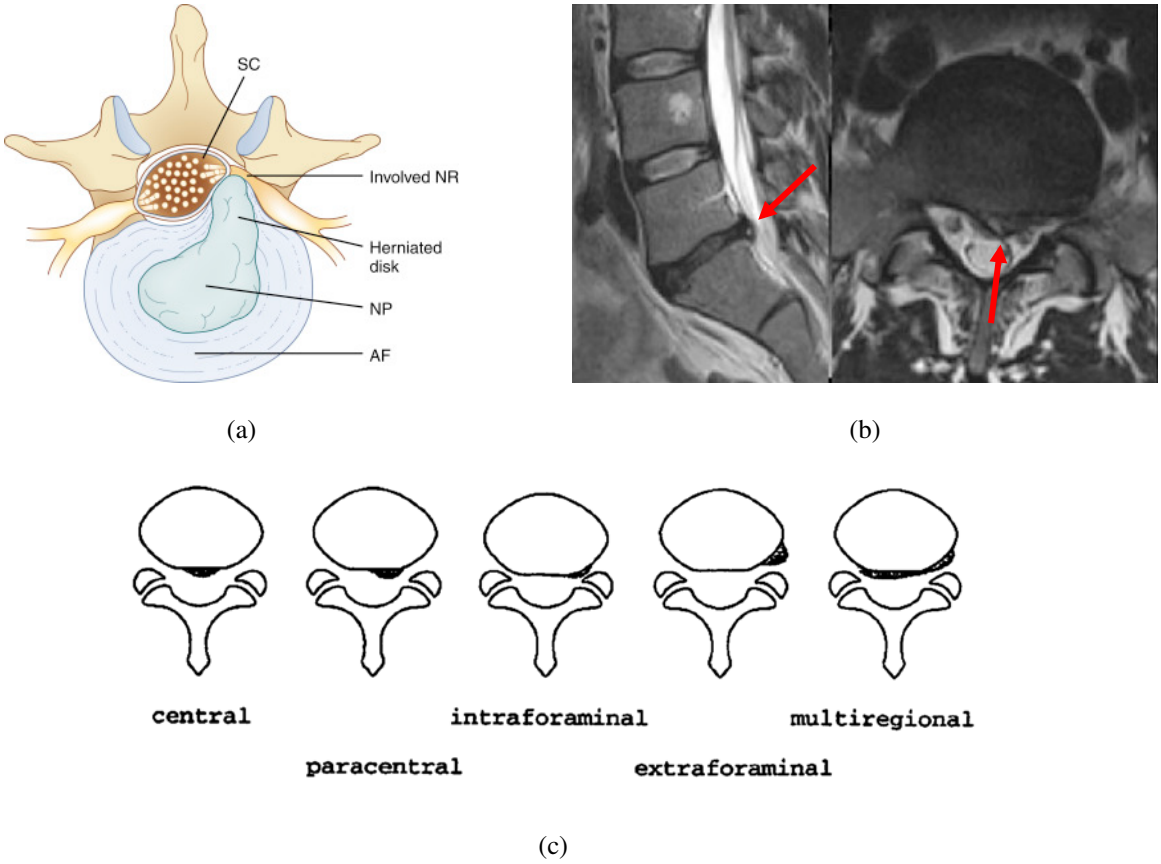

Figure 4. Herniation of the IVD disc: **(a)** cross-section schematic of disc herniation in the transverse plane showing relevant anatomy (spinal cord, SC, and nerve root, NR; adopted from Malik & Benzon[83] with permission from Elsevier), **(b)** sagittal and transverse plane radiographs of an L5S1 level disc hernia indicated by red arrows (adopted from Malik & Benzon[83] with permission from Elsevier), and **(c)** circumferential locations of disc hernias shown in the transverse plane (adopted from Knop-Jergas et al.[82] with permission from Wolters Kluwer Health, Inc.).

1.4. Treatment of Intervertebral Disc Disease

The majority of initial treatments for disc herniation are conservative due to the high rates of recovery from symptoms after one year[84]. These initial treatments are non-surgical and typically involve rest, non-steroidal anti-inflammatory drugs, and physical therapy[85]. Additional non-surgical treatments are also implemented, including translaminar epidural injections[86] and selective nerve root blocks[87]. However, these initial therapies are generally palliative and, accordingly, physicians observe remarkably high rates of pain recurrence[16].

When initial therapies are ineffective, surgical treatment is frequently required. These invasive procedures range in complexity based on specific patient needs. The simplest and most common surgical option is a laminectomy with partial discectomy, whereby the lamina of the vertebral body cranial to the diseased disc is removed, and the obtruding section of disc (both AF and NP) is extracted[88]. The objective of partial discectomy is for scar tissue to patch the damaged section of disc and mitigate sciatic pain. Various solutions have been proposed to close the residual laminectomy defect to reduce scarring and regenerate functional tissue, however, no improvements have yet been observed as compared to no closure of the AF[84].

The next most complex approach to treat spinal hernia is vertebral interbody fusion[89]. A fusion is performed via a variety of surgical approaches, however, the underlying theory is mutual; hardware is implanted into the disc space and/or adjacent vertebrae to rigidly fix the vertebral bodies surrounding the hernia. This fixation stimulates osteogenesis within the disc space and, ultimately, drives bony fusion of the two vertebral bodies. However, there is no guarantee of complete bony fusion, pain relief may be insignificant, and, when successful, the range of motion of the spine is substantially impaired[89,90]. Additionally, fusion may not provide long-term relief

because the biomechanics of the spine are altered and the underlying pathology can spread to adjacent vertebrae[91,92].

The most complex surgical treatment for disc hernia is lumbar disc arthroplasty (total disc replacement)[93,94]. In lumbar disc arthroplasty, the diseased disc is surgically removed and hardware is implanted to the adjacent vertebrae. These implants are engineered to form a mechanical coupling in the disc space that mimics the motion of a healthy disc. Various designs for disc prostheses have been proposed, involving a range of materials and surgical approaches[91,95]. However, complications limit the efficacy of lumbar disc arthroplasty, including poor implant integration with the body, implant wear, and heterotopic ossification[94,96]. Further, despite recovering some of the physiological motion of the native disc, there is little evidence that total disc replacement is superior to spinal fusion to prevent adjacent segment pathology[97].

Due to the avascularity and associated limited healing potential of the IVD, clinicians are currently restricted to palliative treatments for IVD disease. All current treatments for disc hernia fail to restore the native tissue's durability and range of motion. Further, the most prominent complications associated with surgical intervention to treat IVD disease are symptomatic reherniation and revision surgery[98]. Current surgical interventions improve short term outcomes for patients but provide little difference in long term outcomes as compared to conservative treatments[99–101]. Accordingly, advanced surgical strategies are essential to treat the impaired function and severe pain associated with common IVD pathologies. Instead of removal or replacement of the IVD, there is a widely acknowledged need for therapeutic alternatives to regenerate the diseased tissue[102–107]. Accordingly, regeneration of the AF represents a paradigm shift in treatment to both alleviate pain and restore physiologic function following IVD degeneration or herniation[108].

1.5. Tissue Engineering

Tissue engineering (TE) is a ubiquitous strategy for the regeneration of musculoskeletal soft tissues. The prevailing approach to engineering orthopedic tissue constructs is to combine natural or synthetic scaffolds with cellular content to restore the complex biological and mechanical functions of native tissues[109–111].

1.5.1. Role of Mechanics in Tissue Engineering

The purpose of fabricating tissue-engineered (TE) scaffolds that replicate native tissue mechanics is to: (1) retain healthy biomechanics and (2) regenerate healthy and functional tissue. The mechanical efficacy of TE scaffolds is, therefore, critical to afford essential structural support, functional performance, resilience to implant failure, and a micromechanical environment conducive for the generation and maintenance of the intended mature tissue[112,113]. Mechanical stimuli are an essential driving factor of cell phenotype in musculoskeletal tissues. Similarly, in TE scaffolds, mechanical stimuli are necessary to stimulate appropriate differentiation of seeded progenitor cells and generation of extracellular matrix[55,59,114–116]. Accordingly, under physiological loading of the TE construct, it is necessary that the *in vivo* state of stress and distortion at the cellular level is conducive to tissue regeneration.

1.5.2. Materials in Tissue Engineering

Biocompatible and biodegradable materials are integral in TE to provide an initial support structure while also providing a temporal degradation profile to enhance tissue development and growth[117]. Accordingly, a prevalent polymer for tissue engineering is polycaprolactone (PCL), a biodegradable polyester which degrades in physiological conditions by hydrolysis[118]. In the presence of water, the ester bonds in PCL are progressively cleaved. Eventually, water-soluble

degradation products (oligomers and monomer 6-hydroxicapronic acid) are formed and removed by the body. The degradation time of PCL is approximately two years; however, copolymers of PCL have been synthesized to reduce this degradation time[119].

1.5.3. Tissue Engineering of the Intervertebral Disc

A variety of novel, TE biomaterials have been proposed for AF regeneration [120–123]. However, effective implementation of these biomaterials to an IVD repair strategy remains elusive. Total disc replacements with regenerative constructs have been evaluated in small animal models[124,125] and large animal models[124,126]. Nonetheless, there remains an unresolved need to translate TE biomaterials into a surgically feasible strategy for IVD repair that can both elicit tissue regeneration and retain healthy spinal biomechanics.

When treating discogenic pain, degenerative changes may exist throughout the whole disc. However, the symptomatic region of the IVD is frequently limited to a smaller annular defect[82]. Therefore, instead of a complete replacement of the IVD, an approach focused on localized regeneration of the AF defect may afford a less invasive solution to prevent reherniation. However, this approach requires careful consideration of implant design and attachment to ensure that the spinal biomechanics and CME within the defect are conducive to tissue regeneration.

1.5.4. Animal Models for Tissue Engineering Strategies

Animal models are invaluable evaluation platforms to translate novel orthopaedic therapies and designs to human clinical applications. Animal models facilitate the evaluation of treatment efficacy in highly controlled study groups that are ethically and practically intractable in human clinical studies. For example, accurate quantification of the spinal biomechanics (e.g., range of motion) following lumbar fusion in humans is limited to cadaveric studies. When investigating the

spinal biomechanics of an orthopaedic treatment, it is essential that an animal model closely reflects the physiological scale and mechanical loading of the human spine. As compared to small animals (rodents, rabbits, etc.), large animal models present a more clinically relevant evaluation platform for IVD treatments with superior predictive validity[127–129]. In particular, the ovine model for lumbar spine treatments is a widely accepted and well-established translational model[130–133]. Therefore, the ovine lumbar spine model is a suitable candidate to experimentally evaluate TE strategies for the IVD.

1.6. Additive Manufacturing

An array of engineered AF repair strategies have been proposed[122,134–136] and a prevalent technique for fabricating AF scaffolds is additive manufacturing (AM)[121,137,138]. The adaptability and flexibility of AM facilitates production of engineered constructs beyond the practical capabilities of traditional manufacturing, including patient-specific design and the seeding of live cells during scaffold manufacture[139]. Biomimetic fibrous composite scaffolds with structural fibers that replicate the native collagen architecture are well suited to AF repair and have demonstrated some *in vitro* success[140,141]. Specifically, three-dimensional fiber deposition (3DF) and melt electrowriting (MEW) are commonly used to fabrication ply-laminate soft tissue scaffolds.

1.6.1. Three-Dimensional Fiber Deposition

Additive manufacturing via 3DF involves extrusion of a thermoplastic polymer melt typically driven by a filament, pneumatic pressure, piston, or auger. The extruded fiber is deposited in three-dimensional space with a translating printhead and/or substrate. 3DF is the most widely adopted additive manufacturing method due to the simplicity of the process and quality of the prints. Moreover, 3DF is easily applied to tissue engineering by using biological, biocompatible,

and/or bioresorbable materials. However, according to the Hagen-Poiseuille equation (Equation 1), the extruded fiber diameter in 3DF has a lower limit in size due to the requisite driving force and melt fluidity. Accordingly, fibers produced via 3DF are relatively large, typically measuring 100-1000 μm diameter[142,143].

$$P = \frac{8QL\mu}{\pi r^4} \quad (1)$$

where P is the extrusion pressure, Q is the volumetric flow rate of polymer melt, L is the length of the extruder nozzle, μ is the dynamic viscosity of the polymer melt, and r is the internal radius of the extruder nozzle.

1.6.2. Melt Electrowriting

MEW is a recently developed additive manufacturing process which utilizes a high-voltage source to generate an electric potential between the printhead and substrate to drive polymer melt jetting[144]. The electric potential drives electrostatic repulsion on the surface of the extruded polymer. With sufficient electric potential, the electrostatic repulsion overcomes the surface tension of the polymer melt. At this critical point, the extrusion is drawn into a Taylor cone and polymer jet (Figure 5a). The characteristics of the polymer jet are dependent on a number of process parameters. The flow rate of extruded polymer melt is governed by the Hagen-Poiseuille equation (Equation 1) and, therefore, the driving pressure, nozzle length, nozzle radius, and viscosity (controlled by the temperature and molecular weight of the polymer) are essential to MEW. Further, electrostatic repulsion is driven by the electric potential and distance between the printhead and collector. To generate a stable Taylor cone and polymer jet, a balance is required between material flow rate and the driving electrostatic repulsion. Generally, reducing the material

flow rate and increasing the electrostatic repulsion results in smaller fibers. However, at some limit, the molecular cohesion of the polymer melt prevents small fibers from jetting continuously. Therefore, material flow rate and electric potential are intimately related and create a small window of printing parameters for stable MEW fiber production.

MEW typically yields fiber diameters much smaller than achievable with 3DF (approximately 25 μm[144]). However, due to the reduced size of the fibers, the volumetric rate of material deposition is substantially lower. Accordingly, extremely long print times and small print volumes currently limit the applications of MEW in tissue engineering. Moreover, for a constant material flow rate, the small MEW fibers require that the polymer is extruded at an appreciably higher velocity as compared to 3DF (Figure 5b). To deposit straight fibers, the printhead must translate relative to the collector at least as fast as the polymer jet, imposing demanding actuation requirements on the printer. Moreover, the requisite translation velocities prohibit deposition of individual MEW fibers into precise geometries; MEW fibers are currently limited to deposition in relatively long, straight lines.

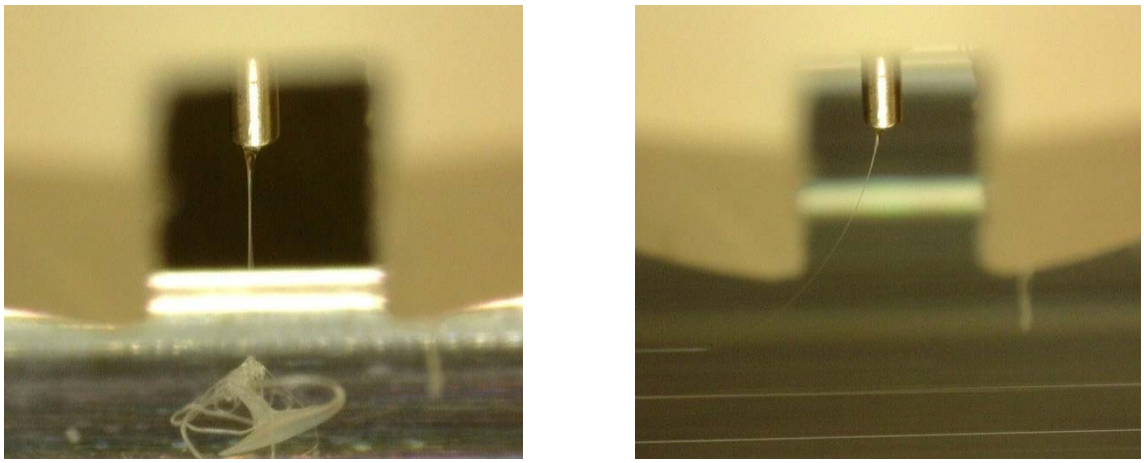

(a) (b)

Figure 5. Digital images of MEW process with PCL: **(a)** formation of polymer jet showing a stabilized Taylor cone at the needle tip of a stationary printhead and **(b)** direct writing of the polymer jet into straight lines by translating the printhead at a high velocity.

1.6.3. Additive Manufacturing in Tissue Engineering

The main limitations in leveraging MEW scaffolds for TE are: (1) prohibitively long fabrication times, (2) a poor ability to form complex scaffolds geometries, and (3) insufficient durability of the fine fibers. Further, for biodegradable TE scaffolds, 3DF fibers provide a slower degradation profile as compared to MEW scaffolds, providing additional time for tissue regeneration. Additive manufacturing via 3DF can yield scaffolds with consistent mechanical properties, and it may be possible to tailor these mechanical properties to replicate the continuum-level mechanics of native AF. However, it remains unclear whether physiological loading of these scaffolds will be sufficient to stimulate progenitor cells to a fibrocartilaginous phenotype. The large scale of 3DF fibers may limit their ability to interact with resident cells in a TE scaffold and influence tissue regeneration. The smaller fibers generated from MEW may provide a greater functional relevance to the resident cells; MEW scaffolds have a similarity in scale to natural collagen fibers[145] and yield a substantially larger surface are per unit volume as compared to 3DF

scaffolds. Accordingly, it is hypothesized that combining 3DF fibers and MEW fibers in a tissue engineering strategy may leverage the mechanical and biological advantages of both fiber scales.

1.6.4. Parameters in Additive Manufacturing

Both 3DF and MEW are commonly used to fabrication ply-laminate soft tissue scaffolds according to a variety of highly-tailorable print parameters[142,143]. These parameters facilitate a simple angle-ply design principle to achieve a diverse range of architectures and resultant mechanics. Print parameters in 3DF can be broadly categorized as design or process parameters. Design parameters typically relate to the scaffold architecture and are generally executed to a high precision. Process parameters are difficult to control due to the specific machine setup and print execution, and therefore, require validation in the printed product. The categorization of pertinent print parameters in angle-ply laminate architectures are shown in Table 2.

Table 2. Examples of fibrous angle-ply laminate print parameters in 3DF and MEW printing categorized as process or design parameters.

Parameters	**Category**
Material properties	Process
Fiber angle	Design
Fiber spacing	Design
Fiber diameter	Process
Interlamellar contact area	Process
Lamellar thickness	Process

1.7. Computational Methods in Tissue Engineering

Experimental methods are essential for developing advanced strategies for AF repair. However, empirical approaches are frequently associated with practical limitations, such as the prescription and measurement of experimental variables. Accordingly, computational methods may be leveraged to provide a theoretical understanding of the underlying physical phenomena and instruct experimental design. In the context of TE of the AF, computational methods can be used to aid in the design of TE scaffolds, the characterization of the cellular micromechanical environment within a TE construct, or the surgical implementation of the tissue engineering strategy.

1.7.1. Computational Methods and Tissue Engineered Scaffold Mechanics

Due to the numerous available print parameters, iterative design of TE scaffold architectures using additive manufacturing is time- and resource-intensive. Hence, there is an interest in computational methods for high-throughput assessment of 3DF scaffold mechanics for broad print parameter design spaces. Moreover, computational methods can provide insight into how foreseeable manufacturing perturbations to process parameters may affect 3DF scaffold mechanics. Finite element (FE) approaches to AM tissue engineering approaches are increasingly popular to tailor mechanics and predict favorable cellular environments[146,147]. For example, FE models have been used to evaluate the strength and fracture modes of ink-deposited ceramic ply-laminate architectures[148], the dynamic stiffness of fiber-deposited ply-laminate architectures[149], and the mechanics of tubular scaffolds fabricated with melt electrowritten fibers[150].

1.7.2. Computational Methods and the Cellular Micromechanical Environment

TE scaffolds have been engineered to replicate specific tissue-level material properties of the AF. However, these scaffolds do not necessarily ensure that the mechanical loads induced at the cellular level are sufficient to drive cell survival, proliferation, and ECM formation. The relationship between tissue-level loading and the cellular micromechanical environment (CME) is, therefore, essential to furthering our understanding of how best to design TE scaffolds. Yet, it is intractable to measure and prescribe the CME in cell-laden matrices of TE scaffolds. The CME is three-dimensional, heterogeneous, and dependent on scaffold loading, materials, and architecture; current experimental methods are not capable of accurately prescribing and/or measuring the CME. For example, in the aforementioned complementary experimental series, there is no physical method to know what CME is generated under global (i.e. tissue level) loading of the TE scaffolds and whether or not that CME will be beneficial for regenerating the desired tissue. Optical strain measurement techniques, such as digital image correlation (DIC) and confocal microscopy, have been used to measure deformations in biological materials[151–153]. However, both DIC and confocal microscopy also require the addition of a texturing material to capture deformations accurately and are not well suited for high-throughput analyses. DIC techniques are limited in that they can only measure two-dimensional surface strains and the resultant surface strains typically do not represent the complete deformation mapping within the scaffold. Confocal microscopy techniques may also be restricted by the opacity of the scaffold and hydrogel.

In addition to the experimental difficulties of measuring CME, TE experiments with dynamic mechanical loading may be prohibitively time consuming to effectively characterize the relationship between tissue-level and cellular-level loading. Due to the complex apparatus required

for precise multiaxial loading, scaffolds may be limited to successive cultures. For a typical culture time of 30 days per specimen, a single study group may take 6-12 months to produce statistically powerful results. Further, subsequent study groups aimed to improve tissue regeneration will have a similar study duration. Therefore, in order to optimize the development timeline of tissue regeneration strategies, it is imperative that the most advantageous study groups are selected for experimental evaluation. However, there is currently no method to identify which scaffold design features and experimental conditions are most likely to drive improved tissue regeneration. For example, is the CME more sensitive to scaffold loading, materials, or architectural parameters?

In the absence of any feasible experimental methods, one possible tool to predict ECM formation in TE scaffolds is the finite element (FE) method. Cell fates in orthopaedic tissues under mechanical loading have been modelled with FE in intervertebral disc[52,154] and bone fracture healing[155] applications. The tissue-level mechanics of TE scaffolds have also been studied using FE methods[153,156–158], and some of these models have been developed to predict mechano-regulation of musculoskeletal regeneration[159–161]. However, there remains a need for a CME model that can: (1) be applied to the available volume that can cells can occupy in heterogeneous TE scaffolds, (2) be applied parametrically to numerous candidate TE scaffold designs, (3) be broadly applied to a range of proposed target mechanics, and (4) be easily compared to *in vitro* cell cultures for validation.

1.7.3. Computational Methods and Spinal Biomechanics

Large animal models provide a suitable translational platform to assess IVD repair strategies. However, it is prohibitively time and resource intensive to study numerous design iterations with sufficient group sizes for statistical power. Further, mechanical loading of an

implant dictates the complex, three-dimensional cellular micromechanical environment (CME) within the implant, which is a critical regulator of tissue regeneration. To address these limitations, computational methods, such as finite element analyses, can be utilized to efficiently predict how changes in implant design and surgical approach may alter the biomechanics and resultant implant micromechanics. For example, a computational model can predict the influence of a complete change of implant geometry or a small perturbation to the implant attachment technique. These perturbations may represent intentional changes to the surgical approach, variability among the population, or reasonably expected variability during surgical implementation. Predictions from computational methods facilitate high-throughput evaluation of design modifications to identify critical design features and drive an efficient and effective experimental approach to AF repair.

1.8. Summary

CLBP is a ubiquitous injury in society and has immense consequences both financially and in quality of life. A leading cause of CLBP is herniation of the intervertebral disc (IVD). The IVD plays an essential mechanical role in the spinal column and degenerative changes to the AF result in a marked increase in susceptibly to IVD herniation. Although there is a variety of established treatments for IVD herniation, no current therapies for IVD herniation effectively alleviate low back pain and restore long-term function of the IVD. Accordingly, there is an impetus for novel strategies to repair the IVD. A prevalent approach to the repair of musculoskeletal tissues is regenerative therapy via tissue engineering (TE). The emergence of advanced manufacturing technology, including the printing of biological content and biocompatible materials, presents new opportunities to regenerate functional tissue replacements. Accordingly, the overall objective of this research is to utilize additive manufacturing to tissue engineer a repair patch for IVD herniation towards a treatment for CLBP.

1.9. Specific Aims

The overarching goal of the proposed research was to develop experimental and computational methods to engineer (1) the overall mechanics and (2) the cellular micromechanical environment of a partial AF replacement that is conducive for the generation and maintenance of functional, healthy intervertebral disc tissue. To achieve the aforementioned goals, three specific aims were proposed. A summary of the specific aims and overall research flow is shown in Figure **6**.

1.9.1. Specific Aim 1

Specific Aim 1 was to characterize the mechanics of additive manufactured angle-ply scaffolds using experimental and computational methods.

Uniaxial and biaxial mechanical testing was conducted on fabricated PCL angle-ply cruciform scaffolds with varying fiber architectures. The resulting mechanical properties were compared to reported design criteria for AF to evaluate the scaffolds for suitability as an AF replacement. Further, a FE computational model of the scaffolds was developed and validated against the experimental uniaxial and biaxial results. This FE model was implemented to predict the relative influence of major scaffold print parameters to identify which of these parameters play a critical role in scaffold mechanics. These data were used to inform the design of TE scaffolds to best emulate native AF mechanics.

1.9.2. Specific Aim 2

Specific Aim 2 was to evaluate the tissue response of cell-laden scaffolds cultured with dynamic biaxial mechanical stimulus using experimental and computational methods.

Using the results of Specific Aim 1, a hybrid 3DF/MEW scaffold architecture was designed, fabricated, and infused with a cell-laden hydrogel. A custom incubator was developed for dynamic multiaxial cell culturing of TE scaffolds to evaluate the survival, proliferation, and attachment of mature AF cells when subject to physiologically relevant multiaxial loads. To supplement this experimental model, a multi-level FE model of cellular differentiation was developed based on the induced micromechanical environment within the augmented scaffold. Hyperelastic mechanical characterization of hydrogels was conducted as a material input for the FE model. The efficacy of the FE model was evaluated against experimental cellular outcomes. Further, parametric studies were implemented on the model to investigate how selected print parameters may influence this cellular micromechanical environment.

1.9.3. Specific Aim 3

Specific Aim 3 was to design an annulus fibrosus repair patch using experimental and computational methods and implement the patch in an ovine lumbar spine model.

An AF repair implant for clinical application was developed based on the results of Specific Aims 1 and 2. In collaboration with human and veterinary orthopaedic spine surgeons, implant geometries were designed and fabricated using additive manufacturing techniques. Methods to mechanically integrate the implant design in the spine were evaluated by utilizing a previously developed FE lumbar spine model[162]. The proposed human implant design was translated to an ovine spine model in collaboration with veterinary surgeons. The designed implant was mechanically evaluated via *ex vivo* implantation in an ovine spine model to verify that: (a) the implant effectively recovered the stiffness and range of motion (ROM) of a functional spine unit, and (b) the implant was resistant to mechanical failure under expected loading conditions. This

mechanical evaluation provided a basis for an acellular *in vivo* investigation of the implant design in an ovine model. This *in vivo* study was evaluated with the same mechanical protocol as was developed for the *in vitro* testing as well as subsequent histologic imaging.

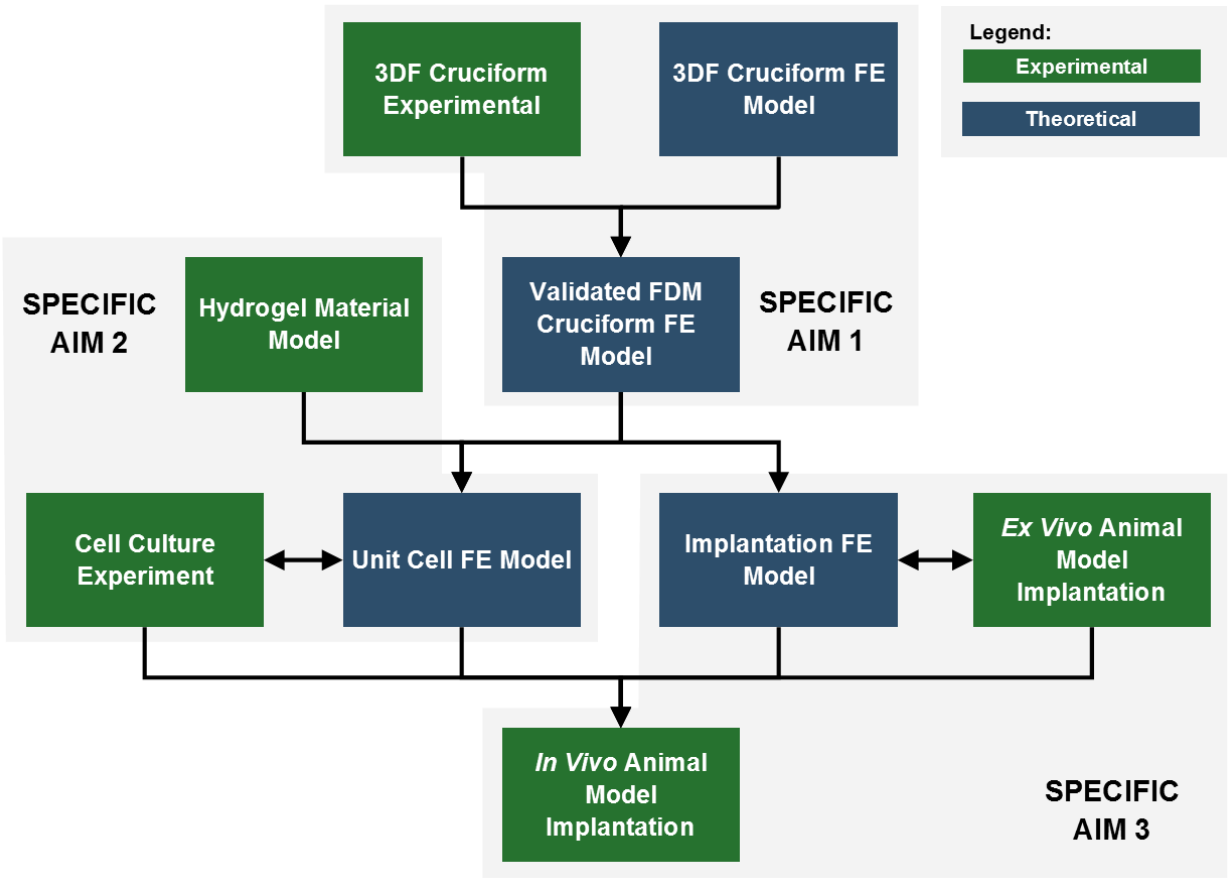

Figure 6. Research flow diagram showing the three proposed specific aims and interactions between the specific aims.

CHAPTER 2 – MECHANICAL CHARACTERIZATION OF ADDITIVE MANUFACTURED ANGLE-PLY SCAFFOLDS

Specific Aim 1 was to characterize the mechanics of additive manufactured angle-ply scaffolds using experimental and computational methods. The experimental and computational aspects of Specific Aim 1 are divided into Section 2.1 and Section 2.2, respectively.

2.1. Experimental Approach[a]

2.1.1. Introduction

Though engineered constructs have been developed to achieve the target mechanics of native AF[125,137], it remains unknown how sensitive construct mechanics (and consequently the underlying micromechanical environment) are to perturbations in the principal print parameters. Given that subtle changes to the micromechanical environment are known to induce dramatic changes in cellular response[55,59,112–116], it is possible that subtle perturbations in print parameters may lead to undesirable tissue responses. It is therefore advantageous to understand the behavior of printed constructs in physiologically-relevant loading modes. To our knowledge, this is the first study of the biaxial mechanics of 3DF angle-ply scaffolds. In this study, five groups of angle-ply laminate scaffolds with varying fiber angle and fiber spacing were mechanically evaluated in uniaxial and biaxial tensile strain and compared to native AF. The results of this study aim to facilitate micromechanical environment-driven design of engineered tissues towards favorable

[a] The content of Section 2.1 has been published as a research article in the Journal of the Mechanical Behavior of Biomedical Materials (DOI: 10.1016/j.jmbbm.2019.06.029). All content has been adapted with permission from Elsevier.

tissue responses that are not confounded by foreseeable perturbations in manufacturing and clinical application.

2.1.2. Materials and Methods

Scaffolds were designed for mechanical testing via melt extrusion 3DF consisting of an alternate ply laminate in a cruciform geometry. These cruciform shapes have been validated for use in biaxial testing protocols and have been used for evaluating native tissue AF[33,163]. Four initial scaffold designs were created using the Bioscaffolder software (SYS + ENG, Salzgitter-Bad, Germany) based on a set of consistent design parameters: number of bilayers (3), fiber spacing (1.0 mm), vertical step height between layers (0.2 mm), and fiber angle (±30°, ±35°, ±40°, and ±45° from the y-axis, with n = 7, 7, 7, and 5, respectively). A fifth group (n = 7) with ±42° fibers and 0.6 mm fiber spacing was also designed to yield a volume fraction of approximately 0.5, which has been reported to be an approximate upper limit for delivering sufficient cell ingrowth[164].

A BioScaffolder 3D fiber deposition system (SYS + ENG, Salzgitter-Bad, Germany) was used to manufacture the cruciforms. Polycaprolactone (PCL) was selected as a candidate material for AF tissue engineering due to its biodegradability, biocompatibility, printability, and approximation of its melt extruded elastic modulus (approximately 265 MPa[165]) to native AF (0.42-87 MPa[29–40]) given the target scaffold volume fraction (approximately 30%). PCL pellets (CAPA 6500, Perstorp, Sweden) were melted at 120 °C in the printer for at least 30 minutes prior to printing. Fibers were deposited though a 25 gauge nozzle (auger speed = 4 rpm; extrusion pressure = 6 bar) onto double-sided adhesive at a printhead (x-y) speed of 400 mm/min with an initial vertical (z-direction) offset of 0.2 mm.

Cruciforms were mechanically tested in a custom biaxial testing apparatus (Figure 7a)[167]. The specimens were fastened with a grip-to-grip gauge length of 22.5 mm. High precision actuators (A-LST0250A, Zaber Technologies, Canada) were used to control two perpendicular grips and two load cells (250 lb capacity, Model 31 Miniature Load Cell, Honeywell, USA) at the opposing grips were used to measure the transmitted load. Transverse linear bearings at each grip were used to mitigate off-axis load distribution, resulting in a pure biaxial load regime. Graphite powder (Powdered Graphite Lubricant, AGS, USA) was applied to each specimen to create a texture for digital image correlation (DIC). A custom LabVIEW program was used to cyclically load each cruciform five times to a peak displacement of 1.5 mm (6.7 % strain) at a quasistatic rate of 0.15 mm/s (0.67 % strain/s). Five mechanical tests were conducted at different global strain ratios (x-direction:y-direction): 1:1 (equibiaxial tensile strain), 0:1 (transverse constrained uniaxial in the y-direction), 1:0 (transverse constrained uniaxial in the x-direction), unconstrained uniaxial in the y-direction, and unconstrained uniaxial in the x-direction. For the unconstrained uniaxial tests, the grips transverse to the load were removed. Digital images of the cruciform were captured at 5 Hz during the load cycles using a high resolution camera (Grasshopper3, Point Grey Research, Canada).

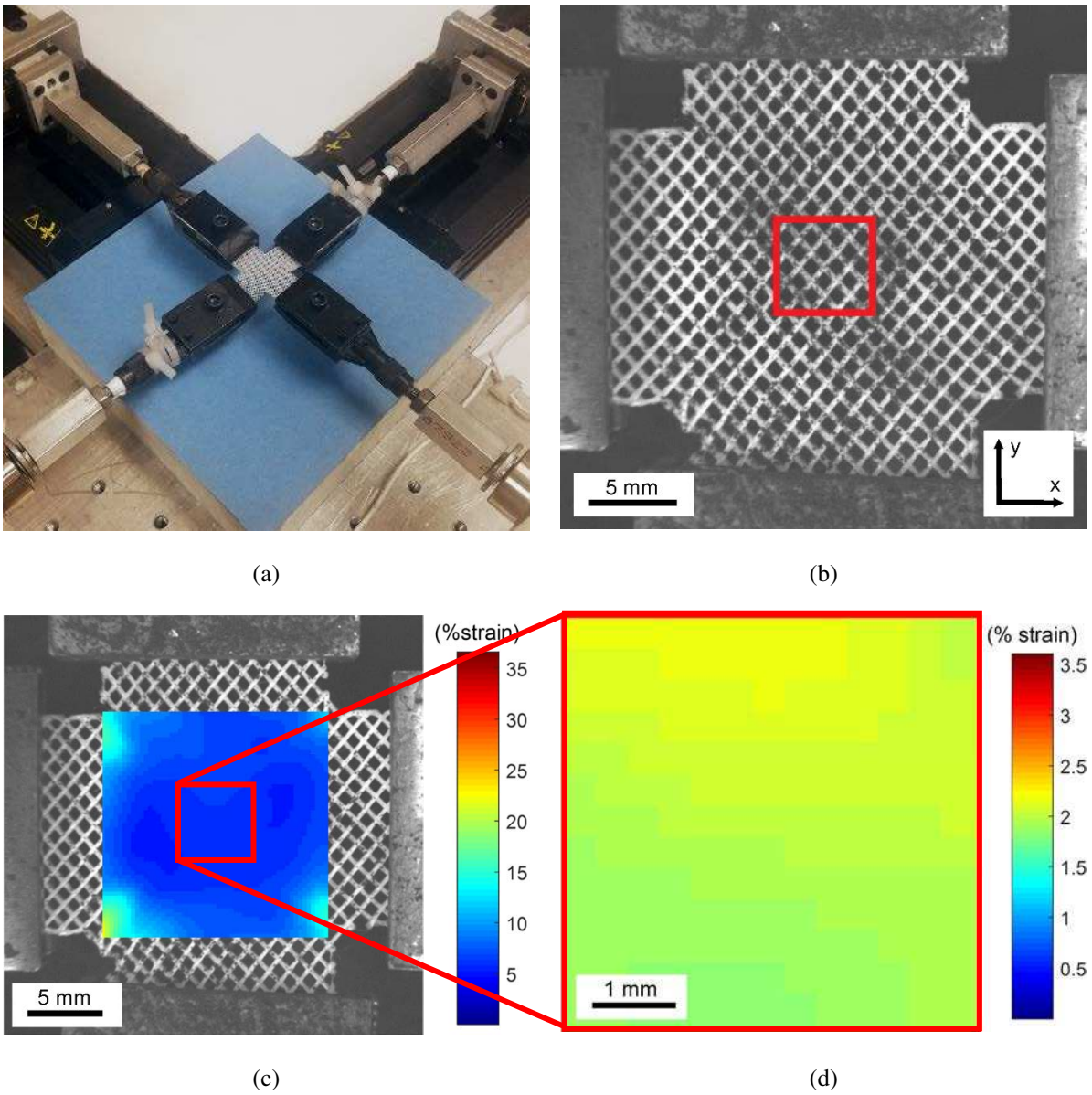

Figure 7. Experimental apparatus for performing biaxial and uniaxial tensile testing of ply-laminate cruciforms in biaxial/transverse constrained configurations. **(a)** Biaxial testing apparatus; **(b)** digital image of clamped cruciform with graphite powder highlighting the central homogeneous region; **(c)** example equivalent finite strain contour map for a cruciform in equibiaxial tension with the ROI highlighted; and **(d)** contour map of equivalent finite strain demonstrating the homogeneous ROI.

The final cycle of mechanical testing was used to evaluate the cruciform properties to allow for pre-conditioning of the scaffold. The 100 images corresponding to the final cycle were evaluated with DIC to determine the average spatial finite strains at each time point. These average

strains were evaluated in both the x- and y-directions in the central 5 x 5 mm region of the cruciform (Figure 7b), which we have previously demonstrated to be a region of homogeneous strain[167]. The resultant average finite strains were synchronized with the measured load data to yield a stress-strain response of the central homogenous region. A linear regression was applied to the final 40% of the load ramp (4 s) to evaluate the Effective Elastic moduli (EE; EE_x and EE_y for the x- and y-directions, respectively). In the equibiaxial case, the ratio of EE_y to EE_x was evaluated as the effective elastic modulus ratio (EE_r). To compare the global biaxial strain experimental data to local biaxial strain targets, a 2D orthotropic constitutive model (Equation (2) was fit to stress and strain data for each fiber angle group (final 40% of final cycle of each test) using a repeated measures linear regression model.

$$\begin{bmatrix}\sigma_x\\ \sigma_y\end{bmatrix} = \begin{bmatrix}C_{xx} & C_{xy}\\ C_{xy} & C_{yy}\end{bmatrix}\begin{bmatrix}\epsilon_x\\ \epsilon_y\end{bmatrix} \quad (2)$$

Where stress (σ) and strain (ϵ) subscripts indicate the corresponding scaffold direction and C_{xx}, C_{xy}, and C_{yy} are the fitted stiffness coefficients. The first image of the loading cycle (corresponding to an unloaded scaffold) was used to digitally measure the average fiber diameter over six locations using ImageJ (National Institutes of Health, Bethesda, MD, USA). ImageJ was also used to validate fiber angle and fiber spacing from the first image of the loading cycle. Total scaffold thicknesses were measured with digital calipers (CD-6”PSX, Mitutoyo, Kawasaki, Japan) at each of the four arms of each cruciform.

EE data from the 45° groups were combined to produce a sample number of n = 10. An Anderson-Darling normality test ($\alpha = 0.05$) and a Levene test for equal variances ($\alpha = 0.05$) was conducted for all groups. If any group failed normality and/or equal variance tests, then all groups were analyzed via one-way ANOVA with *post-hoc* Games-Howell analysis ($\alpha = 0.05$) assuming

non-equal variances in order to detect significant differences in EE and EE_r between groups. Student's t-tests were performed to determine if (1) the 45° group mean EE_r was significantly different from 1.0 and (2) any group mean EE_r was significantly different to the circumferential-to-axial ratio of native AF biaxial moduli (0.55). Orthotropic constitutive models were bootstrapped (10^4 simulations) to predict the mean and 95% confidence interval of mean biaxial moduli when subjected to local equibiaxial strain and local transverse strain. The normality of these bootstrapped predictions was measured via Shapiro-Wilk normality tests. Assuming unequal variances, predicted means of fiber angle groups were compared to the means of other fiber angle groups and reported target mechanics with individual z-tests. Returned p-values less than 0.05 were considered to convey statistical significance.

2.1.3. Results

The average and standard deviation of measured diameters and thicknesses for each study group are presented in Table 3. Deviations from the designed fiber angles and fiber spacings were not observed in the digital images. During equibiaxial tension preconditioning, some degree of fiber yielding was observed in one or more cruciform corners during preconditioning in all of the scaffolds. Nevertheless, no fiber failures were observed in the study and no further yielding was observed in subsequent tests. An instability in elastic modulus was generally observed at the initial load ramp of each cycle.

Table 3. Scaffold thickness and fiber diameter (mean and standard deviation) data for each study group.

Prescribed Fiber Angle	**Prescribed Fiber Spacing**	**Average Fiber Diameter (Stdev)**	**Average Scaffold Thickness (Stdev)**
(deg)	(mm)	(mm)	(mm)
30	1.0	0.33 (0.04)	1.08 (0.05)
35	1.0	0.35 (0.03)	1.03 (0.01)
40	1.0	0.34 (0.02)	1.05 (0.02)
45	1.0	0.33 (0.04)	1.10 (0.08)
42	0.6	0.28 (0.01)	1.05 (0.02)

The equibiaxial EE data for the 45° fiber angle group failed the normality test (though the EE_r for the 45° fiber angle group passed) and the equibiaxial EE data failed the equal variance test. Therefore, all groups were assessed via one-way ANOVA with *post-hoc* Games-Howell analysis ($\alpha = 0.05$).

The observed elastic moduli were obtained from highly linear correlations between stress and strain (Figure 8). Linear regression analyses of the 198 tests yielded $r^2 > 0.99$ for 179 tests. The remaining 19 tests were equibiaxial loading experiments. A subset of these tests (six) produced $r^2 < 0.975$ (range 0.563 to 0.933), and all of these tests were from the 40° fiber group in the non-dominant fiber direction.

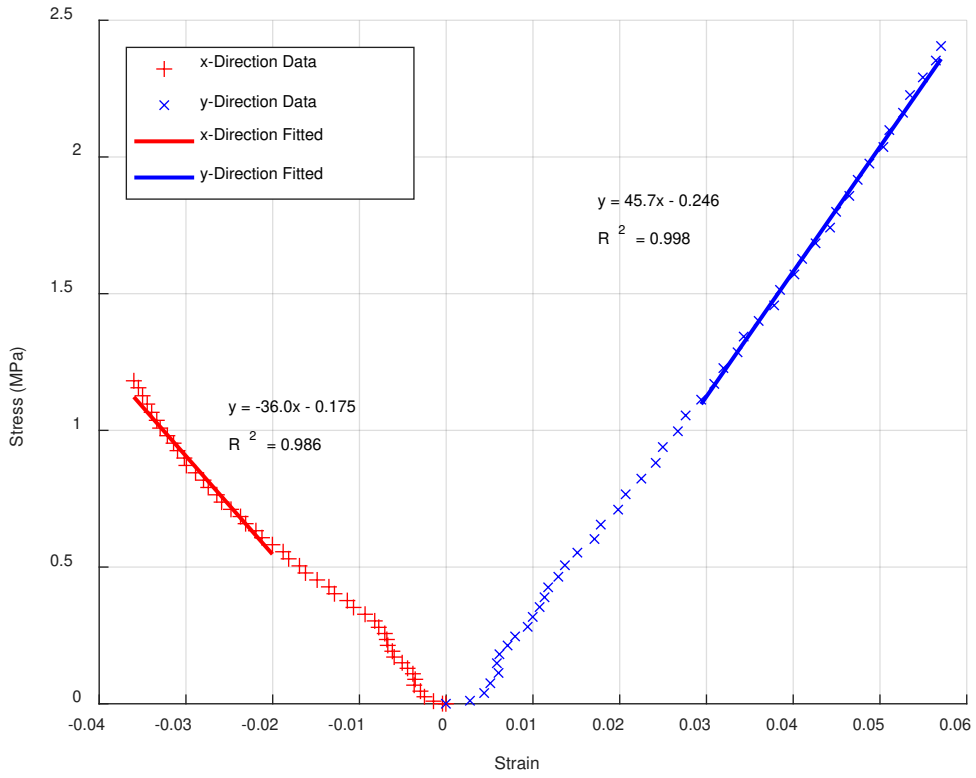

Figure 8. Example biaxial stress-strain data and linear elastic fits for a 35° fiber angle scaffold in equibiaxial tension. The x-direction data exhibited a negative elastic modulus and the y-direction exhibited a positive elastic modulus, yielding a negative EE_r.

Within the equibiaxial tension EE data (Figure 9), there were no significant differences between: (1) fiber angle groups ranging from 30 to 40°, (2) fiber angle groups ranging from 42 to 48°, and (3) fiber angle groups ranging from 55 to 60°. The 50° group was not significantly different from any other group due to its relatively large variance, which spanned both positive and negative EE. Groups with a fiber angle below 50° had consistently positive EE (increasing in magnitude with fiber angle), whereas groups with a fiber angle greater than 50° had consistently negative EE. Variances in EE were relatively large within the proximity of the 50° fiber angle group.

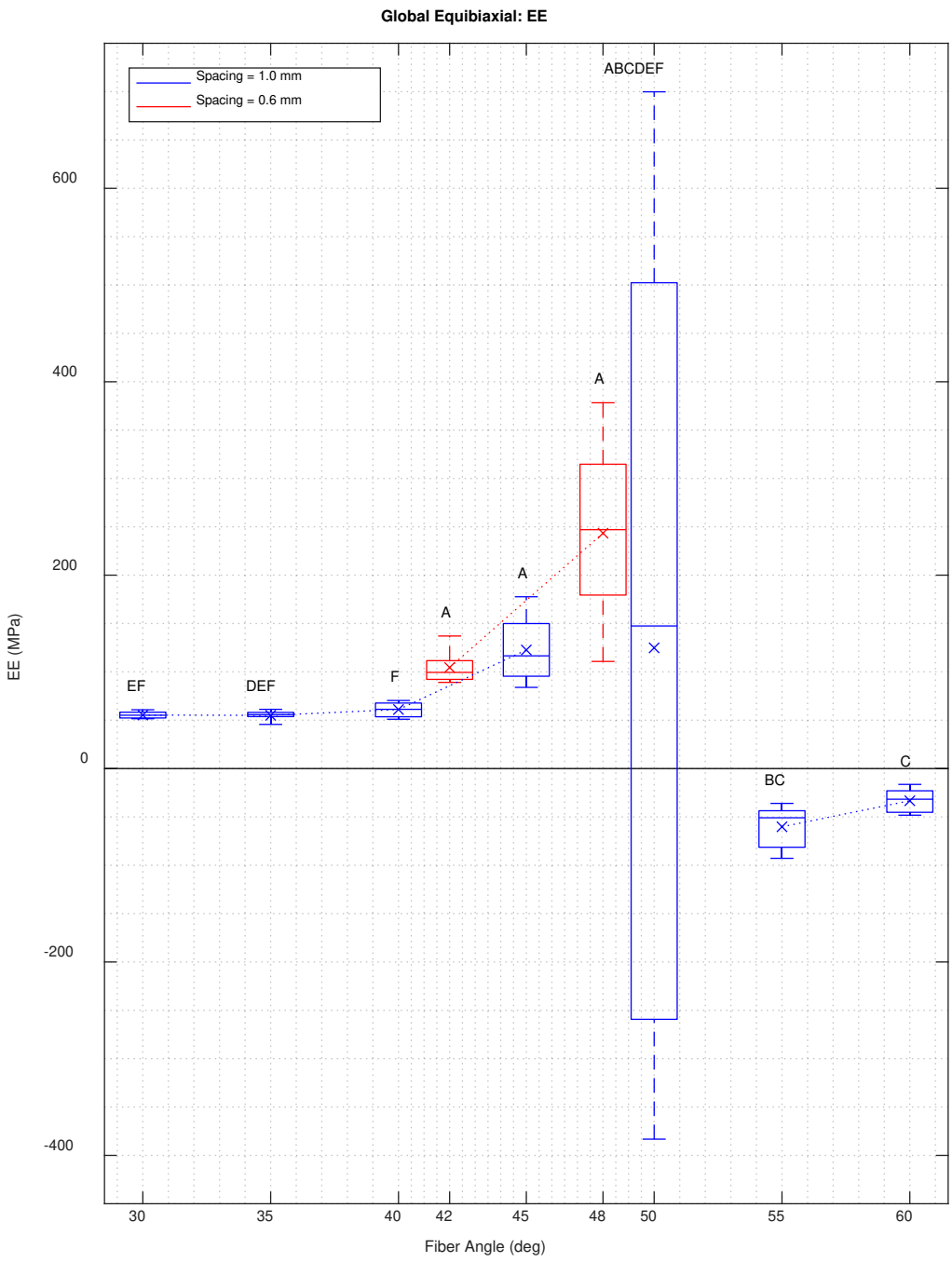

Figure 9. Effective elastic modulus (EE) as a function of fiber angle from the corresponding loading direction for the five scaffold groups in equibiaxial tension. EE represents a combination of EE_x and EE_y, where fiber angle data from 30° – 45° (from the loaded direction) were obtained from EE_y and fiber angle data from 45° – 60° (from the loaded direction) were obtained from EE_x. Boxplots indicate minimum and maximum (dashed error bars) data, 25% quartile and 75% quartile data, median (solid horizontal line) data, and mean (x) data. Continuous trends between means of scaffold groups with the same spacing are shown as dotted lines. Significant differences ($p < 0.05$) in means are indicated by groups that do not share a common letter.

The equibiaxial tension EE_r (Figure 10) increased with increasing fiber angle from the y-direction. The 30° fiber angle group had significantly lower EE_r than the 35° fiber angle group. Both the 30° and 35° groups had negative mean EE_r and were significantly less than the fiber angle groups ranging from 40 to 45°. No significant differences in EE_r were found between the 42° fiber angle group and the nearest fiber angle groups (40° and 45°), although there was a significant difference in EE_r between the 40° and 45° groups.

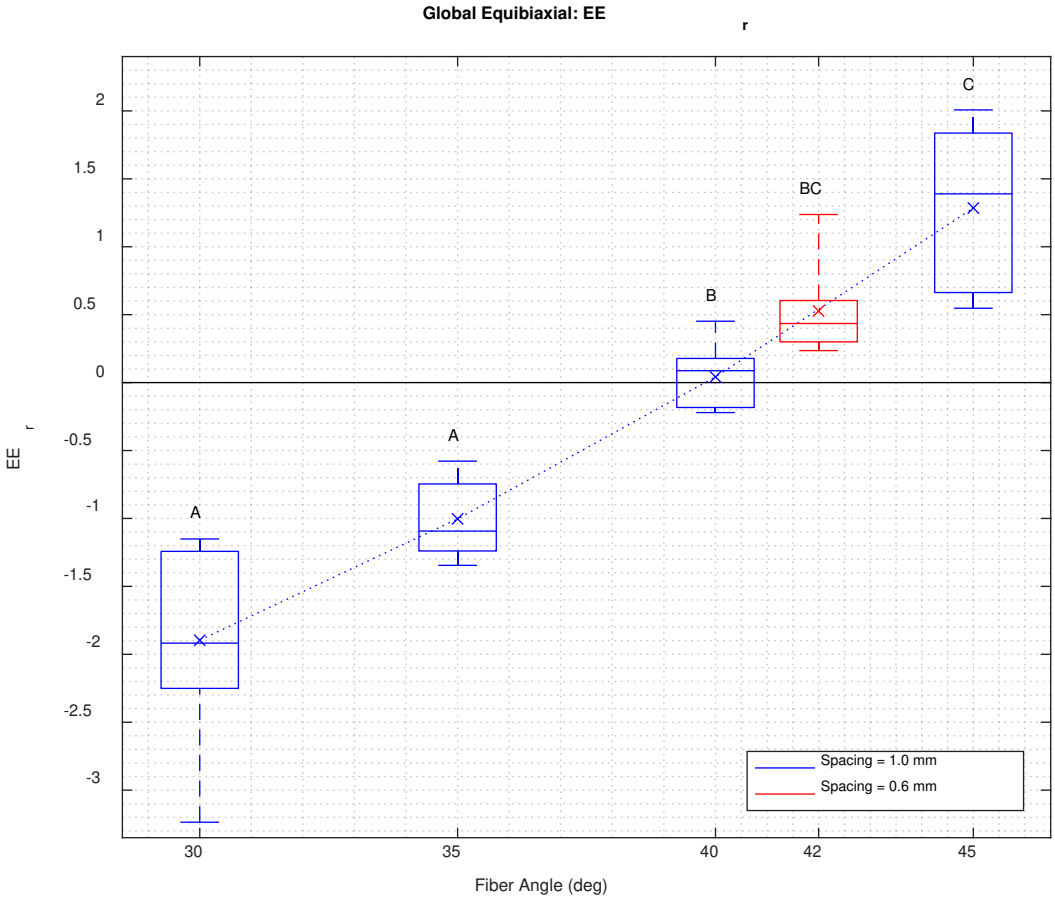

Figure 10. Effective elastic modulus ratio (EE_r) as a function of fiber angle from the y-direction for the five scaffold groups in equibiaxial tension. Boxplots indicate minimum and maximum (dashed error bars) data, 25% quartile and 75% quartile data, median (solid horizontal line) data, and mean (x) data. Continuous trends between means of scaffold groups with the same spacing are shown as dotted lines. Significant differences ($p < 0.05$) in means are indicated by groups that do not share a common letter.

Transverse-constrained uniaxial data (Figure 11) demonstrated generally decreasing EE with increasing fiber angle away from the loading direction. Of the samples with 1.0 mm spacing, the 30° and 35° fiber angle groups had significantly greater EE than all other groups. The 45-60° fiber angle groups exhibited decreasing EE with increasing fiber angle away from the loading direction that were all significantly different. The 40° fiber angle group did not have significantly different EE than the 45° and 50° groups and exhibited a mean EE less than the 45° group. The 42° and 48° fiber angle groups (0.6 mm spacing) also had significantly greater EE and larger variances than the fiber angle groups in the range from 40 to 50° (1.0 mm spacing).

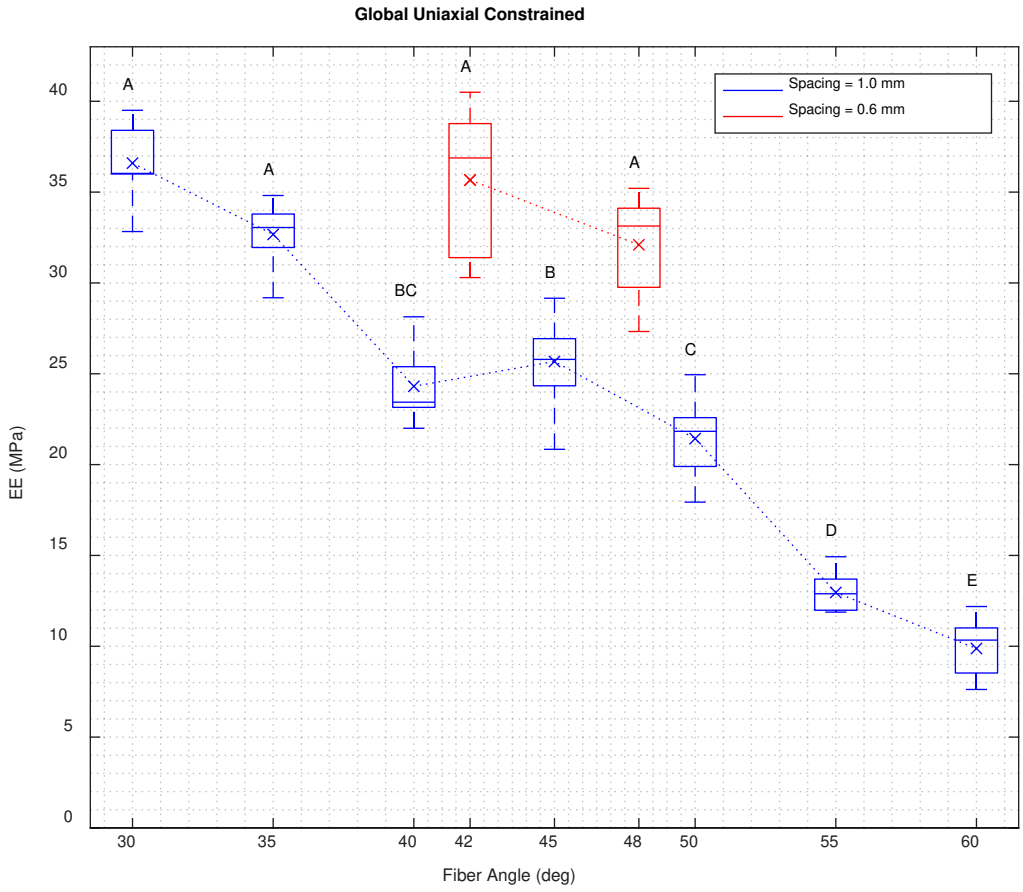

Figure 11. Effective elastic modulus (EE) as a function of fiber angle from the loading direction for the five scaffold groups in unconstrained uniaxial tension. EE for fiber angles 30° to 45° (from the loaded direction) were obtained from EE_y with strain ratio (x:y) of 0:1 (transverse constrained uniaxial in the y-direction) and EE for fiber angles 45° – 60° (from the loaded direction) were obtained from EE_x with strain ratio of 1:0 (transverse constrained uniaxial in the x-direction). Boxplots indicate minimum and maximum (dashed error bars) data, 25% quartile and 75% quartile data, median (solid horizontal line) data, and mean (x) data. Continuous trends between means of scaffold groups with the same spacing are shown as dotted lines. Significant differences ($p < 0.05$) in means are indicated by groups that do not share a common letter.

Unconstrained uniaxial data (Figure 12) also showed generally decreasing EE with increasing fiber angle away from the loading direction. Of the samples with 1.0 mm spacing, the 30° and 35° fiber angle groups had significantly greater EE than all other groups. The 40° and 45° fiber angle groups had significantly greater EE than the 50° and 55° fiber angle groups and the 60° fiber angle group had significantly lower EE than all other groups with 1.0 mm spacing. Similar to the transverse constrained uniaxial data, the mean EE for the 40° fiber angle group was lower

than the 45° fiber angle group, although this difference was not significant. Both the 42° and 48° fiber angle groups (0.6 mm fiber spacing) were significantly greater than the 40° group (1.0 mm fiber spacing); only the 42° fiber spacing group was significantly greater than the 45° group (1.0 mm fiber spacing). All uniaxial EE observed in this study were within the target range.

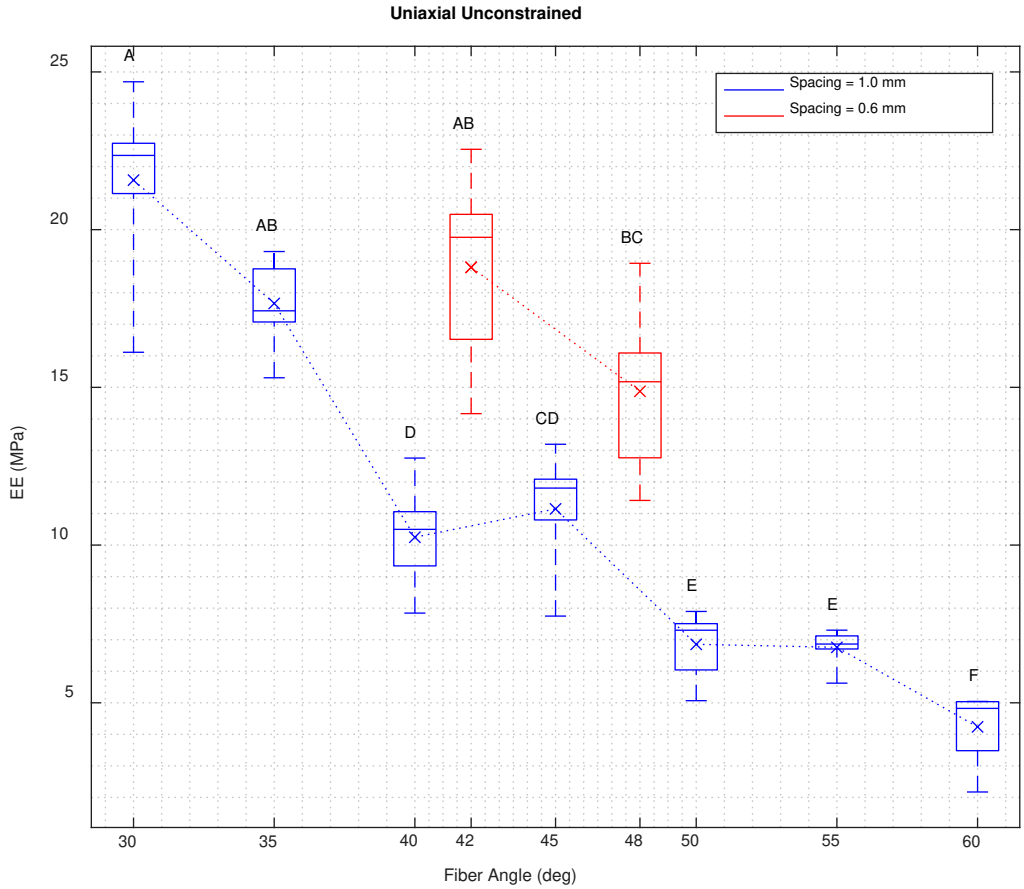

Figure 12. Effective elastic modulus (EE) as a function of fiber angle for the five scaffold groups in unconstrained uniaxial tension. EE for fiber angles 30° – 45° (from the loaded direction) were obtained from uniaxial EE_y and EE for fiber angles 45° – 60° (from the loaded direction) were obtained from uniaxial EE_x. Boxplots indicate minimum and maximum (dashed error bars), 25% quartile and 75% quartile, median (solid horizontal line), and mean (x). Continuous trends between means of scaffold groups with the same spacing are shown as dotted lines. Significant differences ($p < 0.05$) in means are indicated by groups that do not share a common letter.

Orthotropic constitutive models of all groups yielded significant fits for all stiffness coefficients ($p < 0.05$), with relatively small standard errors (

Table **4**). Stiffness coefficients C_{xx} and C_{xy} increased with increasing fiber angle from the y-direction for the 1.0 mm spacing groups. Further, stiffness coeffcient C_{yy} decreased with increasing fiber angle from the y-direction, except for the 30° group which was lower than the 35° and 40° groups. The 0.6 mm group demonstrated larger stiffness coefficients as compared to the 1.0 mm spacing groups.

Table 4. Summary of fitted orthotropic stiffness coefficients for all fiber angle groups. Standard errors of the coefficient are indicated in parentheses.

Fiber Angle		**30°**	**35°**	**40°**	**42°**	**45°**
Fitted Stiffness Coefficients (MPa)	C_{xx}	7.46 (0.17)	15.8 (0.3)	22.7 (0.3)	35.0 (0.5)	29.0 (0.7)
	C_{xy}	11.3 (0.2)	18.4 (0.3)	24.3 (0.3)	31.5 (0.5)	24.6 (0.6)
	C_{yy}	32.2 (0.4)	35.5 (0.4)	34.1 (0.3)	44.2 (0.5)	30.5 (0.7)

Orthotropic constitutive model predictions for local equibiaxial strain conditions (Figure 13) exhibited no significant differences from a normal distribution ($0.14 \leq p \leq 0.58$). Of the 1.0 mm spacing models, a maxima in predicted mean EE (58.4 MPa) was observed at a 40° fiber angle from the y-direction and was significantly different as compared to all other predicted mean EE ($p < 5.5 \times 10^{-3}$). The predicted mean EE for fiber angles on each side of this peak (35° and 45°) were not significantly different ($p = 0.74$). The 0.6 mm spacing model predicted mean EE values which were significantly greater than all of the 1.0 mm spacing models. All fiber angles were predicted to have mean EE values within the target AF range, except for the 60° model which was significantly different from the lower target bound of 27 MPa ($p < 10^{-16}$).

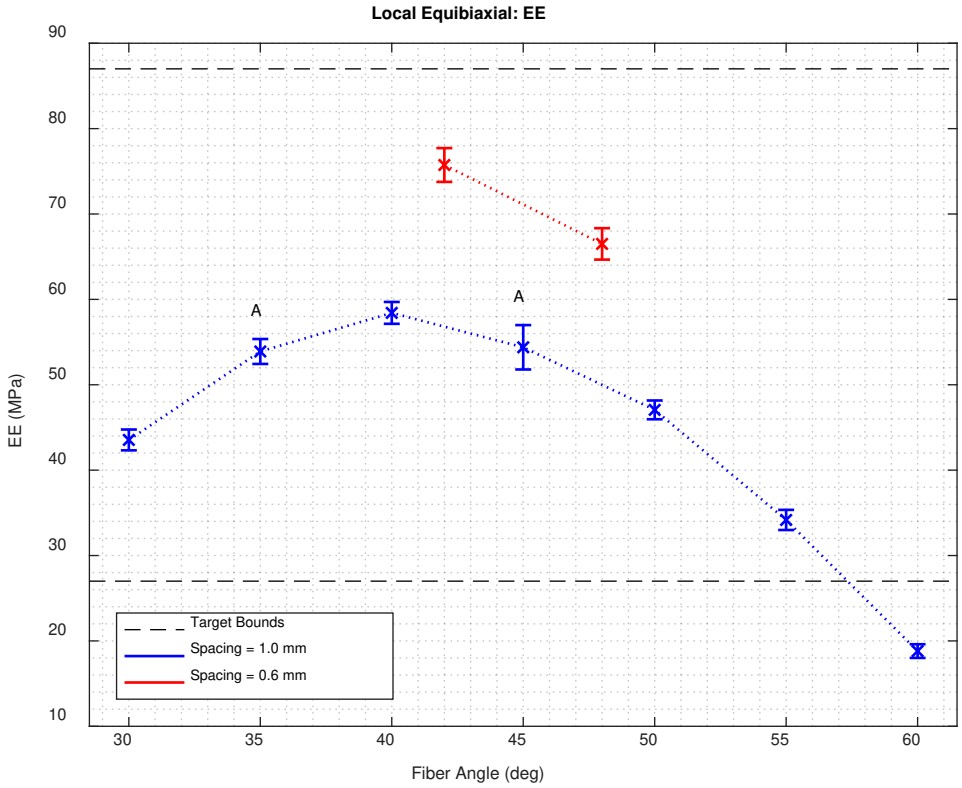

Figure 13. Mean effective elastic modulus (EE) as a function of fiber angle predicted from orthotropic constitutive models in local equibiaxial tension. Fiber angles 30° to 55° were predicted within the reported range of target AF mechanics (27 – 87 MPa). Error bars indicate 95% confidence interval of the predicted means from the constitutive model. Continuous trends between predicted means of scaffold models with the same spacing are shown as dotted lines. Significant differences ($p < 0.05$) in predicted means are indicated by models that do not share a common letter.

Under local equibiaxial strain conditions (Figure 14), EE_r consistently increased with fiber angle from the y-direction and all predicted mean EE_r were significantly different from all other predicted mean EE_r. No fiber angle model predicted EE_r values within the target AF range were not significantly different to the target AF range. However, the target range was bounded by the 30° and 35° models ($EE_r = 0.43$ and $EE_r = 0.63$, repsectively). The predicted mean EE_r of the 0.6 mm spacing model clearly falls within the trend of the predicted mean EE_r of the 1.0 mm spacing models.

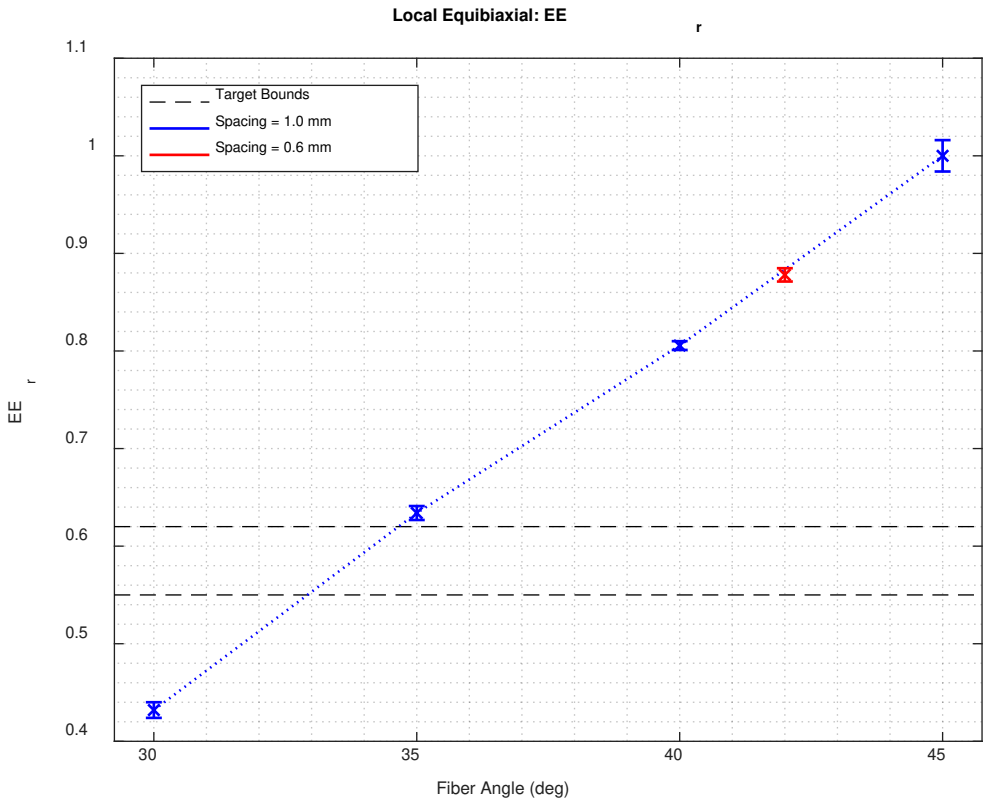

Figure 14. Mean effective elastic modulus ratio (EEr) as a function of fiber angle predicted from orthotropic constitutive models in local equibiaxial tension. No fiber angle group was predicted within, or not significantly different to, the reported range of target AF mechanics (0.55 – 0.62). Error bars indicate the 95% confidence interval of the predicted means from the constitutive model. Continuous trends between predicted mean EEr of scaffold models with the same spacing are shown as dotted lines. Each predicted mean EEr was significantly different to all other predicted mean EEr ($p < 0.05$).

Orthotropic constitutive model predictions for local transverse-constrained strain conditions (Figure 15) all exhibited no significant difference from a normal distribution ($0.11 \leq p \leq 0.79$). A maxima in predicted mean EE of the 1.0 mm spacing models (35.5 MPa) was observed at a 35° fiber angle from the y-direction. However, the 35° model was not significantly different from the 40° model ($p = 0.22$). The predicted mean EE for fiber angles on each side of this peak (30° and 40°) were not significantly different ($p = 0.068$). The 42° model (0.6 mm spacing) predicted mean EE significantly greater than all 1.0 mm spacing models, however, the 48° model

(0.6 mm spacing) was not significantly different to the 35° and 40° models ($p = 0.64$ and $p = 0.40$, respectively). Fiber angles 50° and 55° were predicted to have mean EE within the target AF range, however, there was a significant difference between all other fiber angle models and the target AF range ($p < 0.05$).

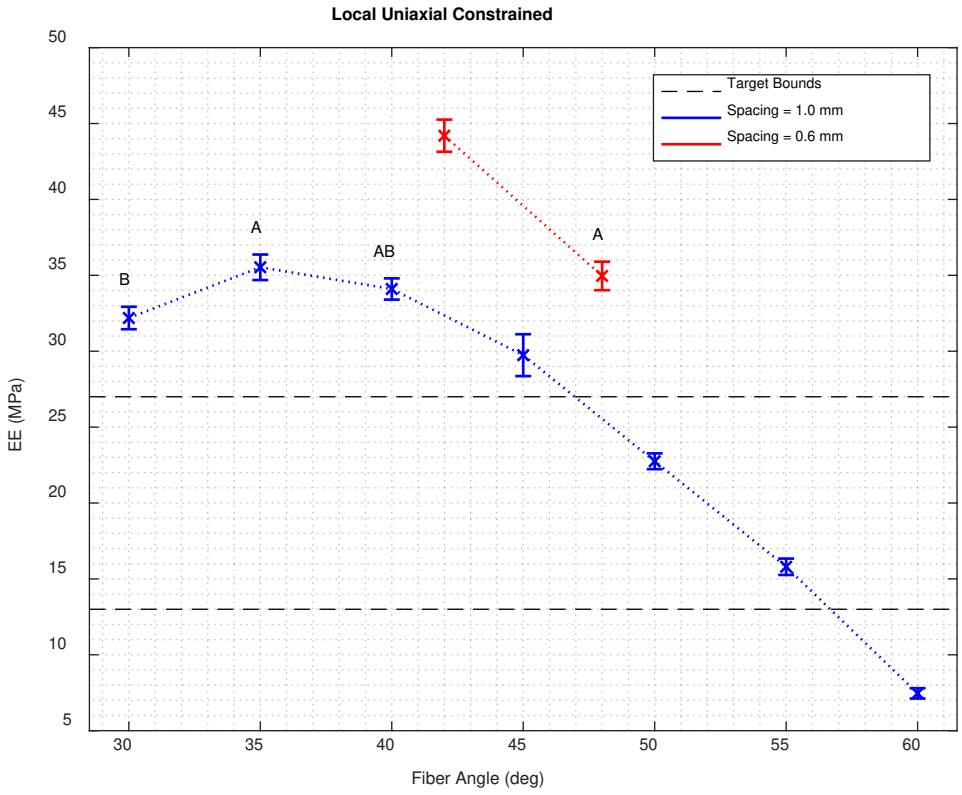

Figure 15. Mean effective elastic modulus (EE) as a function of fiber angle predicted from orthotropic constitutive models in transverse-constrained uniaxial tension. Fiber angles 50° and 55° were predicted within the reported range of target AF mechanics (13 - 27 MPa). All other fiber angle models were significantly different to the target range. Error bars indicate the 95% confidence interval of the predicted means from the constitutive model. Continuous trends between predicted mean EE of scaffold groups with the same spacing are shown as dotted lines. Significant differences ($p < 0.05$) in predicted mean EE are indicated by models that do not share a common letter.

2.1.4. Discussion

In this study, the equibiaxial, transversely-constrained uniaxial, and unconstrained uniaxial moduli of 3DF angle-ply PCL laminates with varying fiber angle and spacing were evaluated. The global equibiaxial data (Figure 9) demonstrated an asymptote in EE at approximately a 40° fiber angle, observed as a discontinuity in EE with large variances. EE_r also increased as the fiber angle tended toward 45°. As expected, the unconstrained uniaxial results (Figure 12) demonstrated a general decrease in construct stiffness as the fibers oriented further away from the loading direction. These findings are congruent with similar studies of oriented fiber scaffolds [121,123]. This relationship between apparent uniaxial modulus and fiber direction appeared to be approximately linear, however one previous study reported a sigmoidal relationship[123]. These data provide important insights with respect to the uniaxial and multiaxial behavior of the scaffold groups. The linear elastic behavior exhibited by the scaffolds facilitated orthotropic constitutive fits for comparison to target AF data. Many of the scaffolds in this study predicted similar local moduli to the target AF properties, though no single scaffold could meet all target properties. Scaffold mechanics may be adjusted by altering print parameters such as layer height, fiber spacing, fiber diameter, or base material, as previously reported by our group and others in mechanical testing of similar 3DF angle-ply scaffolds[143] and FE analyses (Section 2.2).

2.1.4.1. Fiber orientation

The experimental data and constitutive model demonstrated the intuitive results that scaffolds behaved stiffer when the fibers were more aligned to the load direction. Further, an increase in the fiber angle from the y-direction was associated with an increase in the coupling stiffness coefficient, C_{xy}, suggesting that the two orthogonal directions have more influence on each other as the fiber angle approaches 45°. The predicted local equibiaxial moduli from the

constitutive model suggested that a fiber angle of approximately 34° may achieve the desired biaxial mechanical targets, which is similar to the collagen orientation within the native AF[168].

An outstanding question remains: if the target engineered tissue mechanics are achieved, then does the orientation of the fibers matter? It has been reported in the literature that collagen fibers tend to align with scaffold fiber orientation *in vitro*[169]. To provide the desired initial engineered tissue mechanics, the present results indicate that the regenerated collagen orientation could differ by as much as 11° from the native collagen orientation[168]. As the scaffold is resorbed by the body and the inter-lamellar contact changes, the regenerated collagen fibers may lead to improper mechanics and adverse results. Alternatively, with a relatively slower scaffold degradation time, collagen fibers might realign (via remodeling) closer to native AF as the cellular length scale mechanics evolve. In any case, alteration of mechanics during construct degradation must be further elucidated in order to fully understand the temporal evolution of the engineered tissue mechanics from implantation to full adoption by the native tissue.

2.1.4.2. Fiber spacing

Both the global equibiaxial data and local equibiaxial predictions suggested that the EE_r for a 0.6 mm spacing scaffold followed the same relationship with fiber angle as the 1.0 mm spacing scaffolds. Accordingly, relative equibiaxial EE_r may be independent of fiber spacing. However, more testing is required to further elucidate this independence.

Although there was only one 0.6 mm spacing group evaluated in the current study, there was a greater than expected variation in uniaxial stiffness as compared to the 1.0 mm spacing groups. The larger number of fiber contacts associated with the lower fiber spacing group may amplify the mechanical effect of contact area variability, and thus, the observed increased variance. This issue warrants further investigation, especially since it may have important implications for

design of nanofibrous scaffolds (achieved using increasingly popular methods such as melt electrowriting[120,170]) where there are considerably more interlamellar contacts.

2.1.4.3. Stiffness asymptote

In global equibiaxial loading, the 30° and 35° groups exhibited relatively low variances compared to the 40 to 45° groups, which appear to have additional contribution to mechanical variance beyond simple perturbations in process parameters. In biaxial loading, there are many conditions where strains transverse to the dominant fiber direction transition from tension to compression. In the context of this study, the smaller fiber angles (30° and 35°) consistently yielded a compressive strain in the x-direction (which is transverse to the y-direction), whereas the 42° and 45° groups consistently exhibited tensile transverse strains. Therefore, there appears to be a critical angle that, under the same loading conditions, would theoretically demonstrate zero transverse strain (i.e. an infinite observed stiffness). Accordingly, it is expected that slight perturbations to this fiber angle would lead to dramatic changes in the observed transverse stiffness of the construct (i.e. increasing or decreasing the angle by 0.1° would lead to extremely large positive or negative stiffness, respectively). Further, small perturbations in many other process parameters may cause a similar effect. A construct with a fiber angle near this critical value would exhibit large variances in transverse stiffness, however, there would be very little associated change in the longitudinal stiffness. With regard to the current study, it is believed the substantial variance observed in the 40° group can be largely attributed to this phenomenon. Accordingly, it may be difficult to accurately prescribe the micromechanical stress state for a 40° scaffold under this specific load condition and, therefore, the cellular responses with these scaffolds may be unpredictable or difficult to control. The observed variance is less pronounced in the 50° group,

despite the data being obtained from the same samples, as the strains are not near zero for the 50° group.

The biaxial ROI loads generated by the imposed global or local equibiaxial strain likely differ from native AF loads *in vivo*. Therefore, it is unknown where this critical fiber angle and associated mechanical variance may occur under physiological loading. If a scaffold was designed near the critical fiber angle for *in vivo* loading, small perturbations in print parameters may lead to dramatic differences with respect to the micromechanical environment within the scaffold. Further evaluation of scaffolds under physiological loading and resultant cellular micromechanical environment may be of interest for tissue engineering AF replacements.

2.1.4.4. Interlamellar contact

The transverse stiffening that causes the stiffness asymptote is largely a consequence of inter-lamellar bonding as loads are progressively transmitted to fibers of alternating directions. Fiber bonding between layers is essential in 3DF to fabricate coherent scaffolds which are resistant to delamination. In ply-laminates, fiber bonding creates rotational and translational constraints between layers. Conversely, in the native annulus there is relatively little mechanical interaction between the structural collagen fibers; AF lamellae are bonded with more compliant collagen and fibrilin bridges, and it has not been explicitly demonstrated that substantial sliding exists between adjacent AF lamellae[171]. This difference in architecture results in such a large discrepancy in mechanics which may cause angle-ply laminates to not sufficiently replicate native annulus mechanics for all multiaxial loading conditions. Accordingly, further sophistication of this simple scaffold design is likely required to produce a more biomimetic AF replacement and favorable long-term outcomes.

2.1.4.5. Boundary conditions

Another likely source of stiffness variance arises due to the boundary conditions of the scaffolds. This is particularly important as these fiber-based constructs are inherently discrete and inhomogenous as the observed length scale is reduced. As such, subtle changes in loading and constraints may lead to discrete and appreciable changes in the observed mechanics. It is intuitive to expect a symmetrical fiber architecture to exhibit an EE_r of 1.0 in equibiaxial tension. The experimental mean EE_r of the 45° group (1.29) was not significantly different from 1.0 ($p = 0.491$), though this experimental group exhibited a relatively large corresponding variance. This variance was found to be independent of print orientation and testing orientation. Therefore, it is hypothesized that slight geometric asymmetries at the cruciform corners (Figure 7b) produced an unpredictable inequality between the longitudinal and transverse stiffnesses. This discrepancy in the boundary conditions may have altered the fiber load distributions, which is amplified by the discrete fiber stress concentrations.

While the aforementioned observed stress concentration is associated with the cruciform geometry, it highlights the substantial influence of boundary conditions in engineered tissue design. These scaffolds are subjected to complex and unpredictable loads and constraints *in vivo*, particularly due to the large variation in human subjects[109]. It is therefore important that the resulting cellular micromechanical environment is insensitive or insulated from changes due to these foreseeable perturbations. Designing scaffolds with more homogeneous architectures that include smaller feature sizes may be an effective strategy to mitigate boundary condition effects. However, this approach may have an inherent lower bound due to the requisite cell ingrowth, as pore size and overall porosity have been shown to be critical for cell infiltration and extracellular matrix production in tissue scaffolds[117].

2.1.4.6. Loading modes

Previously reported biaxial testing of AF has utilized ROI strain feedback control, which creates consistent local strains for mechanical evaluation without the need for constitutive fitting[31]. The present study utilized global displacements to generate local biaxial strains within the central region, however, the ROI strains can vary between different samples. Therefore, the present study required constitutive fitting for comparison to previously reported mechanical targets. Nonetheless, biaxial testing with global strain control affords greater experimental simplicity. This experimental convenience is particularly advantageous when ROI strain feedback control is prohibitively complex, such as in long-term cell cultures and fatigue testing, which are valuable experiments to evaluate the mechanical and biological function of these tissue engineering scaffolds.

The data reported herein suggest that evaluation of angle-ply scaffold mechanics should be focused on physiologically relevant loading conditions (i.e. the local biaxial strain ratios which are experienced in the disc) rather than global and local strain ratios which are implemented for experimental convenience. In addition, it remains unknown as to how the mechanical sensitivity of a scaffold changes with biaxial strain ratio. A scaffold that replicates the equibiaxial properties of native AF with low mechanical variance may lead to unintended cell differentiation *in vivo* if it does not replicate native AF properties at other physiological strain ratios. Further, the mechanical sensitivity of the scaffold may be considerably larger at a different strain ratio and small perturbations in print parameters and boundary conditions may lead to dramatic and unexpected mechanical responses.

2.1.4.7. Implications for design

Ideally, a functional tissue engineering design process would focus on altering design parameters to achieve the objective mechanics while minimizing mechanical variance through optimization and tight control of process parameters. However, process parameters such as fiber diameter and inter-lamellar contact area, which were not considered in this study, may integral in achieving target mechanics and, therefore, convolute this idealized process. Moreover, print parameter perturbations from manufacturing are relatively easy to measure and observe (such as the measured variances in fiber diameter in this study), however, perturbations due to *in vivo* boundary and loading effects are more difficult to control. An alternative design process which includes validated computational (FE) models which are specific for regenerative scaffold design and include the relevant anatomy (such as whole lumbar spine models) may provide more rapid and broad analysis of the mechanical roles and interaction of the various print parameters. These models could also be leveraged to predict how different implantation/implementation strategies affect the resultant micromechanical environment.

2.1.4.8. Limitations

In biaxial testing of fabrics and biological fiber-composite materials, the gripped arm length of cruciform specimens has been shown to induce an artificial stiffening affect due to the fibers that are fully contained between the grips [172]. Though this artificial stiffening was possible in the present study, it is not considered confounding because: (1) the 3DF scaffolds have considerably greater mechanical bonding between fibers than the materials which exhibited artificial stiffening, and (2) the biaxial apparatus incorporated transverse linear bearings that mitigated load transfer through fully gripped fibers. The current angle-ply laminates were designed with a consistent fiber angle, however the native collagen orientation varies with radial position in

the AF. AM allows similar gradation through the layers of the scaffold for more advanced biomimicry, however, this is expected to lead to increasingly more complex mechanics, again highlighting the case for FE analysis. AM also facilitates multiphase fabrication, in particular, the incorporation of cell-laden hydrogels or bioinks within polymer scaffolds[173,174]. Hydrogels were not present in the void-space of the scaffolds of this study, however, they are prevalent in current regenerative tissue designs to seed cells or provide growth factors[32,139,140,175]. The primary role of hydrogel incorporation is typically not mechanical, however there may be secondary mechanical contributions of hydrogels (which has been demonstrated in compressive loading-based studies[176]) and may require evaluation. Further, the bulk PCL material is highly linear elastic, however the native AF is known to be nonlinear and viscoelastic in nature, which was not considered in the present study. AF repair constructs must also undergo sufficient strain before the onset of yield[32], though minor yielding at the cruciform stress concentrations was observed in this study. It is possible to tailor print parameters to improve the yield strain of a scaffold. For example, increasing fiber spacing yields longer unsupported fiber element lengths, which facilitates obtaining larger deflections in a bending deformation mode. However, yield strain is a complex interaction between axial, bending, and shear deformation mechanisms. Design should, therefore, prioritize the micromechanical environment and tailor base materials for obtaining sufficient yield strain.

2.1.5. Conclusions

The results of this study demonstrated that the ply-laminate scaffolds considered in this investigation exhibited generally similar effective elastic moduli to native AF targets in uniaxial, transverse constrained uniaxial, and biaxial testing. However, no scaffold group matched all native AF targets in all loading regimes simultaneously. This study presents important insights into the uniaxial and multiaxial behavior of 3DP angle-ply laminate scaffolds, providing a basis for further

design to meet functional requirements. The ideal design outcome is the fabrication of scaffolds which both achieve the target mechanics and are minimally affected by predictable perturbations in mechanics such that the local mechanical environment is conducive for regeneration. The results reported herein are highly generalizable and may also be translated to fiber-reinforced scaffolds for the repair or replacement of numerous other biological soft tissues including cartilage, tendon, ligament, vascular tissues, and skin[110,177].

2.2. Computational Approach[b]

2.2.1. Introduction

In this study, a parametric FE model was developed and evaluated to elucidate the influence of various print parameters on the uniaxial and biaxial tensile mechanics of 3DF angle-ply laminate scaffolds. The aims of this study were: (1) to generate a more efficient method of assessing angle-ply laminate mechanics in order to fabricate micromechanically-tailored scaffolds which are not confounded by foreseeable perturbations in manufacturing and clinical application, and (2) to perform parametric analyses of design parameters in order to explicate which design features may be most prominent for AF scaffold development.

2.2.2. Materials and Methods

This FE study was conducted using the commercial FE package ABAQUS (Dassault Systemes SIMULIA, Johnston, RI, USA) via scripts written in Python (Python Software Foundation, USA). The following describes: (1) the methods for generating and assembling parts for the FE geometry; (2) the material model; (3) meshing technique; (4) constraints and boundary conditions imposed on the model; (5) analyses of the predicted FE results; and (6) the parametric studies considered in this investigation.

2.2.2.1. Geometry and Assembly

A solid geometry was created within ABAQUS to represent a single lamellae of an angle-ply scaffold. A set of print parameters were used to define the geometry (Table 5, Figure 16b). A

[b] The content of Section 2.2 has been published as a research article in the Journal of the Mechanical Behavior of Biomedical Materials (DOI: 10.1016/j.jmbbm.2019.103395). All content has been adapted with permission from Elsevier.

cruciform geometry (Figure 16a) was used to simulate biaxial testing specimens that our group created for a series of physical experiments (Section 2.1). To mimic an angle-ply architecture, a single lamella was stacked six times in the vertical z-direction in an alternating orientation (i.e. reflected about the y-axis). The full cruciform geometry was required because the individual lamellae lacked geometric symmetry and pilot studies demonstrated that symmetry boundary conditions were not suitable. Fibers within the scaffold were simplified as rectangular sections rather than the printed experimental circular sections. This approximation: (1) reduced geometric complexity to enhance mesh quality, and (2) simplified contact mechanics by creating planar interfaces between adjacent lamellae to vary the size of the contact region independent of other geometric parameters. Ultimately, the use of rectangular fibers gave similar results to circular fibers (see supplemental data in Appendix A), improved computational performance and, therefore, facilitated high-throughput analyses. To maintain the deformation characteristics of the experimental scaffold, the rectangular fibers were designed to replicate the axial (Equation (3)) and bending (Equation (4)) stiffnesses of the corresponding circular fibers:

$$E_1 I_1 = E_2 I_2 \tag{3}$$

$$A_1 E_1 = A_2 E_2 \tag{4}$$

where E is elastic modulus, I is cross-sectional moment of inertia, A is the fiber cross-sectional area, and the subscripts 1 and 2 denote the circular fibers (idealized physical print) and rectangular fibers (FE model), respectively. As the vertical (z-direction) height of the fibers (Z) was fixed as a print parameter, the fiber width (b) and elastic modulus (E_2) were modified by manipulating Equations (5) and (6), where D is the fiber diameter (Table 5).

$$\mathrm{b} = \frac{\sqrt{3}}{2} D \tag{5}$$

$$\mathrm{E}_2 = \left(\frac{\pi}{2\sqrt{3}} \frac{D}{Z}\right) E_1 \tag{6}$$

Table 5. Description and quantification of the seven principal print parameters considered in the study. Print parameters are classified as either design parameters or process parameters. Contact radii and layer spacing are expressed as a factor of the fiber diameter, D. Fiber angle is measured from the y-direction.

Print Parameter	**Variable**	**Type**	**Base Value**	**Negative Pertubation**	**Positive Pertubation**
Fiber angle	Θ	Design	30°	-	1° steps to 45°
Fiber spacing	S	Design	1.0 mm	0.9 mm	1.1 mm
Fiber diameter	D	Process	300 µm	250 µm	350 µm
Contact radius	C	Process	0.30 × D	0.39 × D	0.48 × D
Elastic modulus	E	Process	265 MPa	239 MPa	292 MPa
Layer count	N	Design	6	4	8
Layer spacing	Z	Process	0.8 × D	0.7 × D	0.9 × D

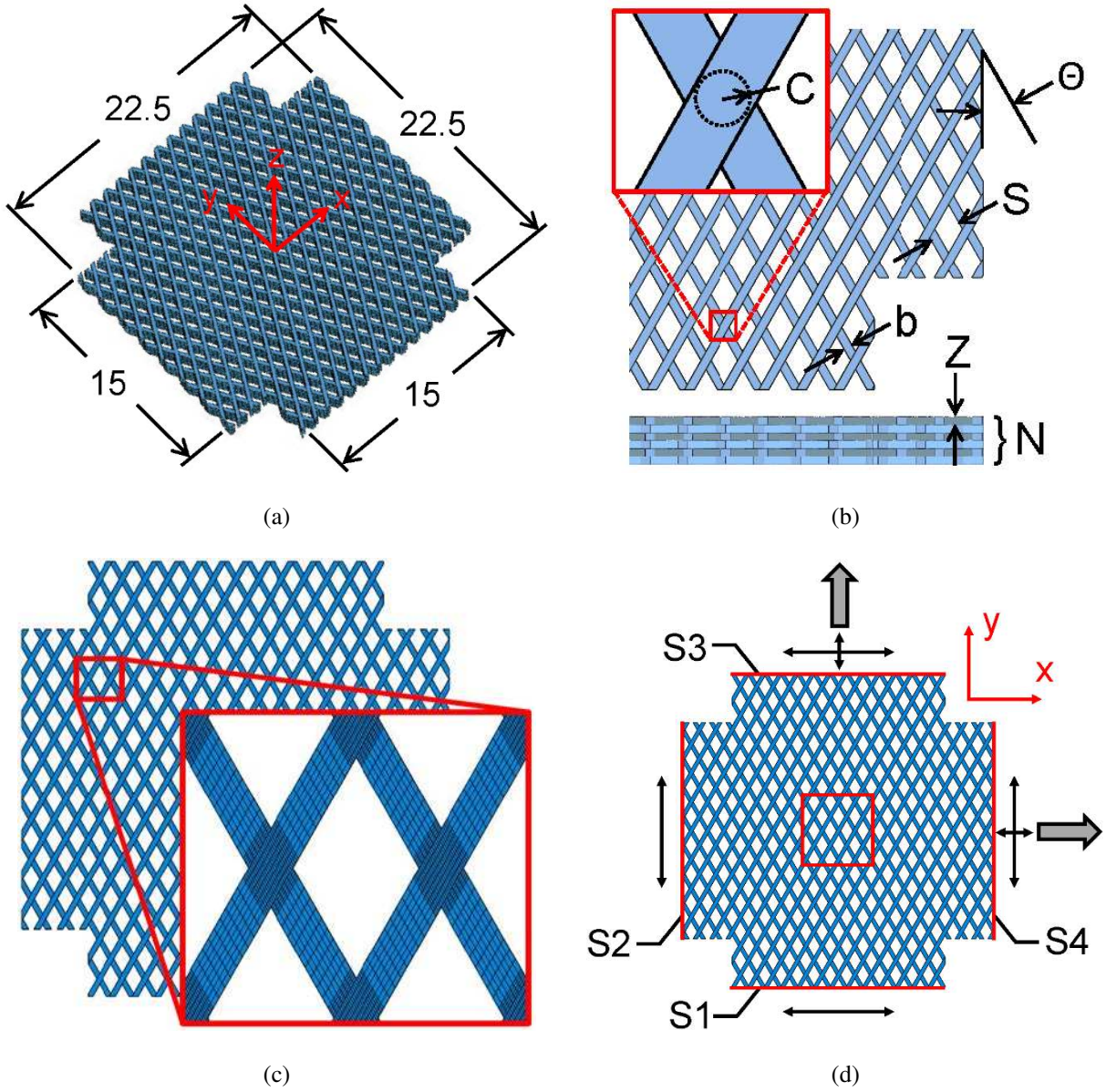

(a) (b)

(c) (d)

Figure 16. Cruciform scaffold geometry showing: **(a)** three-dimensional view of cruciform with base print parameters indicating the coordinate system and dimensions (in mm); **(b)** x-y plane view (top) and x-z plane view (bottom) demonstrating critical design dimensions of the scaffold studied in the current investigation; **(c)** magnified view of model mesh showing element refinement at interlamellar contacts; and **(d)** FE model showing the central homogeneous ROI (5 x 5 mm) highlighted in red and boundary condition specifications indicating node sets (i.e. surfaces) S1-S4 in red (double-headed arrows indicate dergees of freedom and large grey arrows indicate where displacement conditions are applied in the x- and y-directions).

2.2.2.2. Materials

In order to mimic our earlier experimental study, the scaffolds were assigned melt extruded polycaprolactone (PCL) material properties and modeled as isotropic and linear elastic (E_1 = 265 MPa, ν = 0.3)[178] over the relatively low strain range (6.7% maximum global strain) imparted on the model.

2.2.2.3. Mesh

The fibers were meshed with hexahedral elements (C3D8). Two meshing regimes were considered: uniform and refined element sizes at the fiber contacts. To ensure continuity of the mesh, the refined mesh was generated by reducing the mesh seed size along the edges which were situated adjacent to fiber contact areas and parallel to the main fiber direction by 50%. A mesh convergence study (Figure 17) was conducted for both regimes in order to determine the computational time and convergence of strain energy for both the whole assembly and a central region of interest (ROI). Mesh convergence was conducted on a scaffold that consisted of base print parameters (Table 5). A seed size of 0.075 mm using the refined mesh converged to within 3% of the finest considered seed size (0.05 mm) in one hour of computational time, and therefore, was used for all subsequent analyses in the current study (Figure 16c).

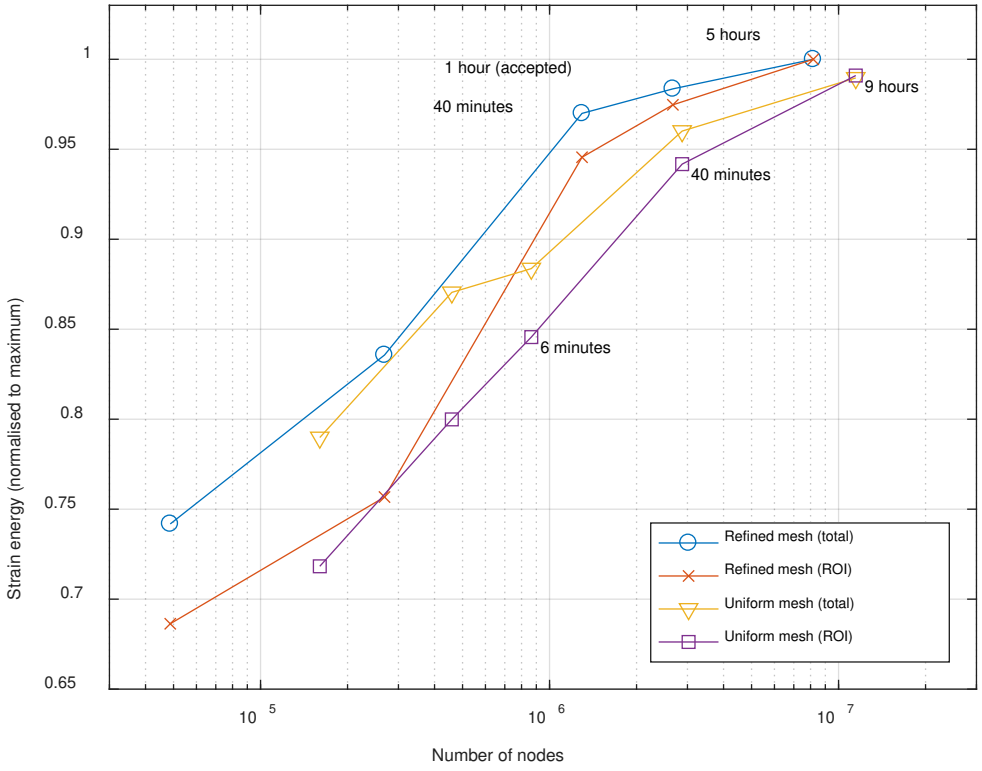

Figure 17. Mesh convergence analysis showing the total strain energy as a function of the number of nodes in the model. The four lines indicate the total strain energy of the model and the ROI comparing both the uniform mesh and mesh with refinements at fiber contact areas. Computational times for relevant datum points are provided and the accepted mesh is indicated (refined mesh with a base seed size of 0.075 mm).

2.2.2.4. Constraints & Boundary Conditions

The nodes at the ends of fibers (i.e. grip locations) were assigned to four sets: S1, S2, S3, and S4 on the -y, -x, +y, and +x surfaces, respectively (Figure 16d). To ensure that each boundary face translated as a rigid body in the unconstrained direction (to simulate fixation within the biaxial testing grips), the nodes at each face were rigidly tied. Orthogonal displacements (or global strains) were prescribed on the S3 and S4 surfaces and all nodal displacements and rotations on the S1 and S2 faces were set to zero, except for the direction of transverse sliding to ensure symmetrical and

purely biaxial loading. For example, the S1 nodes (nodes in the x-z plane) were restricted against displacement in the y- or z-directions, but were not kinematically constrained in the x-direction. The S3 and S4 faces were also prescribed freedom in the transverse directions and were defined displacements normal to the face. All other displacements and rotations were constrained.

In 3DF, when new fibers are extruded onto existing fibers, an inter-lamellar contact region is created where these adjacent fibers adhere. By assuming ideal bonding between lamellae, these inter-lamellar contacts were defined by creating rigid tie constraints between nodes within circular regions on mating faces (tie radius equal to the contact radius). This circular contact region was implemented to reduce model complexity by approximating the ideal case of an elliptical contact region between two intersecting cylindrical fibers. Due to the difficulty of predicting and measuring contact radius experimentally, it was considered an independent parameter in this study. Contact nodes coinciding with the boundary conditions were excluded from the contact sets to prevent over-constraint. The ROI elements and nodes were defined to reflect the homogenous deformation region from the experimental biaxial testing series (Figure 16d) [167]. The element ROI was defined as all elements within the top two layers and a central square with sides one-third the length of the cruciform center (i.e. 5 mm). The nodal ROI was defined within the same square, however, nodes were only taken from the top face of the top two layers to best represent what is observed by digital image correlation (DIC) in the experimental testing[167].

2.2.2.5. Analyses

Output files were generated to: (1) record the initial coordinates and predicted deformation components of all nodes within the ROI, and (2) record the solution metadata (model and solution details), the strain energy in the total assembly and ROI, the components of the 2D strain tensor (including coefficients of determination), and the reaction forces at all boundary conditions. For

each solution, linear regressions were used to evaluate the gradient of nodal displacements (u and v, in the x- and y-directions, respectively) with respect to initial coordinate positions (x and y) and corresponding r^2 values. Accordingly, by considering the ROI on a continuum level, this determined the average normal components of the 2D infinitesimal strain tensor ($\underline{\epsilon}$) in the x-y plane:

$$\underline{\epsilon} = \begin{bmatrix} \epsilon_{xx} & \epsilon_{xy} \\ \epsilon_{yx} & \epsilon_{yy} \end{bmatrix} = \begin{bmatrix} \dfrac{\partial u}{\partial x} & \dfrac{1}{2}\left(\dfrac{\partial u}{\partial y} + \dfrac{\partial v}{\partial x}\right) \\ \dfrac{1}{2}\left(\dfrac{\partial v}{\partial x} + \dfrac{\partial u}{\partial y}\right) & \dfrac{\partial v}{\partial y} \end{bmatrix} \tag{7}$$

where ϵ_{xx} and ϵ_{yy} are the normal components of the infinitesimal strain tensor in the x- and y-directions, respectively, and $\epsilon_{xy} = \epsilon_{yx}$ are the shear components of the infinitesimal (Section 2.1) strain tensor. This method is consistent with the ROI strain evaluation of an experimental series if the small-strain condition of infinitesimal strain theory is satisfied. The stresses in each direction were evaluated from the corresponding support reaction forces divided by the bulk cross sectional area (cruciform width, 15 mm, multiplied by the total thickness, Z x N). The single stress-strain point was used to determine the model Effective Elastic modulus (EE; EE_x and EE_y in the x- and y-directions, respectively). For the equibiaxial case, the ratio of EE_y to EE_x was evaluated as the effective elastic modulus ratio (EE_r), which is a measure of continuum level anisotropy of the scaffold in the circumferential-axial plane. This method of evaluating EE simulated the linear elastic behavior observed in the experimental biaxial testing series (Section 2.1). An equibiaxial displacement ramp of 0.5 mm, 1.0 mm, and 1.5 mm was used to validate the linearity of the solution using the base parameters (Table 5). A linear regression of the displacement ramp yielded $r^2 = 1.00$, thus the stress-strain response was deemed linear and the

final displacement step (i.e. 1.5 mm displacement) alone could be used to determine the moduli for all analyses.

2.2.2.6. Validation

To validate the FE model, measured print parameters from fabricated scaffolds used for a biaxial experimental series (fiber spacing = 1.0 mm, fiber diameter = 0.338 mm, layer height = 0.43 x D; Section 2.1) were used as geometric inputs. The elastic modulus and interlamellar contact radius were used as optimization variables due to difficulty in quantifying these parameters in their "as-printed" conditions. These two optimization parameters were iteratively varied to determine a minimum in the absolute standard error of the FE model EE_x and EE_y predicitions as compared to the experimental EE_x and EE_y values in all loading regimes simultaneously. A Chi-Squared test ($\alpha = 0.05$) was conducted to statistically evaluate the fit of the FE model to the experimental data.

2.2.2.7. Parametric Studies

A total of 1584 FE simulations were conducted to evaluate the influence of perturbations to the print parameters from the base values. All values of the print parameters considered are reported in Table 5. Each perturbation was evaluated for all fiber angles and all contact radii. Fiber angle was selected as a critical design parameter for tailoring the mechanics, and contact radius was selected as it is one of the most difficult process parameters to control and measure in printed constructs. Accordingly, quantification of these two parameters was identified as two of the most pertinent for scaffold design analysis.

2.2.3. Results

A typical cruciform deformation in equibiaxial tension with von Mises equivalent stress contours is shown in Figure 18. The optimized FE model used for validation visually fit all three

loading regimes well (Figure 19). The optimized model yielded an elastic modulus of 114 MPa and contact radius of 0.27 mm (0.9 x D). The Chi-Squared test yielded no significant difference between the optimized FE model predictions and experimental data ($p = 0.079$). Continuum strains within the ROI were obtained from highly linear correlations between nodal displacements and undeformed positions. All EE_y values were calculated from y-direction normal strains (dv/dy) with r^2 values larger than 0.90 (of 1584 linear regressions, 2 had $r^2 < 0.95$ and 89 had $r^2 < 0.97$). Of the 1584 x-direction normal strains (du/dx) used to calculate EE_x, 1510 had $r^2 > 0.90$ (169 had $r^2 < 0.95$ and 263 had $r^2 < 0.97$). All of the x-direction normal strains with $r^2 < 0.90$ were associated with near-zero strain magnitudes for fiber angles ranging 40° to 44°.

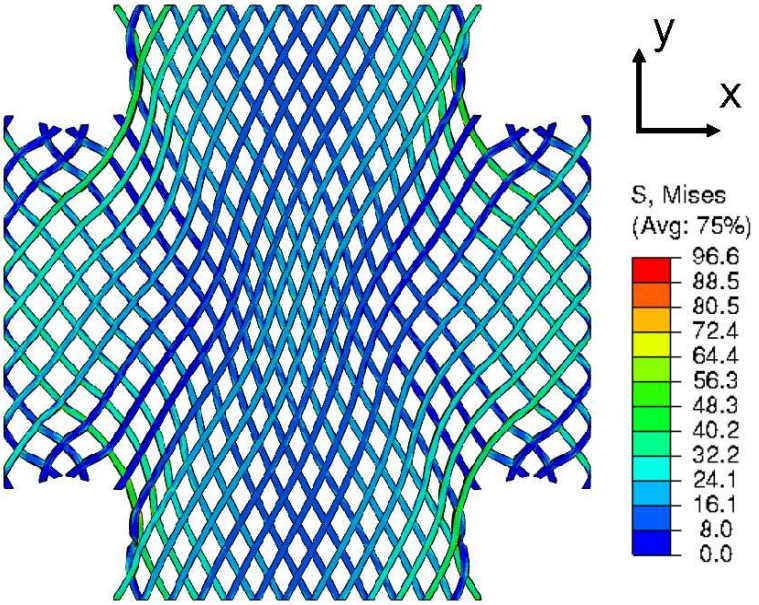

Figure 18. Solution for the cruciform model subject to equibiaxial tension with base parameters (Table 5) showing Mises equivalent stress contours (MPa).

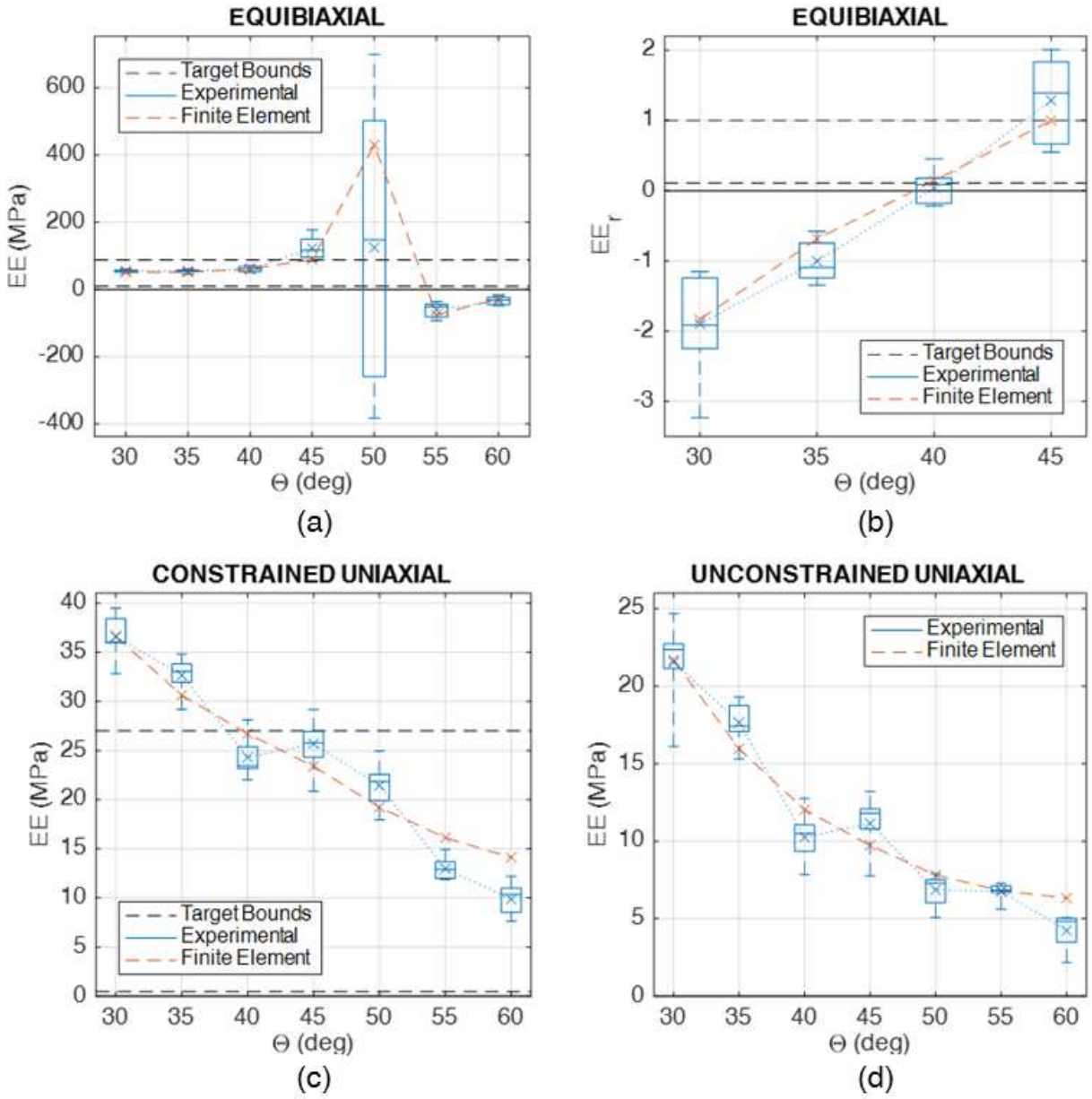

Figure 19. Mechanical properties of the optimized FE model as compared to experimental boxplot biaixial data of 3DP PCL cruciforms demonstrating general agreement between the idealized computational model and physically printed cruciforms. Data shown are: **(a)** EE_y in equibiaxial tension, **(b)** EE_r in equibiaxial tension, **(c)** EE_y in transversely constrained uniaxial tension, and **(d)** EE_y in unconstrained uniaxial tension. The range of native AF target mechanics are shown with dashed black lines[29,31–42]. All unconstrained uniaxial data fell within the target bounds.

All EE data exhibited clear trends as a function of fiber angle (Θ; Figures Figure **19**-Figure **22**). These data are also functionalized with respect to perturbations in fiber spacing, fiber

diameter, and layer count. Each figure also includes perturbations in fiber contact radius in combination with each of these three other parameters. The base model predicted the equibiaxial EE_y to remain within the target bounds for native AF (9.7 to 88 MPa) at low fiber angles. However, at approximately 43°, the EE_y was predicted to increase dramatically up to a maximum of 115 MPa at a fiber angle of 45°. The equibiaxial EE_r for the base model predicted a steady increase in EE_r as fiber angle was increased. The EE_r transitioned from negative (compression in the x-direction) to positive (tension in the x-direction) between 42° and 43°, matched the native AF EE_r between 43° and 45°. As expected, equibiaxial EE_r reached exactly 1.0 at a fiber angle of 45°. The transverse constrained uniaxial and unconstrained uniaxial both predicted a steady decrease in EE_y with increasing fiber angle. The constrained uniaxial data were within the native AF target bounds (0.46 to 27 MPa), and ranged from 26.1 MPa to 16.4 MPa at the 30° and 45° fiber angle scaffolds, respectively. The unconstrained uniaxial data were within the bounds of the native AF target (0.084 MPa to 45 MPa), and ranged from 13.7 MPa to 3.9 MPa at the 30° and 45° fiber angle scaffolds, respectively.

Equibiaxial EE_y was generally greater for larger fiber diameters (D; Figure 20a), however this trend reversed between 44° and 45° and the 45° scaffold indicated that a smaller D would have a marginally greater EE_y. Equibiaxial EE_r was consistently more positive for larger D (Figure 20b). The predicted effect of D was more pronounced at lower fiber angles and converged to 1.0 at a fiber angle of 45°. A larger D was also predicted to: (1) yield a positive EE_r at lower fiber angle as compared to smaller D and (2) yield a lower rate of change of EE_r with change in D. Both the transverse constrained (Figure 20c) and unconstrained uniaxial data (Figure 20d) indicated an increase in EE_r for larger D that was more pronounced at lower fiber angles. In all testing regimes, the influence of fiber contact radius was consistently greater for larger D.

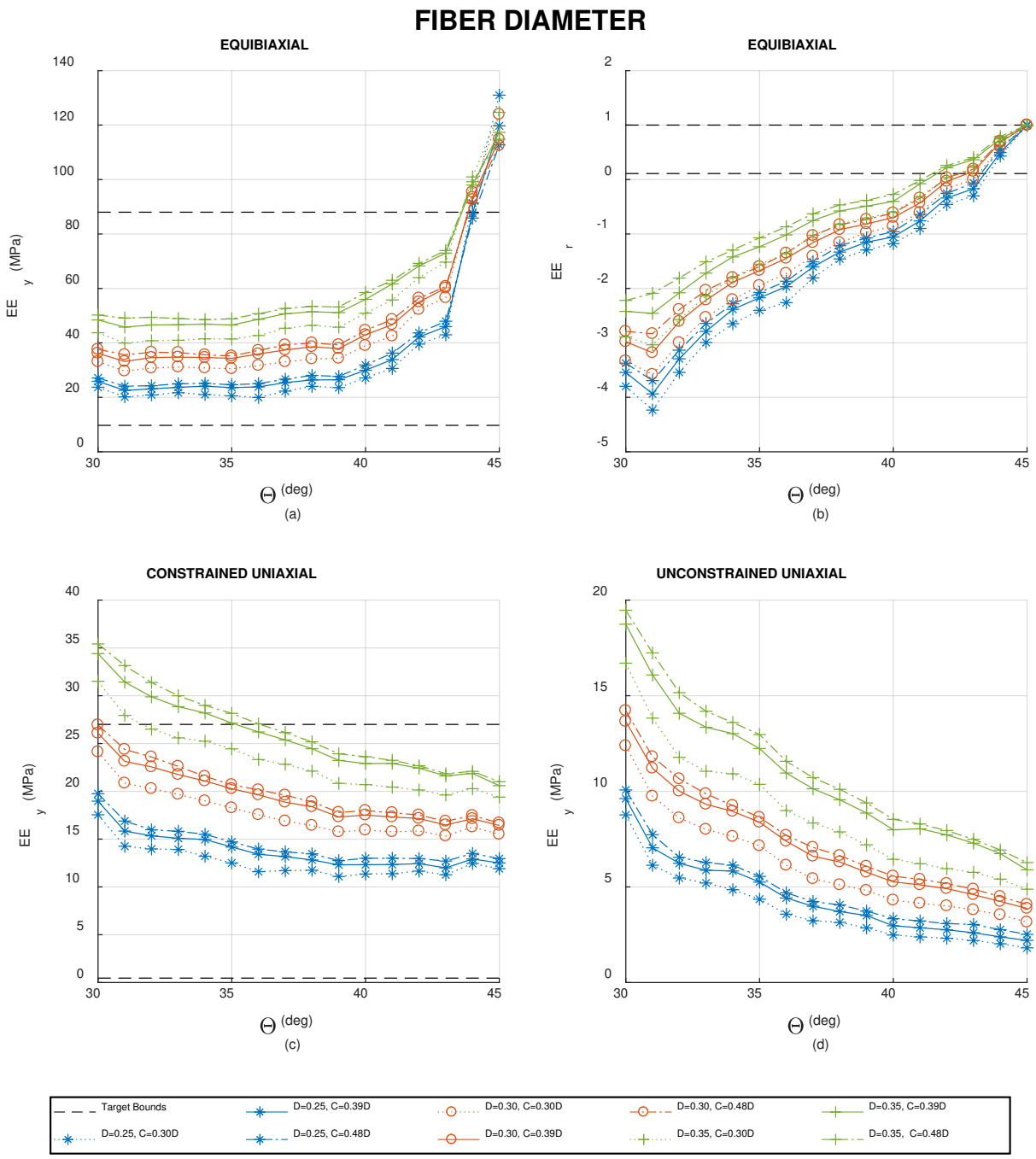

Figure 20. Cruciform effective elastic moduli as a function of fiber angle from the y-direction for combinations of three fiber diameters (D) and three contact radii (C). Data shown are: **(a)** EE_y in equibiaxial tension, **(b)** EE_r in equibiaxial tension, **(c)** EE_y in transversely constrained uniaxial tension, and **(d)** EE_y in unconstrained uniaxial tension. The range of native AF target mechanics are shown with dashed black lines[29,31–42].

The predicted effect of fiber spacing (S) in equibiaxial tension was a generally larger EE_y for lower S (Figure 21a). The magnitude of this effect was not consistent, and the S = 0.8 mm scaffold predicted a lower EE_y as compared to the S = 1.0 mm scaffold at the 44° and 45° fiber angles. The equibiaxial EE_r was generally more positive for smaller S (Figure 21b), however, there was again no consistent trend. The transverse constrained (Figure 21c) and unconstrained (Figure 21d) uniaxial data both predicted a greater EE_y for smaller S and, additionally, the increase in EE_y between S = 1.0 mm and S = 0.8 mm was consistently greater than the increase in EE_y between S = 1.2 mm and S = 1.0 mm. In all testing regimes, the influence of fiber contact radius was consistently greater for smaller S.

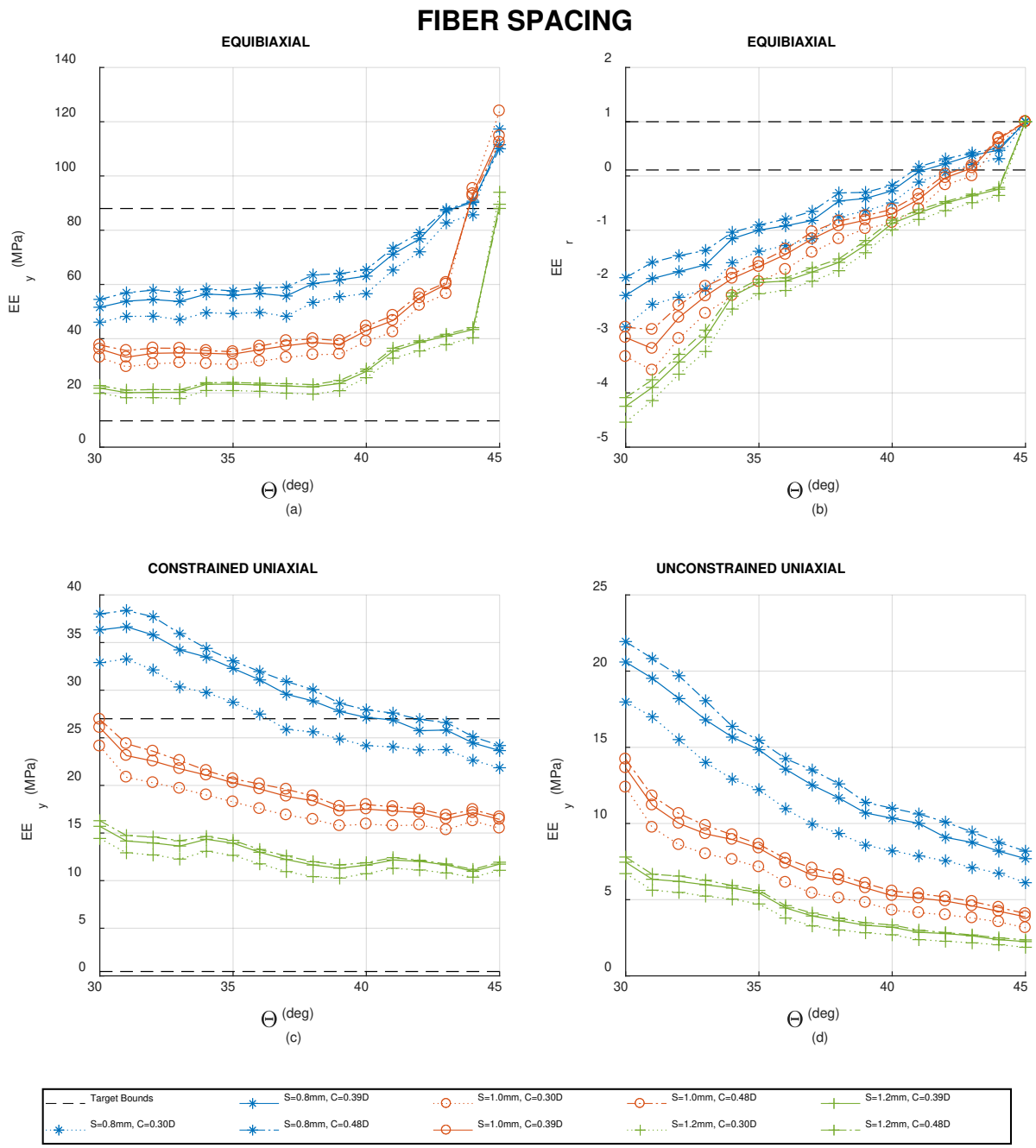

Figure 21. Cruciform EE as a function of fiber angle from the y-direction for combinations of three fiber spacings (S) and three contact radii (C). Data shown are: **(a)** EE_y in equibiaxial tension, **(b)** EE_r in equibiaxial tension, **(c)** EE_y in transversely constrained uniaxial tension, and **(d)** EE_y in unconstrained uniaxial tension. The range of native AF target mechanics are shown with dashed black lines[29,31–42].

A larger layer count (N) predicted a generally larger equibiaxial EE_y (Figure 22a) and generally more positive EE_r (Figure 22b), although these effects were relatively small in magnitude. The transverse constrained (Figure 22c) and unconstrained (Figure 22d) uniaxial data also predicted little change in EE_y with N. The increase in EE_y between N = 4 and N = 6 was consistently greater than the increase in EE_y between N = 6 and N = 8. Fiber contact radius had a greater influence on EE_y as compared to N for all loading regimes.

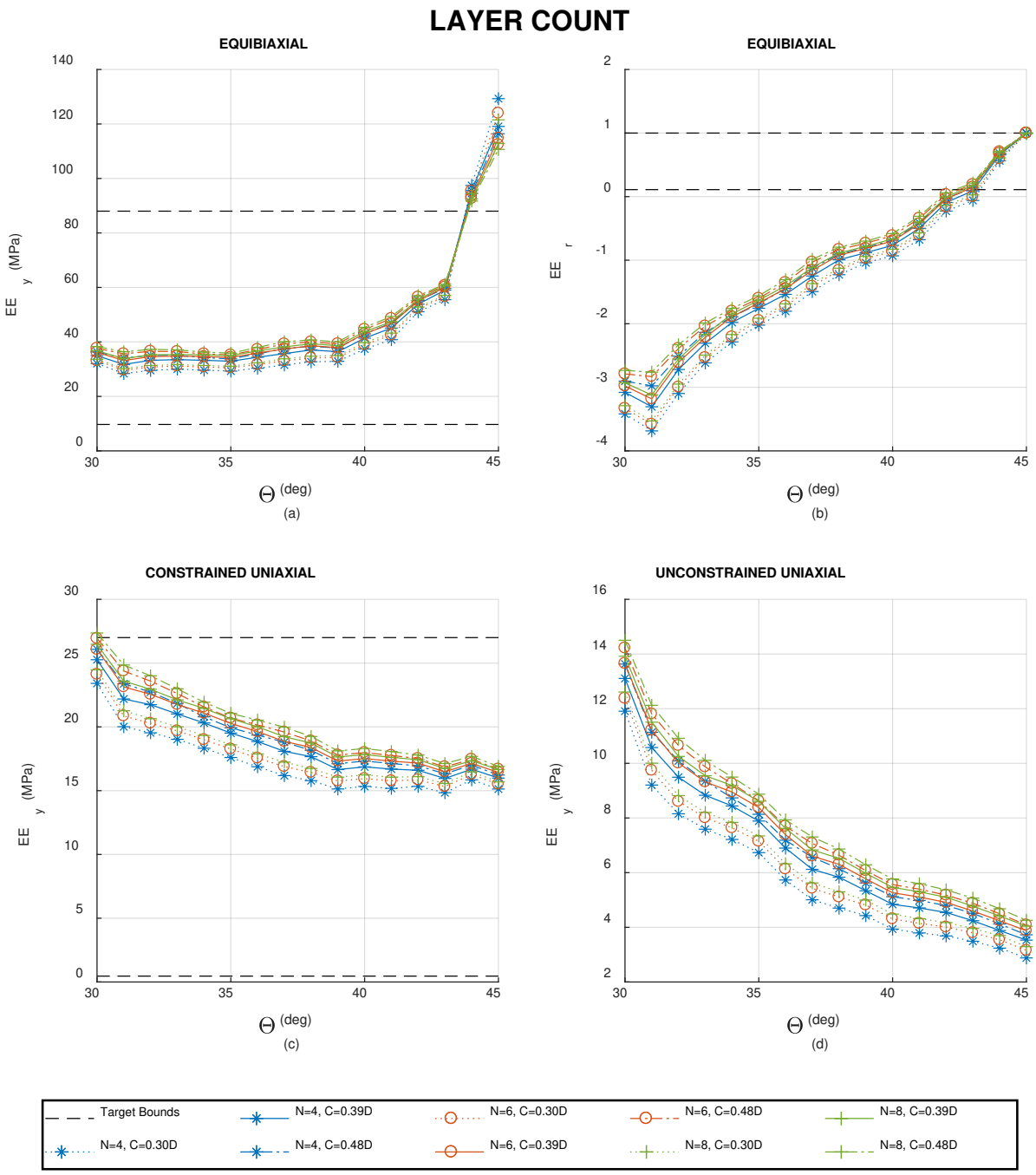

Figure 22. Cruciform elastic moduli as a function of fiber angle for combinations of three layer counts (N) and three contact radii (C). Data shown are: **(a)** EE_y in equibiaxial tension, **(b)** EE_r in equibiaxial tension, **(c)** EE_y in transversely constrained uniaxial tension, and **(d)** EE_y in unconstrained uniaxial tension. The range of native AF target mechanics are shown with dashed black lines[29,31–42].

Graphically, the perturbations in both elastic modulus (E) and layer thickness (Z) were predicted to scale the stiffness data uniformly for all Θ and contact radii (C). When normalized to E, the predicted deviations in EE due to the negative and positive perturbations to E had a mean and maximum of 1.2×10^{-4} % and 2.1×10^{-4} %, respectively, for all three test regimes (equibiaxial, transverse constrained uniaxial, and unconstrained uniaxial), all C, and all Θ. Similarly, Table 6 shows the percentage error of the negative and positive perturbations to layer thickness normalized by multiplying by the layer thickness (i.e. a force-strain stiffness). The residual changes in EE due to perturbations in layer thickness that were not explained by changes in stress area resulted in consistently higher EE and lower EE for the negative and positive perturbations to layer thickness, respectively. Similarly, the residual errors resulted in consistently lower EE_r and higher EE_r for the negative and positive perturbations, respectively. The maximum absolute percent errors in EE and EE_r reported in Table 6 occurred at an asymptote in the stiffness.

Table 6. Errors in cruciform EE compared to the base layer thickness (0.8 D) after normalization to the total scaffold thickness (i.e. normalization to overall stressed area). The EE_y data include all three test regimes (equibiaxial, transverse constrained uniaxial, and unconstrained uniaxial), all contact radii (C), and all fiber angles (Θ). The equibiaxial EE_r data include all contact radii (C) and all fiber angles (Θ).

EE Variant		**EE_y**		**EE_r**	
Layer Thickness (Z)		**0.7 D**	**0.9 D**	**0.7 D**	**0.9 D**
Absolute % Error	Minimum	0.60	0.85	4.3 × 10-5	6.4 × 10-5
	Median	2.6	3.9	0.048	0.079
	Maximum	5.6	100	0.083	0.15
	Mean	3.0	4.7	0.046	0.072

2.2.4. Discussion

In this study, the EE and EE_r of a FE model of an angle-ply laminate cruciform was predicted in equibiaxial tension, transversely constrained uniaxial tension, and unconstrained uniaxial tension. Perturbations to a variety of print parameters were made to the model and the influence on the EE and EE_r was presented. Highly linear correlations were found between nodal displacement and undeformed position within the ROI, indicating a high degree of continuum-level homogeneity in the central region of the cruciforms. The strong fit of the FE model to the experimental data (Figure 19) indicates that the FE model captures the overall mechanical behavior of the angle-ply architecture. The measured fiber diameter and spacing were similar to the FE model base parameters and within the bounds of the FE model parameters considered in the present study**.** The measured layer height was smaller than the bounds considered in the study, however, this condition represents a worst-case distortion of the idealized geometry from the true fabricated geometry. The optimized PCL elastic modulus (114 MPa) was 42.9% of the assumed bulk PCL modulus (265 MPa [178]).This lower elastic modulus is reasonable and expected in the fabricated scaffolds due to thermal effects on the PCL during the printing process[178]. The optimized contact radius of 0.27 mm is also intuitively larger than the fiber radius (0.169 mm) as it represents a region where excess material at the intersection of fibers forms a "weld-like" region. Further, circular interlamellar contacts are a simplification of the more ellipse-shaped contact areas that are typically observed in the printed constructs. Accordingly, a larger circular contact radii may be required to generate the same rotational stiffness (i.e. polar moment of inertia) as an elliptical fiber intersection with the same contact area.

Distinct trends in EE and EE_r were apparent with changes in Θ. Perturbations to fiber diameter and fiber spacing also exhibited appreciable changes in the EE and EE_r, however,

perturbations in the number of laminate layers (N) showed only minor changes in EE and EE_r. Perturbations in layer spacing (Z) and material elastic modulus (E) demonstrated little or no change in EE and EE_r after normalization to Z and E, respectively.

2.2.4.1. Fiber angle

The fiber angle (Θ) was predicted to have a dramatic influence on scaffold EE in all three loading regimes. These trends in EE_y and EE_r with varying Θ demonstrated a relatively non-smooth behavior. This observation is likely caused by the discrete fiber architecture of the scaffold such that small changes in Θ may appreciably change the fiber location at the boundary conditions, as depicted in Figure 23. Additionally, the FE model predicted that scaffolds with a positive EE_r all had $EE_r < 1.0$ which indicated that these scaffolds were stiffer in the non-dominant fiber direction (x-direction) than the dominant fiber direction (y-direction). This predicted response is in agreement with data from the experimental biaxial series (Section 2.1).

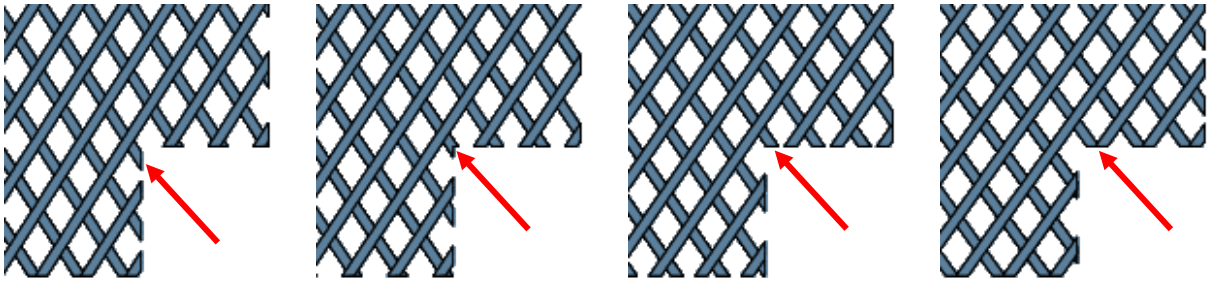

Figure 23. Deformed model images demonstrating fiber wrapping at the boundary conditions. Shown is one cruciform corner of the base parameter model with: **(a)** 33° fiber orientation where the fiber near the corner (indicated by the arrow) is on the vertical boundary, **(b)** 34° fiber orientation where the fiber near the corner (indicated by the arrow) transitions between horizontal and vertical boundaries, **(c)** 35° fiber orientation where the fiber near the corner (indicated by the arrow) is on the horizontal boundary, and **(d)** 36° fiber orientation where the fiber near the corner (indicated by the arrow) is on the horizontal boundary and is attached to an adjacent fiber to transmit loads.

2.2.4.2. Fiber diameter

It was shown that a larger fiber diameter consistently generates a more positive EE_r (Figure 20) which becomes tensile in both cruciform directions at lower fiber angles. This is an important attribute for AF scaffold design for three main reasons. Firstly, there was a larger range of fiber angles that generated equibiaxial tensile stresses in both cruciform directions; this effect assists in matching the native AF mechanical properties. Secondly, the magnitude of EE (Figure 20a) is more sensitive at larger fiber angles, therefore, designing within the lower fiber angle regime is desirable and is achievable by incorporating larger fiber diameters. Thirdly, a larger fiber diameter demonstrated a lower sensitivity of EE_r to fiber angle with (i.e. larger fiber diameters exhibited a lower gradient in Figure 20b) and, therefore, less likely to generate compressive stresses in the transverse direction due to orientation and loading perturbations in clinical application.

Layer thickness was defined relative to the fiber diameter, and thus, the scaffolds thickness (and ultimately the stress area) increased with larger fiber diameters. However, despite the relatively larger stress areas, the models with larger effective fiber diameter exhibited distinctly larger EE in all three test regimes. This result indicates that increasing the fiber diameter is a valid method to increase the stiffness of angle-ply scaffolds, despite the corresponding increase in layer thickness. The contact radius was also defined relative to fiber diameter; there is a corresponding increase in the EE variability due to perturbations in contact area with increase in D, likely as the perturbations in contact area also increased with fiber diameter (contact area ~ D^2). Overall, these data demonstrated the complexity of tailoring scaffold mechanics using a process parameter (i.e. fiber diameter) as outcomes are convoluted with many other process parameters, which lead to secondary effects. These data also highlighted the importance of establishing tight control of fiber diameter. Fluctuations in fiber diameter during the fabrication process may lead to unexpected

results due to direct influence of fiber diameter (as described above) but also the secondary influence on other process parameters (such as scaffold thickness and contact area).

2.2.4.3. Contact radius

General inferences with respect to the effect of layer contact on construct mechanics can also be made from the current parametric studies. For example, the fiber spacing results (Figure 21) demonstrated that a greater contact radius (C) resulted in greater EE and EE_r and, conversely, a lower C resulted in lower EE and EE_r. This trend in EE can be attributed to a stiffening of the in-plane rotational deformation constraint at the fiber contacts. Perhaps to a lesser extent, the effective fiber element length between contacts is reduced by a larger contact area and, accordingly, all deformation modes are reduced. The same observed trend in EE_r indicates that C influences the dominant fiber direction (y-direction) mechanics more than the non-dominant direction (x-direction). Further, the effect of C was predicted to be nonlinear; the increase in EE from C = 0.30D to C = 0.39D was substantially greater than the increase in EE from C = 0.39D to C = 0.48D.

2.2.4.4. Fiber spacing

The influence of fiber spacing was predicted to be nonlinear; the difference in EE between 1.0 and 0.8 mm spacing was more pronounced than the difference between 1.2 and 1.0 mm spacing. This indicates that appreciable gains in stiffness can be generated by further reducing the fiber spacing (along with a reduced sensitivity of EE_r to Θ). This nonlinear trend is likely due to a quadratic increase in the number of fiber contacts as the fiber spacing is reduced and the nonlinear influence of fiber element length in bending deformation. The increase in stiffness is limited by the volume fraction of the scaffold as previous studies have suggested a volume fraction less that approximately 50% is required to afford sufficient cell ingrowth and proliferation [164].

2.2.4.5. Material modulus

The data clearly demonstrated the expected result that FE predictions of EE scale identically with material modulus. The residual error in this exact relationship may be attributed to numerical/computational approximation. Two major implications can be drawn from these data. Firstly, the well-documented reduction of the materials modulus and anisotropy associated with the melt extrusion process[165,178,179] can be easily accounted for by simply scaling the data. Secondly, the mechanics of identical architectures with new materials can be reasonably estimated by scaling the material modulus, as long as the new material exhibits linear elasticity within the expected strain range. A possible confounding factor of scaling the material modulus in new materials is differences in fiber shape (e.g. cross-sectional circularity and longitudinal straightness) and layer contact strength due to variation in the chemical and thermal properties between materials.

2.2.4.6. Layer count

The influence of the layer count on EE was relatively small as compared to perturbations in contact area (Figure 22). Based on the small sample size of three different layer counts, the moduli appeared to converge (i.e. the change in modulus from four to six layers appears consistently larger than the change in modulus from six to eight layers). Extrapolating this result indicates that the biaxial data from thin cruciform specimens (N = 6 layers) may be useful for approximating the elastic response of thicker, more clinically relevant geometries, however this extrapolation requires further validation.

2.2.4.7. Layer thickness

Smaller layer thicknesses exhibited greater EE and a more positive EE_r for all Θ and contact radius (C) as compared to larger layer thicknesses. Table 6 shows that most of the variation in EE and EE_r from perturbations to the layer thickness could be explained by normalizing to the total scaffold thickness. Therefore, changes in EE due to layer thickness are almost exactly proportional to the change in stressed area. In other words, scaffolds with the same layer count exhibit comparable force-displacement characteristics regardless of layer thickness. The residual error is likely due to changes in adjusted material elastic modulus, as a smaller layer thickness (Z) for a given fiber diameter (D) must have an increased E_2 (Equation (6). Although this increase in adjusted elastic modulus is only a phenomenon of the model, it represents a physical flattening of the fiber cross-section in the z-direction to accommodate a smaller layer and the corresponding increase in bending stiffness in the x-y plane. These results from perturbations to the layer thickness demonstrate an important aspect of printed scaffolds; the stiffness depends largely on the number of layers and not the height at which they are stacked. Conversely, when printing an implant for a specific anatomical location or regenerative medicine application, it is the overall height of the scaffold which is critical and this could be achieved with many different numbers of layers with different heights. Accordingly, the FE model demonstrates that control of layer thickness during the printing process is essential to producing consistent scaffold mechanics. Additionally, a reduction in layer thickness in physical scaffolds (resulting in flattened fiber cross sections in the z-direction) likely increases the contact radius and associated apparent-level stiffening.

2.2.4.8. Implications for design

It seems intuitive that the previously described boundary condition effect (Figure 23) would be reduced in less discrete and more homogeneous structures. Indeed, the moduli with a smaller spacing (Figure 21) appeared to have a more continuous trend with changes in fiber angle. A smaller fiber spacing and larger fiber diameter both reduced the sensitivity of EE to Θ in equibiaxial tension, although this sensitivity was increased in both uniaxial modes. Fiber diameter is a process parameter that can be difficult to control and larger diameters do not reflect the size scale of the structural collagen in native AF. Therefore, it appears that two design parameters, fiber spacing and fiber angle, are the most useful parameters for tailoring scaffold mechanics to the native AF mechanics. Further, whilst layer count and layer thickness may be inversely proportional (for a constant construct thickness), the influence of these two parameters on construct EE can be explained independently.

2.2.4.9. Mechanical evaluation of tissue scaffolds

Fiber composite models that capture affine fiber reorientation during loading are a candidate to predict the mechanical behavior of angle-ply laminates. However, in 3DF fabrication, bonding between layers restricts affine reorientation of the fibers and, therefore, the local deformations within the FE model are not affine with respect to the macroscopic deformation. Accordingly, fiber composite models may not be appropriate. Angle-ply laminates may also be suited to frame-element structural analysis which captures the axial, shear, and bending deformation mechanisms of the unsupported fiber sections in the scaffold. Indeed, many basic inferences may be made by considering an array of frame elements with rotationally-compliant connections. However, frame analyses are not represented as volumes, and therefore, cannot be augmented with other FE constructs as easily as three-dimensional FE analyses. Accordingly, this

study was designed to use FE analysis due to the practicality of translating the model into further, more clinically relevant geometries and loading conditions, specifically for incorporation into a larger validated FE spine model[162]. Additionally, FE analyses pose an efficient method to explore new geometries, such as graded mechanical properties to drive varied changes in cellular outcomes that may be useful for integration with the native tissue (such as the implant-native tissue interfaces).

The data in this study would have been extremely difficult and time consuming to generate through experimental analyses. A similar evaluation of physical scaffolds would require the fabrication of a number of samples for sufficient statistical power at each design point, followed by multiple mechanical tests and corresponding post-processing. Moreover, physical testing of scaffolds would consume considerable machine time and printing materials. This study demonstrates the utility of FE analyses to drive design and then validate the selected design. Future steps for the fiber angle-ply laminate FE model are to validate the predicted stiffnesses against experimental data of corresponding scaffolds. Based on the indications of this study, the scaffold parameters can then be optimized to identify a set of parameters which replicate the native AF mechanics and predict minimal sensitivity to critical print parameter perturbations (such as listed in Table 5). The optimized parameters would then be further validated and changes made to the FE model accordingly.

2.2.4.10. Limitations

The FE model is an idealized approximation of a printed geometry and it is expected there are geometric variances and mechanical interactions that may not be included in the current model. Shear deformation may be another pertinent deformation mechanism and the rectangular fibers do not identically match the shear behavior of circular fibers. In addition, the data presented in this

study may only apply to the cruciform geometry and it is possible that the mechanical behavior may be different for different geometries, in particular due to boundary condition effects. The FE model used an isotropic elastic modulus based on the bulk material. As previously discussed, melt deposition reduces the overall elastic modulus, however, it may also stiffen the material in the fiber direction (i.e. axial direction) relative to the transverse plane[179]. The melt deposition process may also induce residual stresses within the scaffold, which were not considered in this study. The influence of fiber anisotropy and residual stresses on the scaffold mechanics may be leveraged to more closely approximate the local mechanics in the future.

2.2.5. Conclusion

The results of this study demonstrated the influence of various print parameters on the biaxial and uniaxial elastic moduli of 3DF angle-ply laminate scaffolds. Of the print parameters considered in this study, fiber angle, fiber diameter, and fiber spacing were found to have to the most dramatic influence on EE and EE_r. Layer thickness and contact area were found to have moderate influence on EE and EE_r, and the number of layers was found to have only a minor influence on EE and EE_r. The material elastic modulus scaled EE to numerical precision, and therefore, EE_r was not affected. The data presented in this study both aid the selection of design parameters and highlight the importance of controlling process parameters in the fabrication of micromechanically-tailored tissue engineered scaffolds.

CHAPTER 3 –THE REGENERATIVE RESPONSE OF CELL-LADEN TISSUE ENGINEERED SCAFFOLDS UNDER MECHANICAL STIMULUS

Specific Aim 2 was to evaluate the tissue response of cell-laden scaffolds cultured with dynamic biaxial mechanical stimulus using experimental and computational methods. The experimental and computational aspects of Specific Aim 2 are divided into Section 3.1 and Section 3.2, respectively.

3.1. Experimental Approach

3.1.1. Introduction

In this study, TE scaffolds were seeded with mature ovine annulus fibrosus cells and cultured under dynamic biaxial tension to observe the influence of physiologically-relevant loading on tissue formation. To consolidate the advantageous mechanical and biological features of 3DF and MEW, a hybrid 3DF/MEW scaffold architecture was developed and implemented in the cell cultures. Ultimately, this study aimed to evaluate the suitability of the proposed scaffold architecture for AF repair and to identify whether multiaxial loading modes may be advantageous to promote AF tissue regeneration.

3.1.2. Methods

3.1.2.1. Scaffold design and fabrication

Cruciform scaffolds were designed based on a previously developed architecture that best replicated the mechanical properties of native AF (Section 2.1). Specifically, an angle-ply laminate

was prescribed for 3DF fabrication (fiber angle = 34°, fiber spacing = 1.0 mm, approximate fiber diameter = 300 µm). The cruciform geometry was used to deliver biaxial loading to a homogenous region (approximately 5 x 5 mm) at the center of the scaffold, as demonstrated in previous work (Section 2.1). To prevent failure of the scaffold at the stress concentrations, webbings were added at the internal corners of the cruciform and reinforcement fibers were added to the flanges at the grip sites (Figure 24). Additionally, MEW scaffolds (fiber angle = *34°,* fiber spacing = 1.0 mm, approximate fiber diameter = 30 µm) were inserted between the lamellae of the 3DF scaffold to generate a hybrid 3DF/MEW scaffold with fibers of multiple size scales (Figure 24). This multi-scale scaffold design was hypothesized to be more advantageous for AF repair. Specifically, the hybrid scaffold contained MEW fibers that were similar to the scale of the resident cells, yet maintained the overall geometrical and mechanical integrity of the implant due to the 3DF fibers.

Scaffolds were fabricated with a 3DDiscovery bioprinter (RegenHu Ltd, Villaz-Saint-Pierre, Switzerland). First, the MEW sheets were prefabricated with a MEW toolhead (MESW module, 26 gauge nozzle, nozzle length = 15 mm, melt temperature = 65 °C, extrusion pressure = 80 kPa, translation rate = 40 mm/s, voltage = 4.5 kV, collector distance = 3.0 mm) and cut into 15 x 15 mm sections. The MEW sheets were made from PCL with number average molecular weight (Mn) of 45,000 (Sigma Aldrich, St. Louis, MO, USA) because PCL with Mn = 80,000 was found to not produce a reliable Taylor cone for MEW. The 3DF architecture was printed with a 3DF toolhead (HM-100 module, 27 gauge nozzle, nozzle length = 6.35 mm, extrusion temperature = 130 °C, extrusion pressure = 100 kPa, translation rate = 3 mm/s, auger speed = 4.5 rev/min). Preliminary biaxial testing of 3DF scaffolds in physiological conditions found that PCL with a Mn of 45,000 fractured under cyclic loading at small strains. Therefore, PCL with Mn = 90,000 (Sigma Aldrich, St. Louis, MO, USA) was used for the 3DF fibers. MEW sheets were manually inserted

between each 3DF bilayer at the center of the cruciform such that the 3DF and MEW fiber architectures aligned. The hybrid scaffold fabrication is illustrated in detail in Figure 24.

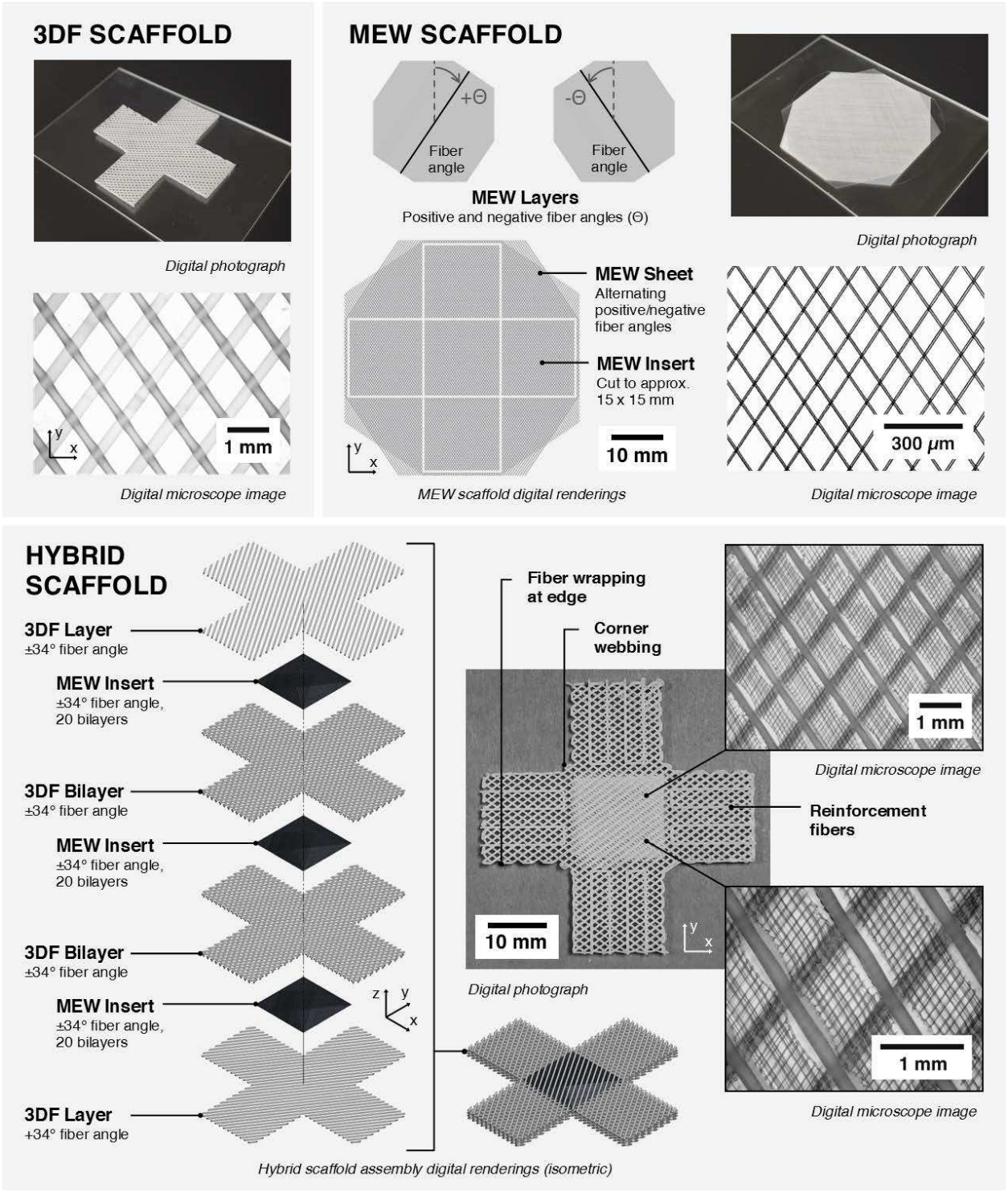

Figure 24. Diagram of the 3DF, MEW, and hybrid scaffolds showing the architecture and relative scales of the 3DF and MEW components of the hybrid scaffold.

To measure the resultant fiber diameters of the MEW and 3DF processes, ten (n =10) additional samples of the MEW sheets and 3DF cruciform (without the MEW layers) were printed with the same prescribed architectural and process parameters as the implants. Only one bilayer of these additional samples were printed to improve image quality. Images of each sample were captured using a transmission light microscope (Olympus BH-2, Tokyo, Japan) and ten random fiber diameters were measured from each scaffold (excluding the initial layer of 3DF fibers) using ImageJ software (National Institutes of Health, Bethesda, MD, USA). The average fiber diameter and spacing for each type of scaffold were then calculated. To observe the hybrid scaffold architecture, three example scaffolds with the combined 3DF/MEW architecture were also fabricated and imaged using the same methods.

Scaffolds were infused with a cell-laden hydrogel for culturing. Fibrinogen was first isolated from whole sheep blood using the Cohn fractionation method[180]. Whole blood collection was performed under approval from the Institutional Animal Care and Use Committee at Colorado State University (protocol #: KP104). The scaffolds were gently soaked in ethanol for sterilization and allowed to dry in a sterile environment. For each scaffold, fibrinogen was isolated from 12 mL of sheep plasma, 1.5 mL of the remaining plasma was retained, and approximately 250,000 ovine AF cells were added to the fibrinogen solution. The fibrin hydrogel was created by pipetting the fibrinogen solution into each scaffold in a custom mold then gently mixing 500 units of thrombin (bovine thrombin; Sigma Aldrich, St. Louis, MO, USA) into the mold with a pipette. The cell-laden scaffolds were allowed to set for 15 minutes at room temperature before being gently removed from the molds.

3.1.2.2. Study design

Cell-laden scaffolds were fabricated in groups of three. Within each group, a single batch of the fibrin-cell mixture was divided between the three samples to minimize variability in the fabrication process. Samples were randomly allocated as either a: (1) time-zero control, (2) sham control, or (3) treatment. The time-zero control sample was processed for histological evaluation immediately following infusion of the cell-laden scaffold. The sham control and treatment samples were cultured under identical environmental conditions for two weeks in a custom incubator. The treatment sample was additionally prescribed a dynamic biaxial mechanical loading protocol.

3.1.2.3. Incubation with dynamic biaxial stimulus

The sham control and treatment samples were cultured in a custom designed incubator with a mechanical system for dynamic biaxial mechanical actuation of the treatment sample (Figure). Detailed design and validation of the biaxial incubator are elucidated in Appendix B. The treatment sample was placed in a custom sterile enclosure and clamped within two orthogonal sets of grips. The culture medium for the study consisted of Alpha minimum essential medium (αMEM) with L-glutamine with 10% fetal bovine serum and 1% penicillin/streptomycin. Twenty-five milliliters (25 mL) of culture media were added to the sterile enclosure before it was sealed and fastened to the biaxial system. The sham control sample was placed in a glass bottle with 25 mL of culture media and the vented bottle was placed in the incubator.

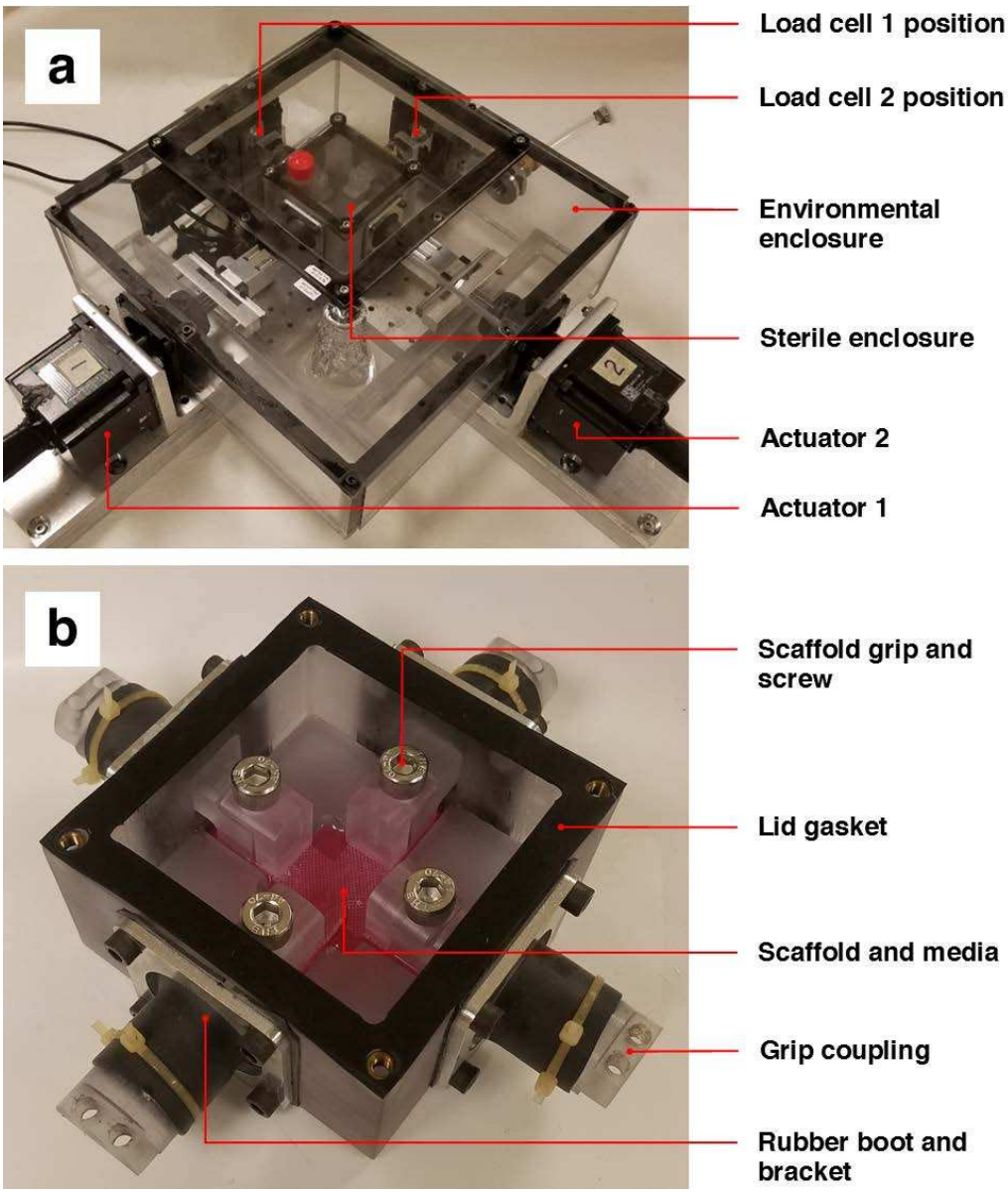

Figure 25. Digital photographs of the custom biaxial incubator design: **(a)** the environment chamber and biaxial mechanical system, and **(b)** the sterile enclosure. The environmental enclosure controlled the gas composition and humidity for the cell culture and was housed within a thermal enclosure at 37°C. The sterile enclosure was located around the center of the biaxial system and within the environmental enclosure. The scaffold was submersed in a well of culture media and was gripped by the arms of the sterile enclosure. Overall, the system allowed the cell-laden scaffold to receive dynamic biaxial stimuli from the biaxial apparatus in a controlled environment.

Once samples were loaded in the incubator, the environment was allowed to equilibrate (temperature = 37 °C, relative humidity > 80%, CO_2 level = 5.0%) and the scaffold was exposed to a dynamic, biaxial strain protocol via two orthogonal linear actuators (Zaber NA34C60-T4,

Vancouver, BC, Canada). In detail, the treatment scaffold was prescribed sinusoidal, global strains with amplitudes of 2.5% and 0.5% in the axial and circumferential directions, respectively, at 0.1 Hz for 8 hours per day (i.e. 2880 cycles per day). The frequency, duty cycle, and biaxial loading modality were prescribed to approximate the *in vivo* loads experienced by the AF. The specific magnitudes of the global strain protocol were adopted based on predicted regeneration potential from a model of the cellular micromechanical environment in the scaffold architecture (Appendix C). Additionally, a 2.5% limit was imposed on the magnitude of the strain protocol because preliminary work found that the scaffolds fractured within 14-days at larger strains. The resultant forces applied to the treatment scaffold during culture were measured using 250 lb load cells (Honeywell AL311CN, Charlotte, NC, USA). The treatment and sham control samples were incubated under these prescribed conditions for fourteen (14) days. The culture media for both samples was changed twice during each culture (at approximately even intervals) by briefly removing the sterile enclosure from the system.

3.1.2.4. Histology

All scaffolds in the study were processed to create ground plastic histological sections. This protocol was used because: (1) preliminary work discovered limitations processing the scaffolds for other sectioning media, such as paraffin sectioning or cryosectioning, and (2) it would allow direct comparison of histological results with a study of similar scaffolds in an in vivo animal model (Section 4.1). To validate the efficacy of evaluating the scaffolds with ground plastic sections, an additional group of scaffolds were infiltrated with a fibrin hydrogel containing AF tissue. Specifically, one whole L4L5 disc was dissected from mature sheep spines, dehydrated in a desiccator, and crushed into fine pieces. The resultant minced IVD tissue was mixed into a fibrinogen solution, and cast in a scaffold using the same technique as previously described for the

culture groups. The scaffold used for this validation group was the same as the culture groups, except it did not contain MEW sheets to allow for greater infiltration of the AF tissue within the scaffold. The scaffold was then cut into eight (n = 8) equal samples for histological processing.

At their prescribed termination time, each sample was fixed in neutral-buffered formalin for 24 hours. The central region was then carefully cut into four pieces with a scalpel such that each piece contained an equal portion of the central 5 x 5 mm ROI (Figure 26). The fixed samples were dehydrated in graded ethanol, cleared with Histo-Clear (National Diagnostics, Atlanta, GA, USA), infiltrated and embedded in methyl methacrylate (MMA; Acrylosin Hard, Dorn and Hart, Loxley, AL, USA). Two sections were cut through the ROI of the embedded scaffolds. Initial sections of approximately 300 µm were taken using a diamond blade saw (Exakt Technologies, Oklahoma City, OK) and were subsequently ground to 60 - 70 µm thickness using a microgrinder (Exakt, Oklahoma City, OK). One half of the sections for each sample were stained with Sanderson's Rapid Bone Stain (SRBS; Dorn and Hart Microedge Inc., Villa Park, IL, USA) with van Gieson counterstain (VGCS; Dorn and Hart Microedge Inc., Villa Park, IL, USA) to identify cell phenotype, tissue structure, cartilage, collagen, and bone. The other half of sections for each sample were stained with toluidine blue stain (TBS; Sigma Aldrich, St. Louis, MO, USA) to detect proteoglycan content.

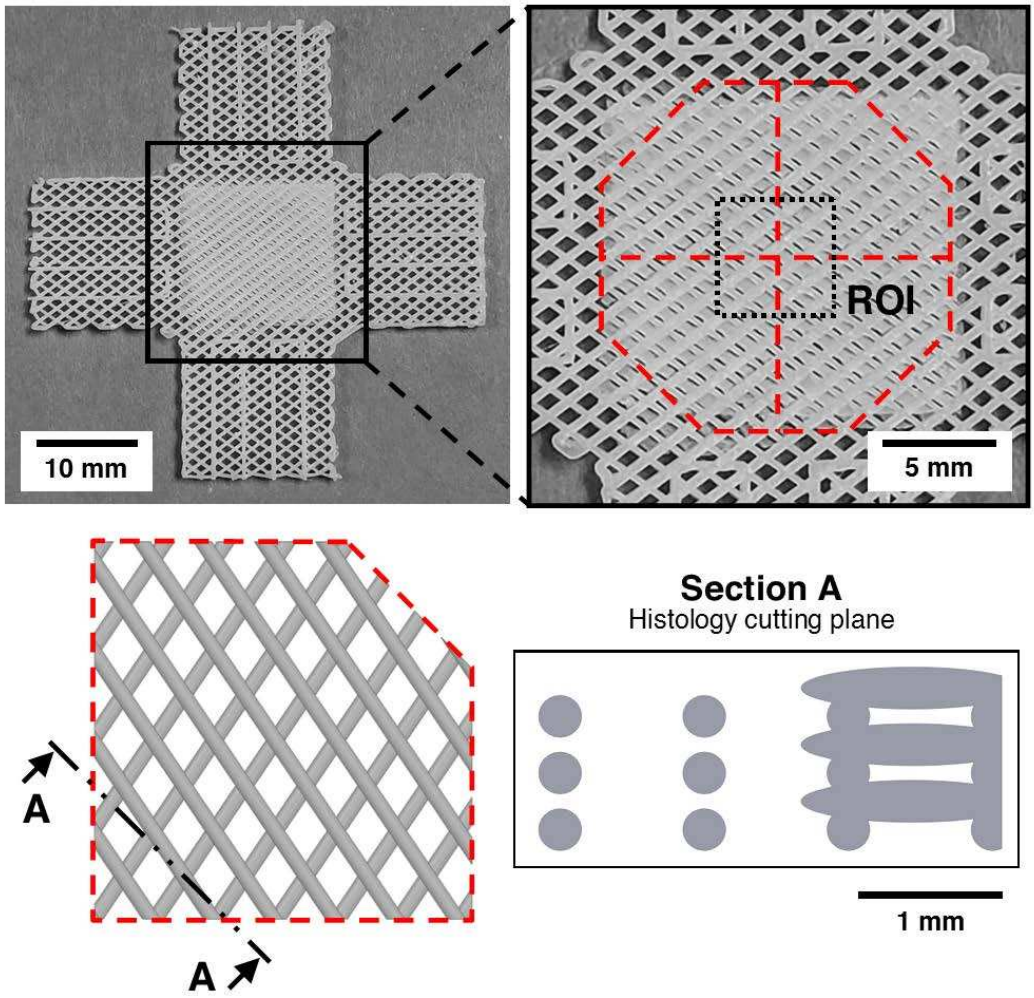

Figure 26. Diagram of the histological sections for the cruciform tissue scaffolds in the dynamic biaxial culture study. Red dashed lines depict how each scaffold was cut into four samples containing the central ROI. The location of the ROI was tracked by clipping the opposite corner of the section. Section view A demonstrates the orientation of the cutting plane used for the histology slides and a representative image of the fibers in the cut section.

Digital images of the stained slides were obtained using a standard transmission light microscope (Olympus BH-2, Tokyo, Japan). To characterize the ECM content within the histological sections, histomorphometric measurements were made using Image Pro software (Media Cybernetics, Silver Spring, Maryland, United States). The ROI for histomorphometric analyses was defined as the full area bound by the scaffold in the histological section plane. Within

each ROI stained with SRBS, the histomorphometric parameters measured were: (1) percent fiber area and (2) percent soft tissue as defined by blue/green stain.

3.1.3. Results

3.1.3.1. Scaffold design and fabrication

The fabricated hybrid scaffolds clearly exhibited that the 3DF scaffold architecture was generated with no apparent defects and the MEW scaffold architecture was mostly retained within the 3DF layers (Figure 24). Digital microscope images revealed that the MEW sheets appeared to melt near the succeeding 3DF fiber, resulting in no attachment between the MEW and 3DF fibers at these interfaces. No melting of the MEW sheets was observed at the intersection with the preceding 3DF layer. Measurement of the 3DF samples yielded a mean fiber diameter of 230 µm (±20 µm standard deviation) and a mean fiber spacing of 990 µm (±10 µm standard deviation). The mean fiber diameter and fiber spacing measured from the MEW samples were 8.7 µm and 105 µm, respectively (±1.1 µm and ±22 µm standard deviations, respectively). Notably, the fiber spacing in the MEW samples was observed to alternative between values smaller and larger than the mean fiber spacing (Figure 24); the mean small fiber spacing was 83 µm (±20 µm standard deviation) and the mean large fiber spacing was 126 (±23 standard deviation).

3.1.3.2. Incubation with dynamic biaxial stimulus

Of the eight total study groups, the treatment samples showed no signs of infection after two weeks of culture for the first six groups. However, the treatment cultures in the final two groups were compromised by infection and these groups were omitted from the study. One unloaded control culture from the final two groups was also omitted from the study due to infection. Culture media was observed to leak from the sterile enclosure during the final two

groups; it was found that the brackets used to clamp the rubber bellows on the sterile enclosure were no longer generating an effective seal for the enclosure. Of the remaining six groups, one unloaded control culture was also compromised by infection and this sample was also omitted from the results. Ultimately, six (n=6) time-zero samples, six (n=6) treated samples, and five (n=5) unloaded control samples were included in the study.

The mean amplitude of the biaxial loads applied to the scaffolds ranged from 2.1 N to 8.7 N (mean of 4.5 N) in the x-direction and from 0.6 N to 2.2 N (mean of 1.4 N) in the y-direction (Figure 27). The corresponding standard deviations for each group ranged from 0.7 N to 1.8 N and from 0.1 N to 1.3 N in the x-direction and y-direction, respectively. The mean magnitude of the biaxial loads was observed to vary between the days of the cell culture. For example, in group 6, the x-direction load progressively decreased from days 1 to 5 and from days 6 to 10 (Figure 27). However, the x-direction loads sharply increased from day 5 to day 6 and from day 10 to day 11, coincident with the change in culture media.

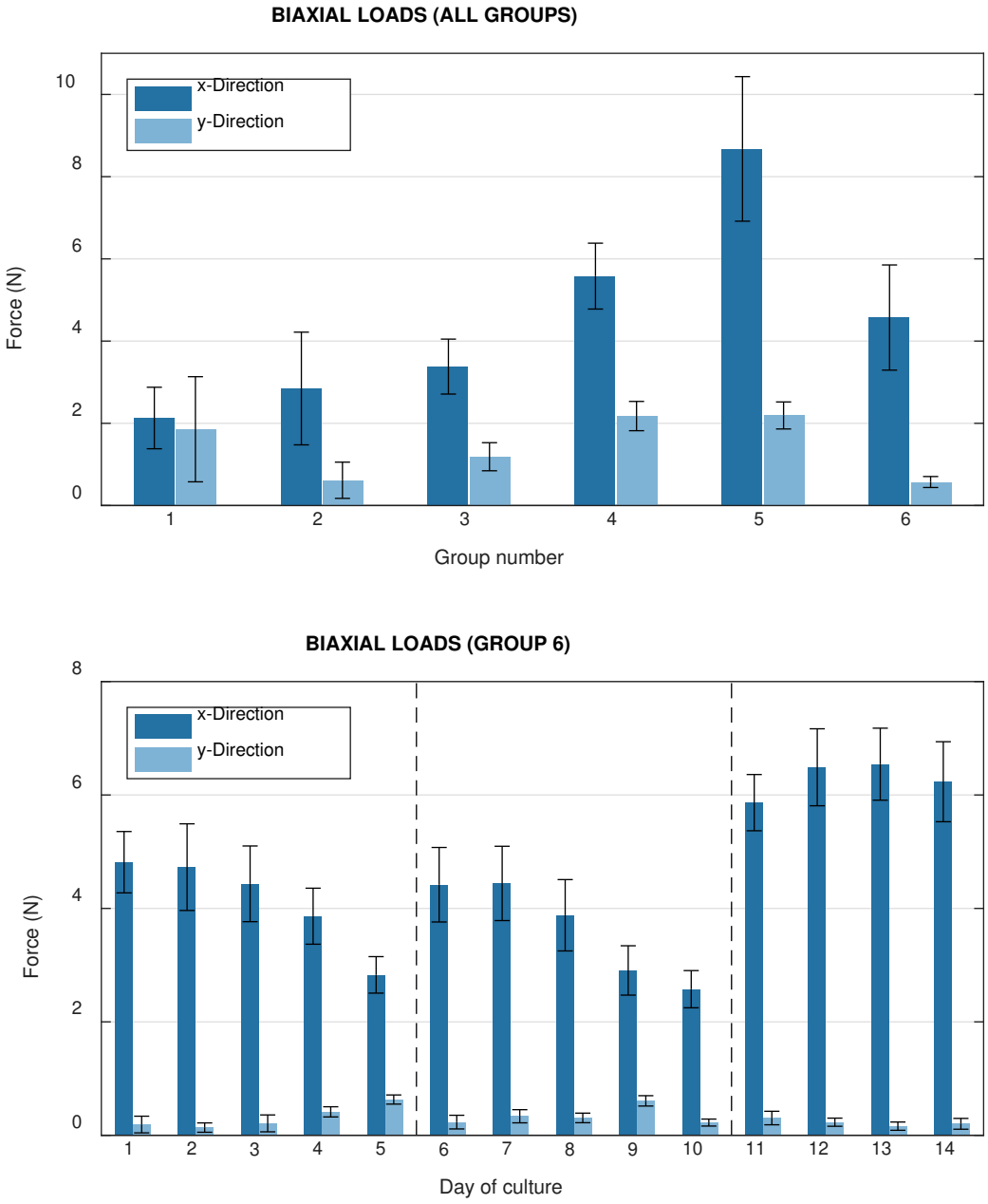

Figure 27. Mean biaxial load amplitudes measured during the loading cycles of the 14-day cell cultures. Shown are the biaxial loads for each study group and an example of the biaxial loads for group 6 for each day of the culture. Error bars indicate the standard deviation of the loading. Dashed black lines indicate when the culture media was changed during the study.

3.1.3.3. *Histology*

All histological sections stained with SRBS and TBS exhibited the 3DF fibers of the scaffold (Figure 28 and Figure 29). The fibers of the MEW sheets were also generally visible, although these fibers could not be identified in all sections (Figure 29). All PCL fibers stained with SRBS had a yellow appearance and some of the fibers also exhibited a darker stain ranging in color from blue to red. Notably, the darker stained fibers were limited to the first three groups of the study. The mean fiber area was 22.1% (±11.0% standard deviation) of the histomorphometric ROI for all samples (mean ±standard deviation of 25.3% ±7.1% for time zero samples, 25.9% ±10.4% for unloaded samples, and 15.2% ±13.0% for loaded samples). Sections stained with TB did not show any apparent staining of the PCL fibers (Figure 28). The scaffold architecture generally showed the expected cross-sectional form (Figure 26) although some defects and deformation of the scaffolds were observed. Staining of the matrix component of the scaffold was partially visible in some of the SRBS sections, observed as small regions of blue staining in proximity to the scaffold fibers (Figure 28). These blue regions were notably more prominent in the last three groups (range 0.0% to 1.6% of the histomorphometric ROI) as compared to the first three groups (all 0.0% of the histomorphometric ROI). Additionally, the blue regions were present in the time-zero scaffolds, unloaded scaffolds, and loaded scaffolds (mean ±standard deviation of 0.3% ±0.6%, 0.5% ±0.6%, and 0.1% ±0.2%, respectively). No matrix component could be identified in the TBS sections. In both the SRBS and TBS sections, no features at cell-level resolution could be clearly identified.

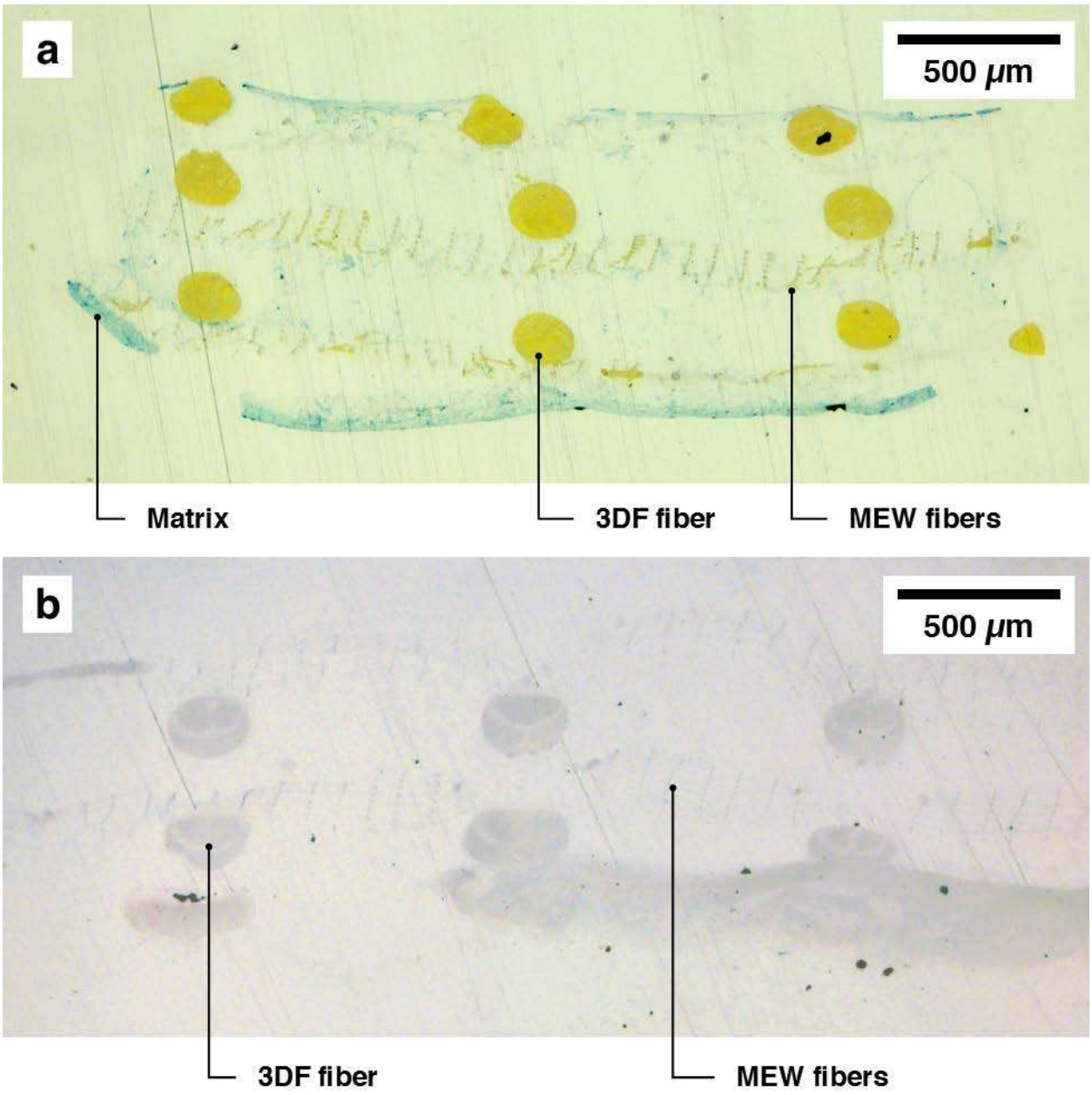

Figure 28. Example digital microscope images of histological slides stained with: **(a)** SRBS and **(b)** TBS. The 3DF and MEW fibers of the scaffold are clearly visible in the SRBS slide and the matrix surrounding the scaffold could be partially observed. No matrix was observed in the TBS slide, although the 3DF and MEW fibers were still identifiable.

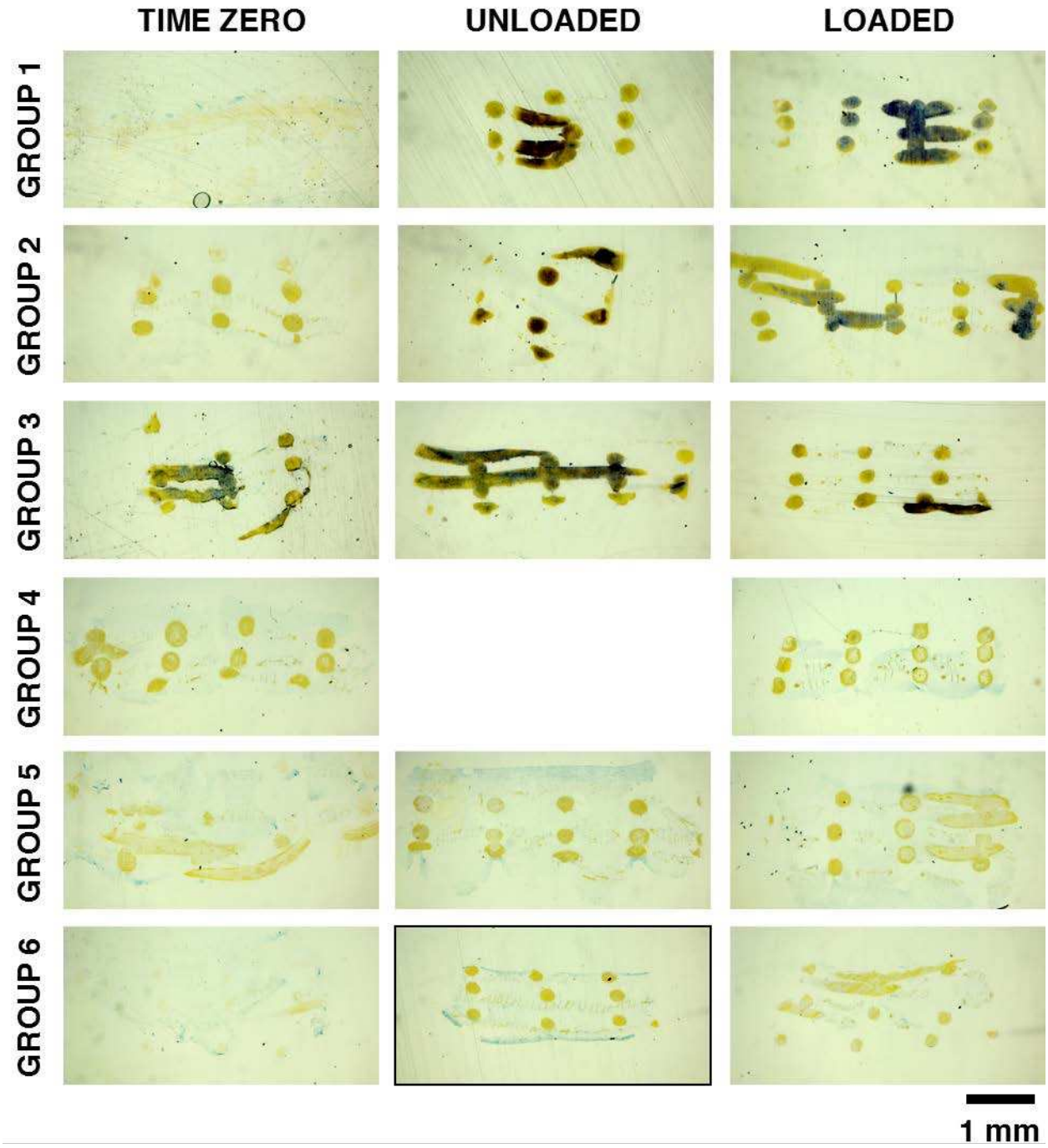

Figure 29. Digital microscope images of histological slides stained with SRBS. All six study groups and all three conditions (time-zero, unloaded, and loaded) are shown. The slide outlined in black (group 6, unloaded) is shown in detail in Figure 28. The unloaded sample of group 4 was omitted due to infection.

In the validation samples stained with SRBS, the scaffold fibers and AF-infused hydrogel were observed in the section (Figure 30). However, the scaffold fibers were not notably stained

and were not clearly identifiable in the histomorphometric analyses. In the matrix region of the scaffold, a mean of 18.1% (±11.7% standard deviation) of the ROI was stained (range 3.4% to 38.9%). The stained areas in the matrix region of the scaffold were further categorized as either dark stain (mean ±standard deviation of 6.1% ±6.5% of the ROI), blue stain (mean ±standard deviation of 9.6% ±5.4% of the ROI), or green stain (mean ±standard deviation of 2.4% ±1.2% of the ROI). The AF-infused hydrogel and scaffold fibers were also visible in the validation samples stained with TBS. Similar to the SRBS sections, the scaffold fibers were not clearly stained and were not distinguishable in the histomorphometric analyses. A mean of 18.2% (±9.2% standard deviation, range 2.4% to 28.4%) of the ROI was stained in the matrix region of the scaffold (further categorized as 13.2% ±7.3% blue stain and 5.0% ±4.2% dark stain).

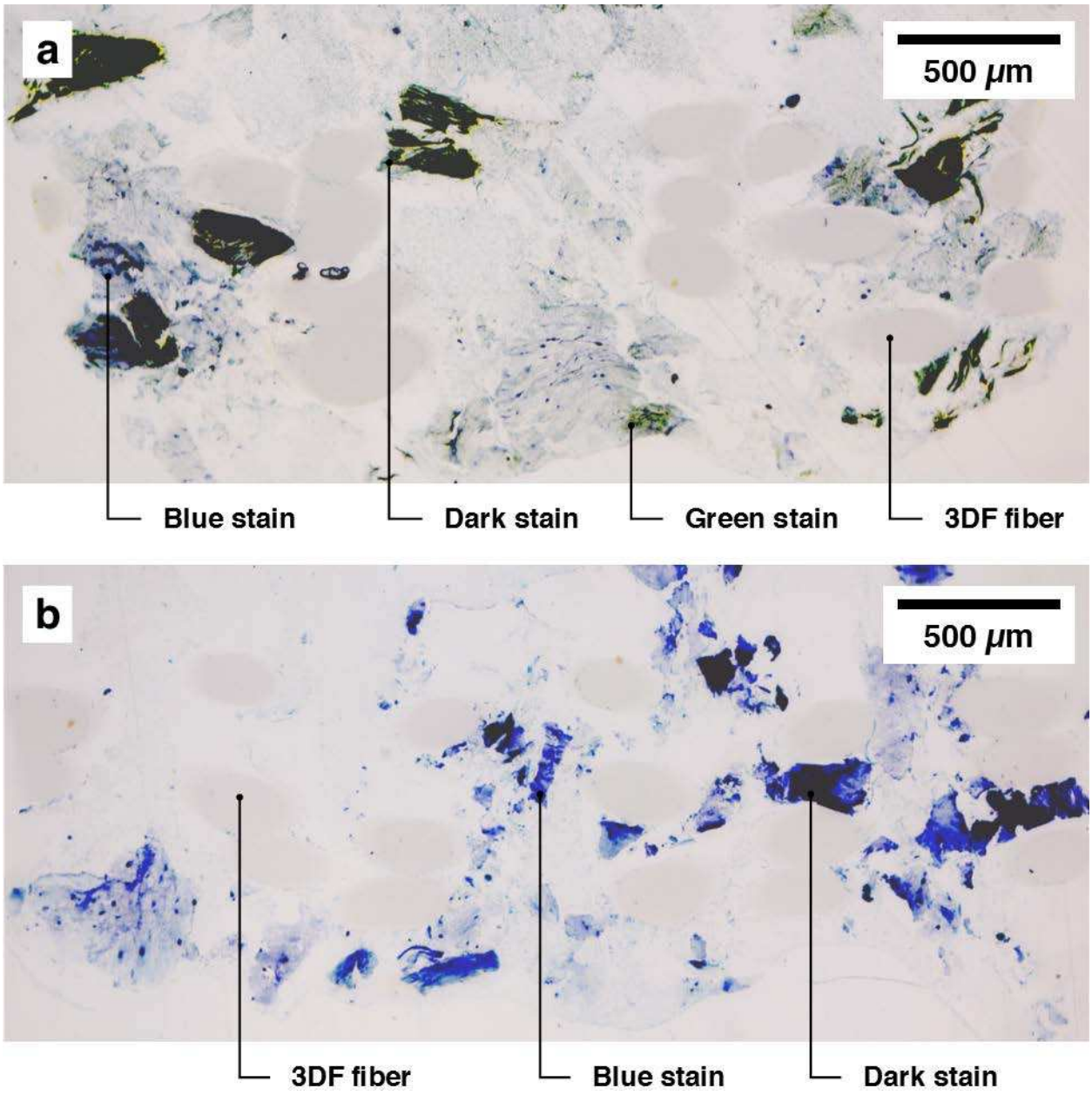

Figure 30. Example digital microscope images of validation sections stained with: (a) SRBS and (b) TBS. The 3DF fibers of the scaffold are clearly visible in both sections. The stain in the SRBS section was categorized as blue, green, or dark and the stain in the TBS section was categorized as blue or dark.

3.1.4. Discussion

In this study, a hybrid MEW/3DF scaffold for TE of the AF was designed, fabricated, and cultured under a biaxial loading regime. The fabricated hybrid scaffolds retained the small-scale MEW fibers within the 3DF scaffold. The developed incubator demonstrated sterility and cell viability following cell culture and successfully delivered the prescribed biaxial strain regime to the cell-laden scaffolds. Histological imaging of the scaffolds displayed the scaffold fibers and architecture, however, the matrix content within the scaffolds was difficult to characterize and did not reveal any consistent correlations with the scaffold loading condition.

3.1.4.1. Scaffold design and fabrication

The hybrid scaffold design was theorized to generate a multi-scale scaffold architecture was that could combine the mechanical and biological advantages of both MEW and 3DF fabrication in TE. Digital microscope images of the fabricated hybrid scaffold demonstrated that both fiber sizes were successfully incorporated. However, the MEW fibers were observed to consistently lack attachment to the subsequent layer of 3DF fibers (Figure 24); these defects can be attributed to melting of the MEW fiber as the hot 3DF fibers were laid on top. As a result, the MEW sheets in the hybrid scaffold were asymmetric and likely added additional anisotropy within the scaffold. In particular, this anisotropy would be expected to alter the CME experienced by the resident cells. An alternative design of the hybrid architecture may be able to mitigate the effect of the defects in the MEW sheets. For example, the MEW sheets could be inserted between every 3DF layer (i.e. within and between each bilayer) to alternate the direction of the defects and restore the symmetry of the scaffold. This approach would, however, double the requisite number of MEW sheets and the associated fabrication time. Accordingly, another approach may be to insert the MEW sheets between every third 3DF layer, however, the corresponding reduction in the volume

fraction of MEW fibers may have implications for the CME generated within the scaffold. A second technique to prevent the defects in the MEW sheets would be to reduce the temperature of the 3DF fibers that are laid on the MEW sheets. This could be achieved by either reducing the melt temperature or cooling the print sufficiently (e.g., conductive cooling via the baseplate or convective cooling via a fan). Lastly, alternative PCL formulations or entirely different materials may be able to better retain the MEW architecture during fabrication.

The 3DF fibers measured in this study (mean fiber diameter of 230 µm) were smaller than fibers in previous, related studies (mean fiber diameter of 338 µm; Section 2.1). This discrepancy was most likely because a different molecular weight of PCL was used between the two studies; PCL with M_n = 90,000 was used in the current study to improve the durability of the fibers as compared to PCL with M_n = 45,000 in previous work. Also, a different printer was used between the two studies, although the nozzle diameter and print temperatures remained consistent. The computational model of the CME within the scaffold that was used to inform the biaxial strain protocol were based off the comparatively large fibers in previous work. As a result, the predicted biaxial strains that were deemed sufficient to elicit a cell response for AF repair may not have been realized in the physical scaffolds with the smaller fibers. Retrospective modelling of a scaffold with the measured fiber diameters and biaxial strain regime in this study found that 0.1% of cells experienced a CME that met a previously proposed criteria for AF repair, as compared to 5.7% that was originally used to justify the biaxial strain protocol (Appendix D). Additionally, the continuum-level mechanics of the scaffold is also dependent on the fiber diameter; under the prescribed biaxial loading regime, the 230 µm diameter 3DF fibers were predicted to generate 63% and 60% lower stresses in the x-direction and y-direction, respectively, as compared to the 338 µm diameter fibers (Appendix D). Importantly, because the mechanical loading regime in the cell

cultures was global displacement control, the predicted magnitude of the local ROI strains for the small fibers (0.4% and 0.3% in the x-direction and y-direction, respectively) were small as compared to the larger fiber diameters (1.4% and 0.1% in the x-direction and y-direction, respectively).

When prescribing the stain protocol for the biaxial cultures, it was assumed that the mechanical contribution of the MEW sheets to the hybrid were negligible because the larger 3DF fibers would dominate the scaffold mechanics. Preliminary computational work on hybrid scaffolds has indicated that addition of the MEW sheets resulted in increases of 12% and 18% in the scaffold stiffness in x-direction and y-direction, respectively (Appendix D). Accordingly, the mechanical contribution of the MEW sheets at the continuum-level may not be negligible and experimental testing of 3DF and hybrid scaffolds may be useful to elucidate this effect. At the cellular-level, the preliminary computational work has also shown that the hybrid scaffold may increase the %PTE as compared to a pure 3DF scaffold under the biaxial strain protocol used in this study (Appendix D). This result supports the hypothesis that the hybrid architecture can create a more advantageous CME as compared to 3DF alone. Additional computational work would be beneficial to further elucidate how the hybrid scaffold may enhance the cellular response to global mechanical stimuli.

3.1.4.2. Incubation with dynamic biaxial stimulus

The developed incubator demonstrated sterile culture of the TE scaffolds with prescribed, measurable mechanical stimuli for the first six study groups. However, the last two groups were compromised by infection which may be attributed to leaking of the culture media at the gasket brackets. Further, two of the unloaded control groups were also compromised by infection, indicating that the sterile enclosure was similarly effective at preventing infection as the vented

bottle. Although the incubator design was initially proven to be effective, design modifications are required to improve the durability of the system. In particular, some parts were designed with plastic for ease of machinability and cost-effectiveness could be replaced with stainless steel. With enhanced resilience to mechanical and thermal cycling, the system can be utilized for future culturing of tissue engineered constructs.

In addition to investigating the cellular response to mechanical stimuli in the TE scaffold, the study found that none of the scaffolds experienced mechanical failure under cyclic, biaxial strain in physiological conditions. This demonstrated fatigue resistance of the PCL scaffold (M_n= 80,000 for the 3DF fibers) under the prescribed biaxial strain protocol. However, preliminary work found that lower molecular weight PCL (M_n = 45,000) was highly susceptible to fracture under cyclic loading in physiological conditions. Higher molecular weight PCL (M_n = 80,000) was also found to be susceptible to fracture at 5% equibiaxial strain. As a result, the prescribed global strains in this study were limited to 2.5% to minimize the risk of material failure while maintaining a theoretically sufficient CME to elicit ECM formation for AF repair. To prescribe larger strains to the TE scaffold in future studies, alternative PCL formations or different materials with greater durability are likely necessary. Relevant measures of the durability of a scaffold material include the as-printed yield stress (i.e., the yield stress of the fibers following extrusion) and the temporal profile of the yield stress during degradation in physiological conditions.

The measured forces delivered to the scaffolds (means of 4.5 N and 1.4 N in the x-direction and y-direction, respectively) were similar to the x-direction forces predicted with a previously developed finite element model of the cruciform (means of 4.2 N and 6.7 N in the x-direction and y-direction, respectively; Appendix D). However, the y-direction loading was appreciably different; the predicted load in the y-direction was larger than the x-direction and the measured y-

direction load was smaller. Only the mean x-direction load for group 5 (8.7 N) was larger than the finite element model prediction. Additionally, these loads varied considerably between scaffold groups and between the days within a particular scaffold group. Both the lower than predicted magnitude of loads and the variation between the scaffold groups can be largely attributed to challenges with: (1) accurately aligning the scaffold in the sterile enclosure and (2) maintaining neutral loading of the scaffold when mounting the sterile enclosure in the biaxial system. In both cases, small discrepancies in the initial load state of the scaffold causes the same biaxial strain protocol to yield highly variable stresses. As compared to conventional mechanical testing settings, the need to maintain absolute sterility of the culture environment prohibited fine adjustment of the scaffold mounting. Moreover, condensation in the sterile enclosure obscured vision of the scaffold to visually check the mounting. It is possible that further development of the apparatus and initialization protocol could reduce loading variability. For example, an alignment instrument could be designed to place the scaffold in the grips, although thorough validation of the sterility this method would be required. Overall, it may be prohibitively challenging to consistently control the loading variability between scaffold experiments. Therefore, it may be of interest to functionalize the quantitative results of scaffold cultures (e.g. ECM production) with respect to the biaxial stresses, rather than assuming a constant biaxial strain.

Variation of the measured loads within each scaffold group also occurred: (1) between different series of days that were separated by a change in the culture of media; (2) within each series of days which were not separated by a change of the culture media; and (3) within each day of loading (Figure 27). First, the discrepancy in loading associated with changes of the culture media likely occurred because the sterile enclosure was temporarily removed from the biaxial system to perform the media change. Although the sterile enclosure was removed and replaced in

the same configuration, minute changes to the system resulted in marked changes in the mechanical loading. This variability in mechanical loading exemplifies the sensitivity of the scaffold stress to the initial position in biaxial regimes, as previously discussed. Second, the variation in loading during a series of days without a culture media change may be attributed to mechanical relaxation of the scaffold, degradation of the PCL fibers, and/or other material changes. Similarly, the variation of the loading within a single day may be attributed to these factors, as well as inherent noise in the load cell measurement. Another possible factor in measuring the mechanical loads could be associated with the boots that provided a sterile seal around the grips of the sterile enclosure; due to size limitations, the boots were designed for relatively minor stress relief and, therefore, it is possible that the boots generated some confounding forces in the mechanical system. However, it is not clear whether the magnitude of the boot forces generated by the small displacements in the study were significant as compared to the scaffold stiffness. Custom boots could be developed in future work to mitigate this potentially confounding effect.

3.1.4.3. Histology

Histological sections of the study and validation groups clearly illustrated the 3DF scaffold architecture and the MEW fibers were also apparent in some of the sections (Figure 28 and Figure 29). This demonstrates that the MMA embedding method successfully retained the form of the 3DF PCL fibers. However, it remains unclear if the MMA embedding caused some of the MEW sheets to not be visible, or if this occurred during the cell culture or chemical processing. Additionally, some samples were warped during MMA polymerization, suggesting that the polymerization process imposed deformation on the scaffold. These stresses may explain the apparent loss of MEW fibers in some of the sections and could also explain the observed lack of

matrix stain (i.e., fibrin and any ECM produced during the study) in some sections. If the forces generated during polymerization were sufficient to deform the matrix, this could confound the measurement of ECM production via histology.

The PCL fibers also appeared to be stained in the SRBS sections, which was advantageous to identify the PCL architecture. The intensity and color of this stain varied between samples; in particular, the first three study groups exhibited dark stain within the PCL fibers indicating that the stain was permeating the polymer. Although all scaffolds were processed using the same protocol, it is possible the stain permeation was enhanced in the first three groups due to subtle processing variations, such as the time of exposure to processing chemicals (formalin solution, ethanol solutions, clearing agents, infiltration solutions, or stains) or differences in the MMA infiltration of the PCL fibers. Further, the scaffolds cultured for 14-days generally presented darker PCL staining than the corresponding time-zero scaffolds, indicating that PCL degradation by hydrolysis may be a cause of increased stain permeation. These histological artefacts should be considered in future studies because they may confound analyses of stain in the scaffold matrix.

Some regions of blue stain were observed in the matrix region (i.e., scaffold volume that was not PCL fibers) of the SRBS sections (Figure 28). This stain could be indicative of ECM formation consistent with soft tissue formation. However, the blue regions were present in time-zero samples, and there was no clear evidence that the level of the stain differed between study conditions. Accordingly, this stain is likely a baseline reading for the fibrin hydrogel. These stained regions also did not fill the entire matrix region space in any sample. As previously discussed, this could be explained by the hydrogel concentrating in these regions during MMA polymerization, and could also be caused during fabrication, culturing, or chemical processing. Within the stained

regions no features at cell-level resolution could be clearly identified or distinguished from histological artefacts.

The validation sections containing AF tissue demonstrated an appreciable degree of stain within the scaffold using the same histological procedure. The SRBS also demonstrated variance in the identified stain color, indicative of differences in the soft tissue composition (i.e., GAGs and collagen). Regions of dark stain were observed in both SRBS and TBS sections, which may have been associated with poor infiltration of the MMA into some of the AF tissue. Because the same infiltration protocol was used for the culture groups and validation samples, it is possible that the level of MME infiltration was sufficient for the cultured hydrogel, yet insufficient for the larger pieces of dense AF tissue. The measured stained area of the validation sections (3.4% to 38.9% for SRBS and 2.4% to 28.4%) was consistently greater than all of the cultured scaffolds (0.0% to 1.6% for SRBS and 0.0% for TBS). It is intuitive that AF tissue has a greater concentration of ECM than the scaffold cultures, however, this result also verifies that the underlying histological protocol was capable of detecting the ECM content of AF. The successful detection of AF tissue within the PCL scaffolds is consistent with the reported use of MMA[181,182] and similar hard resins[183,184] as embedding media for histological sections in the literature. Further, although preliminary work for this study found the PCL scaffolds to be incompatible with paraffin sectioning, the use of this technique has been reported for 3DF PCL scaffolds[185,186]. Similar PCL scaffolds fabricated with smaller via electrospinning and electrowriting have also been histologically processed with paraffin sectioning[187] and cryosectioning[188]. It is possible that further exploration of histological methods may yield sections of 3DF scaffolds from paraffin embedded samples and/or cyrofrozen samples.

3.1.4.4. Limitations

A major limitation of this study was the capacity of the biaxial incubator. Because only one scaffold with the loaded treatment could be cultured at a time, each group of scaffolds were cultured in series. As a result, the eight total groups of this study took 16 weeks of incubator time and only yielded six usable groups. To experimentally investigate how alternate culture parameters (e.g. different mechanical loading regimes, scaffolds designs, or the addition of biological factors) may improve ECM production, each different condition would take similarly long to achieve sufficient statistical power. This issue also highlights the need for informed selection of culture parameters; because each culture parameter group represents a significant investment of time and resources, it is critical to select the most advantageous parameters to enhance TE outcomes. Accordingly, computational models to predict the CME in TE scaffolds may provide a basis to identify the most promising candidates to mediate tissue regeneration. One such computational model was used as a rationale for the biaxial strain protocol in this study. The computational model used a proposed window of mechanical loading to predict a catabolic response of AF cells, however, this model requires validation from experimental results such as the current study.

All histological sections of the culture groups yielded only a small intensity of stain. Accordingly, it is possible that the sensitivity of the histological method was insufficient to detect ECM production in the scaffolds for the prescribed culture conditions. An alternative method of characterizing ECM formation in the TE scaffolds with greater sensitivity are chemical assays. For example, established procedures exist to quantify collagen content (hydroxyproline assay[189] and Sirius Red dye binding[190]), proteoglycan content (dimethyl methylene blue assay[191]), and baseline DNA content (Hoechst 33258 assay[192]). These techniques could be implemented to measure the relative content of collagen and GAGs within the hydrogel in the three scaffold conditions used in

this study (i.e. time-zero control, unloaded control, and loaded treatment). However, these assays are limited because they do not provide spatial characterization of the analyte. Computational models have predicted that the mechanoregulation of ECM formation is inhomogeneous within TE scaffolds (Section 3.2) and, therefore, spatial variance in collagen and GAG production is expected. Histological methods may afford spatial quantification of analytes, though are limited to two-dimensional sections of the scaffold. Multiple sections of a scaffold could be produced to generate three-dimensional spatial resolution, however, this is associated with a considerable increase in the required time and resources. Overall, including assay-based analyses in future studies may be beneficial.

The lack of definitive histological results in the study may also have been due to a low level of ECM generation by the resident cells. This leads to another limitation of the study: the fatigue resistance of PCL in physiological conditions. Preliminary testing of PCL demonstrated repeated material failure during cyclic strain in physiological conditions. To prevent the scaffolds fracturing during cell culture, the magnitude of strains that could be delivered to the scaffold was limited and, subsequently, the mechanoregulatory stimuli delivered to the resident cells was limited. Overall, ECM production during cell culture may have been inhibited by the poor durability of the scaffold. Lastly, even if correlations between scaffold loading and ECM production can be identified in idealized *in vitro* conditions, those loading conditions may be prohibitively difficult to accurately prescribe *in vivo*. However, future results may provide insights on how sensitive ECM production is to the loading regime, how physiological loading may modulate in AF regeneration, and how to manipulate scaffold loading in vivo to enhance healing.

3.1.4.5. Implications for future work

Although no qualitative or quantitative differences between scaffolds loading conditions were identified from histological imaging, there is insufficient evidence to conclude that mechanical loading does not mediate the cell response in the TE scaffolds. Therefore, further investigation with revised experimental design is necessary to explicate the influence of scaffold loading on ECM production. In particular, future work should continue to explore improved methods to increased ECM production during cultures and evaluate the results with more sensitive analyses. Additionally, it would be beneficial to increase the experimental throughput in order to more rapidly resolve study limitations and a broader scope of scaffold designs and culturing protocols. For example, with a greater experimental throughput, the challenges encountered in this study may have been resolved sooner.

To increase the experimental throughput of the TE scaffold cultures, additional biaxial incubators could be developed to run multiple study groups simultaneously. Alternatively, a system could be developed to culture multiple scaffolds simultaneously within a single biaxial system. However, experimental throughout will always be inherently limited. To identify the scaffold designs and culturing protocols that may be most advantageous for tissue regeneration, computational methods may serve as a tool to assess a broad scope of candidate solutions in a considerably shorter duration and with less resources. For example, this could be achieved with a finite element model to predict the CME in TE scaffolds (Section 3.2), although experimental validation of the model is essential to vastly improve the predictive power. Future work should focus on developing both experimental and computational methods to enhance AF regeneration.

The level of ECM production in the scaffold could be enhanced with a number of study modifications, including: (1) longer culture durations to allow more time for resident cells to

respond to mechanical stimuli; (2) adding biological factors, such as growth factors and exosomes, to elicit an increased baseline level of ECM production; (3) using different cell lines, such as stem cells, which may have a greater intrinsic regenerative potential; (4) utilizing different mechanical loading conditions, such as higher magnitude biaxial strains or a radial compression, both of which have been predicted to enhance ECM production (Section 3.2); and (5) modifying the scaffold design, such as increasing the surface area or enhancing the surface topology to increase cell adhesion to the scaffold fibers, which has also been predicted to enhance ECM production (Section 3.2). However, increasing the culture duration may be unfavorable due to the associated reduction in experimental throughput and lower expected yield (e.g., due to increased risk of exposure to infection). To increase the magnitude of biaxial strains delivered to the scaffold, future work will also need to focus on enhancing the resilience of the scaffolds to failure due to degradation and fatigue in physiological conditions.

Finally, improved histological protocols and chemical assays are both viable methods to improve the sensitivity of detection of ECM production within the TE scaffolds. More sensitive analyses may be achieved with ground MMA sections using alternative processing and staining methods. However, it is likely that more clearly identifiable tissue stains with greater spatial resolution may be achieved by resolving the limitations associated with thin plastic sections, paraffin sections, and/or cryosections. Assay-based analyses lack spatial resolution, however, are likely to detect smaller concentrations of analytes in the scaffold. Ultimately, a combination of histological and assay-based methods should be leveraged in future work.

3.1.5. Conclusions

Overall, this study demonstrated the development and implementation of a method of culture TE scaffolds for AF repair with a prescribed, multi-axial mechanical loading protocol. The histological protocol used in the study did not detect any changes in ECM production in scaffolds with mechanical loading, as compared to unloaded and time-zero controls. However, it remains unclear whether this was due to insufficient sensitivity of the histological protocol or due to a lack of ECM production. ECM production may have been inhibited by experimental challenges, and numerous considerations for futures studies have been described. Nonetheless, this study provided a platform to improve our understanding of the relationship between global scaffold loading and the ECM production of resident cells in TE constructs for AF repair. Ultimately, this work has the potential to drive the design of regenerative medicine strategies for IVD herniation and various other musculoskeletal pathologies.

3.2. Computational Approach[c]

3.2.1. Introduction

Organ healing via regenerative medicine will afford revolutionary treatment for a myriad of diseases. The goal of tissue engineering (TE) is to drive native and introduced cells to produce a healthy, functional extracellular matrix to repair and regenerate diseased native tissue. To enhance the regeneration potential, TE constructs are commonly laden with exogenous progenitor or stem cells. Consequently, the fate of these cells is paramount to establish long-term biological function and mechanical integrity of the engineered tissue.

A major regulator of cell fate is mechanical loading. Localized stresses and strains have been shown to dictate cell viability, differentiation, and extracellular matrix (ECM) deposition[55–58]. As compared to other systems, the musculoskeletal system experiences a broad magnitude of mechanical loads. Consequently, cell fates in muscle, bone, articular cartilage, fibrocartilage, tendon, and ligament are all driven largely by mechanical cues. For example, models of bone fracture healing have used hydrostatic stress history and maximum principal strain history as mechanical measures to predict regeneration[59,60].

This study focused on the specific example of regeneration of the annulus fibrosus (AF), a fibrocartilaginous component of the intervertebral disc (IVD). The biological and mechanical integrity of the AF is contingent on the production and maintenance of ECM by AF cells[21,51], and diseased states of the IVD have been associated with a loss of tissue cellularity and dramatic changes to the organization and regeneration of the ECM[52–54]. Further, mechanical loading has

---

[c] The content of Section 3.2 has been published as a research article in JOR Spine (DOI: 10.1002/jsp2.1152). All content has been adapted with permission from John Wiley & Sons, Inc.

been linked to inflammatory responses of AF cells, which may be critical for tissue homeostasis, or may invoke degenerative sequelae at supra-physiological strains[193–196]. The viability and ECM production of AF cells have been shown to depend on the magnitude and three-dimensional combinations of mechanical loading. *In vivo*, the posterolateral AF experiences biaxial tensile strains of approximately 4-6% in the circumferential and axial directions and hydrostatic pressure generated by the adjacent nucleus pulposus[28,45].

AF cells isolated from rabbits have demonstrated anabolic responses at maximum principal strains (ϵ_1) of 3% to 18%, and this response was maximized at 6% strain[64]. At 1% strain, rabbit AF cells have demonstrated no significant changes in proteoglycan production, cell death, MMP-1 expression, or MMP-3 expression as compared to static loading[65]. This remodeling window is supported in studies of human AF cells. Upregulation of catabolic factors associated with disc degeneration has been demonstrated at 20% strain [48]. Decreased catabolic gene expression has been shown for human AF cells at 10% strain[66], and increased cell proliferation, collagen production, and glycosaminoglycan production has been reported at this strain magnitude[67]. Accordingly, a maximum principal strain remodeling window of 3% to 18% was proposed for this study as a target for cell-level loading to drive AF regeneration. Similarly, AF cells have exhibited anabolic responses for compressive hydrostatic strains ($\epsilon_h < 0$)[68–72] and an upper limit of 1 MPa compressive hydrostatic stress (-1 MPa $> \sigma_h > 0$ MPa) has been proposed for eliciting catabolic responses[69,73]. Therefore, a hydrostatic stress remodeling window of 0 to 1 MPa was proposed for this study as a target for cell-level loading to drive AF regeneration. This proposed CME target envelope based on strain and hydrostatic pressure is also in general agreement with previously reported micromechanical criteria for cartilage and fibrous tissue formation in fracture healings models[59,60].

A ubiquitous strategy within the TE community is to fabricate composite constructs consisting of a biodegradable scaffold with a cell-laden matrix. Such TE scaffolds have been engineered to replicate specific tissue-level material properties of various musculoskeletal tissues[156–158], including AF[41,141]. However, these scaffolds do not necessarily ensure that the mechanical loads induced at the cellular level are sufficient to drive cell survival, proliferation, and ECM formation. The relationship between tissue-level loading and the cellular micromechanical environment (CME) is, therefore, essential to furthering our understanding of how best to design TE scaffolds. Yet, it is intractable to measure and prescribe the CME in cell-laden matrices of TE scaffolds. The CME is three-dimensional, heterogeneous, and dependent on scaffold loading, materials, and architecture; current experimental methods are not capable of accurately prescribing and/or measuring the CME. For example, in the aforementioned complementary experimental series, there is no physical method to know what CME is generated under global (i.e. tissue level) loading of the TE scaffolds and whether or not that CME will be beneficial for regenerating the desired tissue. Optical strain measurement techniques, with image capture via high resolution digital camera or confocal microscopy, have been used with digital image correlation (DIC) to measure deformations in biological materials [151–153]. However, both DIC and confocal microscopy are not well suited for high-throughput analyses. Digital photogrpahy techniques are limited in that they can only measure two-dimensional surface strains and the resultant surface strains typically do not represent the complete deformation mapping within the scaffold. Confocal microscopy techniques may also be restricted by the opacity of the scaffold and hydrogel.

In addition to the experimental difficulties of measuring CME, TE experiments with dynamic mechanical loading may be prohibitively time consuming to effectively characterize the

relationship between tissue-level and cellular-level loading for a broad range of loading conditions. Due to the complex apparatus required for precise multiaxial loading, scaffolds may be limited to successive cultures. For example, *in vitro* investigation of TE scaffolds require sufficient culture time to elicit a measurable cell response, such as ECM production. Additionally, the need for complex apparatus to deliver precise multiaxial loading may limit a study group to successive cultures, which may take appreciable time to produce statistically powerful results. Subsequent study groups aimed to improve tissue regeneration will have a similarly protracted study duration. Therefore, in order to optimize the development timeline of tissue regeneration strategies, it is imperative that the most advantageous study groups are selected for experimental evaluation. However, there is currently no method to identify which particular scaffold design features and experimental conditions are most likely to drive improved tissue regeneration. For example, is the CME more sensitive to scaffold loading, materials, or architectural parameters?

In the absence of any feasible experimental methods, one possible tool to predict ECM formation in TE scaffolds is the finite element (FE) method. Cell fates in orthopaedic tissues under mechanical loading have been modelled with FE in intervertebral disc[52,154] and bone fracture healing[155] applications. The tissue-level mechanics of TE scaffolds have also been studied using FE methods[153,156–158] and some of these models have been developed to predict mechano-regulation of musculoskeletal regeneration[159–161]. However, there remains a need for a CME model that can: (1) be applied to all of the available volume that can cells can occupy in heterogeneous TE scaffolds, (2) be applied parametrically to a numerous candidate TE scaffold designs, (3) be broadly applied to a range of proposed target mechanics, and (4) be easily compared to *in vitro* cell cultures for validation. Therefore, in this study, a FE model of CME was developed to predict the regeneration potential of TE scaffolds. The influence of scaffold loading, materials, and

architecture on theoretical healing potential were investigated. The results of this model were used to inform the design of a TE scaffold for AF regeneration in an ongoing experimental study.

3.2.2. Materials and methods

3.2.2.1. Scaffold base model

The development of a repeating unit cell model for evaluation of the CME is shown in Appendix E. In brief, the unit cell is an idealized geometry of a 3DF, angle-ply scaffold which has previously demonstrated anisotropic material properties similar to the most relevant properties of native AF tissue (Figure 31a). The unit cell model was parametrized based on scaffold architecture, materials, and loading. Base parameter values of all scaffold parameters are summarized in Table **7**.

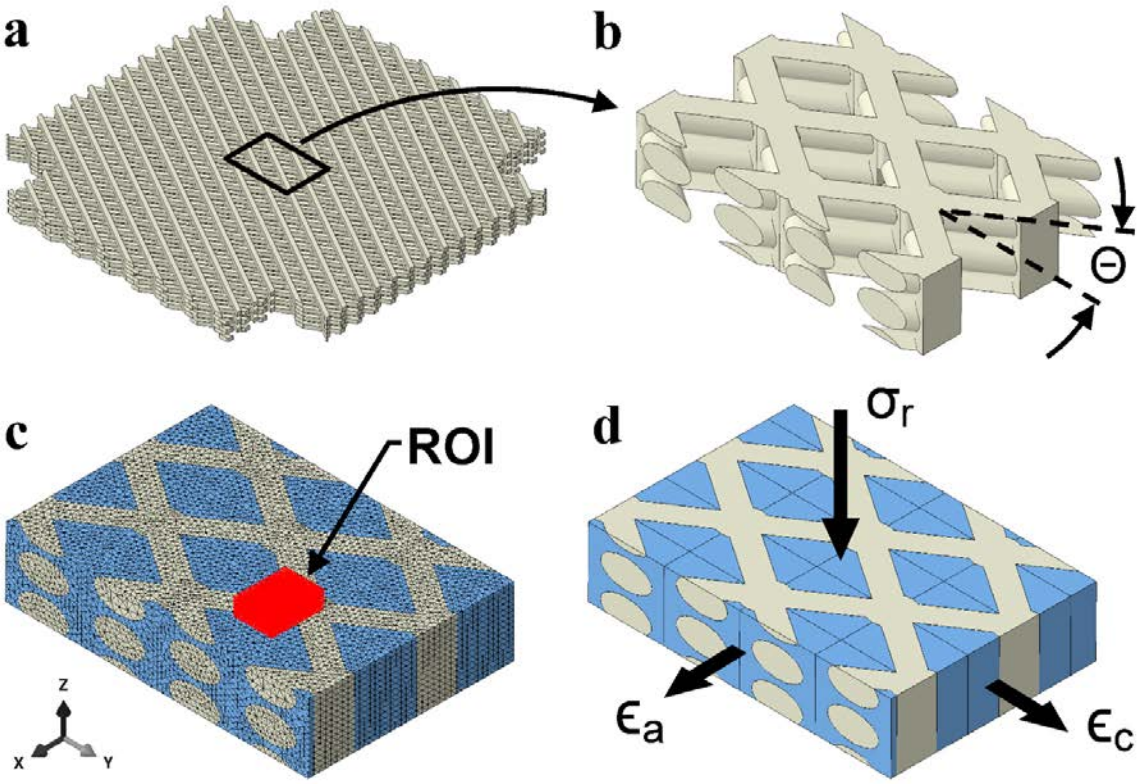

Figure 31. Scaffold model for the base geometry showing: **(a)** the previously validated angle-ply fiber scaffold (Section 2.2); **(b)** the double unit cell of the fiber scaffold with the definition of fiber angle (Θ); **(c)** the final unit cell including the hydrogel infill showing the FE mesh and region of interest (ROI) for CME evaluation; and **(d)** tri-axial loading definitions of axial strain (ϵ_a), circumferential strain (ϵ_c), and radial pressure (σ_r). The x-, y-, and z-directions represent the axial, circumferential, and radial directions of the IVD, respectively.

Table 7. Parameters and associated values for the scaffold base model. Parameters are categorized as either architectural, material, or loading.

Category	Parameter	Symbol	Base model value	Ref.
Architecture	Fiber angle	Θ	34°	Section 2.2
	Fiber spacing	S	1.0 mm	Section 2.2
	Fiber diameter	D	0.3375 mm	Section 2.2
	Layer height	-	0.6×D	Section 2.2
	Fiber contact radius	-	1.58×D	Section 2.2
Materials	Hydrogel elasticity	C_1	172 Pa	Appendix E
		C_2	383 Pa	Appendix E
	Hydrogel compressibility	D_1	3.41	Appendix E
		D_2	0.0806	Appendix E
	Fiber elastic modulus	E	265 MPa	Section 2.2
	Fiber poisons ratio	ν	0.3	Section 2.2
Loading	Axial strain	ϵ_a	5.0 %	-
	Circumferential strain	ϵ_c	5.0 %	-
	Radial pressure	σ_r	0 MPa	-

Fibers were prescribed linear elastic material properties of polycaprolactone (PCL) and the hydrogel infill was modelled with the compressible, second-order reduced polynomial hyperelastic material properties of fibrin (Equation (8)[197].

$$U = C_{10}(I_1 - 3) + C_{20}(I_1 - 3)^2 + D_1(J - 1)^2 + D_2(J - 1)^4 \quad (8)$$

where U is the strain energy potential, C_{10} and C_{20} are the fitted material elasticity constants, I_1 is the first invariant of the strain tensor, D_1 and D_2 are the fitted material compressibility constants, and J is the Jacobian determinant of the deformation gradient tensor.

Tensile strains were applied to the model in the axial direction (x-direction) and circumferential direction (y-direction) to emulate the dominant *in vivo* loads experienced by the posterolateral AF[198–201]. All nodes on the unit cell faces normal to the negative axial and circumferential directions were constrained against displacement in those respective directions; therefore, in-plane sliding was allowable. Biaxial displacements were prescribed on the positive axial and circumferential faces to generate global strains. On the positive z-direction face, all fiber nodes were constrained to equal z-displacements and all fiber nodes on the negative z-direction face were constrained against out-of-plane displacement. Previous results showed that constraining all nodes on the positive and negative z-direction faces increased the region of interest (ROI) strain energy by 196% and 179%, respectively. To address this sensitivity of the ROI mechanics to the z-direction boundary conditions, these two constraints were reviewed in the current study[197].

In the center of the unit cell, a region of interest (ROI) of mesh elements was defined to contain all possible positions of cells within the hydrogel matrix with respect to the fiber architecture (Figure 31d). Using these ROI elements, a custom post-processing script generated representative cell volumes of seeded progenitor cells in the hydrogel matrix (20μm equivalent seed size) and evaluated the theoretical micromechanical environment of these cells.

3.2.2.2. CME evaluation

A CME post-processing algorithm was developed to facilitate the evaluation of a constant three-dimensional strain tensor for cell-sized volumes in the ROI while maintaining the stability,

accuracy, and efficiency of an FE model with larger and more complex elements (Appendix F). Specifically, the whole volume of the ROI was considered to characterize the CME in the scaffold. The deformation solution of each model with quadratic tetrahedral (C3D10H) elements was reverse-engineered to yield Green strain tensors for cell-sized linear tetrahedral elements (C3D4). These linear tetrahedral elements had an effective seed size (20 μm) that is similar to the size of mature AF cells[202,203]. From the cell-volume strain tensor, the CME for all cell-sized volumes in the ROI was categorized as either within ("satisfying") or outside ("not satisfying") the proposed target mechanics envelope. These target mechanics were derived from previously published 3D micromechanical criteria for anabolic responses of mature human AF cells. Specifically, the target mechanics envelope was based on maximum principal strain ($3\% < \epsilon_1 < 18\%$)[48,64–67] and hydrostatic stress (-1 MPa < σ_h < 0 MPa)[68–73] as shown in Figure 32.

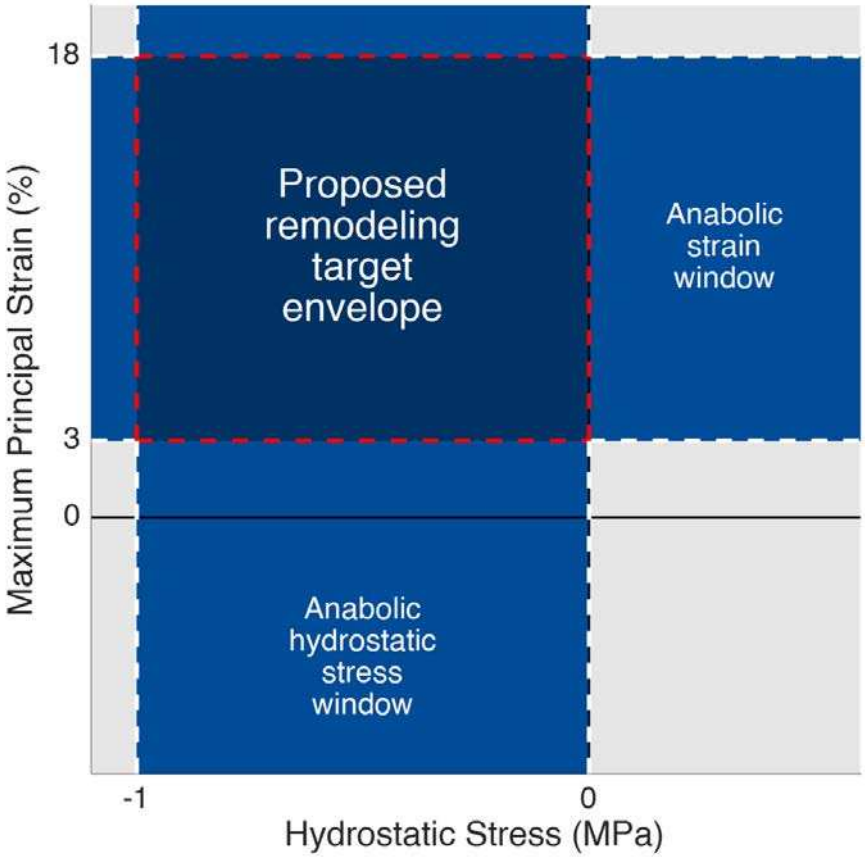

Figure 32. The proposed micromechanical target envelope for AF tissue regeneration based on hydrostatic stress and maximum principal strain criteria. The window of anabolic responses based on hydrostatic stress has a lower bound of -1 MPa (i.e., hydrostatic compression) and an upper bound of 0 MPa.[68–73] The window of anabolic responses based on maximum principal strain has a lower bound of 3% and an upper bound of 18%.[48,64–67]

3.2.2.3. Parametric studies

Following validation, the loading, materials, and architecture of the base model were modified parametrically to investigate their relative influences on the predicted CME.

3.2.2.4. Scaffold loading

To evaluate the influence of biaxial loading on CME, the base model was prescribed the following biaxial strain conditions: (1) +6.0% and -6.0% axial strain with an array of circumferential strain from -6.0% to +6.0% in increments of 1.0% strain and (2) +6.0% and -6.0%

circumferential strain with an array of axial strain from -6.0% to +6.0% in increments of 1.0% strain. These 48 combinations of biaxial strain were denoted as load array 1. The load ramps of these solutions were analyzed to yield a full series of biaxial loading conditions between -6.0% and +6.0% strain (e.g., the solution for 6.0% equibiaxial strain contained the solution for 5.0% equibiaxial strain). Following preliminary results, two subsets of load array 1 were considered in the study and used in the analyses of scaffold materials and architecture. Load array 2 was utilized to capture the complete range of load array 1 whilst minimizing the number of study points to reduce computational burden. Specifically, load array 2 was defined as the eight biaxial combinations of -5.0%, 0.0%, and +5.0% strain (excluding the unloaded condition). To capture the most pertinent scaffold loading based on the results of load array 1, load array 3 was defined as the two conditions of equibiaxial (+5.0% axial and circumferential strain) and transverse-constrained circumferential strain (+5.0% circumferential strain and 0.0% axial strain)

In addition to biaxial strain combinations, the influence of a compressive load in the radial direction was investigated by applying a pressure up to 1.0 MPa to the positive radial face following the full biaxial load. Due to numerical complexity, two cases of radial pressure were considered: prior to the biaxial strain and following the biaxial strain. This compressive load was considered for the base model under load array 3.

3.2.2.5. Scaffold materials

Eight conditions of modified material properties were evaluated under load array 2 (positive biaxial strains). Specifically, the following material property modifications were evaluated: (1-2) upper and lower 95% confidence bounds of hydrogel compressibility coefficients (D_1 and D_2), (3-4) upper and lower 95% confidence bounds of hydrogel elasticity coefficients (C_{10}

and C_{20}), (5-6) ten-fold increase and decrease of the hydrogel compressibility coefficients (C_{10} and C_{20}), and (7-8) increase and decrease of the fiber elastic modulus (E) by 20%.

3.2.2.6. Scaffold architecture

Modifications to four architectural parameters were explored. Scaffold fiber angles (Θ) ranging from 30° (increased biaxial asymmetry as compared to base model) to 45° (biaxial symmetry) were considered. The fiber spacing (S) in the scaffold was ranged from 0.6 mm to 1.4 mm, in increments of 0.1 mm and the fiber diameter (D) was studied from 0.20 mm to 0.45 mm (based on the range of common polymer fiber diameters produced via 3DF[41,142,143,173]). Finally, the relative cell size was progressively increased to ten times the original size. This generated effective architectural scale factors of 0.1 to 1.0 whilst maintaining the accuracy of the base model. Each scaffold architecture was prescribed the two loadings conditions of load array 3.

3.2.3. Results

3.2.3.1. Base model

In the base model, the cell-sized volumes within the ROI exhibited a distribution in hydrostatic strain and maximum principal strain (Figure 33). Specifically, the CME that satisfied the proposed target envelope was predicted for 7.2% of cell volumes (i.e., a predicted target envelope, PTE, of 7.2 percent or 7.2 %PTE). A concentration of CME was observed for small positive hydrostatic strains (0 – 4%) and maximum principal strains ranging 5 – 15%. In equibiaxial 6.0% strain, the strain magnitudes experienced by some cell volumes exceeded 20%. The PTE varied between two subsets of cell volumes: (1) cells with direct contact with the PCL fibers and (2) cells with no direct contact with PCL fibers. These two subsets represented 88.4% and 11.6% of the total number of cells, respectively, and the PTE for these subsets were 6.1 %PTE

and 15.6 %PTE, respectively. At 5.0% equibiaxial loading, the base model had 8.1 %PTE. The two alternative boundary conditions with all nodes (hydrogel and fibers) constrained on the bottom and top faces resulted in increases in the PTE of 4.6 %PTE and 8.1 %PTE, respectively, as compared to the base model.[197]

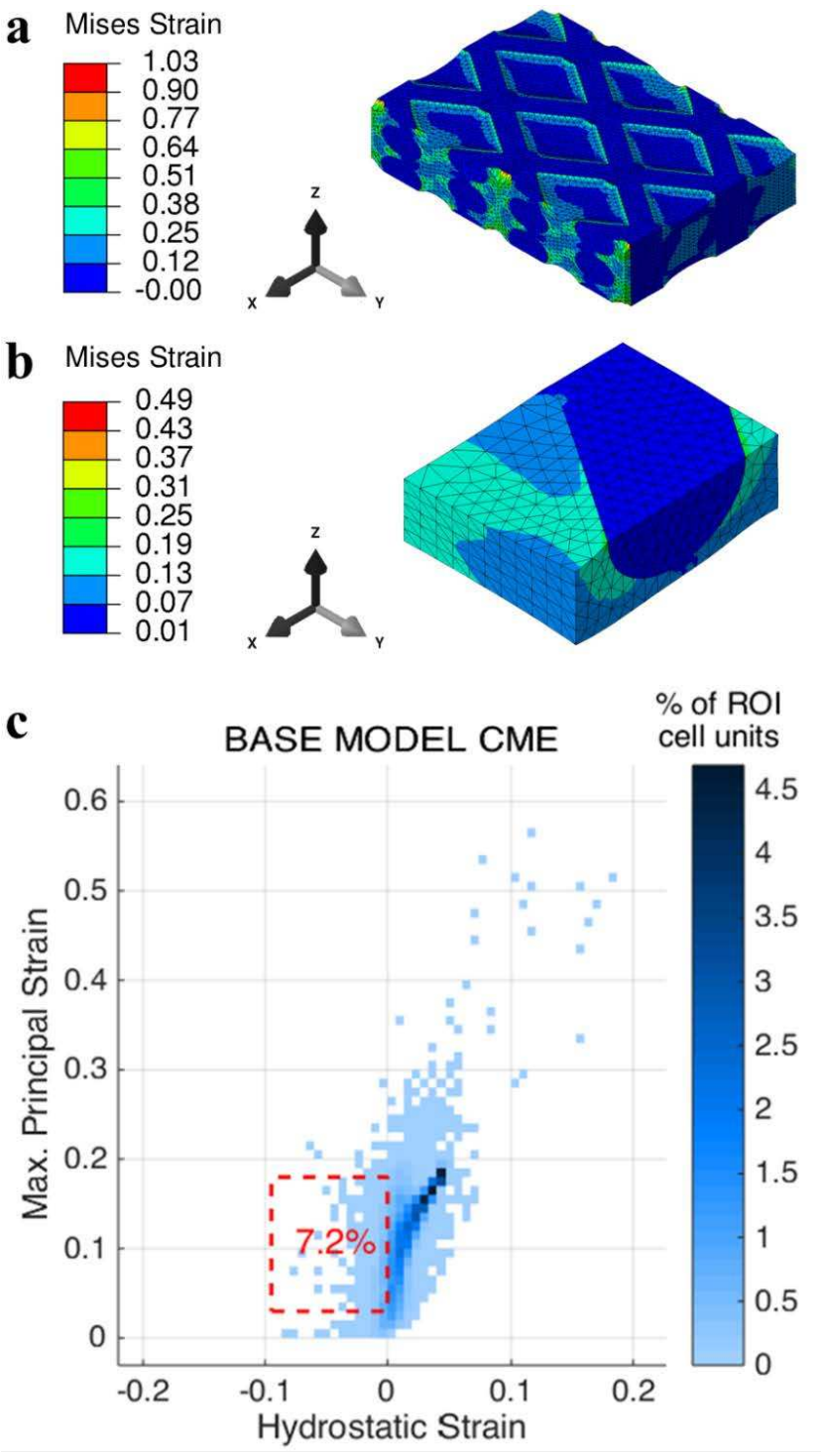

Figure 33. Unit cell solution for the base scaffold model with prescribed 6.0% equibiaxial strain: **(a)** Mises strain contours of the full model, **(b)** Mises strain contours of the ROI, and **(c)** distribution of CME as a function of hydrostatic strain and maximum principal strain for all ROI cell volumes. The red dashed box indicates the proposed micromechanical target envelope which contains 7.2% of the CME distribution for this model (7.2 %PTE).

3.2.3.2. Scaffold loading

The PTE was found to vary as a function of equibiaxial strain magnitude (Figure 34). Despite 7.2 %PTE for 6.0% equibiaxial strain, a peak of 9.5 %PTE was observed at 2.7% equibiaxial strain. The PTE rapidly and monotonically increased to this peak from 0.0 %PTE at approximately 0.7% equibiaxial strain and appeared to decrease approximately linearly following the peak. As compared to all cell volumes, the PTE for cells with no attachment to scaffold fibers (88.4% of cell volumes) was lower for all load fractions with a peak value of 8.9 %PTE. Cells with fiber contact (11.6% of cell volumes) exhibited increasing PTE with increasing load fraction and a peak value of 15.6 %PTE at 5.0% equibiaxial strain.

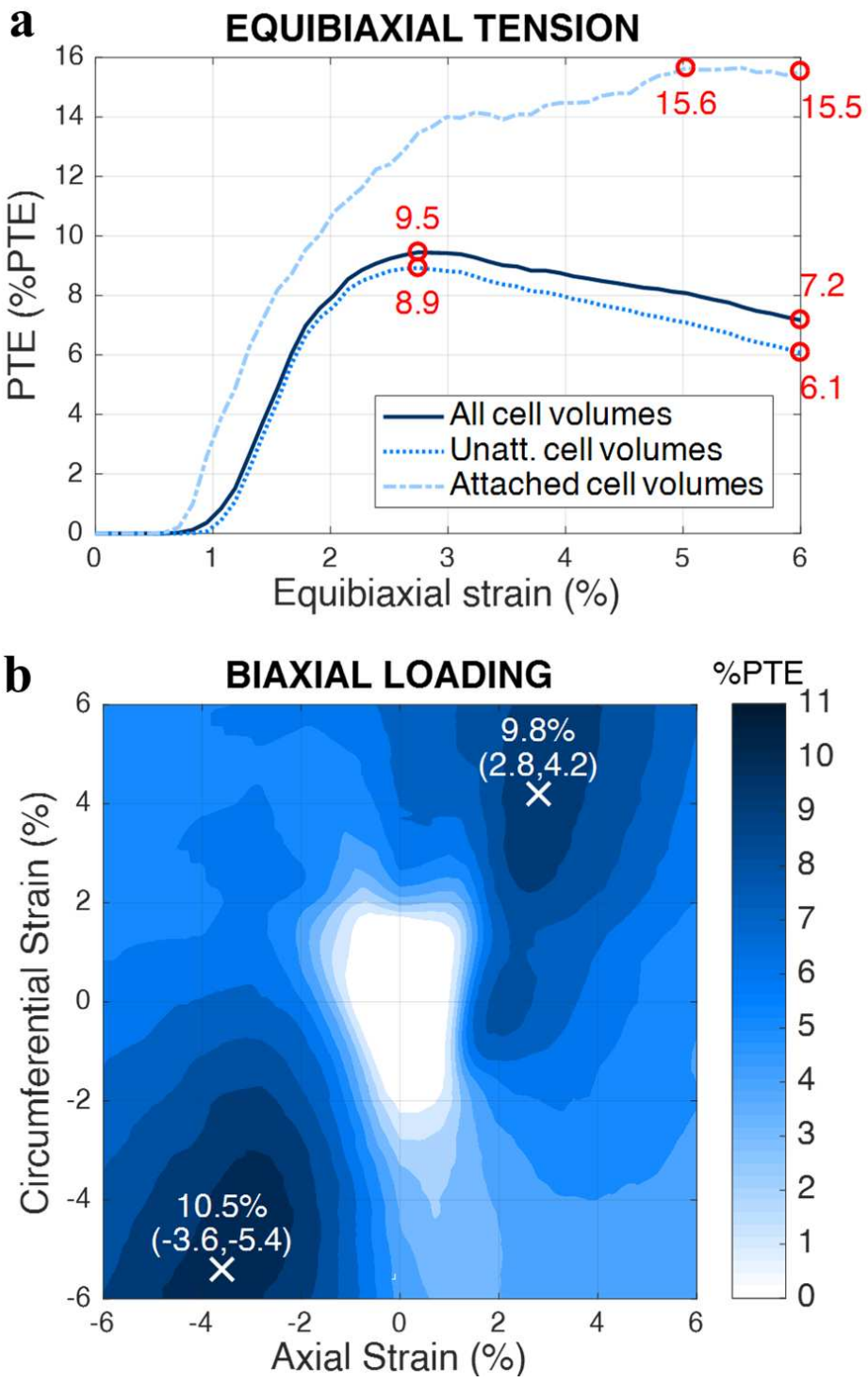

Figure 34. PTE as a function of: **(a)** loading magnitude in equibiaxial tension and **(b)** biaxial strain ratios for the base scaffold model. In Figure 34a, the peak and final value of PTE are identified with red circles for all cells volumes, cell volumes with no contact to fibers, and cell volumes in contact with fibers. In Figure 34b, contours are shown in increments of 1.0 %PTE. Two local maxima are indicated with a white 'X' and labelled with the corresponding %PTE and biaxial strain in parentheses.

The base model prescribed with a biaxial loading array (load array 3) demonstrated a clear relationship between the biaxial load and the PTE (Figure 34b). The regions experiencing relatively low loading (less than approximately 1% strain in either direction) had no PTE (0.0 %PTE). Two local peaks in the PTE were observed, one in biaxial tension (9.8% for 2.8% axial and 4.2% circumferential strains) and one in the biaxial compression (10.5% for -3.6% axial and -5.4% circumferential strains). The biaxial compression peak was higher in magnitude and broader in loading range as compared to the biaxial tension peak. The average angle of the maximum principal strain directions from the loading plane were distinctly different between the two peaks (0.3° and 78° for biaxial tension and compression, respectively).

Numerical instabilities occurred when a radial pressure was applied to the model prior to biaxial strain. However, radial pressures of at least 50 kPa were resolvable following the application of biaxial strains of different magnitudes (Figure 35). In the absence of biaxial strain, the radial pressure of 37.5 kPa yielded 17.2 %PTE which was greater than any equibiaxial strain in the absence of radial pressure (maximum of 9.5 %PTE). At all magnitudes of radial pressure, a peak in the PTE was observed; for all non-zero pressures, this peak was at 2% equibiaxial strain (maximum of 66.5 %PTE for 50 kPa radial pressure). Similarly, the influence of radial pressure was most pronounced near the peak in the PTE, as evidenced by a 40.5 %PTE increase from 0.0 kPa radial pressure to 12.5 kPa.

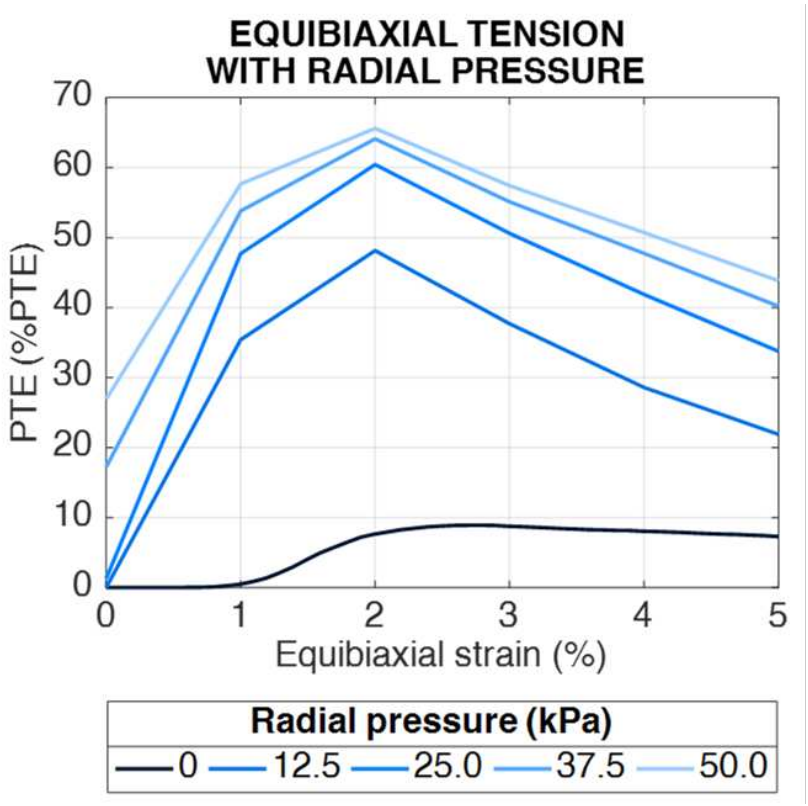

Figure 35. PTE for combined loading conditions of radial pressure and equibiaxial strain. The plotted lines shown the PTE for constant pressures in increments of 12.5 kPa and all non-zero pressure lines are sampled increments of 1% equibiaxial strain. The %PTE is shown as a function of the load magnitude for constant radial pressures.

3.2.3.3. Scaffold materials

Overall, the changes in PTE within the 95% confidence bounds in hydrogel elasticity and compressibility were less than 0.3 %PTE (Figure 36). Nonetheless, distinct trends were observed as a function of scaffold loading. The lower confidence bound of hydrogel elasticity and compressibility both demonstrated increased PTE in biaxial tension and decreased PTE in biaxial compression, with a gradual change in between. The inverse trend was observed for the corresponding upper confidence bounds. These trends are supported by the more extreme changes to the hydrogel properties.

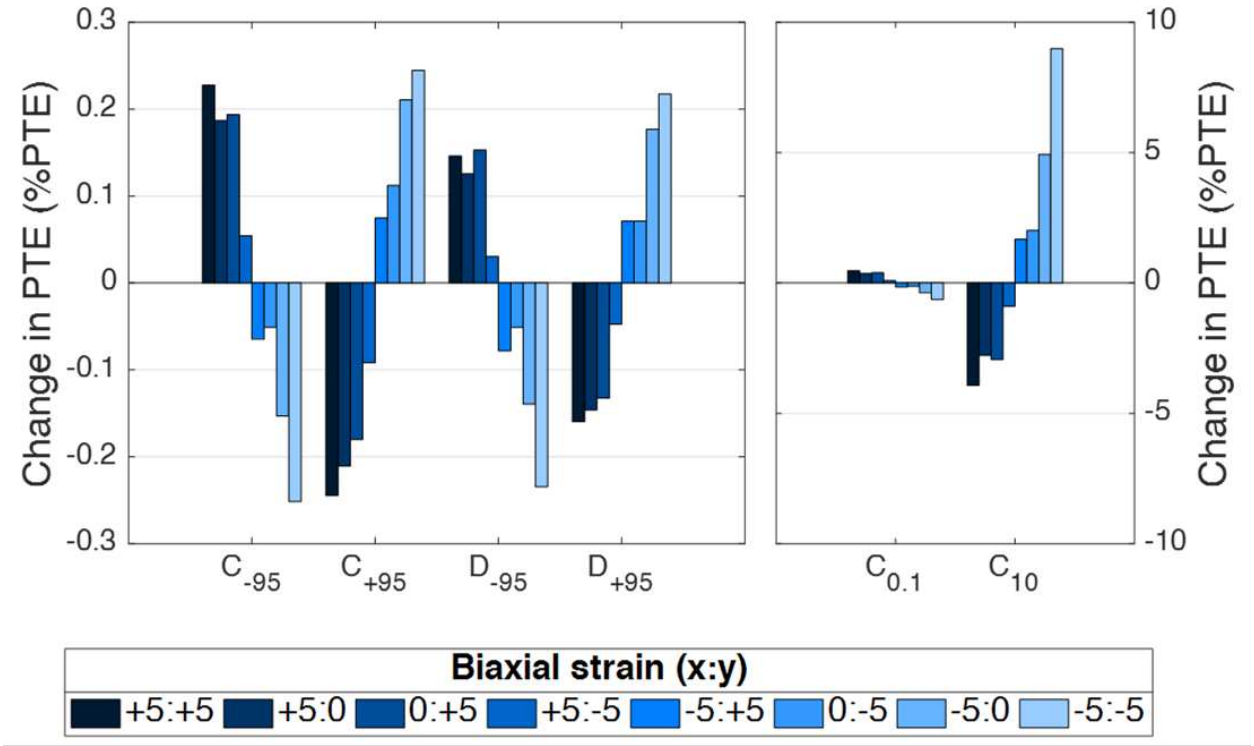

Figure 36. Changes to the PTE due to perturbations of material mechanical properties. The considered material perturbations were to the hydrogel elasticity constants (C) and hydrogel compressibility constants (D). The subscripts -95 and +95 represent the lower 95% and upper 95% confidence bounds, respectively. The subscripts -20 and +20 represent a 20% decrease and 20% increase of the base material values, respectively. $C_{0.1}$ and C_{10} represent the tenfold increase and decrease in hydrogel elasticity, respectively. For each material condition, trends are shown as a function of biaxial loading.

Similar to the upper 95% confidence interval, the PTE was increased in biaxial compression and decreased in biaxial tension for a tenfold increase in C_1 and C_2, and vice versa for a decrease in C_1 and C_2 (Figure 36). Decreasing the order of magnitude of the hydrogel elastic coefficients (C_1 and C_2) tenfold resulted in changes to the PTE within ±0.7 %PTE for all loading conditions. Conversely, a tenfold increase in C_1 and C_2 changed the PTE by ±0.9 to ±9.0 %PTE.

All conditions of changes in fiber elastic modulus changed the PTE by less than 0.02%. However, the changes in fiber elasticity were associated with proportional changes in stress on the

unit cell For example, the 20% increase in fiber elastic modulus resulted in a 20% increase in the circumferential and axial stresses required to generate the same global strains.

3.2.3.4. Scaffold architecture

The PTE as a function of the four architectural parameters for 5% equibiaxial strain and 5% uniaxial tension (while constrained in the circumferential direction) are shown in Figure 37. Overall, the fiber spacing, fiber angle, fiber diameter, and architecture scale demonstrated a total range of 3.8 to 17.2 %PTE. For these load conditions, the attached fibers exhibited a greater PTE than the unattached fibers at full load in all considered architectures. However, for all variants of fiber angle and fiber diameter, the attached fibers only accounted for 9.4 – 12.7% of the total cell volumes in the ROI. The fraction of attached cells increased for decreasing fiber spacing (from 7.1% at 0.6 mm to 23.0% at 1.4 mm) and decreasing fiber scale (from 32.9% at 0.2 scale to 11.6% at 1.0 scale). These increases in attached fibers corresponded with an observable divergence of the PTE for all cells and unattached cells.

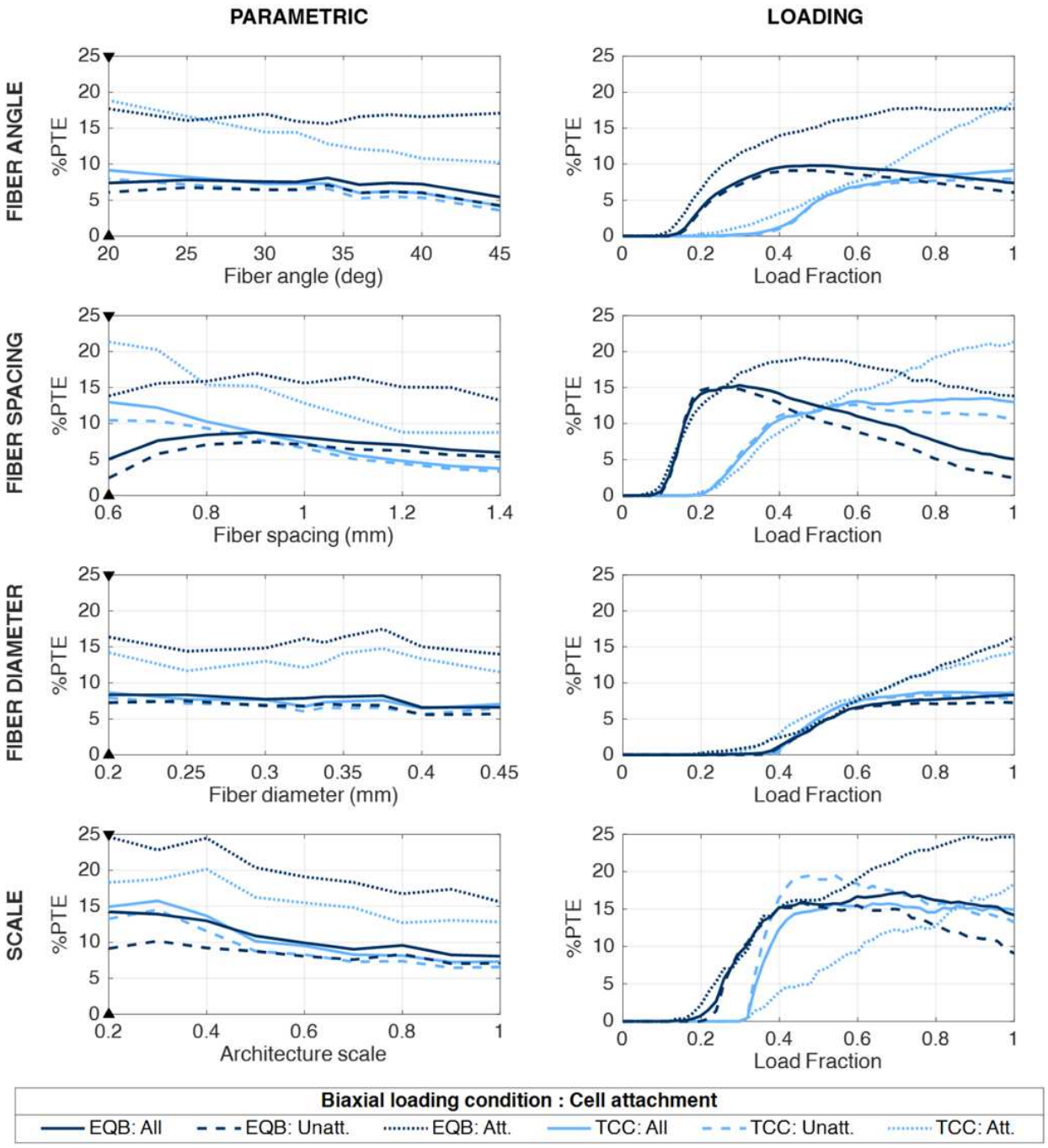

Figure 37. PTE in the scaffold model for four architectural parameters: fiber angle, fiber spacing, fiber diameter, and architecture scale. In the left column of plots, the %PTE is shown as a function of the architectural parameters. A selected value of each parameter is indicated with black arrows at the top and bottom of the plot. For each of these selected values, the %PTE is shown as a function of the strain magnitude in the right column of plots. In each plot, the PTE is shown for equibiaxial 5.0% strain (EQB, dark blue) and axially-constrained circumferential 5.0% strain (TCC, light blue) as well as for: all cells (solid lines), cells not attached to fibers (dashed lines, denoted as unatt.), and cells attached to fibers (dotted lines, denoted as att.).

For the selected values of fiber angle, fiber spacing, and architecture scale, the axially-constrained circumferential strain exhibited a greater PTE at full load as compared to equibiaxial strain. However, the loading profile data show that the equibiaxial strain has greater peaks in PTE during the load ramp. Many other trends and features were predicted as a function of the four architectural parameters, as detailed below.

3.2.3.5. Fiber angle

In equibiaxial tension, PTE appears to show no strong correlation with fiber angle, regardless of cell attachment (range of 5.4 to 8.1 %PTE for all cell volumes). In axially-constrained circumferential strain, the PTE generally decreased with increasing fiber angle for all conditions of cell attachment (range of 4.2 to 9.2 %PTE for all cell volumes).

The loading profile data for a 20° fiber angle (Figure 37) showed a similar trend to the base model in equibiaxial strain (Figure 34), including a rapid increase in PTE (starting at a load fraction of approximately 0.1). Likewise, in axially-constrained circumferential strain, a rapid increase in %PTE was shown, however, beginning at a greater load fraction (approximately 0.3). The axially-constrained circumferential strain data demonstrated a monotonic increase in PTE with increasing load fraction.

3.2.3.6. Fiber spacing

In equibiaxial strain, the PTE generation exhibited a peak as a function of fiber spacing (8.8 %PTE at 0.9 mm fiber spacing). This maximum had a pronounced reduction in the model's PTE in the direction of reduced fiber spacing (decreasing to 5.1 %PTE at 0.6 mm fiber spacing). In axially-constrained circumferential strain, a monotonic decrease in PTE was observed with

increasing fiber spacing (range of 3.8 to 13.0 %PTE for all cell volumes). In both loading cases, similar trends were observed for attached and unattached cells.

The equibiaxial loading profile data for 0.6 mm fiber spacing demonstrated a peak in PTE of 15.3 %PTE at 0.30 load fraction. Near this peak, the unattached cells exhibited a higher PTE than the attached cells. A similar phenomenon was shown in axially-constrained circumferential strain, which also appeared to plateau at approximately 13 %PTE (all cell volumes) for load fractions greater than 0.6.

3.2.3.7. Fiber diameter

In both loading conditions, variations in fiber diameter showed no distinct change in %PTE, regardless of cell attachment (range of 4.2 to 9.2 %PTE for all cell volumes). The loading profile data for the 0.2 mm fiber diameter demonstrated a monotonic increase in PTE when equibiaxial strain was applied, and a plateau in PTE in uniaxial loading (with circumferential strain constraint). Both loading conditions provided prediction of less than 10 %PTE for all load fractions.

3.2.3.8. Architecture scale

The ROI strain energy for architecture scales of 0.2 and greater were within 1.0% of the base model in both loading conditions. However, the 0.1 scale ROI strain energy differed by at least 257% from the base model and was omitted. The circumferential and axial reaction forces varied proportionally with the respective constrained areas such that the applied stresses varied by less than 0.02% for all architecture scales.

In both equibiaxial strain and axially-constrained circumferential strain, the PTE generally increased with reduced scale factor for all cells as well as the cells both attached and unattached

to fibers. Loading profile data for the 0.2 scale demonstrated peaks of 17.2 and 15.7 %PTE for the equibiaxial strain and axially-constrained circumferential strain conditions, respectively. In the axially-constrained circumferential strain load ramp, the unattached cell volumes had a greater PTE than attached cell volumes up to a load ratio of 0.86.

3.2.4. Discussion

In this study, a finite element model was implemented to predict the CME within a TE scaffold. Specifically, a repeating unit cell of an angle-ply laminate scaffold for AF regeneration was prescribed a variety of loads, materials, and architectures to assess the relative influences of these factors on the CME. The model with base parameters (optimized to match the tissue-level properties of native AF) exhibited a distribution in maximum principal strain and hydrostatic strain (Figure 33c). Of this distribution, a fraction of the hydrogel volume fell within the proposed target envelope CME for AF regeneration. This level of PTE changed for all considered loads, materials, and architectures, however, the relative sensitivity of the PTE varied between these design factors.

3.2.4.1. Base Model

The base model demonstrated a distribution of the complex, three-dimensional mechanical state within the hydrogel matrix of the TE construct (Figure 33c). This heterogeneity can be attributed to the composite architecture. The fibrous scaffold is necessary to provide tissue-level mechanical integrity to the TE construct. However, the fibers also transmit mechanical stimuli to progenitor cells seeded in the matrix and induce heterogeneity in the cell-level mechanical environment. The results of this study predicted that the scaffold dramatically influences the CME; in the base model, some cell-level strains exceeded 20% for just 5% global equibiaxial strain. Further, the transmission of mechanical loads to progenitor cells is highlighted by the consistently

higher rate of PTE for cells attached to fibers as compared to cells with no fiber attachment (Figure **34**a). This prediction of an enhanced cell response is consistent with the results of experimental cell cultures on fibrous scaffolds[204–206].

3.2.4.2. What is a sufficient level of PTE for AF repair?

Mature, healthy AF has a cell density of around 9000 cells/mm^3 [22,207]. Based on the tetrahedral volumes in this study, only 1 %PTE is theoretically required to maintain this healthy cell volume. However, it is unlikely that such a low fraction of satisfactory CME (i.e. CME that meets the requisite mechanics for ECM formation) would be sufficient for AF repair. Firstly, a higher cell density may be required for the enhanced ECM production required for AF healing, as compared to the maintenance of healthy tissue. Secondly, seeded progenitor cells are dispersed within the hydrogel and do not occupy all available volumes. Therefore, the intersection between the distribution of satisfactory CME and the distribution of progenitor cells within the scaffold would likely lead to a lower fraction of cells with a satisfactory CME than predicted. For example, in the current study the satisfactory CME appeared to be concentrated around the scaffold fibers, however, the seeded cells may not be equally concentrated around these fibers. Thirdly, a 1 %PTE indicates that 99% of cell volumes experience a CME outside of the target mechanics. The cells that occupy these regions may not contribute to the AF regeneration and could potentially produce some deleterious outcomes, including: apoptosis, cellular inactivity, altered cellular phenotypes, catabolic responses, and inflammatory cytokine release. Moreover, even if a small fraction of cells are apoptotic, this may induce apoptosis throughout the scaffold[208], regardless of CME.

The proposed CME target region for AF regeneration is also likely to influence the level of PTE. This target region was based on CME criteria from published data of uniaxial strain and hydrostatic stress experiments. These data resulted in discrete boundaries of the proposed AF

target region. However, this is likely a simplification of the underlying continuous response of AF cells to three-dimensional mechanical stimuli. Further, different cell types or variations in the cytoskeletal morphology may lead to deviations in the requisite CME to elicit and anabolic response. However, possible disparities in the specific anabolic range for cells with different cytoskeletal structures falls outside of the length scale (i.e. subcellular modeling) consideration for this study. The CME criteria also did not include data from combined loading, which may alter the anabolic response of AF cells. However, as the influence of the micromechanical environment on AF remodeling is further explicated the literature, the CME target presented in this model may require revision. For instance, this study serves as a design tool for an ongoing experimental series of TE scaffolds cultured with a prescribed mechanical loading regime. Results from experiments such as these may be leveraged to recursively evaluate the validity of the proposed remodeling windows.

Based on these factors, there is likely no distinct PTE threshold for AF repair. Accordingly, maximizing the level of PTE appears to be the most suitable approach to optimize the level of satisfactory CME. The highest PTE in this study resulted in only 33.5% of the hydrogel volume with an insufficient CME, which seems an acceptably low fraction of non-compliant CME. If the proposed CME target correlates well with anabolic cell responses, the highest levels of PTE are predicted to maximize the probability of a successful regenerative response within the TE scaffold.

3.2.4.3. Scaffold Loading

The PTE throughout the equibiaxial load profile demonstrated that the CME is highly dependent on the magnitude of scaffold loading (Figure 34a). The peak in PTE suggests that an optimal load magnitude exists. At lower loads, the PTE was dramatically reduced and converged toward zero. At higher loads, the PTE decreased more gradually. Given the stochastic distribution

of *in vivo* loading, these results suggest that over-prescribing mechanical stimuli may best ensure that the target mechanics are met. Further, the physiological loads *in vivo* are cyclic and, therefore, many CME conditions in the load profile would be experienced during each cycle.

The biaxial loading array also revealed an influence of the relative magnitudes of in-plane loads on PTE (Figure 34b). Two distinct regions of biaxial loads presented elevated rates of PTE with similar peak values (one in biaxial tension and one in biaxial compression). The major difference between these two regions was the average orientations of the maximum principal strains. The proposed CME target envelope in this study aimed to promote anabolic responses in AF cells for enhanced extracellular matrix production, including collagen, which is a major component of AF. Maximum principal strains were used as a mechanical criteria for predicting the anabolic responses. However, the direction of this maximum principal strain has substantial implications for repair because it has been hypothesized to dictate the orientation of collagen fibers in organs[209,210] and tissue engineering scaffolds[211]. Because collagen in healthy AF is highly oriented in the circumferential-axial plane[23], these results suggest that the peak in PTE associated with biaxial tension in the circumferential-axial plane (similar to *in vivo* loading of the AF) is more likely to restore the native collagen structure of the AF. Accordingly, subsequent studies on scaffold loading and architecture were focused on this biaxial tensile region to minimize computational time. Specifically, load array 3 was used to encapsulate the region of peak biaxial tensile strain.

The peak in biaxial strain (2.8% axial strain and 4.2% biaxial strain) may also reflect the dominant constraints of AF tissue *in vivo*; AF is constrained by the relatively rigid vertebral bodies in the axial direction and by the relatively compliant adjacent AF tissue in the circumferential direction. Accordingly, it is possible that the biomimetic architecture is replicating the structural

organization of the native AF tissue that regulates the anabolic responses of AF cells. This peak also occurred within the typical range of physiological strains experienced by the AF (up to 6%)[45], further suggesting that the scaffold may be reproducing the healthy mechanoregulatory environment of the AF.

Although the dominant physiological loads experiences by the AF are in the circumferential-axial plane, the AF also experiences a radial pressure from the nucleus pulposus. The nucleus pressure dissipates radially from the inner to outer annulus, such that the pressure typically ranges from of 0 - 1 MPa[212]. Accordingly, this additional, third dimension of loading was considered in the study. Validation of the unit cell model indicated that the ROI CME may be sensitive to the radial direction boundary conditions[197]. Accordingly, the specific values of applied radial pressure in this model may not translate to the true scaffold boundary conditions *in vitro* or *in vivo*. Regardless, the underlying trends give insight to the influence of radial pressure on the CME. It was evident that radial pressure alone could produce greater PTE than the peak in pure biaxial strains. This result can be attributed to the three-dimensional mechanical equivalence of uniaxial compression and biaxial tension. In the absence of radial pressure, the CME distribution for biaxial tension showed a dense population of cell volumes with hydrostatic strains slightly more positive than the CME criteria (Figure 33). It is intuitive that superimposing a compressive load (i.e., generation of more negative hydrostatic strains) would result in a dramatic increase in PTE; the combination of biaxial tension and radial pressure provided the greatest PTE (66.5 %PTE). Moreover, the influence of radial pressure appeared to be exacerbated for biaxial strain ratios with greater PTE.

3.2.4.4. Scaffold Materials

The confidence intervals of the hydrogel mechanical properties yielded minimal changes to the PTE (Figure 36). These confidence intervals represent reasonably expected variation in the hydrogel properties due to fabrication or composition. This variation is unlikely to lead to substantial changes in the CME and resultant satisfactory mechanics. Conversely, the tenfold changes in magnitude of the hydrogel elasticity may represent the selection of a different hydrogel material. These material alterations did result in appreciable changes to the PTE. For example, increasing the hydrogel stiffness increased the PTE by up to 9.0 %PTE (from the baseline of 8.1 %PTE). This increase in PTE can be attributed to the stiffer hydrogel sharing a greater proportion of the global loading with the scaffold, however, with little impact on the global scaffold mechanics. As such, the results suggest that changing the hydrogel material may be an advantageous method to modify the CME without modifying the overall mechanics of the composite construct.

Changes to the fiber elasticity had negligible effect on the PTE for a consistent scaffold strain. This intuitive result may be advantageous because TE processes can alter material properties, such as thermal degradation during additive manufacturing[213]. However, the changes to fiber elasticity also altered the overall scaffold mechanics, as observed by proportional changes to the necessary stresses (i.e., reaction forces) for a given deformation. Though changes to material properties lead to negligible changes to the CME for a given strain, *in situ* the scaffold deformation is driven by loading. Therefore, the scaffold materials are more likely to have an indirect influence the CME by changing the scaffold deformation for a given mechanical load.

3.2.4.5. Scaffold Architecture

The fiber angle, fiber spacing, and fiber diameter all had minimal direct influence on the CME. Although the PTE demonstrated some correlation with these parameters, the trends were sensitive to the ratio and magnitude of biaxial loading. The nature of these trends may be associated with the competing factors of: (1) fiber surface area per unit volume (i.e. the fraction of cells in proximity to the scaffold fibers), (2) the total volume fraction of matrix in the construct, and (3) the deformation of each fiber segment. For example, for a given construct loading, increasing the fiber spacing resulted in increased fiber strain but a corresponding decrease in surface area per unit volume. Overall, changing the fiber angle, spacing, or diameter are not good candidates for enhancing the PTE generation.

In, contrast, reduction of the overall architecture scale (i.e. maintaining a constant ratio of fiber spacing and fiber diameter) consistently increased the PTE. This increase can be attributed to an increase in fiber surface area per unit volume, whilst maintaining the fiber deformation. Accordingly, reducing the fiber scale appears to be a viable methods to tailor the CME in TE constructs. The scale factor with the greatest PTE (0.2 scale) corresponded to a fiber diameter of 67.5 μm. Extrapolation of the scale results suggests that even smaller fiber diameters may yield smaller architecture scales and further improved level of satisfactory CME. In order to create these fine architectures, technologies such as melt electrowriting (MEW) can be used to precisely deposit fibers of PCL and other biodegradable polymers with diameters of 1-100 μm[214].

3.2.4.6. Which design factor is most critical for control of the CME?

The critical determining factor for controlling the CME in the TE scaffold was the multiaxial loading modality of the scaffold, as demonstrated by the combined biaxial strain and radial pressure. Reducing the overall architecture scale could also be leveraged to enhance the

CME whilst maintaining the tissue-level mechanics of the TE construct. The remaining material and architectural alterations (hydrogel elasticity, fiber elasticity, fiber angle, fiber spacing, and fiber diameter) may be utilized to tailor the global scaffold properties with minimal influence on the CME. The tissue level properties are essential for mechanical support to maintain the overall stiffness and range of motion of the spine. However, these tissue-level loads will dictate the scaffold deformation and indirectly influence the CME. The proposed pathway of influence for scaffold materials, architecture, and loading modality is summarized in Figure 38.

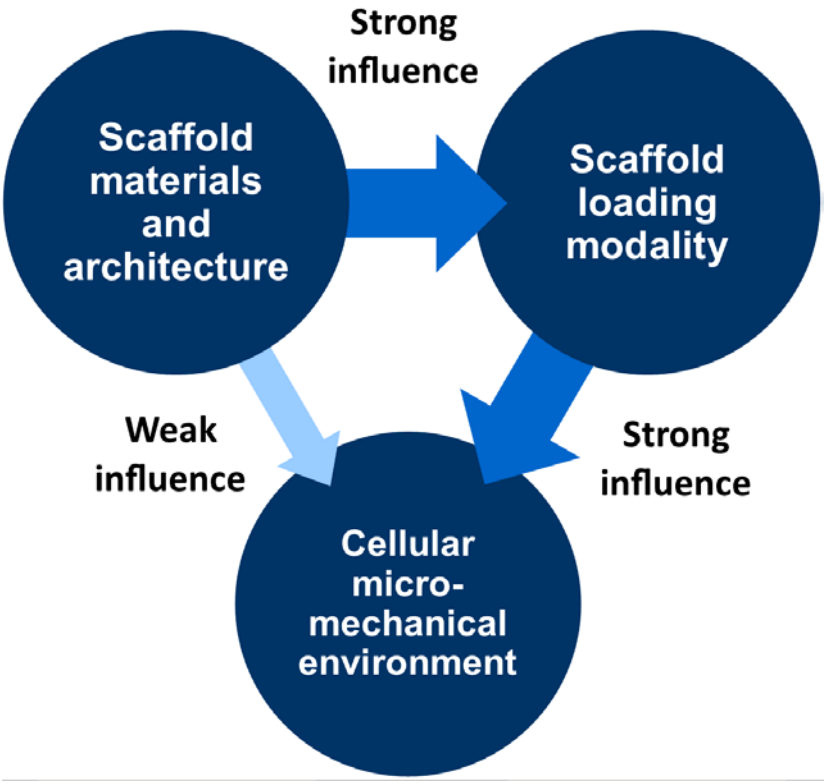

Figure 38. Diagram of the proposed influence of TE scaffold design factors on the CME. The scaffold materials and architecture strongly influence the scaffold loading modality, which strongly influences the CME. The scaffold materials and architecture only had a weak influence on the CME.

3.2.4.7. Implications for the design of experiments and implants

The strong influence of scaffold loading on CME indicated the importance of delivering physiological loads to TE constructs to stimulate regeneration. Accordingly, in the context of *in vivo* implants, the attachment conditions of TE construct may be essential for the generation and maintenance of new tissue. Suturing is a simple and ubiquitous surgical technique which may afford mechanical integration of TE implants. However, sutures only provide discrete attachment points between the implant and the adjacent tissues that may not transmit loads optimally. A promising range of products for complete mechanical integration of an implant surface to an adjacent tissue are bioadhesives[215,216], which may afford more consistent implant attachment as a continuum.

Similarly, in the context of *in vitro* tissue cultures, there is a need for advanced experimental apparatus to apply and measure the requisite mechanical loads. The resources necessary for such equipment may prohibit experimental groups from being cultured concurrently. This limitation exemplifies the need for predictive tools such as this to understand tissue engineering results and drive informed design changes. An example of this model-aided design was demonstrated in the scaffold loading results; by visualizing the distribution in predicted CME, the radial pressure was identified as a potential method to increase the level of PTE, and subsequently verified. A similar approach may be used to drive experimental design. In the complementary series of TE scaffold cultures, there was no available tool to measure or predict the CME generated in the scaffold under global biaxial loading. The results of this study provided a rationale to select specific values of biaxial strain that would theoretically maximize the level of PTE in the scaffold.

The relationship of materials and architecture with the CME also indicates that the tissue-level and cell-level mechanics can be tailored relatively independently. Therefore, it seems promising that design constraints for both scaffold mechanics and CME can be met simultaneously. This result also suggests that variable architecture design could be implemented to afford greater control of the scaffold loading. For example, the scaffold architecture could be varied near stress concentrations in an implant geometry or varied in order to drive a gradient in tissue phenotype.

3.2.4.8. Study assumptions and limitations

The lack of experimental validation remains a limitation of this work. The need for complex experimental apparatus and statistically powerful study groups inhibits a thorough validation of all presented results. Nonetheless, pertinent scaffolds designs (i.e., loading regimes, materials, and architectures) will be experimentally cultured to validate key results. Histological analyses can be conducted on experimental cultures to quantify the ECM formation as an analog of the model PTE. Further, histological images can be analyzed spatially to assess the influence of cell-fiber attachment. As previously discussed, the extensive time and resources required for cell cultures highlights the importance of predictive models to understand the relationship between tissue-level and cell-level mechanics. Ultimately, this model is an advantageous tool to explain and interpret tissue engineering results, and inspire hypotheses for improved TE strategies.

Several assumptions were made in the model that idealize the TE scaffold for computational practicality. However, it is possible these assumptions result in model limitations that fail to capture the complex and variable behavior of physical scaffolds. The fiber scaffold model idealized fibers from fused deposition as perfectly cylindrical and, therefore, does not account for printing flaws, such as fiber sagging and fiber topology. Similarly, both the fibers and

hydrogel were assumed as heterogeneous and isotropic materials, however, tissue engineering fabrication methods may induce some level of heterogeneity and anisotropy. The hydrogel was assumed to completely fill the scaffold with no voids or flaws and was assumed to fully bond with the PCL fibers at all material interfaces. It follows that progenitor cells seeded in the hydrogel are also assumed to perfectly attach to the fibers. The validity of these simplifications are dependent on the quality of the fabrication method, however, the model may not capture alterations to the CME due to imperfections in a fabricated scaffold. The material properties of the matrix were simplified as an isotropic, continuum solid, and the measures for the CME criteria (i.e., hydrostatic strain and maximum principal strain) were a result of this simplification. Future work may also incorporate other mechanoregulatory factors, such as osmolarity or oxygen tension, into the model and CME evaluation. The presented work also predicted the ECM for the acute phase of the regenerative response. However, it is expected that the matrix material properties would temporally evolve due to tissue adaptation (i.e., ECM synthesis), which may be of interest to further enhance the model.

3.2.5. Conclusion

This study demonstrated high-throughput, computational analyses to predict the relationship between the tissue-level and cell-level mechanics of TE scaffolds with prescribed loading, materials, and architectures. The scaffold loading modality was identified as the most pertinent factor in tissue engineering of the AF. Scaffold materials and architecture were also predicted to control the scaffold loading, and therefore the CME indirectly. By understanding the relationship between tissue-level and cell-level mechanics, the CME may be tailored to drive anabolic cell responses and promote tissue regeneration. The theoretical framework presented in this study is highly tailorable and can be adapted to alternative TE strategies or incorporated in

larger scale biomechanical models. Ultimately, this tool provides a CME-based rationale to predict which TE study conditions are most likely to leverage improved tissue regeneration.

CHAPTER 4 – DESIGN AND IMPLEMENTATION OF AN ANNULUS FIBROSUS REPAIR PATCH

Specific Aim 3 was to design an annulus fibrosus repair patch using experimental and computational methods and implement the patch in an ovine lumbar spine model. The experimental and computational aspects of Specific Aim 1 are divided into Section 4.12.1 and Section 4.2, respectively.

4.1. Experimental Approach

4.1.1. Introduction

In this study, an AF repair patch was developed for the treatment of lumbar IVD herniation. The repair patch was prescribed a hybrid scaffold architecture of 3DF and MEW fibers to leverage the mechanical and biological functions of both fiber scales. An ovine lumbar spine model was used as large animal translational model to investigate the biomechanical and biological effects of the AF repair patch. *Ex vivo* biomechanical characterization was conducted to compare the biomechanical function of healthy, injured, and repaired spines. Additionally, the AF repair patch was implemented in an *in vivo* ovine lumbar spine model and assessed via biomechanical and histological analyses after twelve weeks post-implantation. The large animal model demonstrated in this study provides a basis for iterative improvement to healing outcomes and a platform for clinical translation of a novel AF repair patch strategy.

4.1.2. Methods

4.1.2.1. Implant design and fabrication

A custom AF repair implant geometry was designed for human application with consultation from a board-certified, orthopaedic spine surgeon (Dr. Vikas Patel, MD, Chief of Orthopaedic Spine Surgery, UCHealth Spine Center, Anschutz Medical Campus, Denver, CO, USA). The resultant AF repair patch design comprised of an insert to fill the annular defect (herein referred to as 'insert') combined with an external plate (herein referred to as 'plate') to facilitate surgical attachment of the implant to the adjacent vertebral bodies with screws (Figure 39). This human implant design was translated to an ovine implant design with consultation from a board-certified, veterinary surgeon with specialization in large animal spinal surgery (Dr. Jeremiah Easley, DVM, Diplomate ACVS, Preclinical Surgical Research Laboratory, Colorado State University, Fort Collins, CO, USA). A digital geometry of the implant was generated in Solidworks (2016 SP4.0, Dassault Systèmes, Vélizy-Villacoublay, France) based on a digital model of an ovine lumbar spine. As a result of consultation with the veterinarian surgeon, the implants used for the *in vivo* were redesigned with the screws holes positioned 2.0 mm further away from the disc (i.e. in the axial direction) than the *ex vivo* implants.

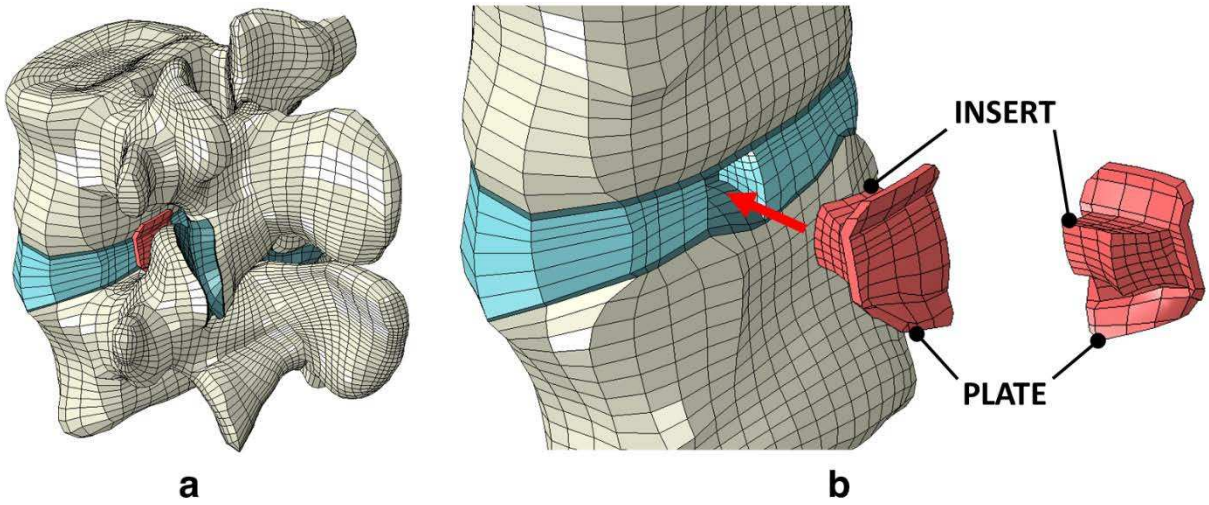

Figure 39. Digital rendering of the AF repair implant design: **(a)** the implant (red) in position in a human lumbar FSU to replace a defect at the posterolateral aspect of the AF (light blue); **(b)** magnified and exploded view showing details of the implant and defect with the posterior features of the spine removed.

The ovine implant design was then adapted for printability via 3DF and prescribed a fibrous architecture that has previously been demonstrated to replicate the pertinent mechanical properties of native AF (Section 2.1). Specifically, the implants architecture was an angle-ply laminate 3DF scaffold with lamellae in the axial-circumferential direction (fiber angle = ±34° from the circumferential direction, fiber spacing = 1.0 mm, layer height = 175 µm). The implant architecture was generated using a combination of BioCAD software (RegenHU, Villaz-Saint-Pierre, Switzerland) and a custom g-code algorithm (Python 2.7, Python Software Foundation, USA). A detailed description of the scaffold design and fabrication process is shown in Appendix G.

Implant fabrication was conducted via 3DF of polycaprolactone (PCL; average Mn 80,000, Sigma Aldrich, St. Louis, MO, USA) using a 3DBiodiscovery bioprinter (HM-100 toolhead, RegenHU Ltd., Villaz-Saint-Pierre, Switzerland; 27 gauge nozzle, nozzle length = 6.35 mm, extrusion temperature = 130 °C, extrusion pressure = 100 kPa, translation rate = 3 mm/s, auger speed = 4.5 rev/min). Two types of implants were generated: (1) hybrid implants consisting of

both 3DF and MEW fibers and (2) pure 3DF implants with no MEW component. Both pure 3DF and hybrid implants had identical 3DF architecture. The hybrid implants were fabricated by first prefabricating sheets of MEW fibers in an angle-ply laminate architecture (fiber angle = ±34° from the y-direction, fiber spacing = 0.1 mm, number of bilayers = 20) using a MEW toolhead (MESW module, 26 gauge nozzle, nozzle length = 15 mm, melt temperature = 65 °C, extrusion pressure = 80 kPa, translation rate = 40 mm/s, voltage = 4.5 kV, collector distance = 3.0 mm). The MEW sheets were then manually inserted between each 3DF bilayer such that the two fiber architectures aligned (Section 3.1). The pure 3DF scaffolds were fabricated to reduce manufacturing complexity; it was assumed that the 3DF component of the implant dominated the global scaffold mechanics and that omission of the MEW layers did not practically alter these mechanics. To achieve high quality fiber deposition throughout the print, the substrate temperature was controlled (initial temperature of 20 °C followed by a linear decrease of 0.33 °C/min to a final temperature of 10 °C). The resultant fiber diameters of the MEW and 3DF processes were measured as previously described (Section 3.1). The pure 3DF implants were used for *ex vivo* biomechanical testing and for implantation in one *in vivo* ovine model (Animal 1). The hybrid implants were implanted in the remaining *in vivo* animal models (Animal 2 and Animal 3).

4.1.2.2. Ex vivo ovine model

Functional spine units (FSUs) of the fourth and fifth lumbar levels (L4L5) were harvested via careful explantation and fine dissection from eight (n = 8) skeletally mature sheep. The spines were wrapped in saline-soaked gauze and stored frozen until biomechanical testing. Each intact FSU was cast in plastic (Smooth-Cast® 321, Smooth-On Inc, Macungie, PA, USA) at the cranial and caudal aspects for rigid mounting in a custom spine biomechanical testing system (Figure 40a)[217]. Motion tracking markers were affixed to each vertebral body with Kirschner wires (Figure

40b) to track the motion of these FSU segments using a four-camera stereophotogrammetry system (Motion Analysis Corp, Santa Rosa, CA, USA). Five cycles of pure moment loading to ±6.0 Nm were applied across the FSU, measured with a six degree of freedom load cell (Advanced Mechanical Technology, Inc. MC3-6-1K, Watertown, Massachusetts, USA). Specifically, the FSU was tested in three anatomical planes: (1) flexion and extension, (2) left and right lateral bending, and (3) left and right axial rotation.

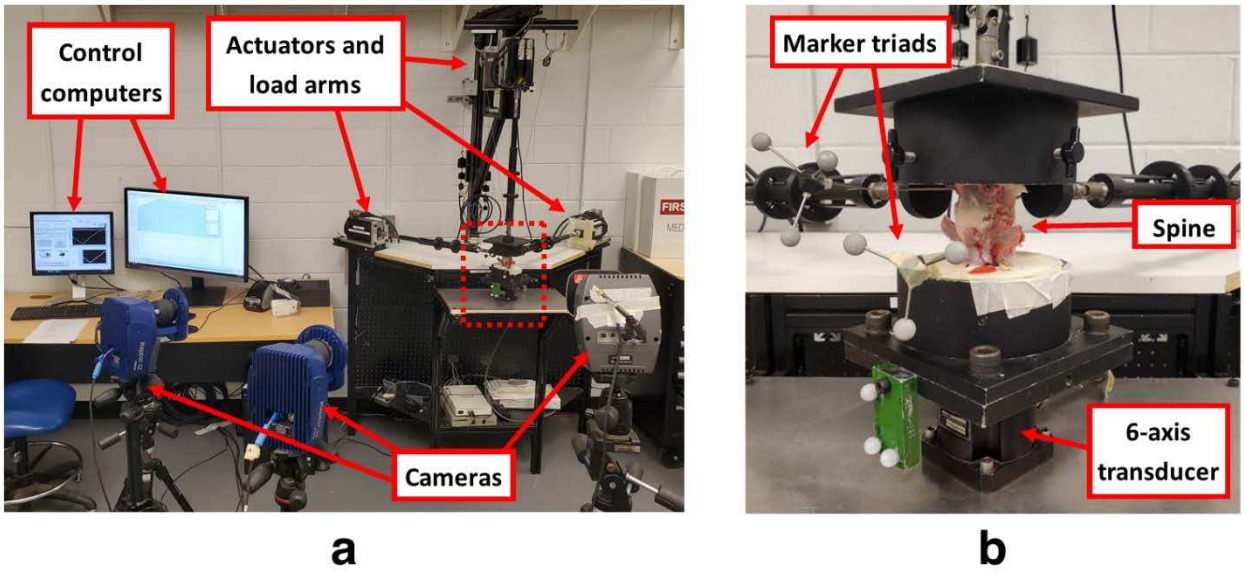

Figure 40. Intact ovine lumbar FSU situated in the biomechanical testing system. **(a)** Full spine testing apparatus showing computers for control and data acquisition, the three-axes of actuators and load arms situated in the testing frame, and three of the four stereophotogrammetry cameras. The dotted box indicates the inset view shown in Figure 40b. **(b)** An FSU embedded in plastic and clamped into the testing frame showing the motion tracking markers and six-axis transducer for moment measurement.

Following biomechanical testing of the intact FSU, a section of intervertebral disc (measuring 8 mm circumferentially, the full disc height axially, and the full AF depth radially) was removed from the FSU using a custom guide (Figure 41). The biomechanical evaluation protocol was repeated on the resultant partial discectomy model using the same testing protocol as the intact

FSU. Pilot holes (1.9 mm diameter) were then drilled in the vertebral bodies and the AF repair implants were inserted within the discectomy and fixed with stainless steel screws (316 Stainless Steel #4-3/8", McMaster Carr, Elmhurst, IL, USA) as shown in Figure 42. A final series of biomechanical testing was conducted on the repaired FSU. Throughout biomechanical testing, sample hydration was maintained via physiologic saline spray at approximately 10 minute intervals.

For each biomechanical test, the recorded motion capture and moments of the final load cycles were processed using previously published methods to identify the range of motion (ROM), stiffness, and neutral zone (NZ) of the FSU[217]. Briefly, the range of motion (ROM) was defined as the difference in angular position of the spine between -6 and +6 Nm of load. The limits of the neutral zone were defined as the central region of the moment-rotation curve bounded by inflections in the curve (identified as local maxima and minima of the second derivative of the moment-rotation curve). The neutral zone was defined as the angular rotation between these inflections and the neutral zone stiffness (NZS) was defined as the least squares fit of a linear line to the NZ moment-rotation curve. The positive and negative elastic zones (i.e., extension/left lateral bending/left axial rotation and flexion/right lateral bending/right axial rotation, respectively) were defined as the moment-rotation curve from +4.5 to +6 Nm and –4.5 to -6 Nm, respectively.

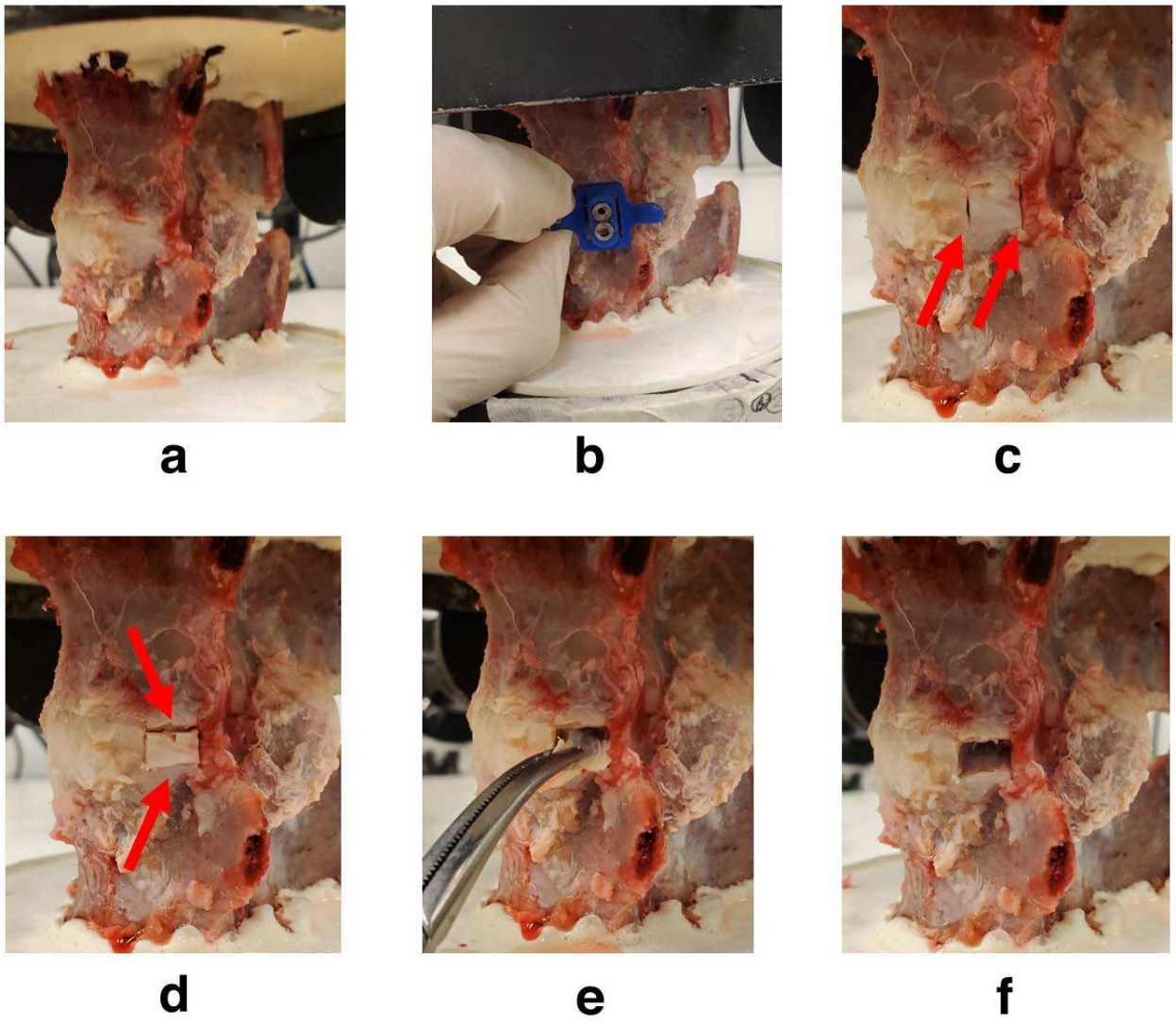

Figure 41. Method of creating the annular defect for surgical sham and treatment levels: **(a)** an intact disc, **(b)** surgical guide used to create axial incisions 8mm apart, **(c)** axial incisions shown with red arrows, **(d)** two circumferential incisions are created along the cartilage endplates to complete the annular window shown with red arrows), **(e)** the window of annulus is removed, and **(f)** the final annular window. All images show the right lateral aspect of the disc.

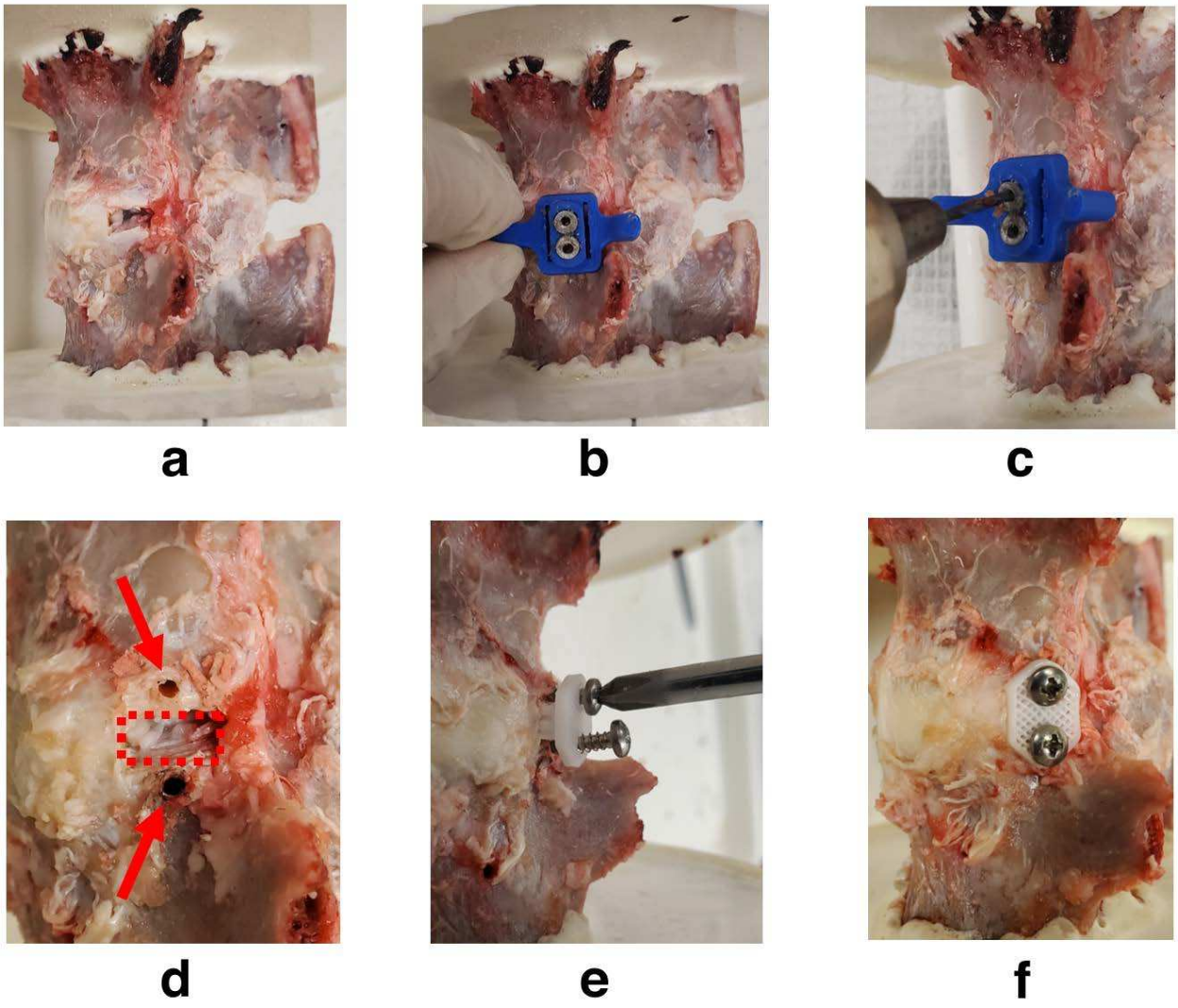

Figure 42. Method of inserting the AF repair implant for the treatment levels: **(a)** the annular defect as per Figure 41, **(b)** the surgical guide aligned to the defect, **(c)** the pilot holes for the vertebral body screws being drilled using the guide, **(d)** the two pilot holes (shown with a red arrow) and the defect (shown with a red dashed box), **(e)** the implant was inserted into the defect and screwed in place using the pilot holes, and **(f)** the inserted implant.

Each group of biomechanical data was tested for normality using Anderson-Darling tests and Levene's test was used to assess equal variance between groups for statistical comparison. An analysis of variance with repeated measures and Tukey *post hoc* comparisons were conducted between the means of the intact, defect, and treated groups for each biomechanical measure and loading condition. All statistical analyses were conducted with a significance level of $\alpha = 0.05$.

4.1.2.3. In vivo ovine model

This study was performed under approval from the Institutional Animal Care and Use Committee at Colorado State University (protocol #: KP1262). Three skeletally mature sheep were used for the study: one sheep was prescribed an implant with a pure 3DF architecture and two sheep were treated with implants with a hybrid scaffold architecture. The L2 through L5 intervertebral spaces were exposed using a left lateral retroperitoneal approach via a plane of dissection through the oblique abdominal muscles to the muscle plane ventral to the transverse processes. An annulotomy was performed at the left lateral aspects of the L2L3 and L4L5 disc spaces by excising an annular window (measuring 8 mm circumferentially and the full disc height axially) and removing the full radial thickness of the AF with pituitary rongeurs. This defect was created to represent the surgical removal of a herniated section of disc. The L2L3 disc spaces were prescribed sham treatments, did not receive an AF repair patch, and remained empty (Figure 43). The L4L5 disc spaces were prescribed the AF repair patch treatment; pilot holes were drilled in the adjacent vertebral bodies using a custom drill guide, an AF repair patch was inserted into the defect, and screws were inserted into the pilot holes to secure the implant (Figure 43). The L1L2 and L3L4 levels were not treated.

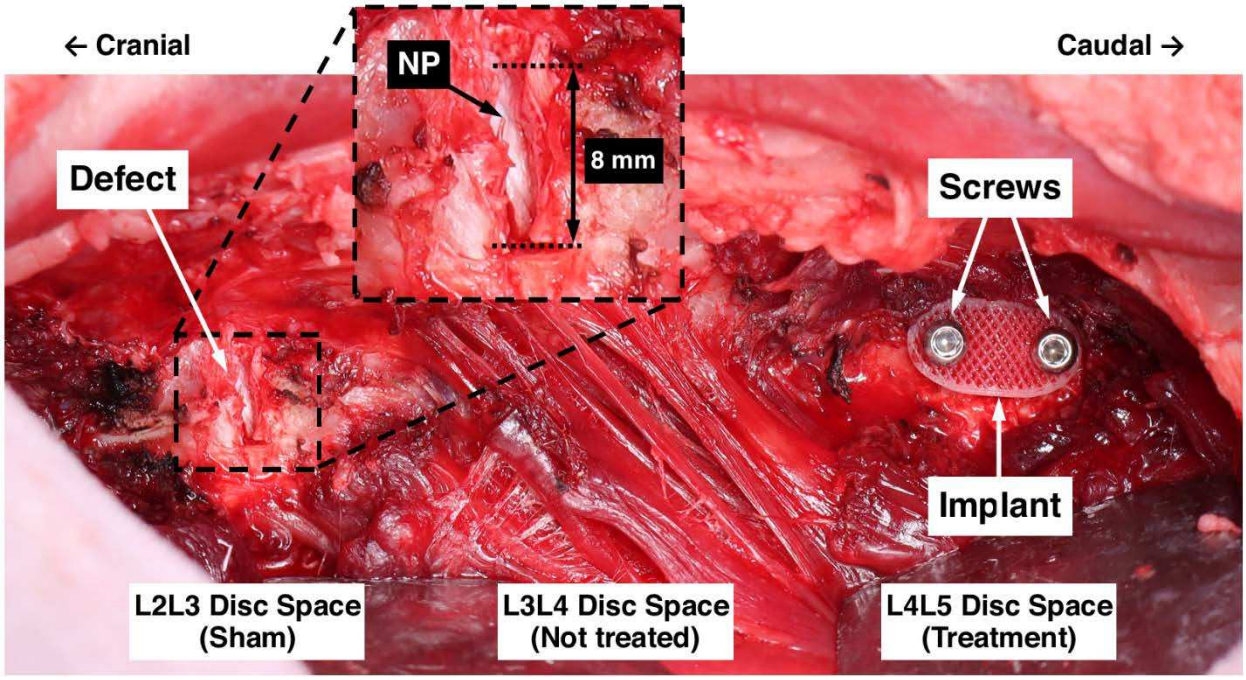

Figure 43. Surgical model for *in vivo* evaluation of the AF repair patch. The L2L3 disc space was prescribed a sham treatment and the defect is shown. The inset shows a magnified view of the defect; labelled are the 8 mm circumferential size of the defect and the exposed NP (white tissue). The L3L4 disc space was not treated. The L4L5 disc space was prescribed the AF repair patch treatment following defect creation; the implant and screws are labelled.

Each animal was radiographed in the sagittal and coronal planes every two weeks during the study and were euthanized 12 weeks following surgery. This study group size (three sheep) and duration (12 weeks) served as a preliminary study to demonstrate the surgical procedure and implant efficacy. Following euthanasia, lumbar spine segments were divided into individual functional spinal units (FSUs) and prepared for non-destructive biomechanical testing, micro-computed tomography (μ-CT) analysis, and histologic processing with histomorphometry.

Kinematic, non-destructive biomechanical testing was conducted on the L1 to L5 disc spaces on each sheep. The same testing protocol was used as for the *ex vivo* analyses (Section 4.1.2.2) with two modifications: (1) the FSUs were not frozen and were tested immediately following euthanasia and (2) the L2 to L5 vertebral bodies were transected in half to facilitate

biomechanical testing of each disc level. Prior to biomechanical testing, each FSU was radiographed in the sagittal and coronal planes. Disc heights were measured from the radiographic images at the 0-week (i.e., post-operative) and 12-week (i.e., post sacrifice) time points. Specifically, the disc height was calculated as the mean distance between the vertebral endplates at five equally spaced locations in the disc in the sagittal plane using, as measured with ImageJ software (National Institutes of Health, Bethesda, MD, USA). Student's t-tests were used to compare the disc heights at the 0-week and 12-week time points. The biomechanical measures of the individual treated levels (L4L5) in the *in vivo* animal study were compared with the mean biomechanical measures of healthy, defect, and treated groups of the corresponding *ex vivo* study (L4L5 FSUs) using one-sample Student's t-tests ($\alpha = 0.05$).

Following biomechanical evaluation, the whole disc was dissected from each FSU by transecting through the vertebral bodies in the transverse plane approximately 5mm from the disc space (Figure 44). These samples were placed in 10% neutral-buffered formalin (10% NBF) for two weeks. During fixation, each level was evaluated using micro-computed tomography (micro-CT) to detect any adverse bone formation in the disc space. The metal screws used to surgically attach the implant were left in place during micro-CT scanning to ensure that the implant remained in place such that the interfaces between the implant and adjacent tissues would remain intact for histological imaging. The micro-CT scans were conducted with 37 x 37 x 37 μm voxel size, 70 kV potential, 500 ms integration time, 114 μA intensity, and 7.98 W power. For each level, the bone volume was quantified in two regions of interest (ROIs), defined as the left and right aspects of the whole disc space. The bone volume within each ROI was computed as the volume with a mineral density between 220 and 1000 mg/cm^3 hydroxyapatite. Following micro-CT imaging,

each FSU section was dissected down to the location of the implant, defect, or corresponding disc tissue (Figure 44) and returned to the 10% NBF solution.

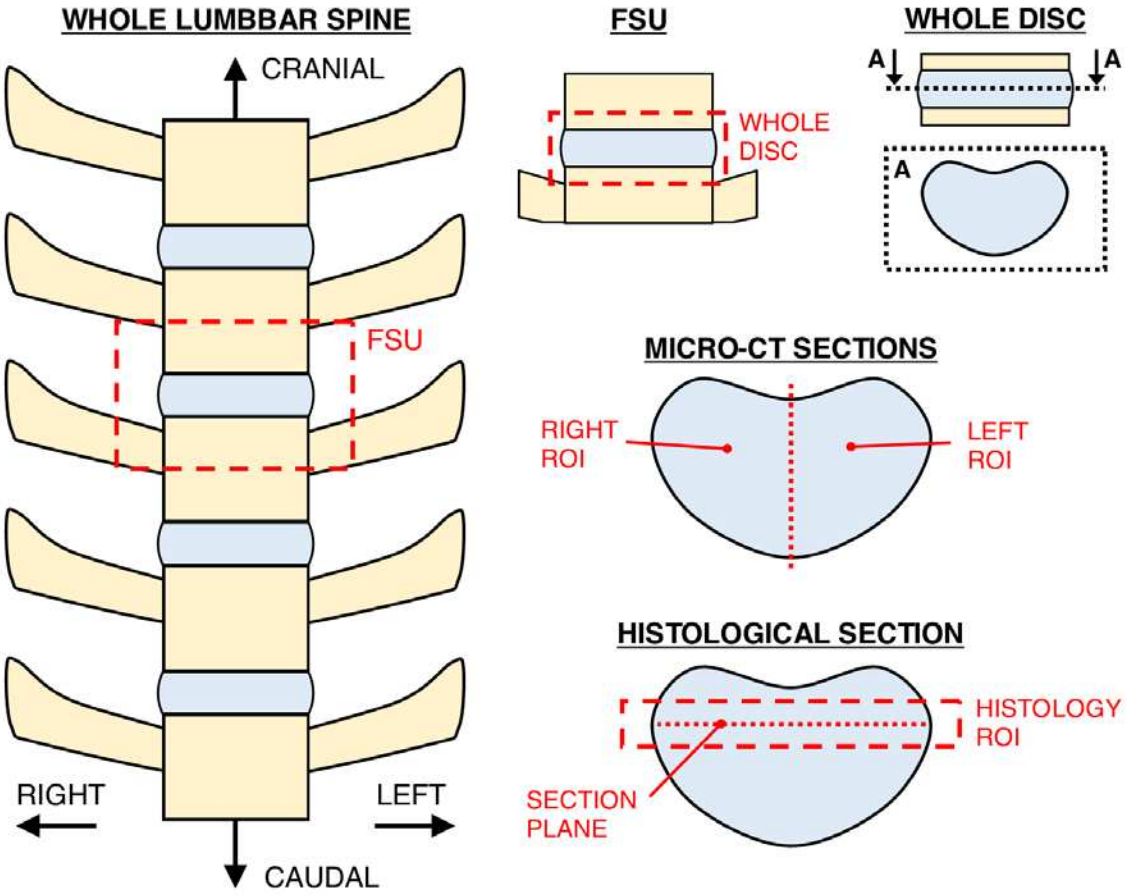

Figure 44. Diagram of a whole ovine lumbar spine showing the functional spinal unit (FSU) for biomechanical testing, the whole disc section for micro-computed tomography (micro-CT), and the partial disc section for histology. Red dashed lines indicate physical cutting of the samples. For bone volume analysis of the micro-CT scan, left and right ROIs were defined by divided the IVD centrally in the sagittal plane. The section plane for histological images is also shown (oriented in the coronal plane).

For histological evaluation, the samples were dehydrated in graded ethanol and cleared with Histoclear (National Diagnostics, Atlanta, GA, USA) followed by infiltration and embedding in methyl methacrylate (MMA; Acrylosin Hard, Dorn and Hart, Loxley, Alabama, USA). At least two sections were cut through the center of each disc ROI in the coronal plane (Figure 44). Initial

sections of approximately 300 µm were taken using a diamond blade saw (Exakt Technologies, Oklahoma City, OK) and were subsequently ground and polished to a final thickness of 60 - 70 µm using a microgrinder (Exakt Technologies, Oklahoma City, OK). One half of the sections for each sample were stained with Sanderson's rapid bone stain (SRBS; Dorn and Hart Microedge Inc., Villa Park, IL, USA) to and counterstained using Van Gieson's stain (VGCS; Dorn and Hart Microedge Inc., Villa Park, IL, USA) to differentiate cells, tissue structure, cartilage, collagen, and bone. The other sections for each sample were stained with toluidine blue stain (TBS; Sigma Aldrich, St. Louis, MO, USA) to detect proteoglycan content.

Histomorphometric measurements were made using Image Pro software (Media Cybernetics, Silver Spring, Maryland, United States) to quantify the tissue structure within each disc level of each study. In the histological section plane, the ROIs for histomorphometric analyses was defined as: (1) the full area of the left AF; (2) the full area of the right AF; and (3) the full area of the NP. An additional ROI was defined for the SRBS sections of the treated levels to characterize the implant, screws and tissue observed outside of the left lateral aspect of the IVD; this ROI was bounded by the cranial edge of the cranial screw, the caudal edge of the caudal screw, the vertebral body, and the peripheral surface of the implant/tissue mass. Within each ROI stained with SRBS, the histomorphometric parameters measured were: (1) percent proteoglycan-rich soft tissue area, as defined by blue stain; (2) percent fibrous soft tissue area, as defined by green stain; (3) percent bone area, as defined by red stain; (4) percent scaffold area; and (5) percent screw area. The histomorphometric parameters for ROIs in the TBS sections were: (1) percent of proteoglycan-rich soft tissue as defined by blue stain and (2) percent scaffold area.

4.1.3. *Results*

4.1.3.1. Implant design and fabrication

The printed implants effectively reproduced the designed implant geometry (Figure 45). Minor stringing of the printed material was observed throughout the implant. Manual inspection of the hybrid implants detected no apparent alterations to the interlamellar bonding as compared to pure 3DF implants.

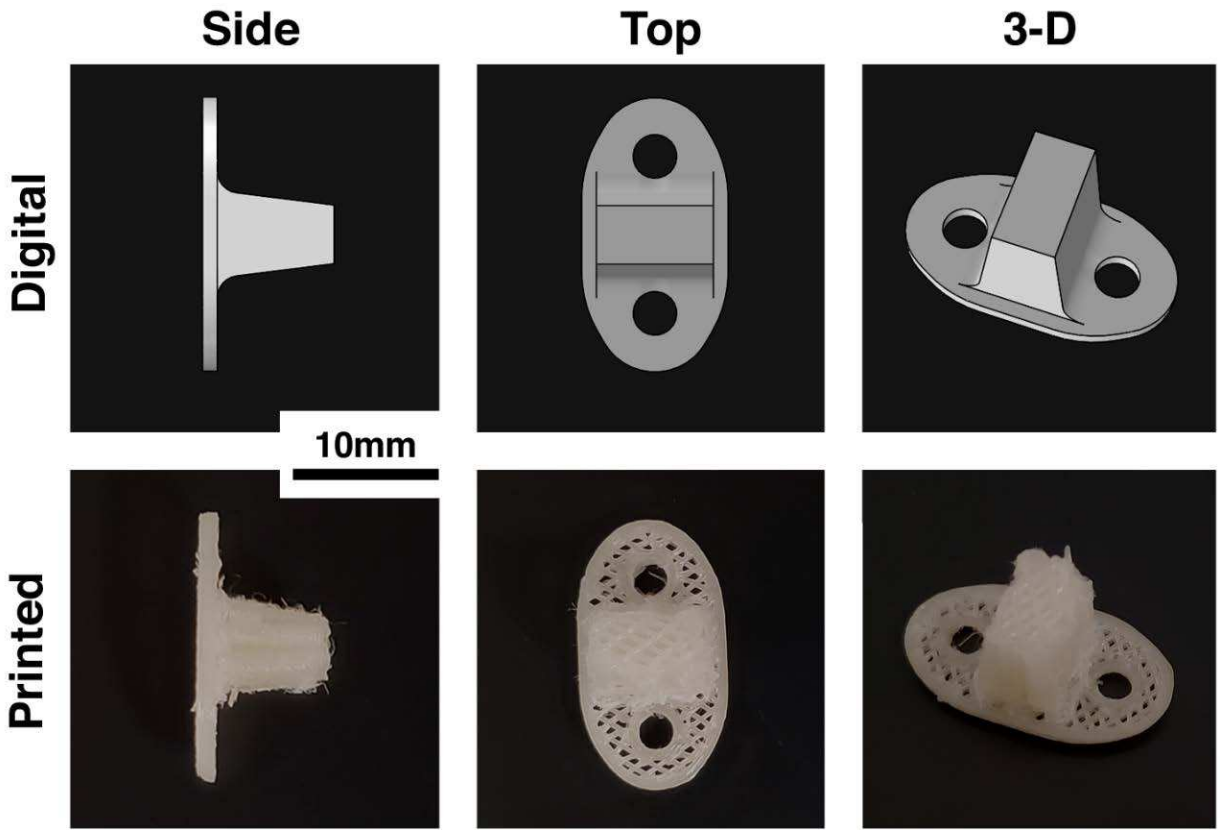

Figure 45. Digital renderings of the ovine AF repair patch design and corresponding printed scaffolds with the hybrid architecture. The 3DF component of the scaffolds was able to reproduce the designed geometry accurately. In the top view of the print, the MEW sheets are observable between the 3DF fibers in the insert (opaque) and compared to the void between the 3DF fibers in the plate (transparent/black). Some residual MEW fibers can be seen in the side view of the print after they were trimmed to the 3DF geometry.

4.1.3.2. Ex vivo ovine model

An example moment-rotation diagram for one ovine L4L5 FSU is shown in Figure 40. The measured FSU angle of rotation generally increased or decreased monotonically with moment loading, facilitating reliable calculation of the ROM, NZ, NZS, and EZS. As compared to the flexion-extension and lateral bending data, a lower signal-to-noise ratio was observed in the axial rotation data which was consistent with lower magnitudes in measured rotation as compared to the other two bending planes for all samples. Summary data for the biomechanics of the healthy spine group are shown in Table 8.

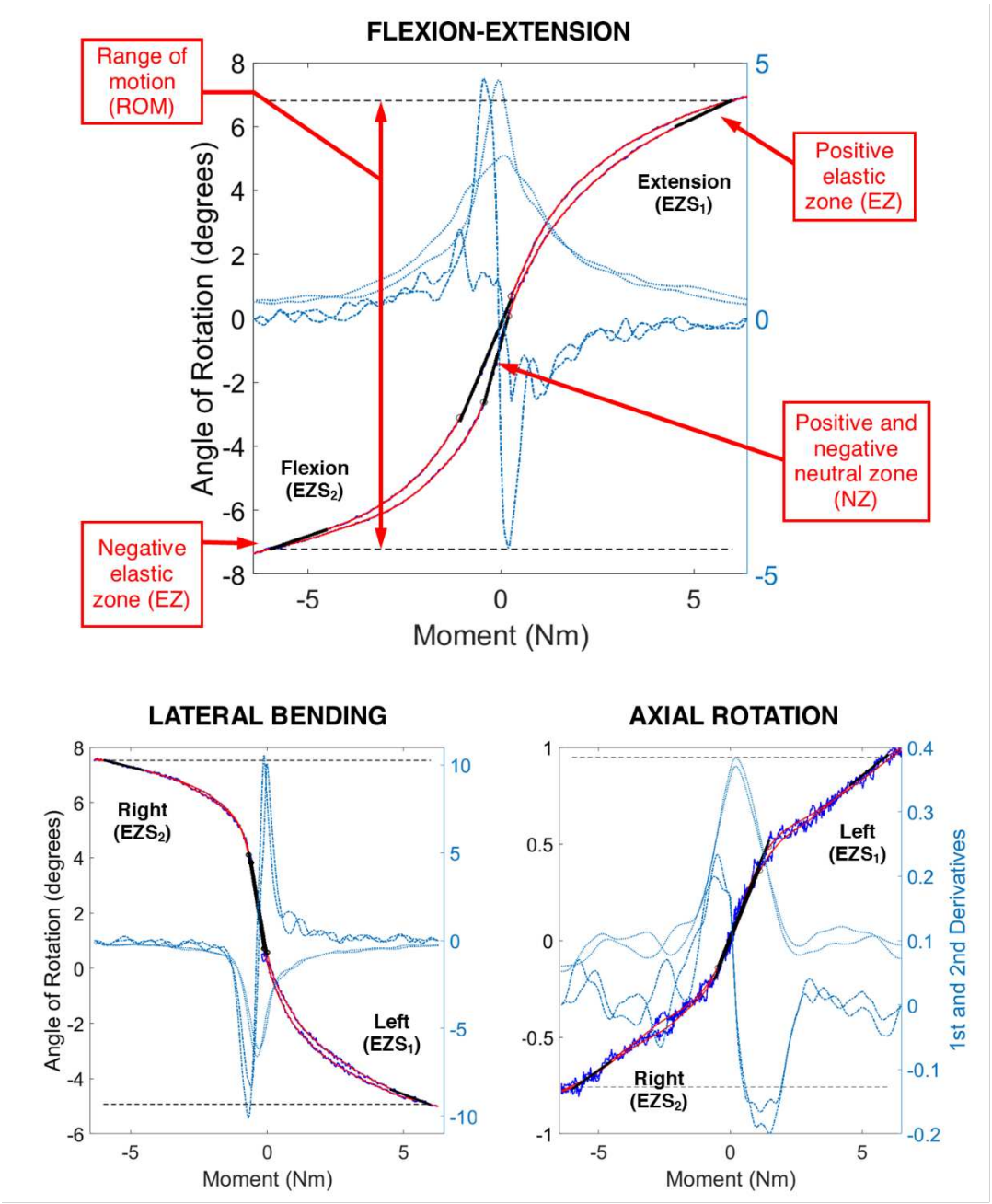

Figure 46. Example moment-rotation data for an ovine L4L5 FSU in three pure-moment loading conditions. Shown are the range of motion (ROM) and the positive and negative linear fits for the neutral zone (NZ) and elastic zone (EZ). The NZ was evaluated between the local extrema in the central region of 2nd derivative of the smoothed data. The EZs were evaluated between a moment of 4.5 Nm and 6.0 Nm (negative and positive).

Table 8. Biomechanical measures (mean ± standard deviation) for the healthy ovine L4L5 FSUs in flexion-extension, lateral bending, and axial rotation.

Loading modality	ROM [°]	NZ [°]	NZS [Nm/°]	EZS1 [Nm/°]	EZS2 [Nm/°]
Flexion-extension	8.15 ±2.30	2.53 ±0.71	0.59 ±0.27	4.18 ±1.54	5.76 ±1.44
Lateral bending	9.57 ±1.40	2.69 ±0.82	0.59 ±0.14	2.60 ±0.41	2.86 ±0.51
Axial rotation	0.95 ±0.27	0.28 ±0.08	9.04 ±3.39	16.28 ±4.92	20.32 ±8.99

In flexion-extension, the ROM was significantly greater than the intact group in both the defect and treated groups ($p < 0.001$ and $p = 0.003$, respectively). The mean increase in ROM of the treated group was less than the defect group (increases of 9.5% and 6.1%, respectively). However, the ROM of the treated group was not significantly different from the defect group ($p = 0.120$).

No significant differences were found between the mean flexion-extension NZ of any groups. As compared to the intact group, the mean flexion-extension NZ of the defect and treated groups decreased by 2.6% and increased by 6.1%, respectively. The NZS was significantly reduced in the defect group as compared to the intact group (mean NZS reduction of 45.3%; $p < 0.001$). However, the treated group (mean NZ reduction of 13.1%) was not significantly different from the intact group ($p = 0.264$) and was significantly different from the defect group ($p = 0.008$).

The flexion extension elastic zone stiffnesses demonstrated no significant changes between any of the groups ($0.075 < p < 0.879$). The mean flexion EZS was increased by 27.7% and 9.49% for the defect and treated groups, respectively, as compared to the intact group. Conversely, the mean extension EZS of the defect and treated groups was decreased by 2.83% and 14.1%, respectively, as compared to the intact group.

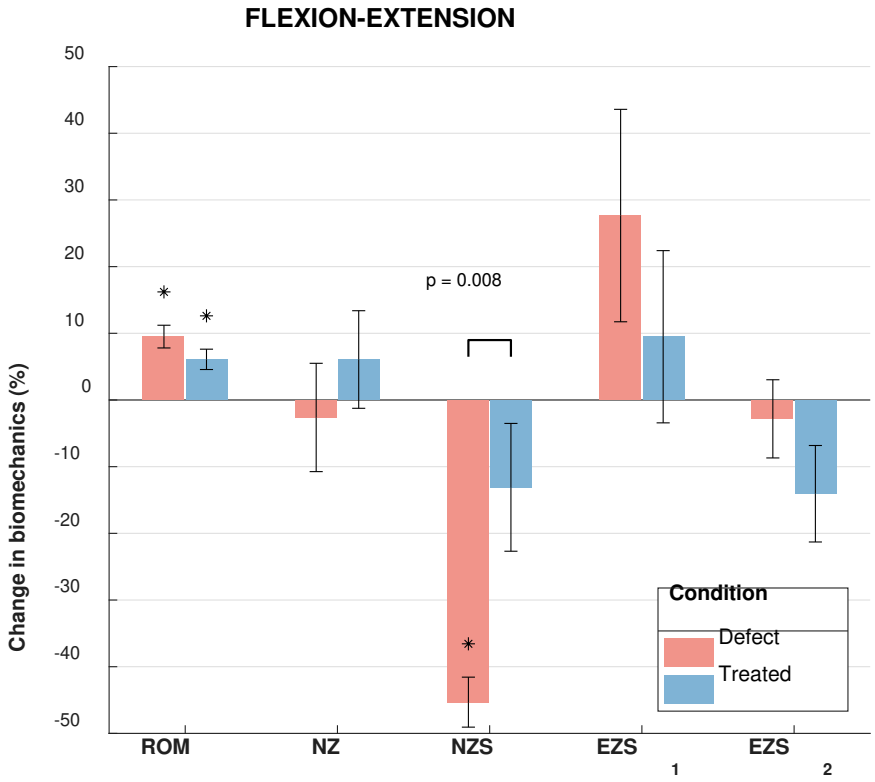

Figure 47. Flexion-extension biomechanics for the defect and treated conditions relative to the intact condition. Error bars shows the standard deviation for each group. Groups with a significant change in biomechanical measures from the intact case are indicated with asterisks ($\alpha = 0.05$) and p-values are shown for significant differences between defect groups and treated groups (no p-value indicates no significant difference between groups).

In lateral bending, significant differences were observed between the mean ROM of all three groups. As compared to the intact group, the mean ROM of the defect and treated groups significantly increased (by 28.6% and 9.7%, respectively; $p < 0.001$ and $p = 0.006$, respectively). Moreover, the mean change in ROM for the treated group significantly less than the mean change in ROM for the defect group ($p < 0.001$).

No significant differences were observed between the mean NZ of any groups. However, the mean increase in NZ of the defect group (23.7%) was greater than the treated group (12.2%). The NZS data yielded significant differences between all three groups ($p < 0.001$ and $p = 0.004$

for the defect and treated groups, respectively, as compared to the intact group). The mean reduction in NZS for the defect group (58.6%) was significantly greater than the treated group (22.1%; $p < 0.001$).

No significant differences were observed between any groups for right EZS stiffness and was associated with low magnitudes in the change of EZS (mean reductions in EZS of 5.8% and 8.1% for the defect and treated groups, respectively; $p = 0.41$ and $p = 0.11$, respectively). However, the mean left EZS for the defect group demonstrated a significant increase as compared to both the intact and treated groups (mean increase in EZS of 16.0% and 12.3%, respectively; $p = 0.020$ and $p = 0.050$, respectively).

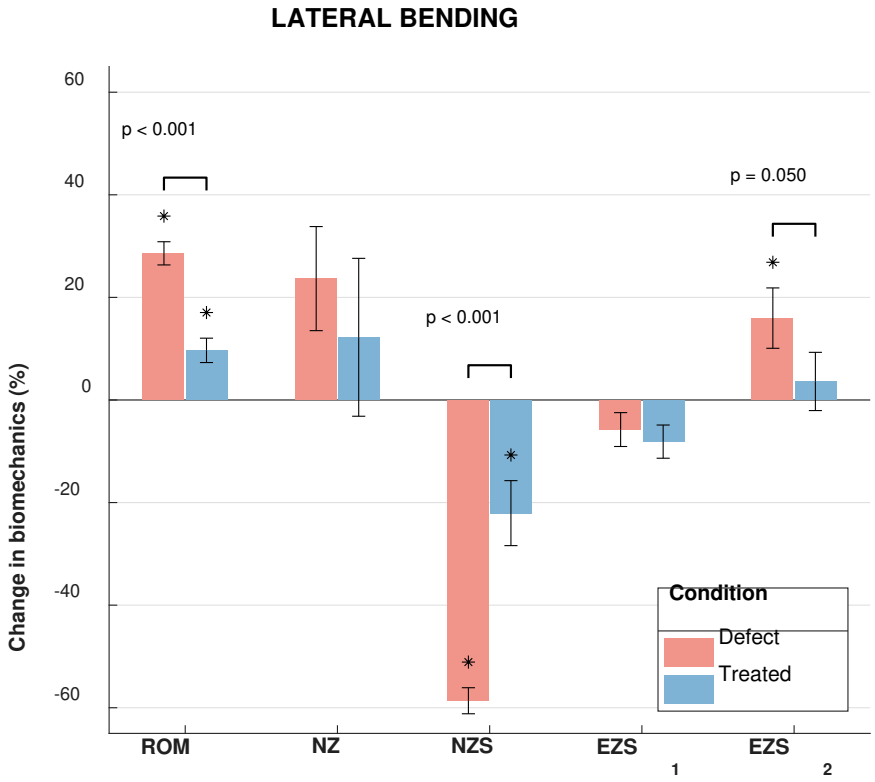

Figure 48. Lateral bending biomechanics for the defect and treated conditions relative to the intact condition. Error bars shows the standard deviation for each group. Groups with a significant change in biomechanical measures from the intact case are indicated with asterisks ($\alpha = 0.05$) and p-values are shown for significant differences between defect groups and treated groups (no p-value indicates no significant difference between groups).

In axial rotation, no significant differences were observed between any groups for NZ and both left and right EZS. The mean axial rotation ROM was significantly increased in the defect group (increase of 23.1%; $p < 0.001$) and treated group (increased of 19.1%; $p = 0.001$) as compared to the intact group. Similarly, when compared to the intact group, the defect and treated groups demonstrated significant decreases in the mean NZS (decreases of 33.5% and 27.5%, respectively; $p < 0.001$ and $p = 0.001$, respectively). In both ROM and NZS, the treated group mean was closer to the intact case than the defect group. However, there were no significant differences between the defect and treated groups.

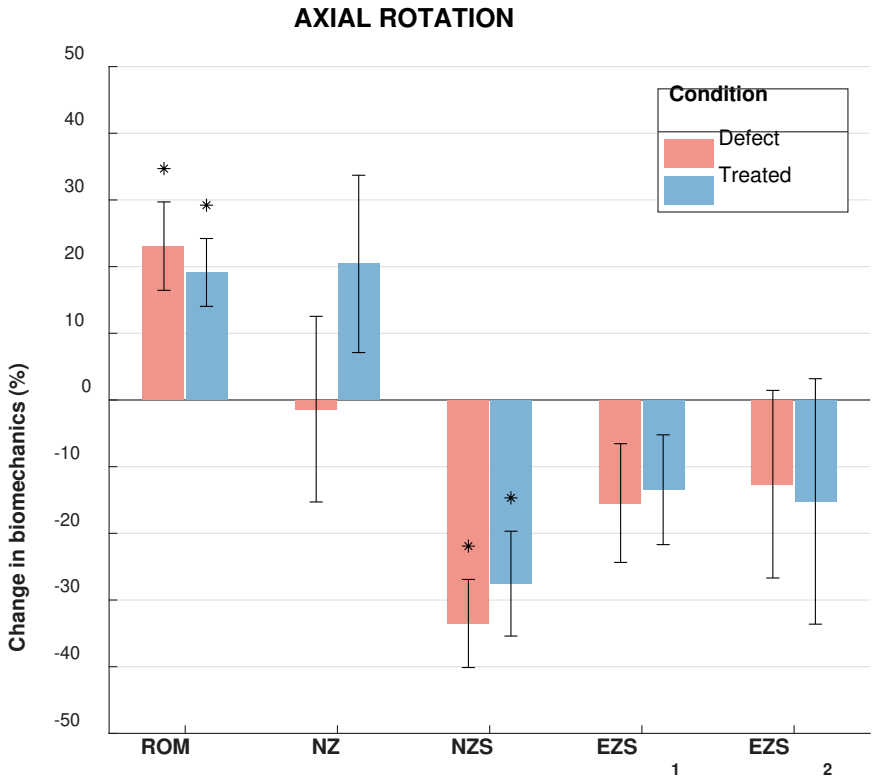

Figure 49. Axial rotation biomechanics for the defect and treated conditions relative to the intact condition. Error bars shows the standard deviation for each group. Groups with a significant change in biomechanical measures from the intact case are indicated with asterisks ($\alpha = 0.05$) and p-values are shown for significant differences between defect groups and treated groups (no p-value indicates no significant difference between groups).

4.1.3.3. In vivo ovine model

Following surgery of Animal 1, it was noted that the sham level was placed in the L1L2 disc (instead of the allocated L2L3 disc) and the treatment was placed in the L3L4 disc (instead of the allocated L4L5 disc). Accordingly, there was no healthy lumbar level on the cranial side of the sham treatment for analyses. Also, the treatment level for Animal 1 (L3L4 disc) was not compared to the *ex vivo* biomechanical groups (L4L5 discs) using statistical analyses because of the disparity in the lumbar level. After sacrifice and fine dissection, fibrous tissue growth at the left lateral aspects of the sham and treated levels was visually observed in all three samples (Figure 50). The

fibrous growth at the treated level consistently appeared larger than at the sham level. No excess fibrous tissue was observed at any of the healthy or contralateral disc spaces. In the treated levels of Animal 1 and Animal 3, the outer surface of the implant plate was visible within the fibrous growth. However, the implant was not visible in Animal 2.

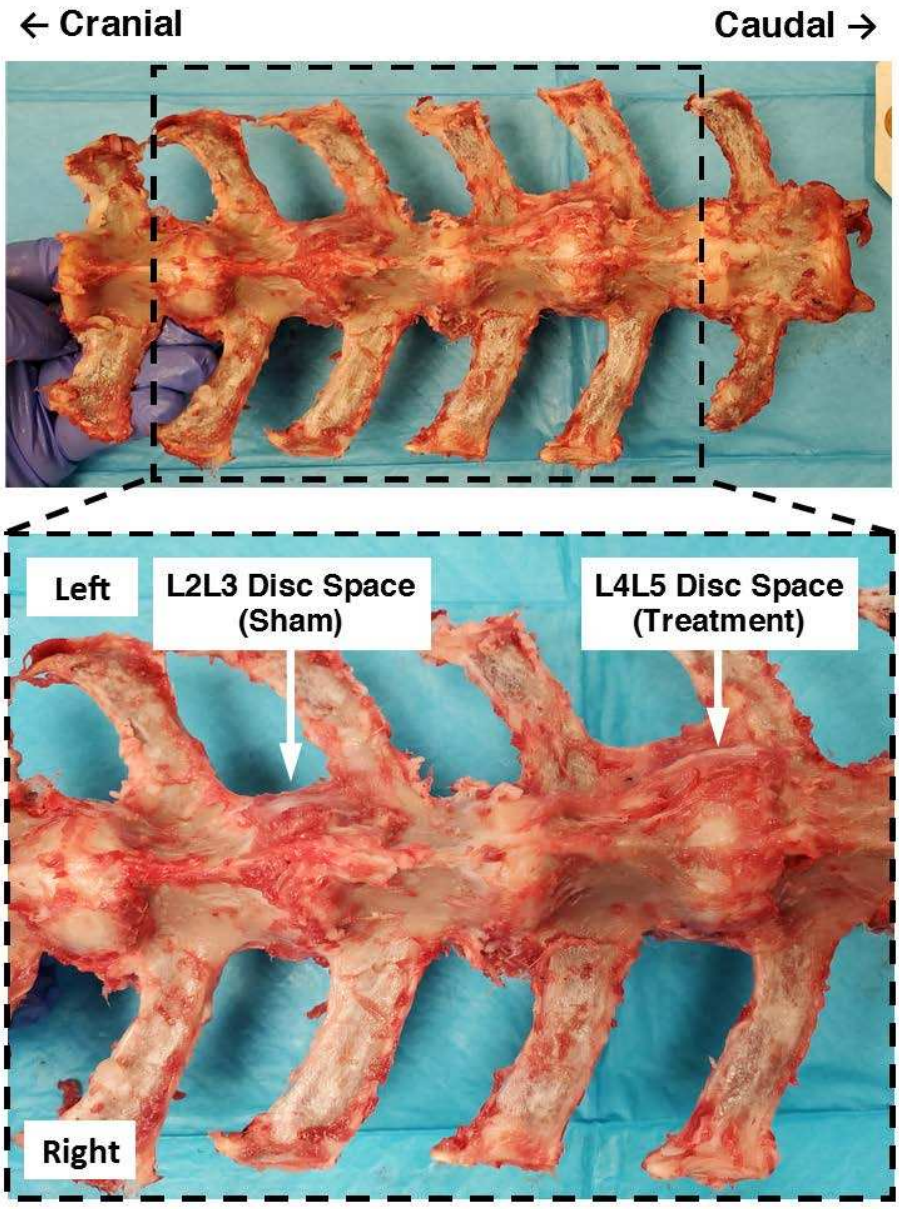

Figure 50. Example digital photographs of the finely dissected whole lumbar spine for sample 2. The spine is shown in the coronal plane. The sham and treatment disc spaces are identified which show fibrous tissue growth at the site of the surgical intervention.

Radiographic images exhibited no clearly identifiable, deleterious effects in any of the disc spaces at any time point in the study. As compared to the healthy and sham levels, a slightly greater radiopacity was observed in the regions surrounding the treated levels at the 12-week time point in two of the three studies (Figure 51; Table 9). These regions were not identifiable in the 0-week time point radiographs. The height of the L1L2 discs (healthy) in Animal 2 and Animal 3 could not be reliably measured from the 0-week time point radiographs. The measured disc heights from the 0-week time point radiographs exhibited no statistically significant differences compared to the twelve-week time points for the sham conditions ($0.16 < p < 0.64$ for the L2L3 levels), healthy conditions ($0.12 < p < 0.77$ for the L3L4 levels) and the treated conditions ($0.43 < p < 0.80$ for the L4L5 levels).

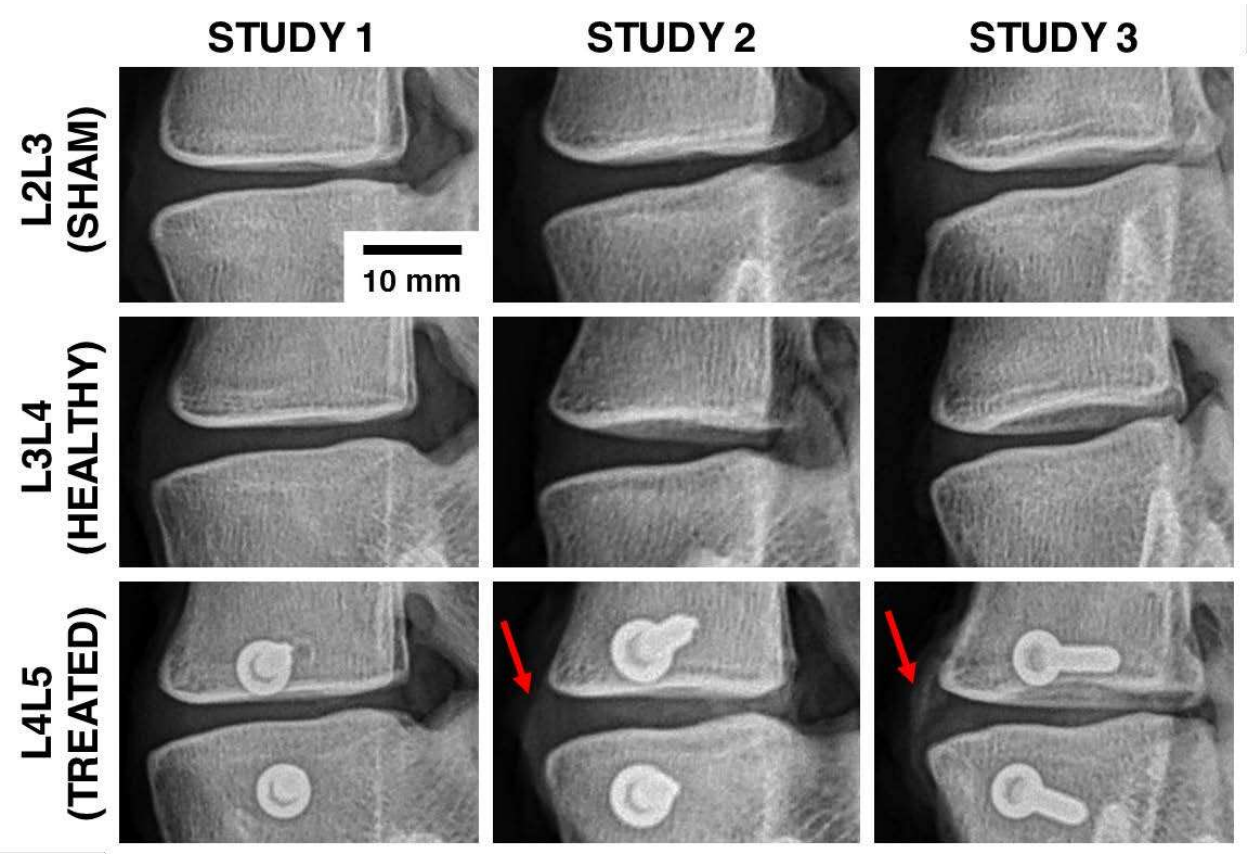

Figure 51. Radiographic images of three disc spaces (sham, healthy, and treated) for the three animal studies at the 12-week time point. The metal screws used to fix the implants are clearly visible in the treated levels. As compared to the corresponding healthy and sham levels, regions of slightly increased radiopacity were observed surrounding the treated levels of study 2 and study 3 (red arrows).

Table 9. Disc height measurements (mean ± standard deviation, s.d.) for the three study animals at the 0-week (i.e., post-operative) and 12-week (i.e., post-sacrifice) time points.

Study	Level	Assignment	Disc height (mean ±s.d.)	
			0 weeks	12 weeks
1	L1L2	Sham	3.9 ±1.3	3.2 ±1.4
	L2L3	Healthy	3.9 ±2.0	3.4 ±1.6
	L3L4	Treatment	3.5 ±1.4	3.3 ±1.5
	L4L5	Healthy	4.0 ±0.9	3.6 ±1.4
2	L1L2	Healthy	-	3.8 ±1.7
	L2L3	Sham	4.6 ±1.5	4.3 ±1.8
	L3L4	Healthy	4.6 ±1.2	4.4 ±1.7
	L4L5	Treatment	4.4 ±1.0	4.0 ±1.2
	L5L6	Healthy	4.4 ±1.3	4.4 ±1.1
3	L1L2	Healthy	-	3.5 ±2.2
	L2L3	Sham	4.7 ±1.5	3.5 ±1.7
	L3L4	Healthy	4.3 ±1.1	3.1 ±1.4
	L4L5	Treatment	4.2 ±1.4	3.5 ±1.6
	L5L6	Healthy	5.0 ±1.4	4.1 ±1.2

In general, the biomechanical measures (ROM, NZ, NZS, and EZS) of the FSUs from the *in vivo* study (L1L2 to L5L6 discs) were similar in magnitude to the healthy, defect, and treated FSUs in the *ex vivo* study groups (Figure 52). In flexion extension, there were no clear trends in any of the biomechanical measures as a function of the FSU condition (i.e., healthy, sham, or treated). The elastic zone stiffness in extension (EZS_1) exhibited a larger spread in the *in vivo* data as compared to the *ex vivo* groups. All biomechanical measures for Animal 3 were not significantly

different to the healthy *ex vivo* group ($0.10 < p < 0.60$). For Animal 2, the ROM and NZ were not significantly different to the healthy *ex vivo* group ($p = 0.08$ and $p = 0.12$, respectively), however, the NZS, EZS_1, and EZS_2 were significantly different ($p = 0.01$, $p < 0.01$, and $p = 0.02$, respectively). Further, the NZS was not significantly different to the *ex vivo* defect group ($p = 0.25$).

In lateral bending, all ROMs and NZs of the treatment levels were less than the sham levels and all NZSs of the treatment levels were greater than the sham levels. In each of these three measures, the difference between the healthy and sham demonstrated the same trend as the *ex vivo* groups (i.e., in both the *in vivo* and *ex vivo* data, the treatment decreased the ROM as compared to the defect/sham). However, neither the healthy nor the defect levels exhibited any clear difference to the healthy levels in these measures. Additionally, the variability in the ROM and both EZSs for the healthy levels was notably larger in the *in vivo* data as compared to the *ex vivo* data. As compared the *ex vivo* biomechanical data, the ROM for Animal 3 and the NZS for Animal 2 were not significantly different healthy spine groups ($p = 0.49$ and $p = 0.62$, respectively). However, all other measures were significantly different to the corresponding measures in the healthy *ex vivo* group ($p \leq 0.02$ for all). For both Animal 2 and Animal 3, the ROM, NZ, and NZS were significantly different to the *ex vivo* defect groups ($p < 0.01$ for all).

The axial rotation biomechanics appeared to show some trend in the ROM, NZS, and right EZS (EZS_2) as a function of the level condition. However, the NZ and left EZS (EZS_1) did not exhibit any appreciable biomechanical changes between the healthy, sham, and treatment levels. The axial rotation ROMs were greater for the sham condition as compared to all healthy conditions, except for the L1L2 disc of study Animal 2. This increased ROM was mitigated by the treatments, which were more comparable to the healthy levels. Similarly, the NZS of the sham levels was less

than all of the healthy levels except for the L1L2 disc of study Animal 2, and the treatment levels exhibited NZS similar to the healthy levels. Lastly, the EZS_2 was generally lower for the defect levels as compared to the healthy and treated levels, which were similar in magnitude. However, this trend was not as clearly defined as the trend in the ROM and NZS because three of the healthy levels had similar EZS_2 to the defect levels (L1L2 and L3L4 discs of Animal 1, and L1L2 discs of Animal 2). However, for Animals 2 and 3, these three measures that demonstrated a trend as a function of the spine condition (ROM, NZS, and EZS_2) were all significantly different to the healthy *ex vivo* group ($p = 0.02$ and $p < 0.01$, respectively, for the ROM; $p = 0.03$ and $p < 0.01$, respectively, for the NZS; and $p = 0.04$ and $p = 0.01$, respectively, for the EZS_1). Further, for Animal 2, all of these three measures were not significantly different to the treated and defect *ex vivo* groups ($0.29 \leq p \leq 0.46$ and $0.14 \leq p \leq 0.70$, respectively). Conversely, for Animal 3, all of these three measures were significantly different to the treated and defect *ex vivo* groups ($p \leq 0.01$ for all).

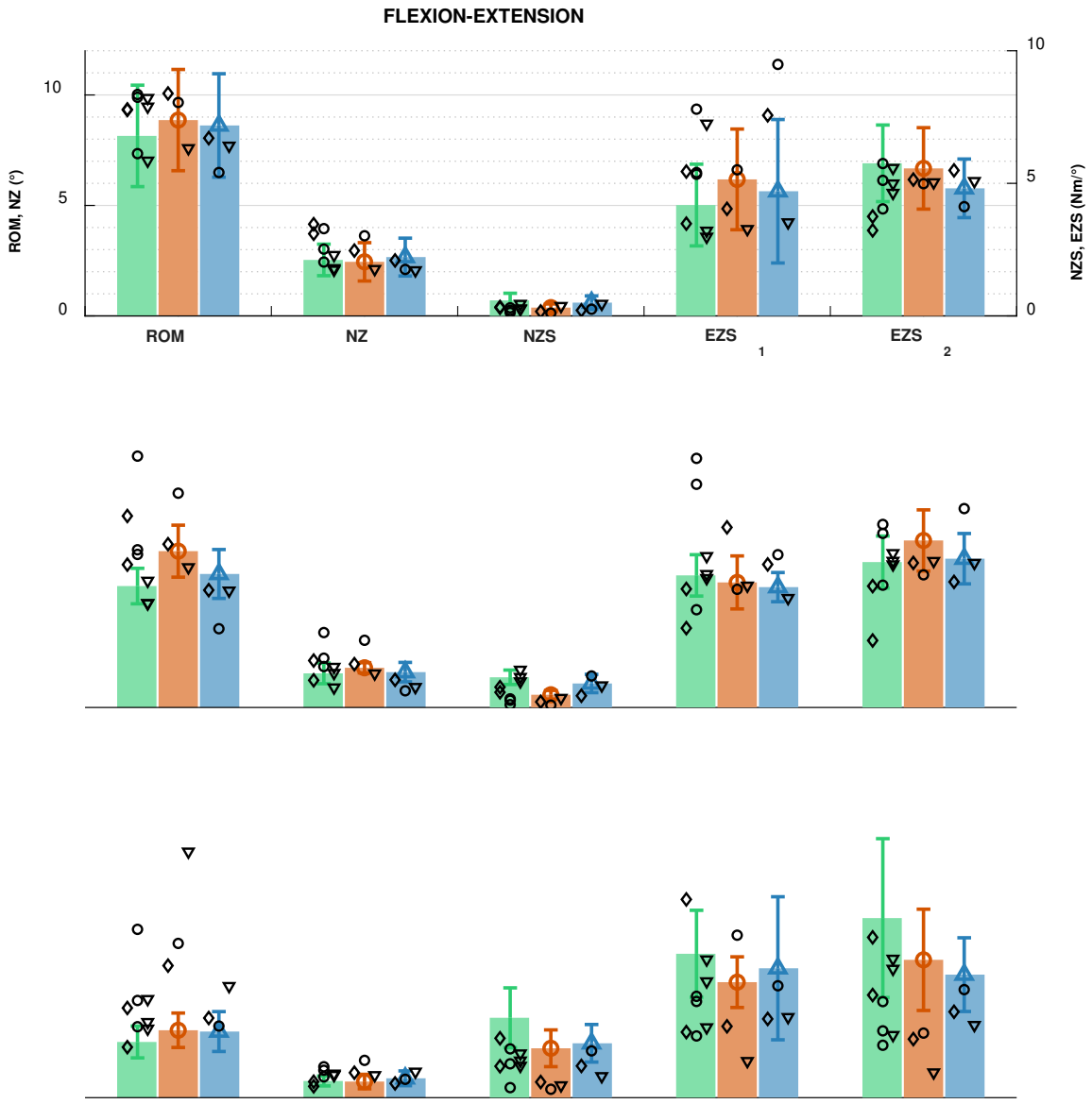

Figure 52. Quantitative biomechanics for the healthy, sham, and treatment lumbar FSUs conditions in three loading modes: flexion-extension, lateral bending, and axial rotation. The biomechanical measures are the range of motion (ROM), neutral zone (NZ), neutral zone stiffness (NZS), and the positive and negative elastic zone stiffnesses (EZS_1 and EZS_2). Data are shown for the three *in vivo* studies (study 1 = ◊, study 2 = ○, and study 3 = ▽) and *ex vivo* study groups (group means are shown with solid bars). Error bars shows the standard deviation for the *ex vivo* groups.

Bone volumes measured by the micro-CT analyses are shown in Table 10. All discs in Animal 1 exhibited a bone volume less than or equal to 0.01%. In Animal 2, the bone volume was less than or equal to 0.01% for the L4L5 disc (treated), L3L4 disc (healthy), and the right side of the L3L3 disc (sham level, contralateral side). The left side of the L2L3 disc (sham level, defect side) exhibited a marginally increased bone volume (0.05%). The L1L2 and L5L6 discs (both healthy) had the greatest measured bone volumes (range 0.07% to 0.95%). In study Animal 3, the bone volume of the L2L3 disc, L3L4 disc, and the right side of the L1L2 disc was less than or equal to 0.01%. The remaining healthy discs (left side of the L1L3 disc and the L5L6 disc) had measured bone volumes ranging from 0.03% to 0.43%. The L4L5 disc (treated) had measured bone volumes of 0.11% and 0.04% at the left side (defect) and right side (contralateral), respectively. In all three animals, artefacts in the micro-CT scans associated with the metal screws were observed for the L4L5 discs. In Animals 1 and 3, the total measured volume of L4L5 discs (1253 mm^3 and 1165 mm^3) were within the range of the other measured discs (ranges of 882 to 1673 mm^3 and 892 to 1674 mm^3). However, in study Animal 2, the total volume of the L4L5 disc (916 mm^3) represented the minimum value for all measured discs (range 1033 to 1266 mm^3). Dense tissue masses were observed near the implant site and outside of the disc space in the treated levels of all three animals (Figure 53). These dense regions were largest in transverse plane cross-section near the screw sites. No similar dense tissues were observed in any of the other lumbar levels.

Table 10. Micro-CT bone volume analyses for all lumbar discs in the *in vivo* AF repair patch study. For the left and right halves of each disc, the total volume (TV), bone volume (BV), and percentage bone volume (BV/TV) are reported. The total measured disc volume (DV) is also reported for each disc.

Study	Level	Side	Assignment	TV [mm^3]	BV [mm^3]	TV/BV [%]	DV [mm^3]
1	L1L2	Left	Sham - Sham	407	< 0.01	< 0.01	882
		Right	Sham - Contralateral	474	< 0.01	< 0.01	
	L2L3	Left	Healthy	495	< 0.01	< 0.01	962
		Right	Healthy	467	< 0.01	< 0.01	
	L3L4	Left	Treatment - Treatment	531	0.07	0.01	962
		Right	Treatment - Contralateral	431	0.04	0.01	
	L4L5	Left	Healthy	646	0.07	0.01	1253
		Right	Healthy	607	< 0.01	< 0.01	
	L5L6	Left	Healthy	808	0.01	< 0.01	1673
		Right	Healthy	865	< 0.01	< 0.01	
2	L1L2	Left	Healthy	595	5.62	0.94	1163
		Right	Healthy	567	0.38	0.07	
	L2L3	Left	Sham - Sham	549	0.25	0.05	1033
		Right	Sham - Contralateral	483	0.06	0.01	
	L3L4	Left	Healthy	626	0.05	0.01	1266
		Right	Healthy	640	< 0.01	< 0.01	
	L4L5	Left	Treatment - Treatment	460	0.05	0.01	916
		Right	Treatment - Contralateral	456	< 0.01	< 0.01	
	L5L6	Left	Healthy	621	12.69	2.04	1266
		Right	Healthy	645	2.98	0.46	
3	L1L2	Left	Healthy	496	0.14	0.03	947
		Right	Healthy	450	0.01	< 0.01	
	L2L3	Left	Sham - Sham	486	0.04	0.01	892
		Right	Sham - Contralateral	406	0.01	< 0.01	
	L3L4	Left	Healthy	601	< 0.01	< 0.01	1113
		Right	Healthy	512	0.01	< 0.01	
	L4L5	Left	Treatment - Treatment	552	0.62	0.11	1165
		Right	Treatment - Contralateral	613	0.23	0.04	
	L5L6	Left	Healthy	886	3.82	0.43	1674
		Right	Healthy	788	2.42	0.31	

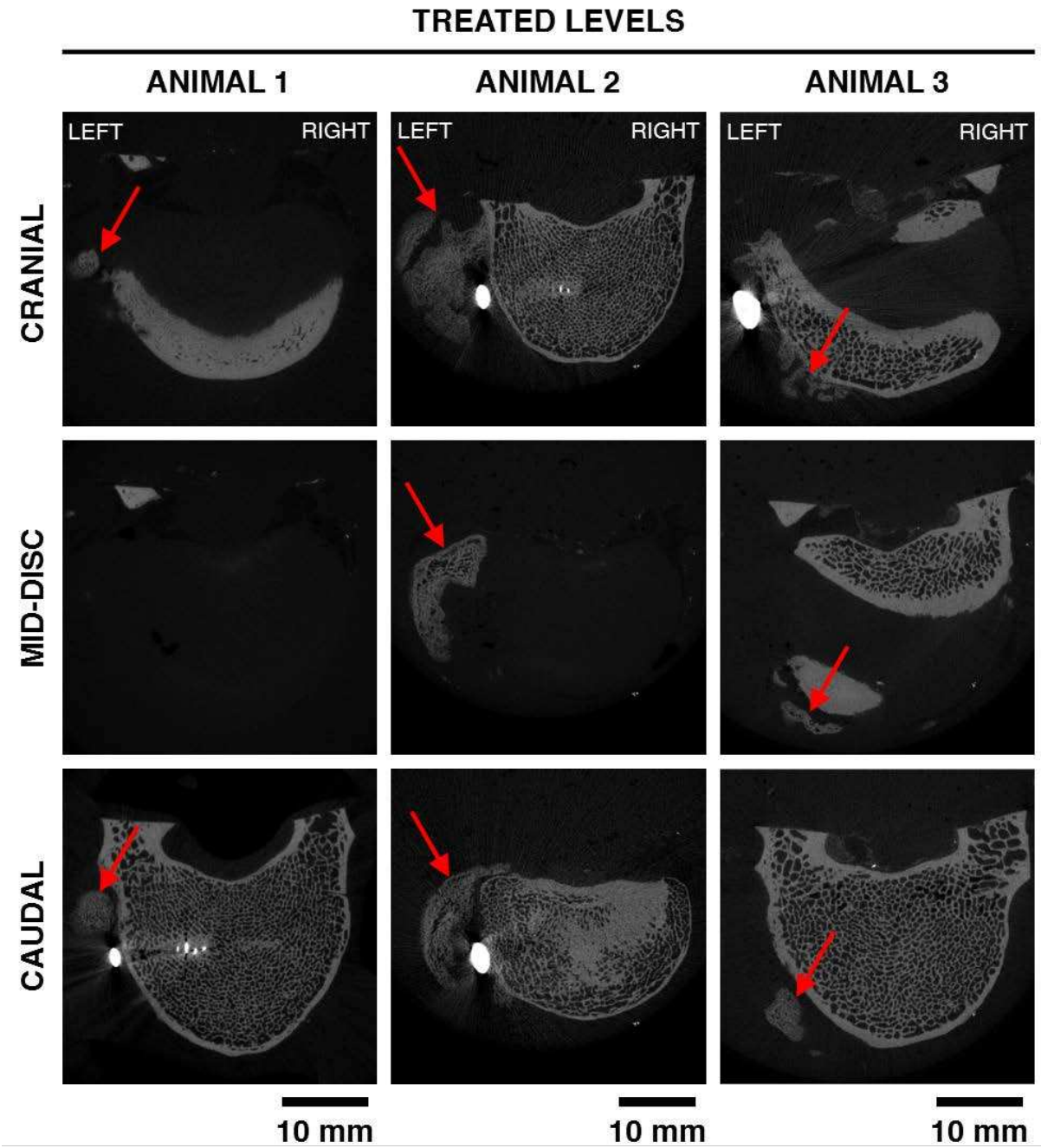

Figure 53. Micro-CT images in the transverse plane of the treated levels for all three studies. Example images are shown at the mid-disc level and at the approximate level of the screws in the cranial and caudal directions. The screws are visible as bright white objects and scanning artefacts associated with the screws are visible as lines propagating from the screw location. Extraneous dense tissue masses are indicated with red arrows. Scale bars are shown for each column of images.

In the histological sections with SRBS, calcified tissue was clearly identified with red stain and soft tissues were identified with green and blue stain (Figure 54). Soft tissues were also identified in blue with the TBS, particularly in the nucleus region of the disc and reducing in intensity radially from the inner to outer AF in healthy sections. Similarly, the healthy AF demonstrated a radial gradient from blue color to green with SRBS. Healthy AF consistently demonstrated a lamellar structure in all histological sections (Figure 55 and Figure 56). Some distinct regions of no stain were observed between lamellae of the AF and within the NP.

In the sections of the treated discs, the metal screws were visible as black (i.e. opaque) objects. Some sections of screw were dislodged from the slides during processing, although the remaining void spaces were clearly visible and were designated accordingly in histomorphometric analyses. The implants were marginally visible in the treatment sections and were differentiable from the background in histomorphometric analyses. In Animals 2 and 3, the implant comprised approximately 50% of the AF ROI, however, in Animal 1, the measured implant area was appreciably less of the total AF ROI (Table 11 and Table 12). The implant plate was clearly detached from the screws in Animal 1 (Figure 57) and was clearly retained by the screws in Animals 2 and 3 (Figure 54 and Figure 57). Across all samples, the size and morphology of the discs varied, and notable variations in the ROI areas were recorded (Table 11 and Table 12).

The morphology and composition of the tissue masses at the treatment site varied between the three animals. Animals 1 and 3 exhibited masses outside of the treatment generally consisting of soft tissues (Figure 54 and Figure 57). However, Animal 2 demonstrated notable calcified tissue formations separated by a relatively dense region of soft tissue (Figure 57). The ROIs of the tissue masses outside of the treated levels measured 95.9 mm^2, 152.9 mm^2, and 65.7 mm^2 for Animals 1, 2, and 3, respectively. In these regions, all three animals demonstrated blue soft tissue areas

(11.8%, 26.9%, and 11.5%, respectively), green soft tissue areas (36.1%, 20.3%, and 24.8%, respectively), screw areas (9.1%, 9.7%, and 30.1%, respectively), and implant areas (25.9% 16.5%, and 23.2%, respectively). In Animal 2, the tissue mass comprised of 22.1% calcified tissue, though only 0.4% and 0.0% calcified tissue was detected for Animal 1 and Animal 3, respectively. Additional, unidentified lesions were observed in the healthy AF and NP of Animal 2 in the micro-CT and histological results (Figure 57).

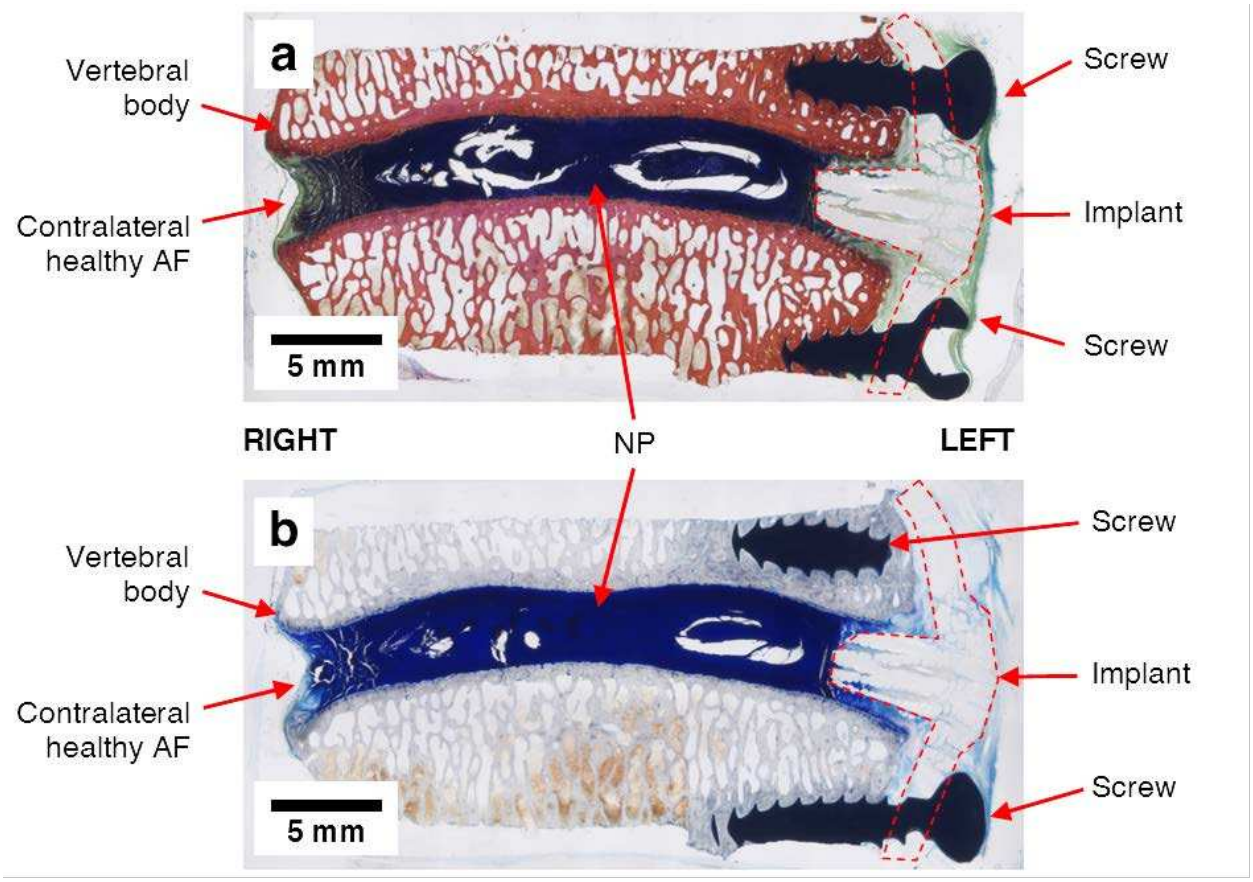

Figure 54. Example histological images of full treated discs (L4L5, Animal 3) strained with (a) SRBS and (b) TBS. The vertebral bodies, screws, and implant (outlined with red dashed lines) are clearly visible.

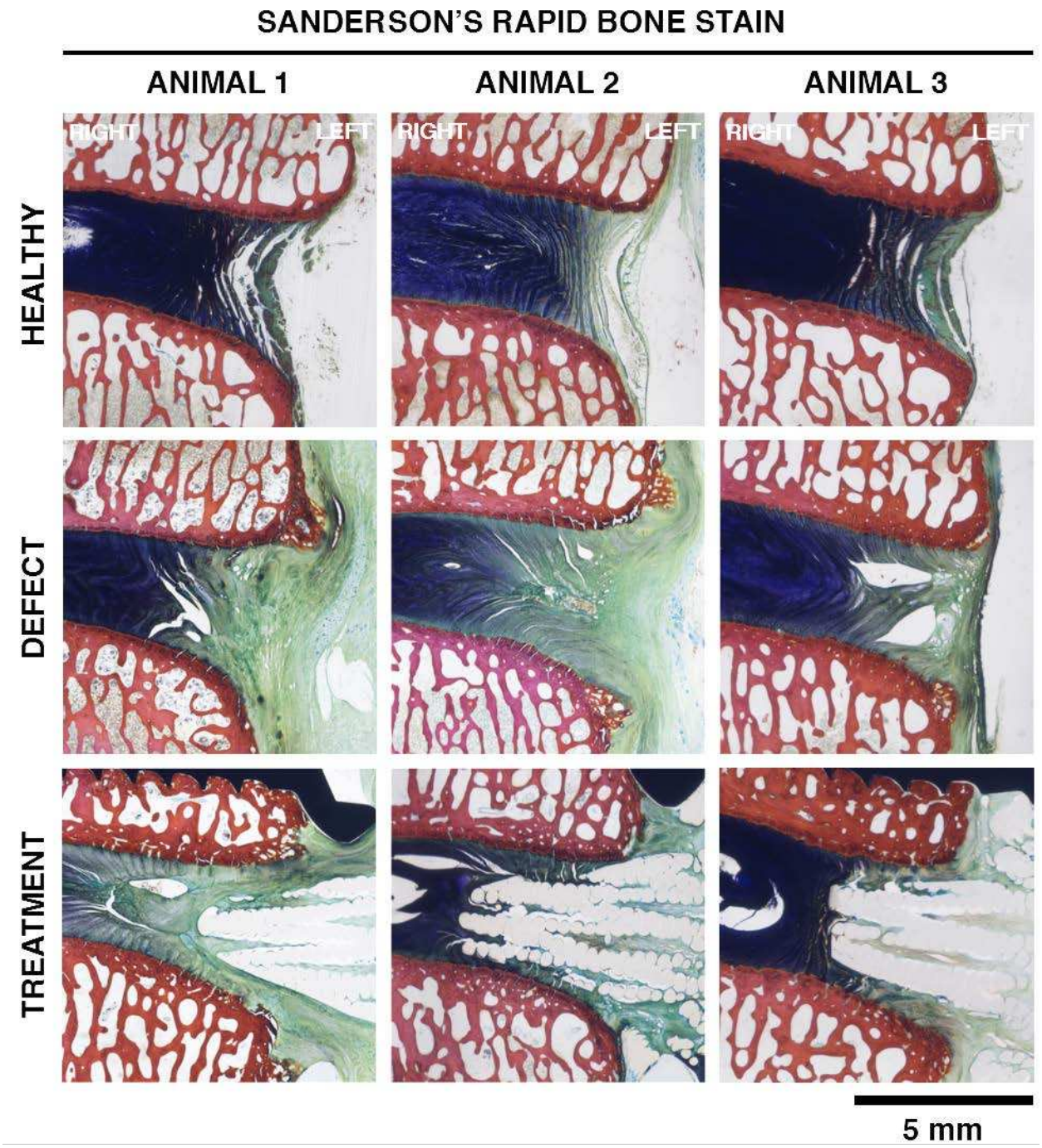

Figure 55. Histological sections of the left AF ROI stained with SRBS. Shown are healthy, defect, and treated AF for all three animals in the study.

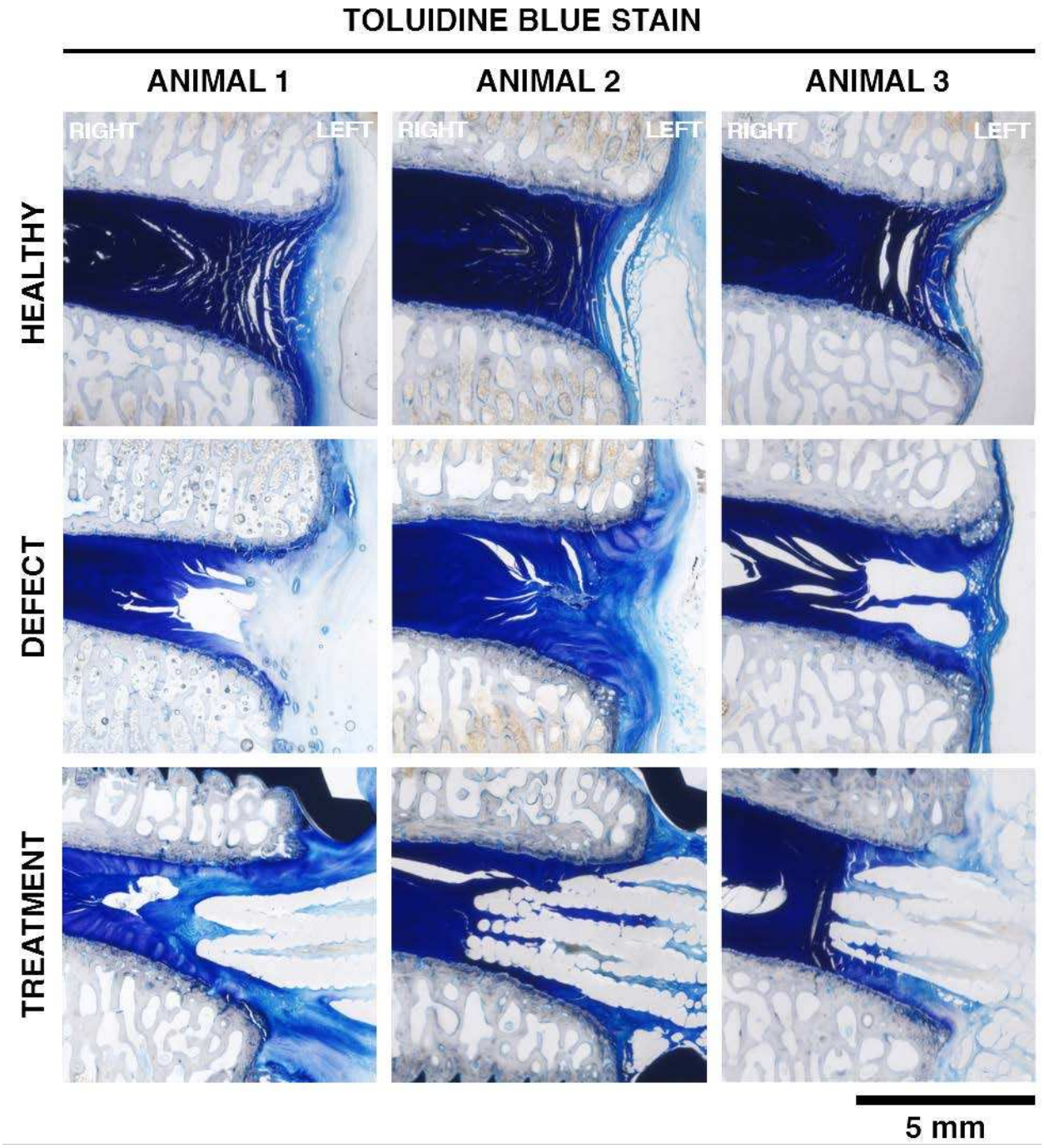

Figure 56. Histological sections of the left AF ROI stained with TBS. Shown are healthy, defect, and treated AF for all three animals in the study.

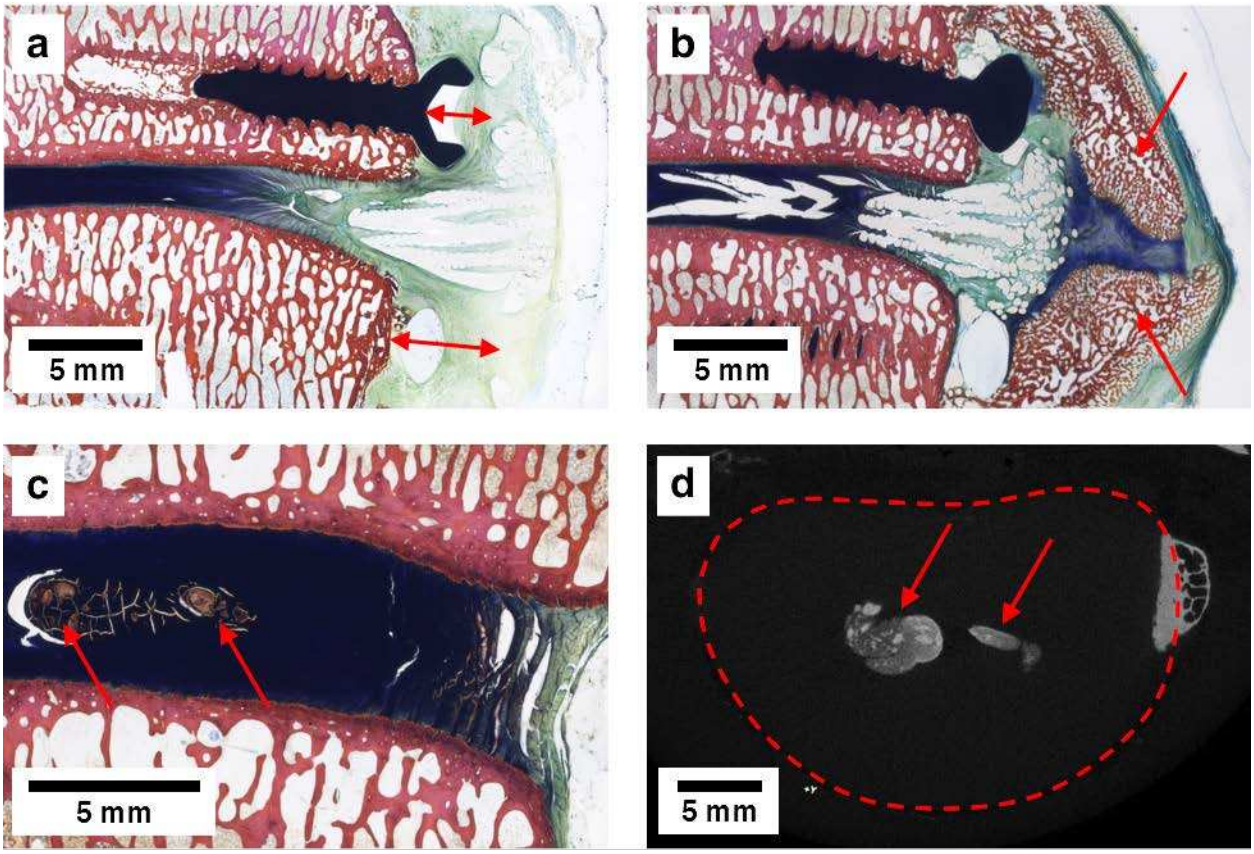

Figure 57. Notable features of the *in vivo* animal study: **(a)** histological image of the treated level of Animal 1 showing the displacement of the implant (red arrows); **(b)** histological image of the treated level of Animal 2 showing the calcified tissue growth (red arrows); **(c)** histological image of the untreated L5L6 disc of Animal 2 showing unidentified lesions in the NP (red arrows); and **(d)** micro-CT image of the untreated L5L6 disc of Animal 2 showing the unidentified lesions (red arrows) within the disc space (red dashed line).

From the histomorphometric measurements (Table 11 and Table 12), blue and green soft tissues were the dominant stains in the healthy AF ROIs (combined blue and green soft tissue area was ≥ 82.6% in all animals). Blue soft tissue area in the defect ROI of SRBS sections was lower than healthy range for all three animals and was similarly lower for Animals 1 and 3 in the TBS sections. In both TBS and SRBS sections, the corresponding AF contralateral to the defect had blue soft tissue area within the healthy range for Animal 2 and Animal 3, but was also lower than the healthy range in Animal 1. The treatment ROI also exhibited distinctly lower blue soft tissue

area than the corresponding healthy ranges in all three animals in both SRBS and TBS sections, and the respective contralateral AF were all similar to the healthy range. Both defect and treatment ROIs were above the healthy range of green soft tissue, and the defect consistently demonstrated a greater level of green soft tissue as compared to the treatment. All contralateral AF ROIs had green soft tissue stain similar to the healthy AF. In the healthy NP, blue soft tissue was the dominant stain (≥ 82.1% ROI area for all animals) for both SBRS and TBS sections. The NP in the defect levels exhibited areas of blue soft tissue similar to the healthy range for all animals. Blue soft tissue in the NP of the treated levels was slightly lower than healthy NP for Animal 3 in the SRBS section, yet was similar in the TBS sections and for the other animals. Small amounts of green soft tissue stain were observed in the healthy and defect-level NP (≤ 2.7% ROI area in all animals), although the treated levels had slightly higher green soft tissue in the NP for Animal 1 and Animal 3. Measured bone area (red stain) was no more than 0.5% in all of the disc ROIs.

Table 11. Summary of histomorphometric measurements for sections of all discs in the *in vivo* study stained with SRBS with VGCS. Measurements for the healthy conditions are presented as the range of all corresponding ROI in the healthy levels. All other measurements are from a single ROI. The healthy contralateral (CL) AF measurements are shown independently from the defect/treatment measurements. Blue soft tissue stain was indicative of proteoglycan-rich tissue and green soft tissue stain was indicative of fibrous tissue.

Animal	ROI	Condition	ROI area [mm^2]	Blue soft tissue area [%]	Green soft tissue area [%]	Bone area [%]	Implant area [%]
1	AF	Healthy	10.3 - 13.2	34.9 - 74.9	16.9 - 47.7	0.0 - 0.3	-
		Defect	10.9	23.7	69.4	0.0	-
		Defect (CL)	8.7	29.1	50.8	0.0	-
		Treatment	16.5	1.7	65.6	0.0	17.7
		Treatment (CL)	8.8	67.2	24.8	0.5	-
	NP	Healthy	20.0 - 61.7	82.1 - 94.5	0.0 - 2.7	0.0 - 0.1	-
		Defect	26.9	97.9	0.8	0.0	-
		Treatment	28.5	92.9	6.8	0.0	-
2	AF	Healthy	7.5 - 13.5	51.6 - 72.3	17.4 - 36.2	0.0 - 0.2	-
		Defect	18.3	28.3	69.0	0.2	-
		Defect (CL)	10.0	58.9	29.8	0.2	-
		Treatment	18.1	28.6	19.7	0.0	46.8
		Treatment (CL)	12.3	69.8	26.4	0.0	-
	NP	Healthy	36.0 - 64.4	97.0 - 99.8	0.2 - 2.2	0.0	-
		Defect	33.7	99.3	0.6	0.1	-
		Treatment	42.5	99.3	0.3	0.0	-
3	AF	Healthy	9.0 - 14.5	44.8 - 64.9	29.9 - 46.8	0.0 - 0.4	-
		Defect	14.2	25.1	56.5	0.1	-
		Defect (CL)	9.9	49.0	42.4	0.1	-
		Treatment	14.8	14.0	32.8	0.0	46.3
		Treatment (CL)	11.3	67.0	31.9	0.1	-
	NP	Healthy	35.4 - 71.1	85.7 - 100.0	0.0 - 1.6	0.0	-
		Defect	38.0	99.9	0.1	0.0	-
		Treatment	63.9	79.2	3.6	0.0	-

Table 12. Summary of histomorphometric measurements for sections of all discs in the *in vivo* study stained with TBS. Measurements for the healthy conditions are presented as the range of all corresponding ROI in the healthy levels. All other measurements are from a single ROI. The healthy contralateral AF measurements are shown independently from the defect/treatment measurements. Blue soft tissue stain was indicative of proteoglycan-rich tissue.

Animal	ROI	Condition	ROI area [mm^2]	Soft tissue (blue) area [%]	Implant area [%]
1	AF	Healthy	11.3 - 58.9	90.4 - 92.2	-
		Defect	46.8	37.6	-
		Defect (contralateral)	34.3	77.7	-
		Treatment	67.5	63.7	19.7
		Treatment (contralateral)	37.5	89.1	-
	NP	Healthy	95.0 - 222.0	94.2 - 94.3	-
		Defect	99.1	92.1	-
		Treatment	109.8	99.3	-
2	AF	Healthy	10.9 - 42.1	83.0 - 98.0	-
		Defect	64.5	94.3	-
		Defect (contralateral)	35.7	92.7	-
		Treatment	17.4	37.5	55.1
		Treatment (contralateral)	10.5	93.0	-
	NP	Healthy	41.6 - 236.2	97.8 - 100.0	-
		Defect	140.6	100.0	-
		Treatment	43.1	97.6	-
3	AF	Healthy	9.3 - 15.9	83.3 - 94.0	-
		Defect	15.0	66.2	-
		Defect (contralateral)	7.4	87.9	-
		Treatment	16.8	40.8	43.8
		Treatment (contralateral)	12.7	90.9	-
	NP	Healthy	45.3 - 74.8	83.3 - 100.0	
		Defect	42.7	83.4	-
		Treatment	64.5	91.5	-

4.1.4. Discussion

In this study, an implant for repair of the annulus fibrosus (AF) was designed, translated to an ovine model, and fabricated using a novel tissue engineering scaffold architecture. A surgical approach for the AF repair strategy was developed using cadaveric ovine lumbar spines and the *ex vivo* biomechanics of healthy, injured, and treated lumbar spines (L4L5) were evaluated. A preliminary *in vivo* study of the AF repair strategy was then conducted in an ovine lumbar spine model. Biomechanical testing, radiographic imaging, micro-CT analyses, and histological evaluation was performed on three lumbar spines 12 weeks post-implantation.

4.1.4.1. Implant design and fabrication

Overall, the fabricated implants effectively reproduced the designed 3DF architecture and the MEW sheets were visible within the 3DF layers. Further, microscopic imaging of samples of hybrid scaffolds has demonstrated that the MEW fibers are retained in the scaffold (Section 3.1). The 3DF scaffold architecture used for the implants was identified in previous work to reproduce the pertinent mechanical properties of AF. Manual inspection of implant fabricated with a hybrid architecture found that the interlamellar bonding between 3DF layers was not noticeably disrupted by the MEW sheets. Accordingly, the assumption that the 3DF scaffold has similar mechanical properties between pure 3DF and hybrid scaffolds appeared valid. In the hybrid scaffold, it was assumed that this 3DF architecture dominated the scaffold mechanics and the contribution of the MEW sheets was negligible. However, preliminary work using a finite element model of 3DF and hybrid scaffold has indicated that the mechanical contribution of the MEW layers may not be negligible (up to 18% increase in scaffold stiffness for one combination of biaxial strains; Appendix D).

Fiber diameters that were measured from the 3DF and MEW processes found that both were smaller than expected (Section 3.1). In particular, the 3DF fibers were appreciably smaller than in the experimental work which validated the mechanics of the 3DF architecture (Section 2.1). As a result, the biaxial mechanics of the fabricated implant may not have exactly matched the designed mechanics. Computational work on the biaxial mechanics of angle-ply laminate scaffolds has shown that a smaller fiber diameter increases the overall scaffold compliance and increases the asymmetry of the biaxial stiffnesses (i.e. axial-to-circumferential biaxial stiffness ratio; Section 2.2). Further computational modelling has predicted that increased implant compliance may be beneficial for delivering mechanoregulatory stimulus to resident cells (Section 3.2). Additionally, the increased implant compliance due to the smaller fibers may be counteracted by the increased implant stiffness due to the addition of the MEW sheets. Further experimental testing may be of interest to elucidate the influence of the MEW sheets on the biaxial mechanics of the hybrid scaffolds.

4.1.4.2. Ex vivo ovine model

The biomechanical data for the healthy ovine L4L5 FSUs was consistent with previously reported values[130,131]. The larger observed noise in axial rotation loading can be attributed to the greater overall FSU stiffness and, therefore, lower signal-to-noise ratio in the measured rotation data as compared to flexion-extension and lateral bending. Overall, the *ex vivo* biomechanics demonstrated that the AF repair implant was generally effective at maintaining the healthy biomechanics of the FSU. Notably, in every instance in the study where the defect group had significantly different biomechanics to the healthy spines, the treated group more closely approximated the intact biomechanics as compared to the corresponding defect group. For example, although the mean lateral bending ROM of the treated group was significantly different

to the healthy spines (9.7% increase in ROM as compared to healthy), it was an improvement as compared to the mean of the defect group (28.6% increase in ROM as compared to healthy).

The greatest magnitude of change in any mean biomechanical measure of the defect group as compared to the healthy state was 45.3%, 58.6%, and 33.5% in flexion-extension, lateral bending, and axial rotation, respectively (all were the NZS). Similarly, the treated group exhibited changes of 14.1%, 22.1%, and 27.5% in flexion-extension, lateral bending, and axial rotation, respectively, as compared to the healthy state (the EZS_2, NZS, and NZS, respectively). These results suggest that all three loading modalities were important considerations for assessing the biomechanical influence of the defect and treatment. In particular, lateral bending may have demonstrated the greatest biomechanical change in the defect group because the removed annular tissue was furthest from the neutral axis of bending and, accordingly, has the greatest impact on the areal moment of inertia of the disc. For the treated spines, axial rotation may have demonstrated the largest magnitude change in biomechanics because the implant failed to restore the circumferential continuity of the AF, resulting in a lower effective polar moment of inertia of the disc as compared to the intact AF.

Across all three loading modes, the ROM and NZS were the biomechanical measures most influenced by the defect and treatment; the defect group generated mean changes to the ROM and NZS that were significantly different to the intact group in all three loading modes. No significant changes in the mean NZ and mean EZS_1 (i.e. extension, left lateral bending, and left axial rotation) were observed between the intact, defect, and treated groups in all loading modes. Further, as compared to the healthy spines, the only significant difference in the mean EZS_2 (i.e. flexion, right lateral bending, and right axial rotation) to the any other study group was the defect group in right lateral bending. Accordingly, the results suggest that the ROM and NZS may be the most pertinent

of the considered biomechanical measures for AF repair. From a mechanistic perspective, the changes in ROM and NZS could be explained by the discontinuity of the structural fibers that was induced by the defect, and not recovered by the treatment. Recruitment of these structural fibers (e.g., collagen) has be demonstrated to be a critical factor for FSU biomechanics[218]. Moreover, the AF implant was designed to replicate the elastic zone mechanical properties of the AF and, therefore, may not be able to reconcile the neutral zone behavior of the AF. This latter mechanical response is dictated by the toe-region of the nonlinear AF elasticity profile.

Although some of the biomechanical differences between the healthy and treated groups demonstrated statistically significant differences, it remains unclear whether these changes are practically relevant at the acute time point of the repair strategy (e.g., does a 22.1% reduction in the lateral bending NZS have a noticeable effect on the function of the spine?). To provide context to the biomechanical changes observed in this study, models of IVD conditions with known functional alterations to the spinal biomechanics may be considered, such as spinal fusion and disc degeneration. As compared to the healthy spines in this study, a previous study of spinal fusion in ovine lumbar FSUs demonstrated reductions in the NZ of over 90%[217], which is considerably larger than any changes observed in the treated groups. In the same study, the ROM was found to increase and FSU stiffness was found to decrease due to spinal fusion, although there were no marked differences in this mechanical parameter to the current study. Another study investigated the influence of disc degeneration of the biomechanics of ovine lumbar spines and demonstrated decreases in ROM of over 60% in flexion-extension and lateral bending[219], which is also appreciably greater than any changes observed in the treated groups. Accordingly, the biomechanical changes induced by the AF repair strategy at the acute time point may not have a substantial impact on spine function, although further investigation may be beneficial.

4.1.4.3. In vivo ovine model

In the *in vivo* ovine lumbar spine model, no clear changes in disc height or morphology of any disc level were observed between the 0-week and 12-week radiographs. Loss of disc height is a hallmark of degenerative disc disease[75] and, accordingly, would be a clear indicator if any of the interventions in the study led to major degenerative alteration of the disc. Measurement of the disc height via radiographs may have been limited by image resolution and orientation, and alternative techniques, such as micro-CT or magnetic resonance imaging (MRI) may be able to enhance the precision of disc height measurements in future studies. The PCL scaffolds were not observable in plain radiographs and micro-CT and the scaffolds were only observed via visual inspection and histological sectioning. Contrast agents could be utilized to improve visualization of the implant in *ex vivo* imaging, however, the implant may be challenging to capture with *in vivo* diagnostic imaging techniques. As a result, it may be difficult to assess the position and condition of the implant post-operatively and throughout the duration of healing. For example, the implant in this study that detached from the screws was not identified until *ex vivo* dissection of the spine was performed. Adding radiopaque markers, such as thin wire, to the implant or using magnetic resonance imaging may be considered in future studies to better image the implant *in vivo*.

The *in vivo* biomechanical data were generally consistent with the *ex vivo* study group; the influence of the defect and implant was typically the same in both models. The greatest changes in biomechanics due to the defect appeared to occur in the axial rotation loading modality and in the ROM and NZS measures for all loading modalities. However, a larger study group with greater statistical power would be necessary to explicate the validity of the trends in the preliminary *in vivo* data. Animal 2 exhibited numerous biomechanical measurements that deviated from the *ex vivo* study group and the other study animals. In the treated levels, this was consistent with the

large calcified tissue mass observed at the treatment site (Figure 57) and in the healthy and defect levels. The disparate biomechanics of Animal 2 may be attributed to the defects observed in healthy discs in micro-CT and histological images (Figure 57). The biomechanical data from the *in vivo* study exhibited a notably larger variation as compared to the *ex vivo* study, which can be primarily attributed to: (1) greater inconsistency of the surgical approach in the *in vivo* setting as compared the *ex vivo* setting; and (2) temporal changes during the *in vivo* study. For example, the FSU biomechanics likely changed during the 12-week healing period due to the observed tissue responses and/or implant failure. The implant design was also slightly different between the *ex vivo* and *in vivo* models (increased screws spacing in the *in vivo* model), and it is possible that this lead to an alteration of the treated FSU biomechanics. Additionally, biomechanical data from the *in vivo* study was generated from different lumbar spinal levels, which may have a greater population variance in the biomechanical measures. Lastly, it was also possible that the sham and treatment conditions induced adjacent level effects, however, this was not indicated by any radiographic, micro-CT, or histological results.

Histological imaging of the healthy ovine IVDs clearly demonstrated the soft tissue composition and structure of the AF and NP. Sections stained with SRBS demonstrated a transition from intense and homogenous blue stain in the NP to green stain with a distinct lamellar organization in the outer AF, consistent with the well-known gradient from proteoglycan rich NP to the more organized collagenous outer AF.[28] In the histomorphometric analyses, the categorization of this gradient between green and blue soft tissue regions may have represented an arbitrary threshold of the two tissues (i.e. tissues stained with a blue-green color were classified as either blue or green). However, the same tissue classifications were used for all analyses and, therefore, the relative changes in proteoglycan and fibrous ECM composition were consistent in

the study. Similar to SRBS sections, the TBS sections demonstrated a gradient from the strong proteoglycan staining in the NP to a lesser intensity in the outer AF. Some voids were observed in the histological sections and were most likely attributable to histological processing. The AF defects did not demonstrate the structure or composition of healthy AF at the 12-week time point. Because symptomatic reherniation of the IVD is believed to be caused loss of mechanical function of the AF[21,80], the AF defects exemplified a healing response that would lead to high risk of reherniation. The treated AF also did not exhibit the structure or composition of the healthy AF and was shown to largely be composed of the implant. Although the treated AF did not present any major adverse tissue response as compared to the defect at the 12-week time point, the presence of the implant within the AF may provide an opportunity for long-term reconciliation of the structure and composition of healthy AF.

Bone formation within the disc space was of interest in this study due to the propensity for osteogenesis or osteophyte formation in the spine when the spinal biomechanics are altered. For example, fixation of the disc space is commonly used to generate bony growth in spinal fusion[89,217] and degenerative changes to the IVD are frequently associated with bony growth (e.g., osteophyte formation leading to spinal stenosis).[220] Accordingly, successful treatment for regeneration of the AF would inherently involve no bone formation in the disc space. The largest bone volume measured by the micro-CT analyses was 2.04% (the left side of L5L6 disc in Animal 2); all other bone volumes were less than 1.0%. Further, imaging artefacts were observed in the scans which may have confounded measures of bone volume, particularly at the treated level which had artefact due to the metal screws used in the surgery. It is possible that the surgical intervention resulted in inflammation or degenerative sequelae in the spine that produced a small amount of adverse bone formation. However, overall, there was no clear evidence from the micro-CT results that indicated

appreciable bone formation within any disc space in the study. This conclusion was further supported by the radiographic images, which did not indicate any observable increase in the density of the tissue in the disc space, and the histological results. However, micro-CT and histological results identified adverse tissue responses outside of the IVD. In particular, one animal developed an appreciable mass of calcified tissue around the implant with a small region of soft tissue in the plane of the IVD that had the appearance of a pseudoarthrosis (Figure 57b). It is possible that this tissue formation was associated with the screw injury, an inflammatory response to the implant, or an underlying pathology (because other abnormalities were observed in the healthy levels of the same animal). However, there is insufficient evidence in the results of this study to determine the cause of the bony growth. Regardless of the composition or cause of this tissue growth, it would be expected to have severely deleterious consequences with respect to long-term regeneration of the AF.

4.1.4.4. Limitations

The primary limitation of this study to investigate the repair of AF herniation was the translatability of the large animal model to human application. Results from the ovine model may not reflect the physiological or biomechanical changes in a human condition[127,128,130,131]. In particular, the disparity between the disc height in human and ovine lumbar spines would be expected to lead to appreciable differences in the size of the AF repair implant, which could have a substantial effect on spinal biomechanics and tissue regeneration. Further, due to limited surgical access of the posterior disc in the ovine model and animal welfare considerations, the implant was placed at the lateral aspect of the IVD. However, disc herniation most frequently occurs near the posterolateral aspect of the IVD in humans[82]. The variation in implant location may have associated biomechanical effects and a laminectomy may also be required to reach the surgical

site, further limiting the predictive power of this animal model. Nonetheless, large animal studies such as this are extensively utilized to provide initial validation of treatment efficacy and to establish a basis for clinical trials and regulatory approval of novel orthopaedic treatments. Incremental changes to this animal model will be beneficial to improve predicative validity for the human condition.

Both the *ex vivo* and *in vivo* animal models of the AF repair strategy also had inherent limitations. First, the *ex vivo* model only provided spinal biomechanics that represented the acute time point. Although the acute phase of the treatment may be critical for biomechanical function of the spine, the *ex vivo* model did not characterize how temporal changes in tissue formation and implant degeneration may alter these mechanics throughout the course of the treatment. Also, the *ex vivo* model simulated the treatment under idealized surgical conditions, and the precision of implanting the construct may be more limited in a true surgical setting. The *in vivo* model was able to characterize the spinal biomechanics at a prescribed time point after the surgery, however, this model was limited because it was not possible to compare healthy, injured, and treated conditions of each specific FSU. These comparisons were limited to other lumbar levels form the same animal or different animals. In this preliminary *in vivo* study, only three animals were investigated and equivalent comparisons could not be drawn across different lumbar levels or between different animals. As a result, only basic comparisons of the biomechanical measures could be made. A larger study group and careful study design will be needed to provide sufficient statistical power to extract meaningful correlations in future *in vivo* work. Lastly, in both the *ex vivo* and *in vivo* models, the treatment was compared to an idealized defect in the AF of an otherwise healthy IVD. This defect was used to represent a partial discectomy to remove a herniated section of the IVD[221].

However, the idealized defect may not accurately mimic this discectomy intervention or other degenerative features in the IVD that are typically associated with IVD herniation[75].

4.1.4.5. Implications for future work

The presented *in vivo* animal study served as a preliminary assessment of the efficacy of the AF repair strategy. In future studies, modifications to the implant design and implementation may be considered based on these initial findings. Modifications to the implant may address the observed extrusion of the implant from the disc space, perhaps by enhancing the durability of the implant or revising the surgical attachment approach. Specific examples of methods to improve the implant durability include: (1) reinforcing the implant at the screw holes to prevent detachment from the screws, and (2) adoption of alternative materials to increase the yield stress and/or fatigue resistance of the scaffold fibers. Supplemental methods to improve the implant attachment may include sutures to the adjacent disc tissue, or bioadhesives between mating surfaces of the implant and the spine. Implant attachment may also be revised because the observed calcified tissue growth near the treatment site may have been associated with the implant screws. Any alternative implant attachment methods should aim to maintain the position of the implant in the disc without eliciting deleterious tissue formation during healing. To enhance the regenerative potential of the implant, bioactive factors could be added to the scaffold, such as growth factors, exosomes, or autologous cells. However, as compared to the acellular scaffold in this study, scaffolds with supplemental cells of biomolecules may be complicated by challenges associated with implant fabrication and sterilization. Due to the diverse range of possible modifications to the implant and surgical attachment, computational models could be leveraged to identify design adjustments that offer the greatest potential for improved AF repair outcomes.

Following any design modifications, a larger study group will be necessary to provide sufficient statistical power to support the preliminary findings and extract further correlations in the data. Future study designs should consider controlling for the biomechanical effect of spinal level by deliberately varying the assignment of the treatment and sham levels. Refining the surgical approach to improve the consistency of the treatments may also be afforded with more developed protocols and surgical guides. More advanced animal studies may be undertaken by implementing the repair strategy on degenerative spines to assess the repair strategy in a more clinically-relevant model. A degenerative model could also be coupled with a NP repressurization strategy to afford a more holistic scheme for repair of IVD hernia. Lastly, to address the disparity in disc size between ovine and human lumbar spines, an alternative animal model with greater disc height could be considered in future studies, such as a porcine model[222].

4.1.5. Conclusions

Overall, this study demonstrated the design, fabrication, and implementation of a novel AF repair patch in a large animal model. A hybrid implant architecture with polymer fiber diameters of multiple length scales was successfully manufactured. A surgical implantation technique was developed on cadaveric ovine lumbar spines and subsequent biomechanical testing demonstrated functional efficacy of the implant. An *in vivo* ovine model of the AF repair strategy was conducted and also demonstrated biomechanical efficacy of the implant 12 weeks post-treatment. However, of the three animals in this study, one exhibited failure of the implant at the screw attachment and one exhibited appreciable adverse tissue formation. These preliminary data serve as a foundation for future development and validation of the AF repair strategy. Ultimately, the developed approach to AF repair holds the potential for a revolutionary method to alleviate pain associated

with IVD herniation while maintaining the long-term biomechanical function of the spine and preventing symptomatic reherniation.

4.2. Computational Approach

4.2.1. Introduction

In this study, the biomechanical influence of an AF repair patch strategy was predicted using a human lumbar spine finite element model previously developed by our group[162]. This computational model of the human lumbar spine served as an analogue to a complimentary experimental series using ovine lumbar spines and also provides a perspective for clinical translation of the ovine model. The computational model was also used to predict the mechanical state within the implant under physiological spinal loading. The corresponding regenerative potential of the implant under physiological loading was then assessed based on a previously developed micromechanical model (Section 3.2). The results of this study can be leveraged to drive AF repair strategies that consolidate both the organ-level biomechanics and cell-level micromechanics for enhanced AF regeneration

4.2.2. Methods

This FE study was conducted using the commercial FE package Abaqus (Dassault Systèmes SIMULIA, Johnston, RI). All work in this study utilized an FE model of a human lumbar function spine unit (FSU) that was isolated from an existing FE model of the lumbar spine which was developed and validated by our group[162]. Unless otherwise specified, the geometry, mesh, and materials of the FSU were not altered from the existing model. The following sections describe: (1) the methods for generating and assembling parts for the FE geometry; (2) the meshing technique for the implants; (3) the material model for the implants; (4) the constraints and boundary conditions imposed on the implants; (5) analyses of the predicted FE results; and (6) the parametric studies considered in this investigation.

4.2.2.1. Geometry and Assembly

The reduced FSU contained two whole vertebrae (fourth and fifth lumbar levels; L4L5), the intervertebral disc, and associated ligaments. As shown in Figure 58, four geometric conditions of the FSU model were considered in this study: (1) the whole, intact FSU; (2) the FSU with a partial discectomy to represent the removal of a diseased section of disc; (3) the FSU with a partial discectomy and treated with a novel annular repair implant (plated implant); and (4) the FSU with a discectomy and treated with a simple annular plug (plug implant). The partial discectomy was created by deleting the full radial thickness of annulus elements at the left posterolateral aspect of the annulus. The two treatment geometries were created in Solidworks (2016 SP4.0, Dassault Systèmes, Vélizy-Villacoublay, France) to exactly conform to the partial discectomy and spinal geometry. The implant geometry was created based on a previously-developed design that was implemented in an *ex vivo* ovine model (Section 4.1). Specifically, the plated implant consisted of an insert to fill the annular defect ('insert') combined with an external plate ('plate') to facilitate surgical attachment of the implant (Figure 58). The plug implant consisted only of the insert section (i.e., matched the removed annular geometry).

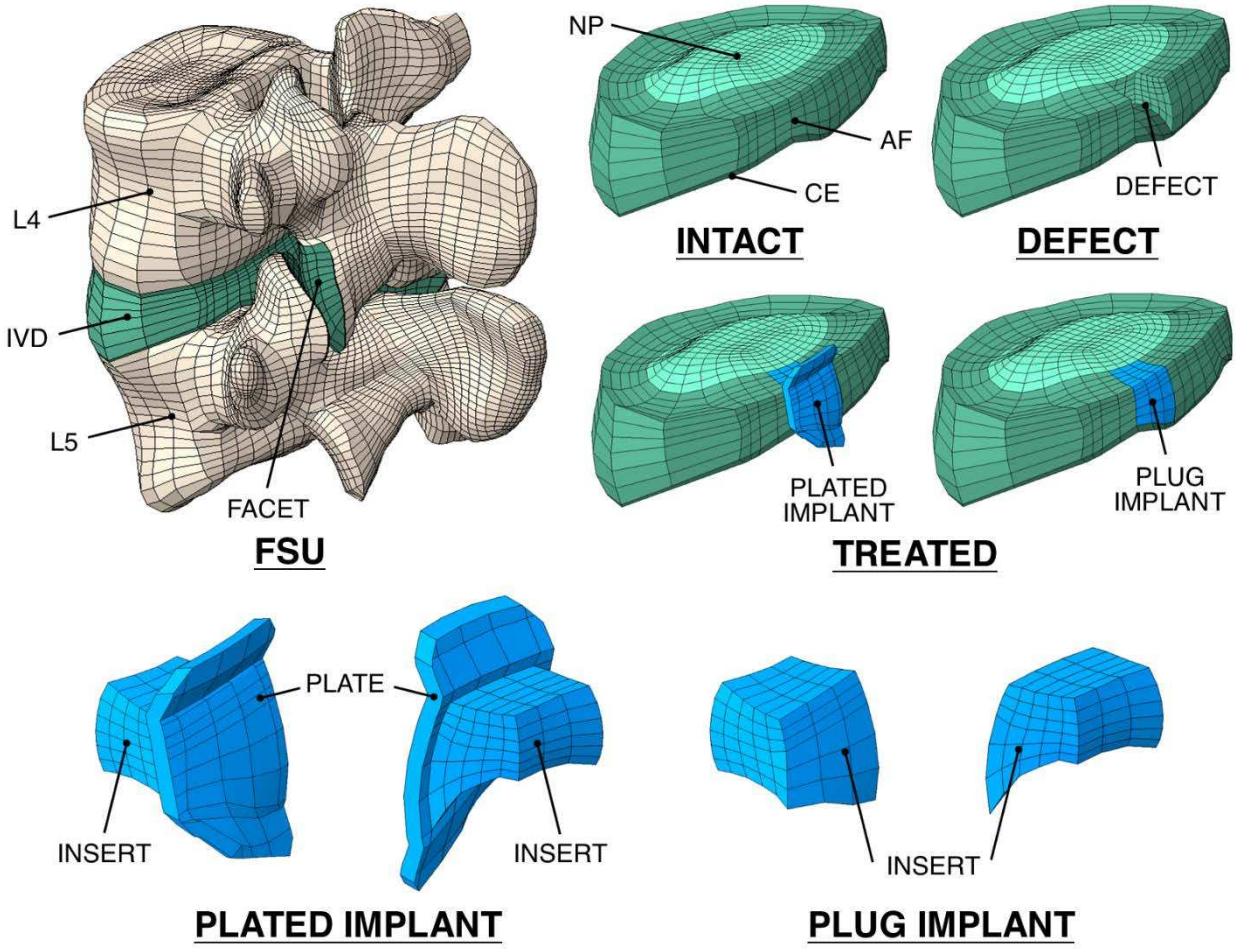

Figure 58. Finite element model showing the human lumbar FSU, the IVD in four conditions (intact, defect, treated with a plated implant, and treated with a plug implant), and detailed views of the two implants. Major aspects of the model are labelled (FSU = functional spinal unit; L4 = fourth lumbar level; L5 = fifth lumbar level; IVD = intervertebral disc; NP = nucleus pulposus; AF = annulus fibrosus; CE = cartilaginous endplate).

4.2.2.2. Mesh

The implant geometry was meshed using quadratic tetrahedral elements (C3D10) with a constant nodal seed size. A mesh convergence analysis was conducted by loading the spine in flexion with the implant assumed to be perfectly bonded to all mating surfaces of the spine. An appropriate seed size was selected based on convergence of the strain energy in the implant and computational time. The selected mesh size was also used for analysis with the plug geometry.

4.2.2.3. Materials

The implant and plug were both prescribed orthotropic, continuum material properties (Table 13). Specifically, the material properties were based on a previous FE model of an angle-ply fiber laminate architecture that has been shown to approximate the healthy mechanics of AF tissue (Section 2.2, Appendix D).

Table 13. Orthotropic material parameters as derived from FE predictions of angle-ply laminate scaffolds and material stiffness matrix components used in the ABAQUS orthotropic material definition. The material coordinates 1, 2, and 3, correspond to the axial, circumferential, and radial directions of the AF, respectively.

Orthotropic Material Parameters								
E_{11} (MPa)	E_{22} (MPa)	E_{33} (MPa)	G_{12} (MPa)	G_{31} (MPa)	G_{23} (MPa)	ν_{12}	ν_{31}	ν_{23}
3.72	15.4	43.2	1.70	2.97	1.98	0.357	0.305	0.109
ABAQUS Material Parameters								
D_{1111} (MPa)	D_{3333} (MPa)	D_{2222} (MPa)	D_{1133} (MPa)	D_{1122} (MPa)	D_{2233} (MPa)	D_{1313} (MPa)	D_{1212} (MPa)	D_{2323} (MPa)
8.84	50.1	37.6	6.92	13.8	15.7	2.97	3.73	2.95

4.2.2.4. Constraints, Boundary Conditions, and Loads

All three spine conditions (intact, discectomy, and treated) were prescribed loading in three steps. First, the NP was pressurized to physiological levels via thermal expansion[162]. Second, a constant axial follower load (220 N in compression) was applied between the centroids of the vertebral bodies. The magnitude of the follower load was calculated in a preliminary study to

reproduce a physiological NP pressure (0.5 MPa[44,223]) in the intact spine in a standing posture. Third, moment loading (up to 7.5 Nm) was applied independently in six physiologically relevant rotations: spinal flexion, spinal extension, left lateral bending, right lateral bending, left axial rotation, and right axial rotation. Moment loading was applied at the cranial endplate of the L4 vertebral body and the caudal endplate of the L5 vertebral body was encastre (i.e., kinematically constrained). Overall, the FSU loading regime represented the three most physiological spinal motions (flexion-extension, lateral bending, and axial rotation) in a standing posture.

In the treated model, the plated implant was initially prescribed perfect (total) bonding on all mating faces between the implant and the spine by constraining the mating surfaces (Figure 59**Figure 60**). To evaluate the influence of implant attachment on the load state within the implant, numerous configurations of the implant attachment were also considered. These configurations defined the interaction between any mating surfaces as perfectly bonded, cohesive, or not bonded. Perfect bonding was defined with rigid surface constraints between the nodes on mating faces. Cohesive bonding was defined with a cohesive constraint between the two mating faces. In each attachment configuration, a hard contact constraint was imposed at all mating faces that were not prescribed perfect bonding. Specific details of the attachment configurations are described in the parametric studies (Section 4.2.2.6).

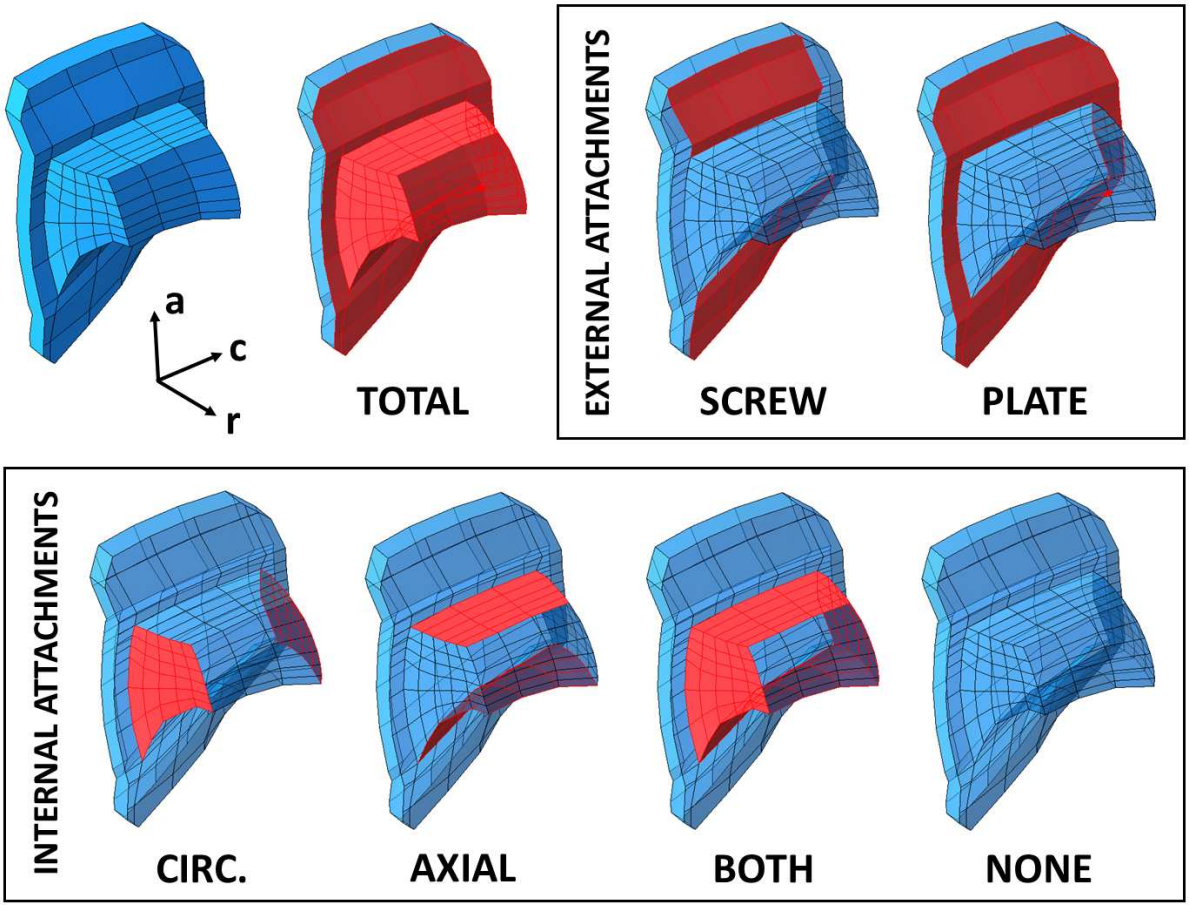

Figure 59. Summary of attachment conditions for the plated implant in the treated spine. Faces shown in red indicate that the face has an attachment condition to the adjacent surface of the spine. The 'total' attachment condition contained all implant surfaces that are adjacent to the spine surfaces. All other attachment conditions were a combination of two sets of faces, categorized as faces that attach to: (1) the external aspects of the spine and (2) faces that attach to the internal aspects of the spine. The coordinate directions are: a = axial, c = circumferential, and r = radial.

4.2.2.5. Analyses

Quantitative FSU biomechanics were evaluated from the moment-rotation data of the FSU to determine the range of motion (ROM), neutral zone (NZ), neutral zone stiffness (NZS), and elastic zone stiffnesses (EZS; EZS_P and EZS_N for the positive and negative elastic zones, respectively) as shown in Figure 60. The ROM was defined as the difference in angular position of the spine between -7.5 and +7.5 Nm of load. The NZ was defined as the angular rotation between

inflections of the moment-rotation curve (identified as local maxima and minima of the second derivative of the moment-rotation curve) and the neutral zone stiffness (NZS) was defined as the inverse gradient of a linear least squares fit to the NZ moment-rotation curve. The EZS_P (i.e., the elastic zone stiffnesses for flexion, left lateral bending, and left axial rotation) and EZS_N (i.e., the elastic zone stiffnesses for extension, right lateral bending, and right axial rotation) were defined as the final 30% of the moment-rotation curve (+5.25 to +7.5 Nm and –5.25 to -7.5 Nm for EZS_P and $EZSP_N$, respectively.

In addition to the FSU biomechanics, the load state within the AF, plated implant, or plug implant was evaluated for the intact condition and all treated conditions. This load state was determined from the average circumferential, axial, and radial element stresses and strains in a 3 x 3 x 3 mm region at the center of the corresponding geometry (i.e., the intact region of AF to be removed in the discectomy, the insert region of the implant, or the whole plug). To compare this load state to previous biomechanical measures of the AF and AF repair constructs, the circumferential and axial strains and the radial stress were used to characterize the load state.

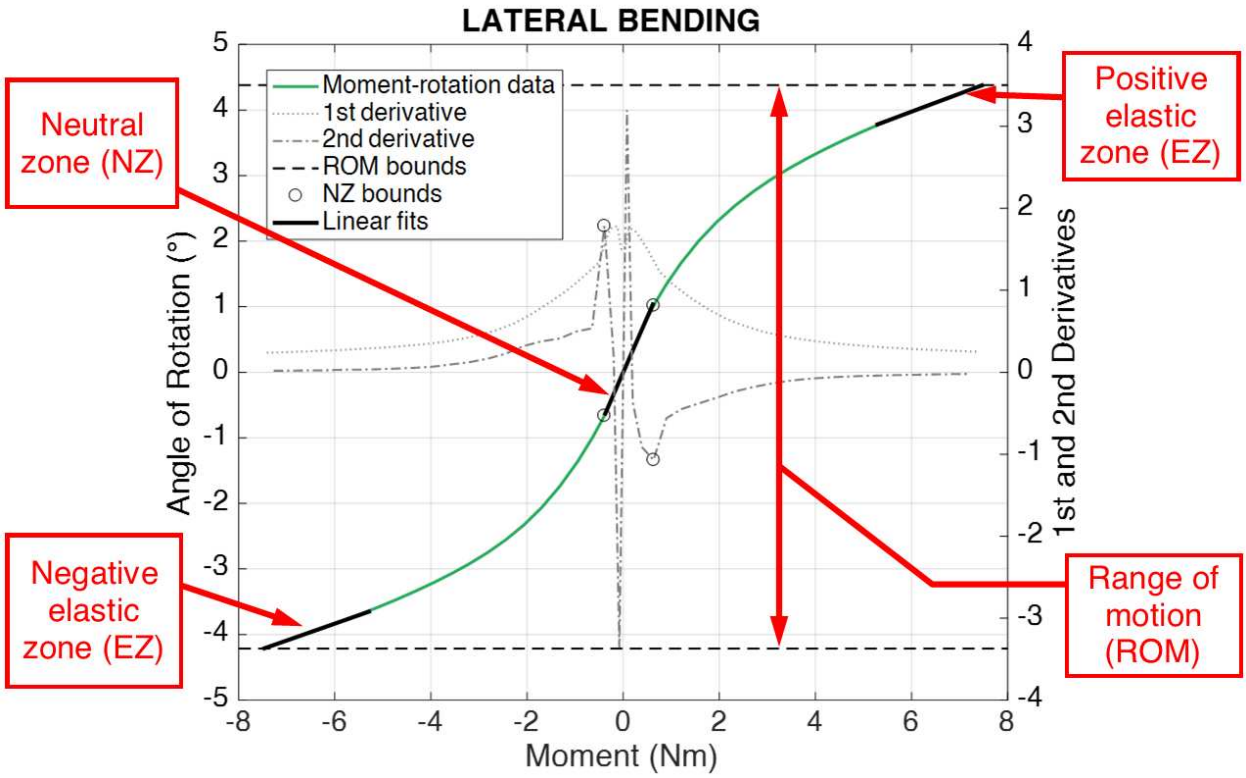

Figure 60. Representative example of the quantitative FSU biomechanical measures from moment-rotation data showing the range of motion (ROM), neutral zone (NZ), and elastic zones (EZs). The neutral zone limits (circles) are defined from local extrema in the second derivative of the moment-rotation curve (grey dashed line). The elastic zones are defined as the stiffness of the final 30% of the moment load in each direction. Linear least-squares fits (solid black lines) show the fits for the neutral zone stiffness (NZ) and elastic zone stiffnesses (EZs).

4.2.2.6. Parametric studies

A series of parametric studies were conducted to assess the influence of changes to the repair protocol, implant design, and implant attachment on the FSU biomechanics and ROI loading. First, the level of nucleus pressurization was varied to assess how loss of nucleus pressure may alter the efficacy of the repair treatment. This may represent loss of pressure due to degenerative changes to the IVD or surgical intervention. The totally-bonded implant was tested in all six loading modes with 50% and 90% of the normal thermal expansion. The follower load and moment loads were not changed from the base model.

Second, four alterations to the base implant model were considered: (1) replacement of the plated implant with the plug implant (2) reduction of the implant stiffness by one half, (3) increase of the implant stiffness by a factor of two, and (4) isotropic implant material properties (E = 21.4 MPa and $\nu = 0.31$ as the averages of the orthotropic stiffness coefficients). Each condition was loaded in all six rotational modes.

Third, various configurations of implant attachment were considered (Figure 59). Two modes of external attachment of the plate section of the implant were considered: (1) 'screw' to represent a rigid screw attachment of the implant plate to the vertebral bodies, and (2) 'ideal' to represent rigid attachment of all implant plate surfaces to the mating spine surfaces. Four modes of internal attachment of the insert section of the implant were considered; (1) no bonding of any faces, (2) perfect bonding of only the circumferential faces to the adjacent AF tissue, (3) perfect bonding of only the axial faces to the adjacent CE tissue, and (4) perfect bonding of both the axial and circumferential faces to the respective tissues. In addition to the total attachment condition, each combination of the two external attachment modes and four internal attachment modes were considered (eight additional attachment configurations) in all six rotational modes. To represent a more clinically-feasible attachment strategy, five further attachment configurations were considered using cohesive attachment conditions on the interior faces. A cohesive attachment may represent use of a bio-adhesive at the implant-spine interfaces. The stiffness of the cohesive bonds at the internal axial and circumferential faces of the implant was progressively varied using stiffnesses between 1 MPa and 10 GPa and the influence on the ROI loading was assessed. Cohesive analyses were only considered in flexion loading of the FSU.

Finally, to demonstrate how the results of this study could be leveraged to enhance tissue regeneration, the most advantageous implant design and attachment conditions were combined to

tailor the implant ROI load state. The results of a previous micromechanical model of regenerative potential was used as an example target set for the ROI load state (Section 3.2). Specifically, the target load states were: (1) biaxial tensile strain in the circumferential-axial direction and a simultaneous positive radial pressure, and (2) biaxial compressive strain in the circumferential-axial direction and a simultaneous negative radial pressure.

4.2.3. Results

4.2.3.1. Mesh refinement

For all meshes considered, the ROI strain energy was within 0.1% of the most refined mesh (48,333 nodes). The solution time monotonically increased as a function of the node count (Figure 61). The ROI strain energy appeared to show a smooth convergence to the final mesh beginning at 12704 nodes. Therefore, the corresponding solution (seed size of 0.7 mm) was selected for all subsequent analyses in this study.

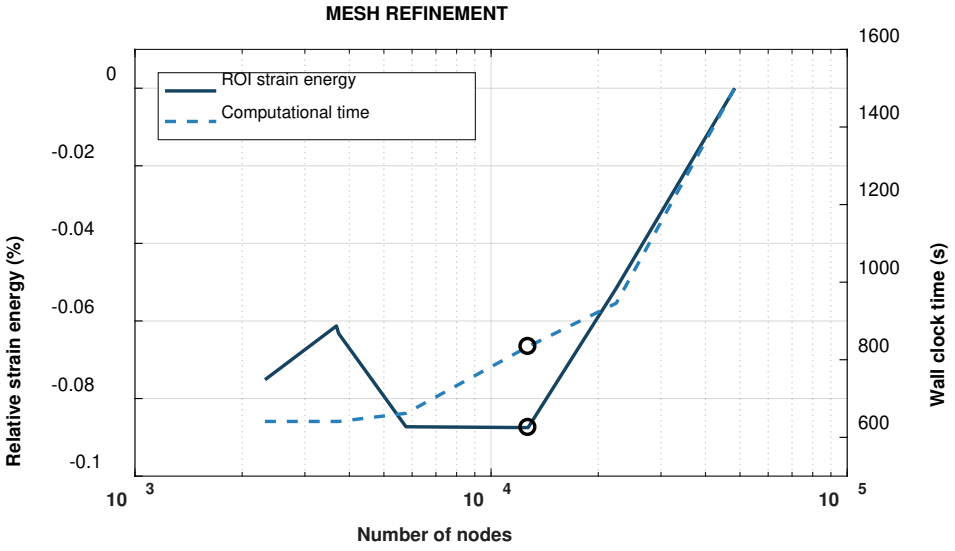

Figure 61. Mesh refinement for the implant in the lumbar FSU model in flexion. Two measures are shown as a function of the number of nodes in the implant: (1) the strain energy as a percent difference from the most refined mesh and (2) the wall clock time for each solution.

4.2.3.2. Spine condition: FSU biomechanics

For all spine conditions, the moment-rotation data exhibited an approximately sigmoidal moment-rotation curve (Figure 62). A sharp change in the moment-rotation curve was observed in extension, which coincided with the initialization of contact at both of the facet surfaces. In all three loading modes, the defect curve was generally similar in shape to the intact curve. However, the defect moment-rotation data demonstrated shifts relative to the intact condition (shifts of +2.4°, -0.4°, and -0.7° in flexion-extension, lateral bending, and axial rotaion, respectively). Quantitatively, the defect data had increaseed ROM as compared to the intact condition in flexion-extension and axial rotation, and a slightly reduced ROM in lateral bending. The NZ decreased prominently in all three loading modes as compared to the intact condition (decreases of 43.0%, 41.6%, and 21.0%, respectively). The NZS increased in flexion-extension and lateral bending (increases of 52.2% and 7.6%, respetively) and decreased by 50.4% in axial rotation. The defect generated a reduced EZS in all loading directions except the left axial rotaion (decreases ranged from 8.3% to 26.5%); in left axial rotaion the ESZ increased by 12.9%.

The treatment moment-rotation curve was generally similar to the intact condition in flexion-extension and axial rotaion. In lateral bending, the treatment moment-rotation curve was shifted by approximately -0.6° relative to the intact curve. Quantitatively, the treatment overcorrected the change in ROM induced by the defect in flexion-extension and axial rotation (overcorrections of 185% and 3%, respectively); in lateral bending the ROM further deviated from the intact condition, however, was still within 0.19° of the intact ROM. The treatment recovered 88% of the change in NZ induced by the defect in flexion-extension and overcorrected the NZ in lateral bending and axial rotation (overcorrections of 24% and 17%, respectively). The NZS was partially corrected in flexion-extension and axial rotaion (corrections of 25% and 74%,

respectively), although further exacerbated the change induced by the defect by 125% in lateral bending. In all loading modes, the change in EZS induced by the defect was partially corrected by the treatment (corrections ranging 19% to 96%).

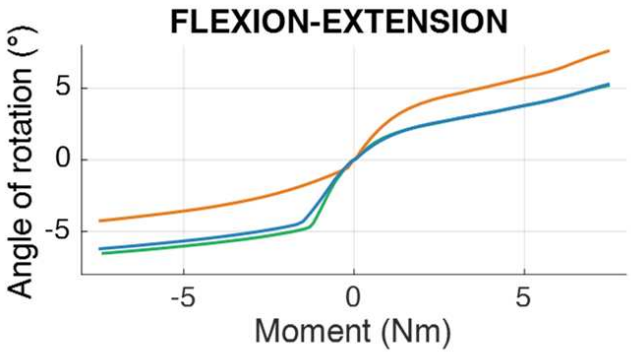

Condition	ROM [°]	NZ [°]	NZS [Nm/°]	EZS_P [Nm/°]	EZS_N [Nm/°]
Intact	11.76	3.09	0.23	1.66	4.86
Defect	11.89	1.76	0.35	1.22	3.66
Treated	11.52	2.94	0.32	1.58	4.59

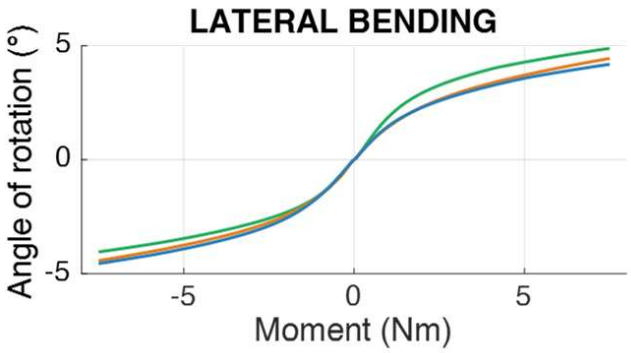

Condition	ROM [°]	NZ [°]	NZS [Nm/°]	EZS_P [Nm/°]	EZS_N [Nm/°]
Intact	8.93	2.43	0.53	4.20	4.40
Defect	8.87	1.42	0.57	3.50	3.73
Treated	8.74	2.67	0.62	4.17	3.99

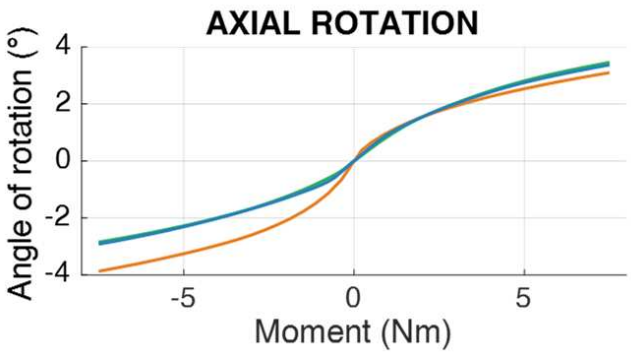

Condition	ROM [°]	NZ [°]	NZS [Nm/°]	EZS_P [Nm/°]	EZS_N [Nm/°]
Intact	6.31	1.43	1.15	4.02	4.48
Defect	6.97	1.13	0.57	4.54	4.11
Treated	6.29	1.48	1.00	4.11	4.18

Figure 62. Moment-rotation data and quantitative biomechanics for the L4L5 FSU in three conditions (intact in green, defect in orange, and treated in blue) and three loading modes (flexion-extension, lateral bending, and axial rotation). For each combination of condition and loading modality, the range of motion (ROM), neutral zone (NZ), neutral zone stiffness (NZS), positive elastic zone stiffness (EZS_P), and negative elastic zone stiffness (EZS_N) are reported.

4.2.3.3. Spine condition: AF and implant loading

The three-dimensional load state of the ROI in both the intact AF and the totally bonded implant were highly dependent on loading modality (Figure 63). In both cases, the relative strain magnitudes were larger in the axial direction as compared to the circumferential direction (ranges of -32.3% to +15.1% and -0.36% to +6.1%, respectively). The axial and circumferential strains demonstrated tension/compression anisotropy in all loading modes for the intact AF. However, for the implant, this trend was only observed in extension, left lateral bending, and right axial rotation. In the remaining three loadings modes (flexion, right lateral bending, and left axial rotation) the circumferential strains were within one standard deviation of zero. As compared to the intact AF, the implant ROI strains in the circumferential direction were consistently more positive (i.e., larger in tension and smaller in compression; average change of +2.5% strain) and were generally similar in the axial direction (average change of +1.8% strain). Most notably, the magnitude of radial stresses in the intact AF were considerably larger in the intact AF as compared to the implant (ranges of -85 to +293 kPa and -24 to +23 kPa, respectively), yet all of the radial stress directions were consistent.

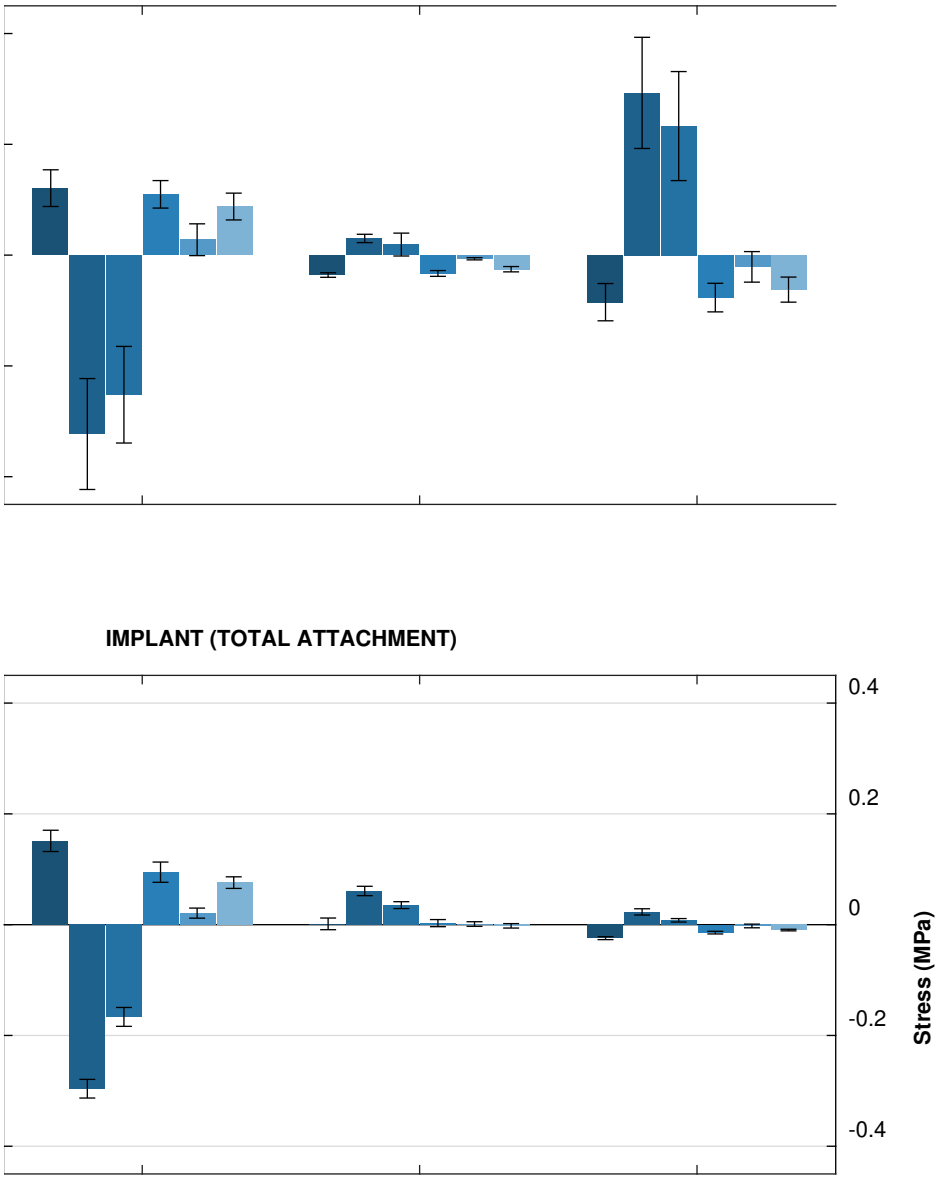

Figure 63. The mean three-dimensional load state within the intact AF and the implant ROI for the six spinal loading modalities. Strains are reported for the circumferential and axial directions and stresses are reported for the radial direction. Error bars indicate one standard deviation from the mean.

4.2.3.4. Spine condition: NP pressure

Reductions in nucleus pressure generated numerical instabilities in the model, which lead to three incomplete solutions (Figure 64). Specifically, the extension loading at 90% and 50% NP pressure demonstrated excessive deformation of the AF elements at the right foramen., resulting in numerical instability. At 50% NP pressure, left lateral bending loading failed to produce a complete solution due to excessive deformation of the AF elements at the left foramen on the lateral side of the implant, which was not directly adjacent to the implant. Despite these incomplete solutions, some quantitative biomechanical measures were observed as a function of the NP pressure. Notably, the NZ dramatically increased in flexion-extension and decreased in lateral bending and axial rotation (changes of +53.7%, -81.6%, and –6.5%, respectively, for the 50% pressure relative to the full pressure). Only minor changes to the NZS were observed in flexion-extension and lateral bending, although at 50% pressure the NZS decreased by 43.3% as compared the full pressure model in axial rotation. Only minor changes to the elastic zone stiffnesses were observed (maximum absolute change of 13.0% relative to the full NP pressure). No comparisons of the flexion-extension ROM were available for the reduced pressure models. However, the ROM was found to increase by 3.5% at 90% NP pressure in lateral bending and decrease by 19.9% at 50% pressure in axial rotation.

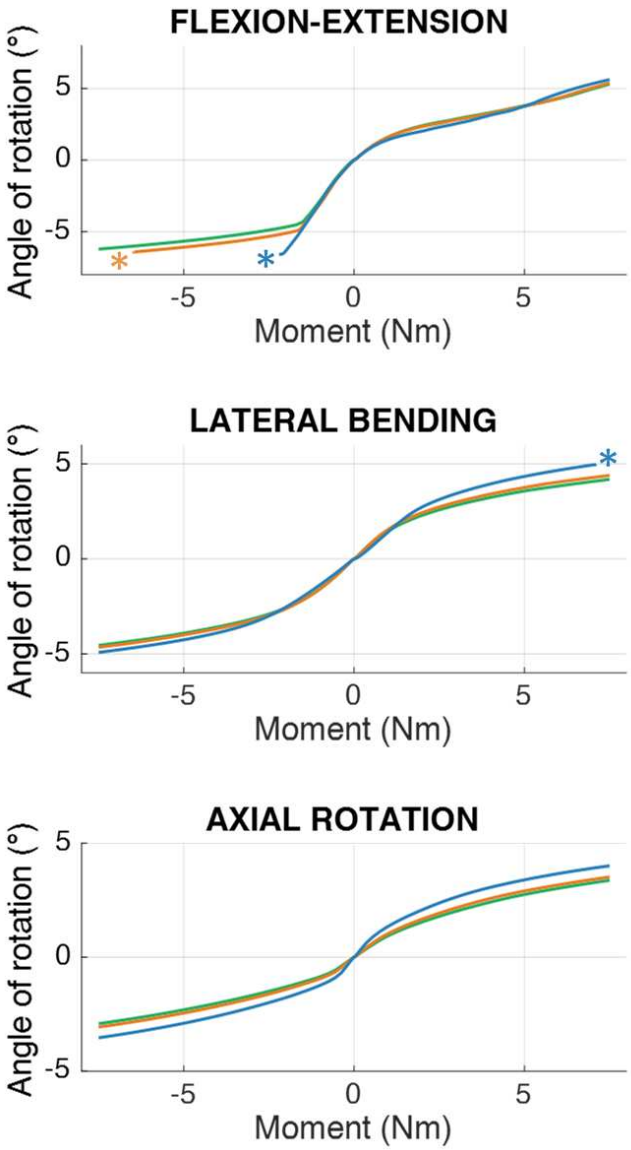

Condition	ROM [°]	NZ [°]	NZS [Nm/°]	EZS_P [Nm/°]	EZS_N [Nm/°]
100%	11.52	2.94	0.32	1.58	4.59
90%	-	3.46	0.31	1.46	-
50%	-	4.52	0.29	1.37	-

** Failure due to excessive deformation of the AF at the right foramen

Condition	ROM [°]	NZ [°]	NZS [Nm/°]	EZS_P [Nm/°]	EZS_N [Nm/°]
100%	8.74	2.67	0.62	4.17	3.99
90%	9.05	2.73	0.61	4.10	3.92
50%	-	0.49	0.65	-	3.85

* Failure due to excessive deformation of the AF at the left foramen, on the lateral side of the implant

Condition	ROM [°]	NZ [°]	NZS [Nm/°]	EZS_P [Nm/°]	EZS_N [Nm/°]
100%	6.29	1.48	1.00	4.11	4.18
90%	6.58	1.49	0.88	4.15	4.15
50%	7.54	1.38	0.57	4.16	4.00

Figure 64. Moment-rotation data and quantitative biomechanics for the L4L5 FSU for three levels of NP pressure and three loading modes (flexion-extension, lateral bending, and axial rotation). For each combination of NP pressure and loading modality that a solution was obtained, the range of motion (ROM), neutral zone (NZ), neutral zone stiffness (NZS), positive elastic zone stiffness (EZS_P), and negative elastic zone stiffness (EZS_N) are reported.

The ROI load state in flexion loading showed a minor dependence on the NP pressure (Figure 65). With reduced radial pressure, the mean axial and circumferential strains increased and

decreased, respectively (at 50% NP pressure the strain magnitudes changed by +4.1% and –1.6%, respectively). No appreciable change was observed in the radial pressure.

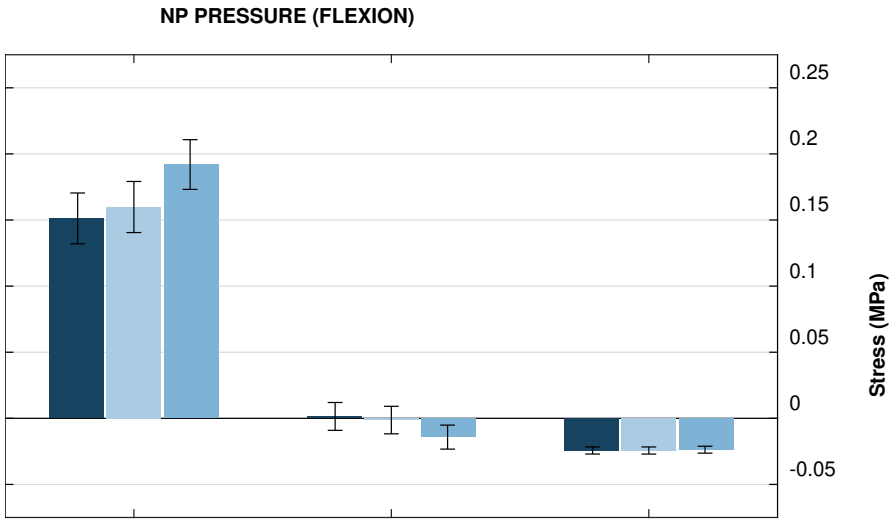

Figure 65. The mean three-dimensional load state within the implant ROI for three NP pressures (P_{NP}) in flexion loading. Error bars indicate one standard deviation from the mean.

4.2.3.5. Implant design

The implant design had an influence on three-dimensional load state of the ROI in all loading modes (Figure 66). Overall, the same trend of relatively large axial strains as compared to the circumferential and axial strains was observed as in the base condition. The directions of the mean ROI stresses and strains were generally the same for all implant design conditions. However, in the double stiffness and isotropic conditions, an inversion (from positive to negative) of the circumferential strain direction was observed in flexion, right lateral bending, and both axial rotations.

The plug geometry condition resulted in no notable changes to the ROI load state as compared to the implant geometry. As compared to the base condition, the half-stiffness condition generally generated an increase in the strain magnitudes. In the axial direction these changes were minor as compared to the strain magnitude. However, in the circumferential direction these changes resulted in a more notable alteration of the ROI load state. In all loading modalities, the double-stiffness material condition had the opposite effect of the half stiffness material condition. In all loading modes, the isotropic material condition reduced the biaxial strain magnitudes and increased the radial stress magnitude as compared to the base condition.

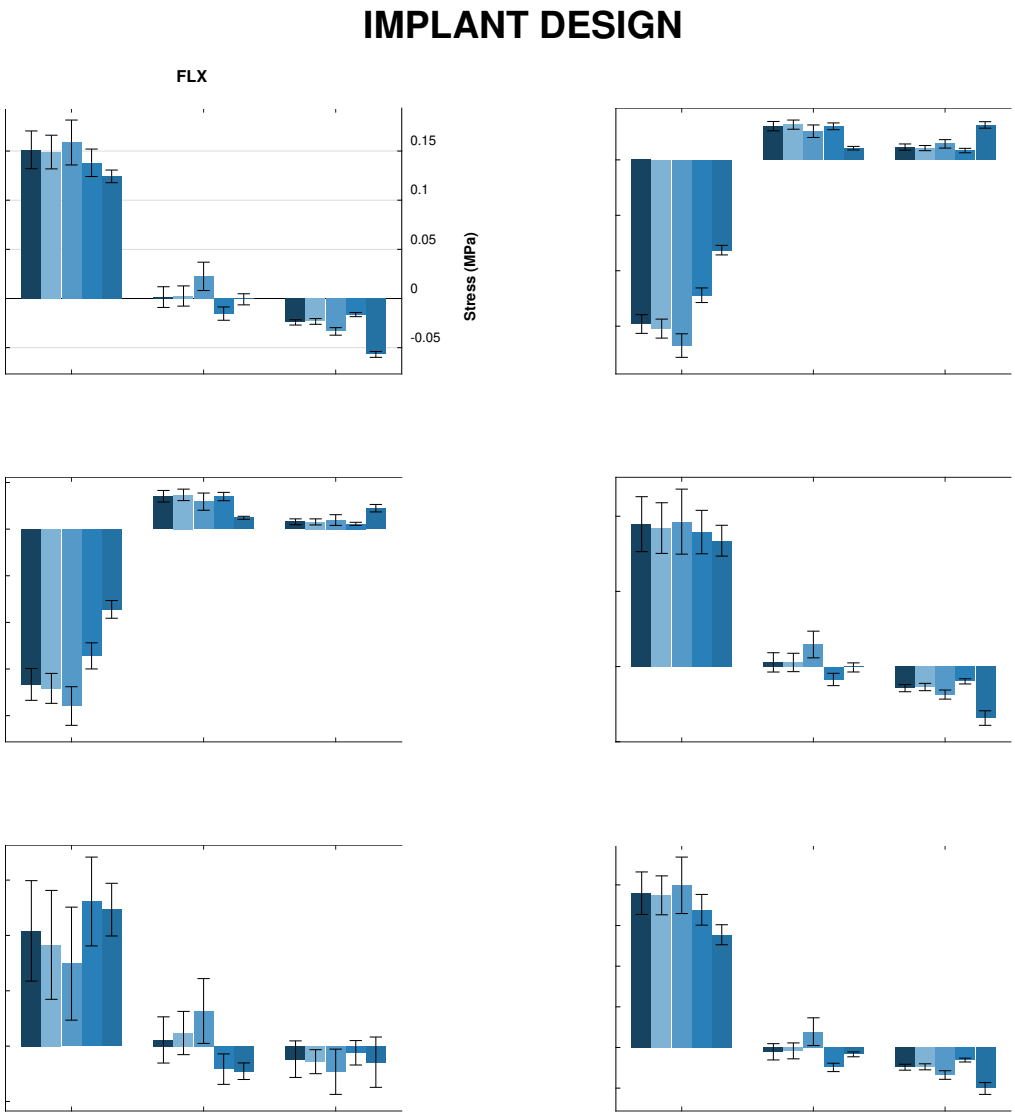

Figure 66. The mean three-dimensional load state within the implant ROI for six spinal loading modalities and five implant designs (the base implant design, the plug geometry, implant with material stiffnesses halved, implant with material stiffnesses doubled, and implant with isotropic material properties). Error bars indicate one standard deviation from the mean.

4.2.3.6. Implant attachment

For all internal attachment conditions, the two external attachment conditions (screw and plate) differed by more than 0.5% strain in only 1 of 57 solutions that resolved for both (45

solutions were within 0.2% strain). The single solution that exceeded 0.5% strain difference between screw and plate attachment was for the circumferential internal attachment condition (0.87% strain difference in the axial strain in flexion). Similarly, the difference in the corresponding standard deviations exceeded 0.5% strain in only 2 of 120 cases (a maximum of 0.85% strain difference).

The implant ROI strains for the different combinations of attachment conditions and loading modes are summarized in Figure 67. As compared to the other loading modes, the implant attachment demonstrated relatively little influence on the implant strains in extension and left lateral bending. The remaining loading modes (flexion, right lateral bending, and both axial rotations) exhibited similar trends in the implant strain as a function of implant attachment. In each of these four loading modes, at least one attachment condition reversed the direction of the strain as compared the total attachment condition. Most notably, the external attachment with internal circumferential attachment generated tensile circumferential strains (as compared to compressive circumferential strains in the total attachment condition).

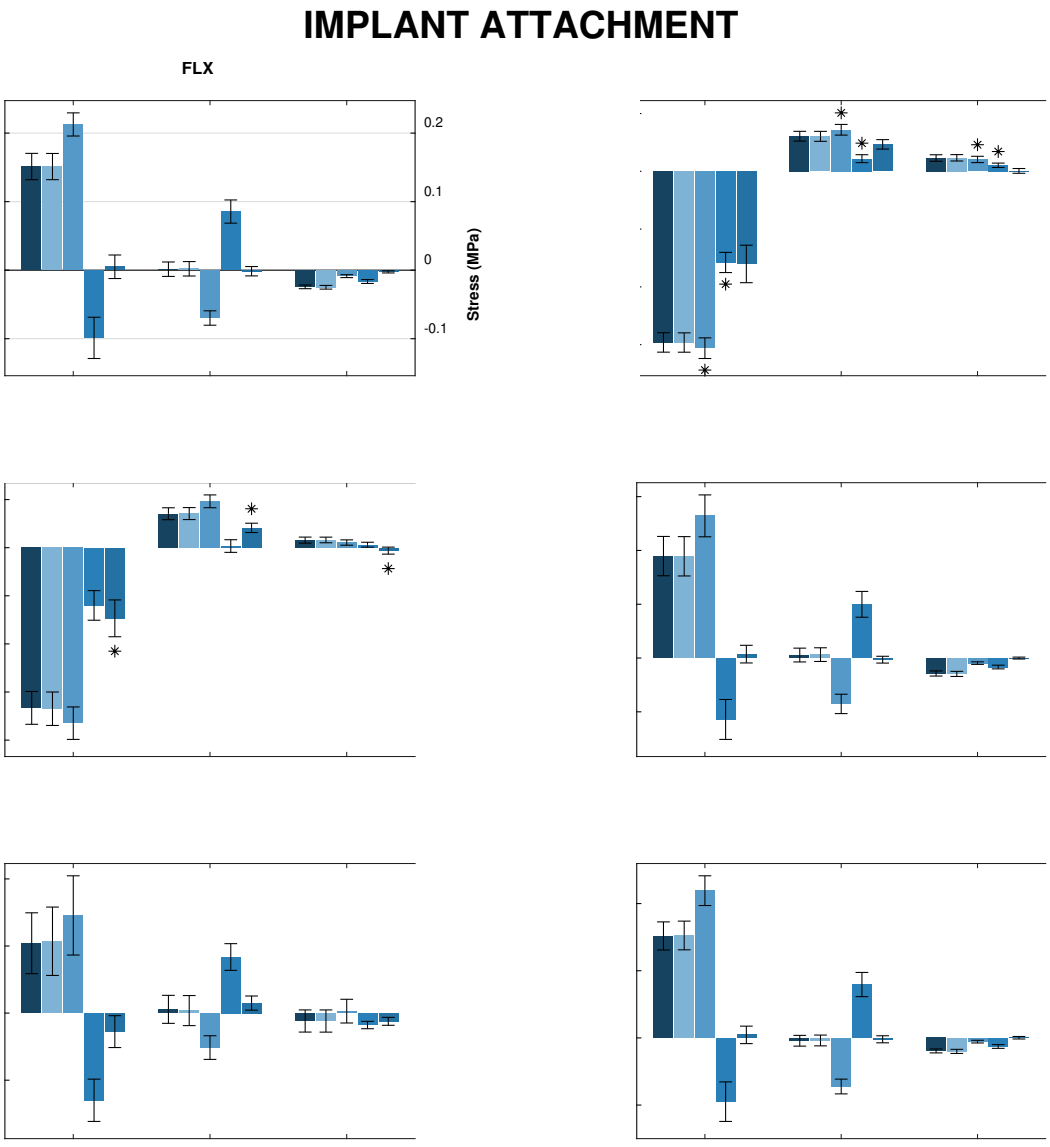

Figure 67. The mean three-dimensional load state within the implant ROI for six spinal loading modalities and five attachment conditions (total = attachment at all mating faces; ext. = external attachment; both = attachment of the internal axial and circumferential faces; axial = attachment of the internal axial faces; circ. = attachment of the internal axial faces). The results shown are for the screw external attachment condition, however, the corresponding combined external attachment result was substituted in when a design point could not be resolved and the (as indicated by an asterisk). Error bars indicate one standard deviation from the mean.

Uniform cohesive attachment of the implant resulted in a reduced magnitude of the mean axial and circumferential ROI strains as compared the total attachment condition in flexion loading (Figure 68). Further, the ROI stresses and strains generally reduced as the cohesive stiffness was reduced. For cohesive stiffnesses of 10 MPa and lower, no mean circumferential and axial strains greater than 0.6% and no mean radial stresses greater than 6 kPa were predicted.

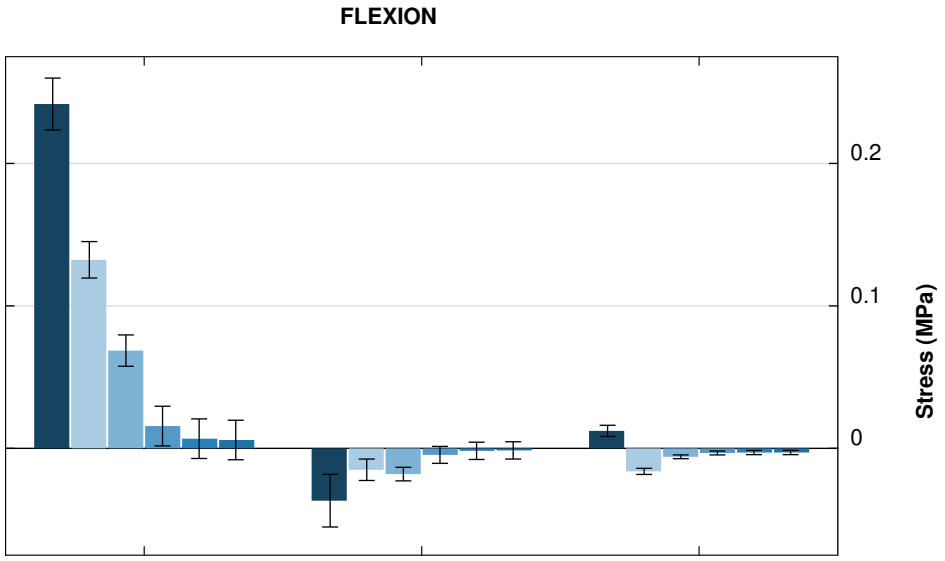

Figure 68. The mean three-dimensional load state within the implant ROI for five uniform cohesive attachment conditions (i.e., equal cohesion stiffness, C_U, in the circumferential and axial directions) in flexion loading. The total attachment conditions is also shown as a reference value. Error bars indicate one standard deviation from the mean.

4.2.3.7. Tailoring the implant loading

As compared to uniform cohesive attachment, the non-uniform cohesive attachment condition demonstrated negligible changes to the ROI load state for low cohesive stiffnesses (10

MPa and 1 MPa for the circumferential and axial faces, respectively; Figure 69). Specifically, in both uniform and non-uniform cohesion, all strains were below 1%, regardless of the material property scale. However, for high non-uniform cohesive stiffnesses (10,000 Pa and 1,000 MPa for the circumferential and axial faces, respectively), the mean axial and circumferential ROI strains both converged to positive values (i.e., tensile strains; mean strains of approximately 2.0% and 3.5% for the high and low material elasticity conditions, respectively). These ROI strains also coincided with negative mean radial stresses (-12.2 kPa and -20.9 kPa for the high and low material elasticity conditions, respectively). No other attachment conditions in this study achieved mean axial and circumferential ROI strains that were both simultaneously positive and greater than 1% in magnitude.

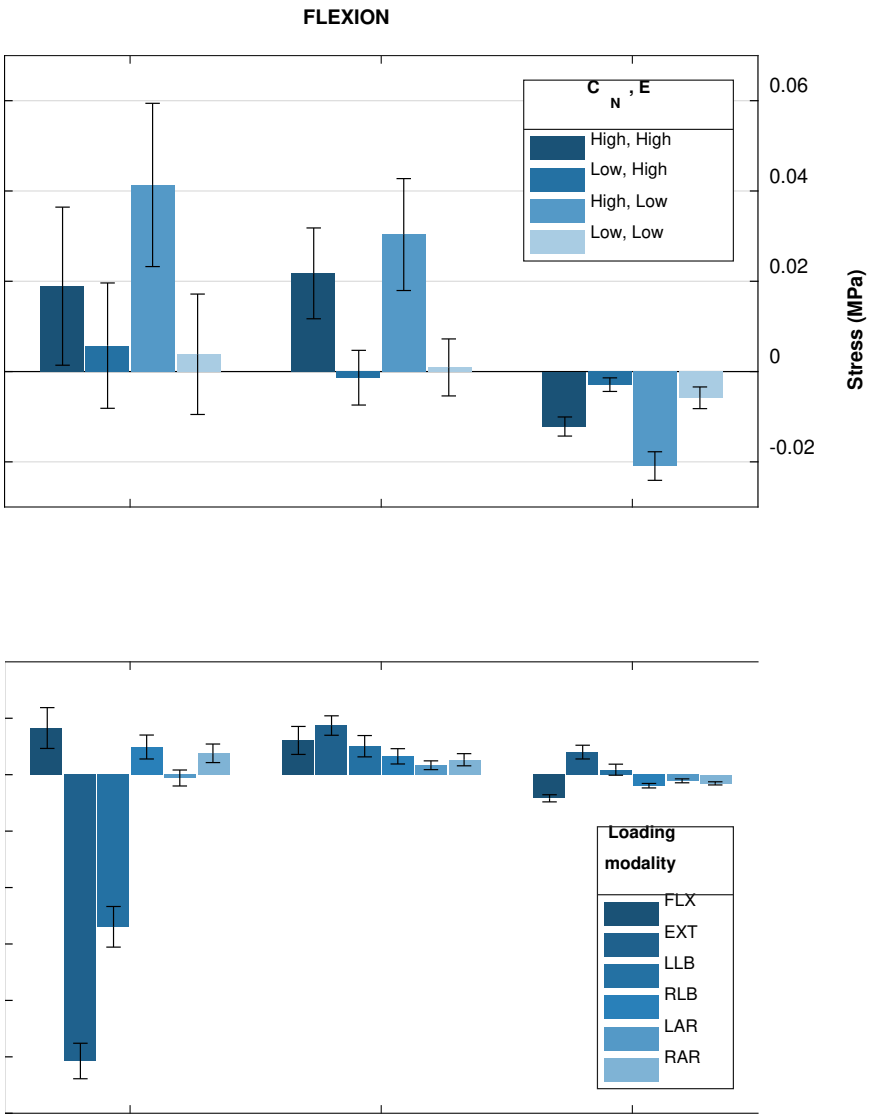

Figure 69. The mean three-dimensional load state within the implant ROI for: (a) four combinations of non-uniform cohesive attachment and variable implant elasticity in flexion loading and (b) a selected combination of these parameters (C_N = high, E = low) in all loading modes. The circumferential and axial cohesive stiffnesses were defined as either high (10,000 MPa and 1,000 MPa, respectively) or low (10 MPa and 1 MPa, respectively). The material elasticity was defined as either high (base model stiffness coefficients) or low (half of base model stiffness coefficients). Error bars indicate one standard deviation from the mean.

4.2.4. Discussion

In this study, the biomechanics of a novel treatment for IVD herniation was compared to healthy and injured spines using the FE method. Moment-rotation biomechanics of a human L4L5 FSU and the load state generated within the proposed implant were predicted to evaluate the efficacy of the treatment. The model explicated changes in the FSU biomechanics and implant loading due to the spine condition (intact, defect, and treated conditions as well as reduced NP pressurization), implant design (geometry and material properties) and implant attachment configurations.

4.2.4.1. Spine condition: FSU biomechanics

For the intact spine, all quantitative biomechanical measures (ROM, NZ, NZS, and EZSs) of the intact spine demonstrated congruence with reported biomechanical properties of the lumbar spine[224–226]. Further, all of the biomechanical changes induced by the defect and treatment were within one standard deviation of the mean reported values for intact spines. Although this result may suggest that none of the predicted changes to the biomechanical measures in this study were practically relevant within a population, it remains unknown whether these changes have practical relevance on an individual basis. Regardless, the deterministic nature of the FE analyses elucidates the relative magnitude and direction of alterations to the FSU biomechanics as a results of the defect and treatment.

Previous experimental work has studied the *ex vivo* biomechanics of ovine lumbar spines in analogous intact, defect, and treated conditions. Specifically, an equivalent implant design was inserted at the lateral aspect of the L4L5 level in cadaveric sheep spines. Although the differences in species and physiological location of the implant prohibit direct quantitative comparison of the FSU biomechanics, the influence of the defect and treatment is similar between the two models.

For example, in axial rotation, both defect models demonstrated increased ROM, slightly decreased NZ, dramatically decreased NZS, and negligible changes in the elastic zone stiffnesses. In both models, these changes were partially recovered (or over-corrected) by the implant.

The most notable changes to the FSU biomechanics induced by the defect was a dramatic reduction of the NZ in all loading modes and variable changes to the neutral zone stiffness. In general, the treatment was able to recover or slightly over-correct the biomechanical changes induced by the defect and the treatment induced no deleterious biomechanical changes for any loading modality. Accordingly, the results suggest that the treatment was effective at maintaining the healthy (i.e., intact) biomechanics of the spine. These observed changes may be attributed to mechanical recruitment of fibers in the AF, which has been demonstrated as a critical factor in the biomechanics of spinal motion segments[218]. The AF defect considered in this study generated a discontinuity in these fibers and may be a key driving factor for the predicted changes in biomechanics. Accordingly, in the treated model with idealized implant attachment, the material continuity at the interface with the adjacent AF tissue was restored. The remaining biomechanical discrepancies between the intact and treated models are likely due to (1) disparity between the material properties of the native AF and the implant, and (2) the addition of the external plate.

In addition to the quantitative biomechanical changes, the moment-rotation curves were observed to be shifted in the defect model as compared to the intact model. A less appreciable shift was also observed in the treatment data. This phenomenon may be attributed to disparity between the rotational positions of the spine in each condition prior to moment loading; the alteration of the IVD mechanics resulted in different deformations of the spine due to the NP pressurization and follower load. The resulting shift may have clinical relevance. First, the altered biomechanics resulting from the defect may induce further degenerative sequelae in the IVD. Second, the surgical

approach for this treatment should consider whether the healthy initial spine position is restored following repressurization of the nucleus and bodyweight loading in a standing position. Moreover, residual strains have been reported in bovine AF[227], and these preloads could be leveraged in the surgical strategy to restore the physiological residual strains in the AF.

4.2.4.2. Spine condition: AF and implant loading

Although complementary experimental work has been conducted on the biomechanics of the intact, defect, and treated FSU, it remains experimentally challenging to characterize the loading within the implant. Surfaces strains of the AF during physiological loading have been experimentally measured and the circumferential-axial ROI strains predicted in the intact AF (Figure 63) are in general agreement with reported values for human AF[199]. However, surface strains do not fully characterize the three-dimensional loading state, which is known to be a critical mechanoregulatory factor for tissue regeneration and homeostasis[55–58]. Accordingly, this highlights an advantage of the FE method: to capture the relative influence of the spine condition, implant design, and implant attachment on the three-dimensional ROI load state in a consistent, high-throughput manner.

The AF and implant load state was generally similar in all directions and for all loading modes. The most notable disparity between the two conditions was the radial pressure, which has been predicted to be a critical regulator of regenerative potential in AF repair (Section 3.2). In all loading modes, the largest deformation was in the axial direction, which can be attributed to two factors: (1) the implant is more compliant in the axial direction and (2) the adjacent tissue in the axial direction (i.e the cartilage endplates and vertebral bodies) is relatively more stiff than in the circumferential direction (i.e., the adjacent AF tissue) and, therefore, transmits more mechanical loading.

4.2.4.3. Spine condition: NP pressure

The NP pressure did not have a major influence on implant loading. The slight increase in loading with reduced NP pressure can be attributed to the implant experiencing a greater load share as the NP is incapable of supporting the axial load. Interestingly, the radial pressure experienced by the implant showed no observable change with reduced pressure of the NP. For the FSU biomechanics, reduction of the NP pressure resulted in increased overall compliance of the IVD. This was observed in the moment-rotation curves and in the available ROM, NZ, and NZS data for all loading modes. The additional FSU compliance coincided with non-convergent solutions due to excessive deformations in the AF, which may be a precursor to mechanical failure of the AF tissue. Notably, all loading modalities that resulted in failure induced compressive axial loads on the implant and failure locations. Mechanical failure of the AF and loss of NP pressure are both considered hallmarks of degenerative disc disease[75,80]. Accordingly, the results suggest that insufficient restoration of the NP pressure as part of an AF repair strategy be required to restore spinal function and prevent symptomatic recurrence of low back pain. A combined AF and NP repair strategy should be considered to recapitulate healthy levels of the NP pressure and achieve functional spinal biomechanics.

4.2.4.4. Implant design

From the considered implant design conditions, the isotropic material condition had the greatest influence on the ROI load state. However, the nature of this influence was inconsistent and dependent on loading mode. For example, the isotropic material condition caused the axial and circumferential strains to converge in flexion, yet diverge in extension loading. Alternatively, the half stiffness condition generally resulted in increased magnitudes of the ROI stresses and strains and was able to generate simultaneous tensile strains in the circumferential and axial

directions. This load state approached the theoretical target load state for AF regeneration based on the cellular micromechanical environment. Despite the base material properties of the implant replicating the native AF properties, the results indicate that under-prescribing the material conditions to generate a more compliant scaffold may afford a greater implant loading and subsequent regenerative potential. However, this material reduction alone did not provide sufficient engineering of the implant loading to meet the prescribed target. Overall, the implant design had only a minor influence on the ROI load state. In ideal attachment conditions, it appears that implant deformation is largely dictated by the overall deformation of the spine, and the considered alterations to the implant design do not impart sufficient influence to alter this deformation.

As compared to the plated implant, the plug implant generated no appreciable differences in the ROI load state in any loading mode. Additionally, the plated implant had no adverse influence on the FSU biomechanics. These results indicate that the plate geometry imparted no effect on spinal function or the regenerative potential of the implant in idealized attachment conditions. However, in practically-relevant attachment conditions which facilitate contact separation and sliding, the plate implant has the ability to retain the implant in position with the additional external attachment sites, which the plug implant inherently cannot deliver.

4.2.4.5. Implant attachment

In extension and left lateral bending, the influence of implant attachment was lower as compared to all other loading modes. As observed in Figure 67, axial deformation was consistently the dominant direction of deformation in the implant. At the posterolateral location of the implant in the model, extension and left lateral bending are consistent with axial compression of the disc space. Although tensile loads require attachment between contacting faces in order to be

transmitted, compressive loads can be transmitted via surface contact, regardless of the surface attachment condition. Accordingly, in extension and left lateral bending, the compressive axial loads that were imparted on the implant resulted in relatively little variation in the implant ROI deformation as compared to other loading modes. Conversely, flexion and right lateral bending are consistent with tensile loading in the left-posterolateral disc space. As a result, the implant deformations were strongly dependent on the transfer of axial loads to the implant. Even though all of the considered conditions had an external screw attachment condition, the axial loading was strongly dependent on whether or not the internal axial face was attached to the vertebral endplate. Therefore, these results suggest that the internal implant attachment plays a critical role in load transfer that the external attachment can not reproduce. This finding is further exemplified by the high degree of similarity between the screw and combined external attachment conditions; attachment of the external circumferential face fielded no practical difference in the implant deformation, yet, attachment of the internal circumferential face consistently resulted in appreciable increases in the circumferential implant strain.

As expected, attachment of the internal circumferential face increased the circumferential strains in the ROI. Further, all attachment conditions without circumferential bonding yielded only compressive circumferential strains or small tensile strains, and combining circumferential and axial attachment negated the increase in circumferential strain. Accordingly, the results suggest that circumferential attachment of the implant to the adjacent disc tissue may be fundamental to control the biaxial tension state and, subsequently, the regenerative environment of the implant. As previously discussed, continuity of the fibrous component of the AF is believed to play a critical mechanical role in the IVD. Accordingly, in the treated model, implant attachment in the

circumferential direction may be more critical in order to restore the material continuity with the fibrous component of the adjacent AF tissue.

The attachment conditions with all faces prescribed as either perfectly bonded or non-bonded are useful to understand the range of influence of implant attachment on the ROI load state. However, perfectly bonded attachment conditions are not feasible in practice; all tensile interfaces between the implant and the spine must have some attributed bonding stiffness. Screws or sutures can fix the implant plate to the spine with a relatively high stiffness, which may be effectively similar to a perfect bond. However, at interfaces where screws or sutures are not feasible (e.g. due to obstruction of the regenerative site or lack of surgical access) the implant may be bonded to the spine via a bioadhesive. The cohesive attachment data represented internal attachment of the implant with bioadhesives of varying stiffness (Figure 68). At high cohesion stiffnesses (10^9 to 10^{10} Pa) relatively large implant loads were generated as compared to the idealized attachment condition. However, bioadhesives that have been developed currently only have stiffness in the range of 10^4 to 10^7 Pa[228,229]. In this range of cohesive stiffness, only minor loads were generated in the implant. Accordingly, there may be a need to develop high-stiffness and high-strength bioadhesives or other novel attachment methods to enhance tissue regeneration strategies.

4.2.4.6. Tailoring the implant loading

For regeneration of the AF, it is desirable to control the load state within the implant to generate a cellular micromechanical environment that is conducive for repair. Two possible rationale for these load targets are: (1) reproduce the loading of the intact AF which regulates homeostasis of healthy AF tissue, and (2) generate implant loading that provides an optimal cellular micromechanical environment for AF regeneration. The latter has been theoretically proposed using a computational model (Section 3.2) and it is likely that empirical data will emerge

to support this rationale. Regardless of which rationale is used, is it advantageous to have a surgical strategy that can control and produce the target loading state.

The results of this study demonstrated that the configuration and stiffness of the implant attachment had the greatest influence on the implant loading. Additionally, it was shown that an increase in the implant compliance can increase the magnitude of implant loading. By combining these parameters, the ROI load state was tailored to meet a target based on a previous micromechanical model of regenerative potential. Based on the uniform cohesion results, the circumferential attachment was prescribed a cohesive stiffness one order of magnitude greater than the axial attachment (analogous of using two distinct bioadhesives), which was sufficient to generate the target tensile strains. However, the low cohesive stiffnesses in the range of current bioadhesives were insufficient to generate appreciable implant loads, independent of implant compliance. It may be possible to further increase the implant compliance, however, this approach may have adverse effects on the FSU biomechanics. Overall, the results showed that bioadhesives are a promising candidate for control of the implant loading and, ultimately, the regenerative potential of the repair strategy.

4.2.4.7. Limitations

The inherent limitation with FE analyses is the need for experimental validation of results. This study facilitated a high-throughput analyses of how the spine condition, implant design, and implant attachment influences the FSU biomechanics and implant loading for a novel treatment for AF herniation. In order for the findings of this study to be leveraged in a clinical application, extensive verification is required such as *ex vivo* cadaveric models and *in vivo* animal models. Another challenge in validating the FE model results is a lack of experimental techniques to

accurately prescribe and measure the model conditions. For example, prescribing the cohesive stiffness in an animal model and measuring the three-dimensional load state within the implant.

Another reason to utilize animal models is to assess the temporal efficacy of the treatment. The analyses in this study represent the mechanics during the acute phase of the AF repair treatment. Although this early period is likely a critical time in the healing process, the results of this study do not consider temporal changes to the implant. For example, it is expected that both ECM formation within the implant and material degradation will change the mechanical properties of the implant and/or change the attachment conditions of the implant to the spine. Another source of altered mechanics that is not captured by the model are the degenerative changes of the spine. The defect injury in the model represented the removal of a herniation in an otherwise healthy spine. However, IVD herniation commonly occurs due to degeneration of the AF, NP, cartilage endplates, and/or facets. Degeneration of these tissues may alter the biomechanical response of the spine and the efficacy of the AF repair strategy. Accordingly, further investigation of how degenerative disc disease may affect the treatment is of interest in future work.

Despite extensive use of solution controls, some FE element solutions in this study did not converge. This typically occurred due to excessive deformations in the model or complex contact mechanics. Consequently, some results could not be fully obtained. This non-convergence may be indicative of a practically-relevant issue, such as excessive strains leading to material failure. However, it is possible that some solutions could elucidate new findings of interest. In order to yield solutions for these models, improvements to the underlying lumbar spine model is likely necessary, such as refinement of the mesh in the intervertebral disc.

4.2.5. Conclusions

In this study, the mechanical efficacy of a novel treatment for repair of an IVD hernia was predicted using the FE method. The moment-rotation biomechanics of a human lumbar FSU and the implant loading to drive tissue regeneration were assessed for various spine conditions, implant designs, and implant attachment configurations. The treatment was able to recover some the biomechanical changes induced by a defect injury and generated no detrimental effects on the FSU biomechanics. The implant attachment was found to be a critical factor in the loads experienced by the implant. Tailoring of the cohesive attachment stiffness and increase of the implant compliance was found to facilitate control of the implant load state to a meet a proposed target for enhanced tissue regeneration. The results of this study highlight the need for advanced bioadhesives, implant design, and surgical strategies in AF tissue engineering. In future work, these findings will be validated with *ex vivo* cadaveric models, *in vitro* tissue engineering cultures, and *in vivo* animal models. This work builds towards an understanding of the organ-level biomechanics and cell-level micromechanics in AF repair strategies and, ultimately, facilitate development of revolutionary treatments for IVD herniation.

CHAPTER 5 – CONCLUSIONS

5.1. Summary of Findings

Overall, the research aims outlined in Chapter 1 formed a multi-scale approach to develop a novel treatment for IVD herniation, as illustrated in Figure 70. The primary objectives of the treatment were to provide long-term pain relief and sustained biomechanical function of the spine by eliciting regeneration of mechanically and biologically functional AF tissue.

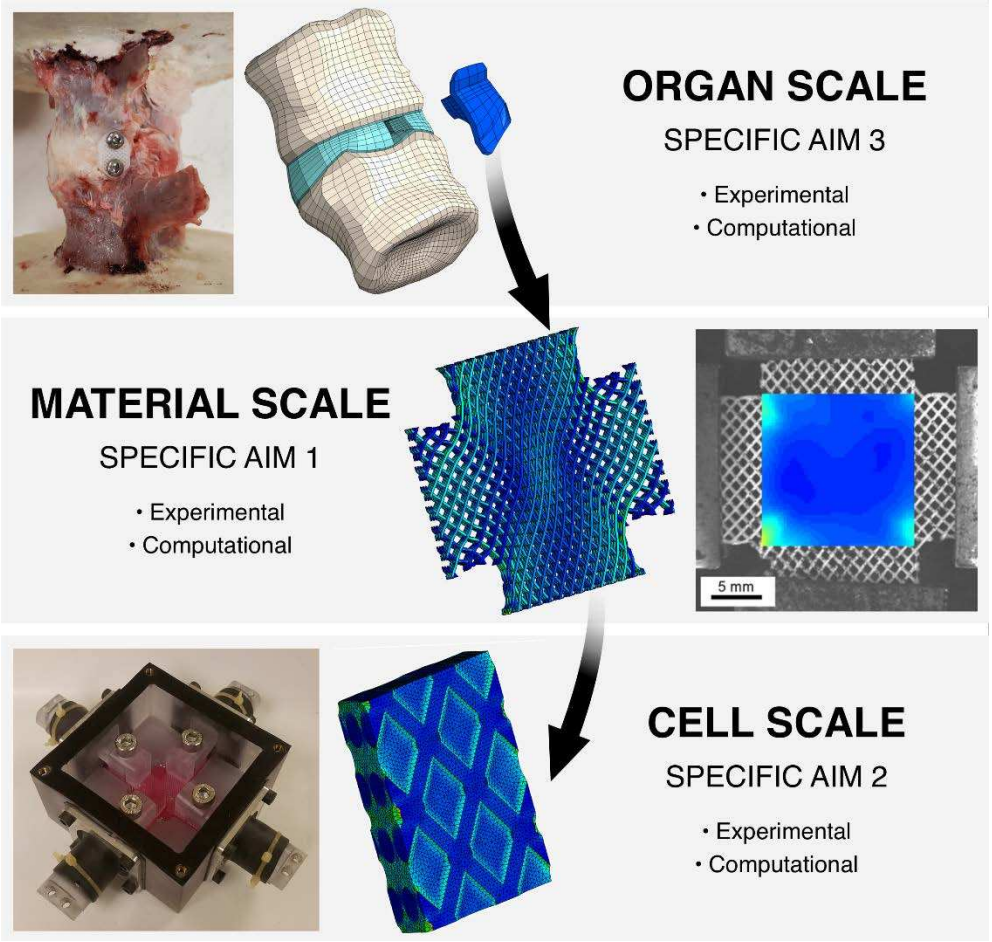

Figure 70. Summary of the aims of the presented work showing the multiscale approach to AF repair.

In Chapter 2, the mechanics of additive manufactured scaffolds for AF repair were experimentally characterized. Biaxial mechanical testing and constitutive modelling of scaffolds found an angle-ply laminate architecture with ±34° fiber angle replicated the biaxial stiffness asymmetry and overall magnitude of the stiffness of native AF tissue. To address limitations associated with experimental throughput, a broader scope of scaffold designs were evaluated with a parameterized finite element model. The finite element model was found to accurately reproduce the experimentally-derived material properties of the scaffolds. Of the considered print parameters, fiber angle, fiber diameter, and fiber spacing were found to have to the most dramatic influence on the scaffold mechanics. The scaffold mechanics were found to be less sensitive to the layer thickness, number of layers, and interlamellar bonding.

A custom incubator was developed in Chapter 3 to evaluate how AF cells seeded in the TE scaffolds respond to a prescribed, multi-axial mechanical loading protocol. A hybrid 3DF/MEW scaffold architecture was fabricated and yielded two distinct scales of fiber diameter in one coherent scaffold. The incubator demonstrated sterile culture of a group of cell-laden scaffolds with measured biaxial loading. However, histological evaluation of the scaffolds found no detectable changes in ECM production in scaffolds due to the mechanical loading protocol. A complementary finite element model was developed to aid in understanding the relationship between global scaffold loading and the local CME within the scaffold. An inhomogeneous distribution of the CME was predicted throughout the scaffold, and a fraction of the CME distribution was found to meet a proposed AF remodeling window. The scaffold loading modality, material selection, and architecture were all predicted to influence the CME within the scaffold. Scaffold loading modality was identified as the most critical factor to promote an anabolic response from AF cells. Scaffold materials and architecture were also found to indirectly modulate

the CME by modifying the scaffold loading. Due to the limitations of the experimental methods, comparison of the ECM production in cultured scaffolds could not be compared to the computational predictions.

Finally, Chapter 4 presented the translation of the developed TE material into an implant for implementation in a surgical strategy was presented. The hybrid scaffold architecture developed in Chapter 3 was successfully implemented in the fabrication of a novel AF repair patch. A surgical implantation technique was developed on cadaveric ovine lumbar spines and subsequent *ex vivo* biomechanical testing demonstrated biomechanical efficacy of the implant as compared to injured spines. The AF repair strategy was implemented using an *in vivo* ovine model and found that treatment had no major influence on FSU biomechanics. However, one treatment failed at the screw attachments and another treatment lead to some adverse tissue responses. A computational (finite element) model of the AF repair strategy in a human lumbar spine was developed to complement the experimental findings of the animal models. Congruent with the experimental results, the computational model identified the implant attachment as a critical design factor for surgical implementation of the implant. In particular, combined attachment of the implant with screws and bioadhesives was identified as a candidate method to regulate the implant loading.

5.2. Future Work

The experimental and computational work reported in this dissertation represent a significant advancement of our ability to implement an AF repair strategy and understand the underlying mechanisms that control AF regeneration. Numerous extensions to this research have been discussed to address experimental limitations, expand preliminary work, and iterate the

current AF repair strategy for improved outcomes. Accordingly, further efforts on the AF repair patch are warranted.

To address the material limitations in the *in vitro* studies, future work should explore alternative materials or PCL formulations to enhance the short-term durability of the TE scaffolds while maintaining the long-term temporal degradation properties for tissue regeneration. Any material changes can be rapidly evaluated using the developed scaffold finite element model and should also consider compatibility with additive manufacturing techniques for scaffold fabrication (i.e. 3DF and MEW). The hybrid architecture may also be further developed with current or new materials to improve the quality of the multi-scale architecture. Eventually, increased mechanical loading can be prescribed during incubation of cell-laden scaffolds to enhance our understanding of the role of scaffold loading on ECM formation. The developed model of CME in TE scaffolds can be leveraged as a rationale for scaffold design and mechanical loading, and the influence of biological factors can be evaluated experimentally. Histological methods to detect ECM formation in cultured scaffolds should be further developed, and biochemical assays may also be employed for more sensitive analyses. Overall, the underlying aim of the *in vitro* studies is to enhance the design and implementation of the AF repair strategy. Future work should, therefore, maintain a perspective of whether the regenerative outcomes under prescribed mechanical loading can be reliably regulated *in vivo*.

The preliminary *in vivo* animal model identified challenges with the AF repair strategy than can immediately addressed in future work. First, methods to improve the surgical attachment of the implant should be explored. For example, the implant could be reinforced at the site of the screws or augmented with bioadhesives to provide a more continuous interface between the implant and surrounding tissues. Second, adverse tissue formation at the treatment site should be

mitigated with improved implant design. Additional *ex vivo* work should be leveraged to develop revised repair strategies, and a statistically powered *in vivo* large animal should be conducted. For all future development of the AF repair strategy, the ease of surgical approach should be considered, which may be aided by novel surgical implantation hardware designs. Other considerations for future work include: (1) the translatability of the ovine lumbar IVD model to human lumbar IVDs; (2) evaluation of how different diseased states of the spine may, such as degenerative discs or a surgical approach requiring a laminectomy, may influence the efficacy of the treatment; (3) evaluation of long-term tissue regeneration; and (4) combined approaches to AF and NP repair. All future animal models of the AF repair strategy should aim to demonstrate healthy biomechanical function of treated spines, improved regeneration of the AF defect as compared to untreated defects, and no iatrogenic effects due to the treatment.

Overall, future work should build on the foundations of the current research presented in this dissertation. A continued, multidisciplinary approach to consolidate biological and mechanical efficacy of the novel AF repair strategy has the potential to restore spine function and provide long-term pain relief following IVD herniation. Ultimately, this approach may facilitate regeneration of the AF and represent a revolutionary treatment for chronic low back pain.

REFERENCES

1. Andersson, G. B. J. Epidemiology of low back pain. *Acta Orthopaedica Scandinavica* **69**, 28–31 (1998).

2. Dagenais, S., Caro, J. & Haldeman, S. A systematic review of low back pain cost of illness studies in the United States and internationally. *Spine J* **8**, 8–20 (2008).

3. Heliövaara, M. *et al.* Descriptive epidemiology and public health aspects of low back pain. *Ann. Med.* **21**, 327–333 (1989).

4. Hart, L. G., Deyo, R. A. & Cherkin, D. C. Physician office visits for low back pain. Frequency, clinical evaluation, and treatment patterns from a U.S. national survey. *Spine* **20**, 11–19 (1995).

5. Taylor, V. M., Deyo, R. A., Cherkin, D. C. & Kreuter, W. Low back pain hospitalization. Recent United States trends and regional variations. *Spine* **19**, 1207–1212; discussion 13 (1994).

6. Praemer, A., Furnes, S. & Rice, D. *Musculoskeletal conditions in the United States*. (Amer Academy of Orthopaedic, 1999).

7. Murray, C. J. L. *et al.* The State of US Health, 1990-2010: Burden of Diseases, Injuries, and Risk Factors. *JAMA* **310**, 591–606 (2013).

8. Maniadakis, N. & Gray, A. The economic burden of back pain in the UK. *Pain* **84**, 95–103 (2000).

9. van Tulder, M. W., Koes, B. W. & Bouter, L. M. A cost-of-illness study of back pain in The Netherlands. *Pain* **62**, 233–240 (1995).

10. Wieser, S. *et al.* Cost of low back pain in Switzerland in 2005. *Eur J Health Econ* **12**, 455–467 (2011).

11. Martin, B. I. *et al.* Expenditures and health status among adults with back and neck problems. *JAMA* **299**, 656–664 (2008).

12. Luoma, K. *et al.* Low back pain in relation to lumbar disc degeneration. *Spine* **25**, 487–492 (2000).

13. Vialle, L. R., Vialle, E. N., Suárez Henao, J. E. & Giraldo, G. LUMBAR DISC HERNIATION. *Rev Bras Ortop* **45**, 17–22 (2015).

14. Freburger, J. K. *et al.* The Rising Prevalence of Chronic Low Back Pain. *Arch Intern Med* **169**, 251–258 (2009).

15. Brinjikji, W. *et al.* Systematic Literature Review of Imaging Features of Spinal Degeneration in Asymptomatic Populations. *AJNR Am J Neuroradiol* **36**, 811–816 (2015).

16. Hoy, D., Brooks, P., Blyth, F. & Buchbinder, R. The Epidemiology of low back pain. *Best Practice & Research Clinical Rheumatology* **24**, 769–781 (2010).

17. Yamada, H. *Strength of Biological Materials*. (Robert E. Krieger Publishing Company, 1973).

18. Lin, H. S., Liu, Y. K. & Adams, K. H. Mechanical response of the lumbar intervertebral joint under physiological (complex) loading. *J Bone Joint Surg Am* **60**, 41–55 (1978).

19. Twomey, L. T. & Taylor, J. R. Age changes in lumbar vertebrae and intervertebral discs. *Clin Orthop Relat Res* 97–104 (1987).

20. Zhao, C.-Q., Wang, L.-M., Jiang, L.-S. & Dai, L.-Y. The cell biology of intervertebral disc aging and degeneration. *Ageing Research Reviews* **6**, 247–261 (2007).

21. Antoniou, J. *et al.* The human lumbar intervertebral disc: evidence for changes in the biosynthesis and denaturation of the extracellular matrix with growth, maturation, ageing, and degeneration. *J. Clin. Invest.* **98**, 996–1003 (1996).

22. Maroudas, A., Stockwell, R. A., Nachemson, A. & Urban, J. Factors involved in the nutrition of the human lumbar intervertebral disc: cellularity and diffusion of glucose in vitro. *J. Anat.* **120**, 113–130 (1975).

23. Humzah, M. D. & Soames, R. W. Human intervertebral disc: Structure and function. *Anat. Rec.* **220**, 337–356 (1988).

24. Coventry, M. B., Ghormley, R. K. & Kernohan, J. W. THE INTERVERTEBRAL DISC: ITS MICROSCOPIC ANATOMY AND PATHOLOGY: Part II. Changes in the Intervertebral Disc Concomitant with Age. *JBJS* **27**, 233 (1945).

25. Inoue, H. Three-dimensional observation of collagen framework of intervertebral discs in rats, dogs and humans. *Arch Histol Jpn* **36**, 39–56 (1973).

26. Johnson, E. F., Chetty, K., Moore, I. M., Stewart, A. & Jones, W. The distribution and arrangement of elastic fibres in the intervertebral disc of the adult human. *J. Anat.* **135**, 301–309 (1982).

27. Ombregt, L. 31 - Applied anatomy of the lumbar spine. in *A System of Orthopaedic Medicine (Third Edition)* (ed. Ombregt, L.) 415-436.e4 (Churchill Livingstone, 2013). doi:10.1016/B978-0-7020-3145-8.00031-4.

28. Cassidy, J. J., Hiltner, A. & Baer, E. Hierarchical Structure of the Intervertebral Disc. *Connect. Tissue Res.* **23**, 75–88 (1989).

29. Elliott, D. M. & Setton, L. A. Anisotropic and Inhomogeneous Tensile Behavior of the Human Anulus Fibrosus: Experimental Measurement and Material Model Predictions. *J. Biomech. Eng.* **123**, 256–263 (2001).

30. Wagner, D. R. & Lotz, J. C. Theoretical model and experimental results for the nonlinear elastic behavior of human annulus fibrosus. *J. Orthop. Res.* **22**, 901–909 (2004).

31. O'Connell, G. D., Sen, S. & Elliott, D. M. Human annulus fibrosus material properties from biaxial testing and constitutive modeling are altered with degeneration. *Biomech Model Mechanobiol* **11**, 493–503 (2012).

32. Long, R. G., Torre, O. M., Hom, W. W., Assael, D. J. & Iatridis, J. C. Design Requirements for Annulus Fibrosus Repair: Review of Forces, Displacements, and Material Properties of the Intervertebral Disk and a Summary of Candidate Hydrogels for Repair. *J Biomech Eng* **138**, 021007 (2016).

33. Bass, E. C., Ashford, F. A., Segal, M. R. & Lotz, J. C. Biaxial Testing of Human Annulus Fibrosus and Its Implications for a Constitutive Formulation. *Annals of Biomedical Engineering* **32**, 1231–1242 (2004).

34. Ebara, S. *et al.* Tensile properties of nondegenerate human lumbar anulus fibrosus. *Spine* **21**, 452–461 (1996).

35. Shan, Z. *et al.* Correlation between biomechanical properties of the annulus fibrosus and magnetic resonance imaging (MRI) findings. *Eur Spine J* **24**, 1909–1916 (2015).

36. Acaroglu, E. R. *et al.* Degeneration and aging affect the tensile behavior of human lumbar anulus fibrosus. *Spine* **20**, 2690–2701 (1995).

37. Isaacs, J. L., Vresilovic, E., Sarkar, S. & Marcolongo, M. Role of biomolecules on annulus fibrosus micromechanics: effect of enzymatic digestion on elastic and failure properties. *J Mech Behav Biomed Mater* **40**, 75–84 (2014).

38. O'Connell, G. D., Guerin, H. L. & Elliott, D. M. Theoretical and uniaxial experimental evaluation of human annulus fibrosus degeneration. *J Biomech Eng* **131**, 111007 (2009).

39. Guerin, H. A. L. & Elliott, D. M. Degeneration affects the fiber reorientation of human annulus fibrosus under tensile load. *J Biomech* **39**, 1410–1418 (2006).

40. Green, T. P., Adams, M. A. & Dolan, P. Tensile properties of the annulus fibrosus II. Ultimate tensile strength and fatigue life. *Eur Spine J* **2**, 209–214 (1993).

41. Page, M. I. *et al.* Biaxial Mechanics of 3D Fiber Deposited Ply-Laminate Scaffolds for Soft Tissue Engineering Part I: Experimental Evaluation. *J. Mech. Behav. Biomed.* **98**, 317–326 (2019).

42. Ayturk, U. M., Gadomski, B., Schuldt, D., Patel, V. & Puttlitz, C. M. Modeling Degenerative Disk Disease in the Lumbar Spine: A Combined Experimental, Constitutive, and Computational Approach. *J Biomech Eng* **134**, 101003-101003–11 (2012).

43. Nerurkar, N. L., Elliott, D. M. & Mauck, R. L. MECHANICAL DESIGN CRITERIA FOR INTERVERTEBRAL DISC TISSUE ENGINEERING. *J Biomech* **43**, 1017–1030 (2010).

44. Wilke, H. J., Neef, P., Caimi, M., Hoogland, T. & Claes, L. E. New in vivo measurements of pressures in the intervertebral disc in daily life. *Spine* **24**, 755–762 (1999).

45. Stokes, I. A. Surface strain on human intervertebral discs. *J. Orthop. Res.* **5**, 348–355 (1987).

46. Wang, S. *et al.* How does lumbar degenerative disc disease affect the disc deformation at the cephalic levels in vivo? *Spine* **36**, E574-581 (2011).

47. Nagel, T. M., Hadi, M. F., Claeson, A. A., Nuckley, D. J. & Barocas, V. H. Combining Displacement Field and Grip Force Information to Determine Mechanical Properties of Planar Tissue With Complicated Geometry. *J Biomech Eng* **136**, (2014).

48. Gawri, R. *et al.* High mechanical strain of primary intervertebral disc cells promotes secretion of inflammatory factors associated with disc degeneration and pain. *Arthritis Res. Ther.* **16**, R21 (2014).

49. Sowa, G. *et al.* Determination of annulus fibrosus cell response to tensile strain as a function of duration, magnitude, and frequency. *J. Orthop. Res.* **29**, 1275–1283 (2011).

50. Rannou, F. *et al.* Cyclic tensile stretch modulates proteoglycan production by intervertebral disc annulus fibrosus cells through production of nitrite oxide. *J. Cell. Biochem.* **90**, 148–157 (2003).

51. Poiraudeau, S. *et al.* Phenotypic Characteristics of Rabbit Intervertebral Disc Cells: Comparison With Cartilage Cells From the Same Animals. *Spine* **24**, 837–844 (1999).

52. Lotz, J. C., Colliou, O. K., Chin, J. R., Duncan, N. A. & Liebenberg, E. Compression-induced degeneration of the intervertebral disc: an in vivo mouse model and finite-element study. *Spine* **23**, 2493–506 (1998).

53. Buckwalter, J. A. Aging and degeneration of the human intervertebral disc. *Spine (Phila Pa 1976)* **20**, 1307–1314 (1995).

54. Gruber, H. E. & Hanley, E. N. J. Analysis of Aging and Degeneration of the Human Intervertebral Disc: Comparison of Surgical Specimens With Normal Controls. *Spine* **23**, 751–757 (1998).

55. Altman, G. *et al.* Cell differentiation by mechanical stress. *FASEB J.* **16**, 270–272 (2001).

56. Haj, A. J. E., Minter, S. L., Rawlinson, S. C. F., Suswillo, R. & Lanyon, L. E. Cellular responses to mechanical loading in vitro. *J. Bone Miner. Res.* **5**, 923–932 (1990).

57. Aarabi, S. *et al.* Mechanical load initiates hypertrophic scar formation through decreased cellular apoptosis. *FASEB J.* **21**, 3250–3261 (2007).

58. Lotz, J. C. & Chin, J. R. Intervertebral Disc Cell Death Is Dependent on the Magnitude and Duration of Spinal Loading. *Spine* **25**, 1477–1483 (2000).

59. Carter, D. R., Beaupré, G. S., Giori, N. J. & Helms, J. A. Mechanobiology of skeletal regeneration. *Clin. Orthop. Relat. Res.* S41-55 (1998).

60. Claes, L. E. & Heigele, C. A. Magnitudes of local stress and strain along bony surfaces predict the course and type of fracture healing. *J. Biomech.* **32**, 255–266 (1999).

61. Thomopoulos, S. *et al.* Fibrocartilage Tissue Engineering: The Role of the Stress Environment on Cell Morphology and Matrix Expression. *Tissue Engineering Part A* **17**, 1039–1053 (2010).

62. Spalazzi, J. P., Vyner, M. C., Jacobs, M. T., Moffat, K. L. & Lu, H. H. Mechanoactive Scaffold Induces Tendon Remodeling and Expression of Fibrocartilage Markers. *Clin Orthop Relat Res* **466**, 1938–1948 (2008).

63. Gilbert, H. T. J., Hoyland, J. A. & Millward-Sadler, S. J. The response of human anulus fibrosus cells to cyclic tensile strain is frequency-dependent and altered with disc degeneration. *Arthritis Rheum.* **62**, 3385–3394 (2010).

64. Sowa, G. *et al.* Determination of annulus fibrosus cell response to tensile strain as a function of duration, magnitude, and frequency. *J. Orthop. Res.* **29**, 1275–1283 (2011).

65. Rannou, F. *et al.* Cyclic tensile stretch modulates proteoglycan production by intervertebral disc annulus fibrosus cells through production of nitrite oxide. *J. Cell. Biochem.* **90**, 148–157 (2003).

66. Gilbert, H. T. J., Hoyland, J. A. & Millward-Sadler, S. J. The response of human anulus fibrosus cells to cyclic tensile strain is frequency-dependent and altered with disc degeneration. *Arthritis Rheum.* **62**, 3385–3394 (2010).

67. Hee, H. T., Zhang, J. & Wong, H. K. Effects of cyclic dynamic tensile strain on previously compressed inner annulus fibrosus and nucleus pulposus cells of human intervertebral disc—an in vitro study. *J. Orthop. Res.* **28**, 503–509 (2010).

68. Walsh, A. J. L. & Lotz, J. C. Biological response of the intervertebral disc to dynamic loading. *J. Biomech.* **37**, 329–337 (2004).

69. Le Maitre, C. L., Frain, J., Fotheringham, A. P., Freemont, A. J. & Hoyland, J. A. Human cells derived from degenerate intervertebral discs respond differently to those derived from non-degenerate intervertebral discs following application of dynamic hydrostatic pressure. *Biorheology* **45**, 563–575 (2008).

70. Hutton, W. C. *et al.* The Effect of Hydrostatic Pressure on Intervertebral Disc Metabolism. *Spine* **24**, 1507 (1999).

71. Handa, T. *et al.* Effects of Hydrostatic Pressure on Matrix Synthesis and Matrix Metalloproteinase Production in the Human Lumbar Intervertebral Disc. *Spine* **22**, 1085–1091 (1997).

72. Wenger, K. H. *et al.* Matrix Remodeling Expression in Anulus Cells Subjected to Increased Compressive Load. *Spine* **30**, 1122–1126 (2005).

73. Fearing, B. V., Hernandez, P. A., Setton, L. A. & Chahine, N. O. Mechanotransduction and cell biomechanics of the intervertebral disc. *JOR SPINE* **1**, e1026 (2018).

74. Simpson, S. T. Intervertebral Disc Disease. *Veterinary Clinics of North America: Small Animal Practice* **22**, 889–897 (1992).

75. Urban, J. P. & Roberts, S. Degeneration of the intervertebral disc. *Arthritis Res Ther* **5**, 120 (2003).

76. Mwale, F., Roughley, P. & Antoniou, J. Distinction between the extracellular matrix of the nucleus pulposus and hyaline cartilage: a requisite for tissue engineering of intervertebral disc. *Eur Cell Mater* **8**, 58–63; discussion 63-64 (2004).

77. Adams, M. A. & Roughley, P. J. What is Intervertebral Disc Degeneration, and What Causes It? *Spine* **31**, 2151 (2006).

78. Fahrni, W. H. Conservative treatment of lumbar disc degeneration: our primary responsibility. *Orthop. Clin. North Am.* **6**, 93–103 (1975).

79. Freemont, A. J. *et al.* Nerve ingrowth into diseased intervertebral disc in chronic back pain. *The Lancet* **350**, 178–181 (1997).

80. Lyons, G., Eisenstein, S. M. & Sweet, M. B. E. Biochemical changes in intervertebral disc degeneration. *Biochimica et Biophysica Acta (BBA) - General Subjects* **673**, 443–453 (1981).

81. Jordon, J., Konstantinou, K. & O'Dowd, J. Herniated lumbar disc. *BMJ Clin Evid* **2009**, (2009).

82. Knop-Jergas, B. M., Zucherman, J. F., Hsu, K. Y. & DeLong, B. Anatomic Position of a Herniated Nucleus Pulposus Predicts the Outcome of Lumbar Discectomy. *Journal ofSpinal Disorders* **9**, 246–250 (1996).

83. Malik, K. & Benzon, H. T. 21 - Low Back Pain. in *Practical Management of Pain (Fifth Edition)* (eds. Benzon, H. T. et al.) 312-327.e4 (Mosby, 2014). doi:10.1016/B978-0-323-08340-9.00021-9.

84. McCulloch, J. ▪ Focus Issue on Lumbar Disc Herniation: Macro- and Microdiscectomy. *Spine* **21**, (1996).

85. Dulebohn, S. C., Ngnitewe Massa, R. & Mesfin, F. B. Disc Herniation. in *StatPearls* (StatPearls Publishing, 2019).

86. Weinstein, S. M. & Herring, S. A. Lumbar epidural steroid injections. *The Spine Journal* **3**, 37–44 (2003).

87. Gajraj, N. M. Selective Nerve Root Blocks for Low Back Pain and Radiculopathy. *Reg Anesth Pain Med* **29**, 243–256 (2004).

88. Gray, D. T. *et al.* Population-Based Trends in Volumes and Rates of Ambulatory Lumbar Spine Surgery: *Spine* **31**, 1957–1963 (2006).

89. Phillips, F. M., Slosar, P. J., Youssef, J. A., Andersson, G. & Papatheofanis, F. Lumbar spine fusion for chronic low back pain due to degenerative disc disease: a systematic review. *Spine* **38**, E409-422 (2013).

90. Turner, J. A. *et al.* Patient Outcomes After Lumbar Spinal Fusions. *JAMA* **268**, 907–911 (1992).

91. Lee, C. K., Langrana, N. A., Parsons, J. R. & Zimmerman, M. C. Development of a prosthetic intervertebral disc. *Spine* **16**, S253-255 (1991).

92. Wang, H. *et al.* Incidence and risk factors of adjacent segment disease following posterior decompression and instrumented fusion for degenerative lumbar disorders. *Medicine (Baltimore)* **96**, (2017).

93. Abi-Hanna, D., Kerferd, J., Phan, K., Rao, P. & Mobbs, R. Lumbar Disk Arthroplasty for Degenerative Disk Disease: Literature Review. *World Neurosurgery* **109**, 188–196 (2018).

94. Guyer, R. & Ohnmeiss, D. Intervertebral Disc Prostheses. *Spine* **28**, (2003).

95. Hedman, T. P., Kostuik, J. P., Fernie, G. R. & Hellier, W. G. Design of an intervertebral disc prosthesis. *Spine* **16**, S256-260 (1991).

96. Lage Barroso, J. C., Mosquera Betancourt, G. & García García, E. A. The disc prosthesis, an alternative to intervertebral fusion. *Gaceta Médica Espirituana* **20**, 74–97 (2018).

97. Wang, J. C., Arnold, P. M., Hermsmeyer, J. T. & Norvell, D. C. Do lumbar motion preserving devices reduce the risk of adjacent segment pathology compared with fusion surgery? A systematic review. *Spine* **37**, S133-143 (2012).

98. Harper, R. & Klineberg, E. The evidence-based approach for surgical complications in the treatment of lumbar disc herniation. *Int Orthop* **43**, 975–980 (2019).

99. Hakelius, A. Prognosis in Sciatica: A Clinical Follow-Up of Surgical and Non-Surgical Treatment. *Acta Orthopaedica Scandinavica* **41**, 1–76 (1970).

100. Lurie, J. D. *et al.* Surgical versus Non-Operative Treatment for Lumbar Disc Herniation: Eight-Year Results for the Spine Patient Outcomes Research Trial (SPORT). *Spine (Phila Pa 1976)* **39**, 3–16 (2014).

101. Weber, H. Lumbar Disc Herniation: A Controlled, Prospective Study with Ten Years of Observation. *SAS Journal* **3**, 30–40 (2009).

102. Sakai, D. Future perspectives of cell-based therapy for intervertebral disc disease. *Eur Spine J* **17**, 452–458 (2008).

103. Richardson, S. M., Mobasheri, A., Freemont, A. J. & Hoyland, J. A. Intervertebral disc biology, degeneration and novel tissue engineering and regenerative medicine therapies. *Histol. Histopathol.* **22**, 1033–1041 (2007).

104. O'Halloran, D. M. & Pandit, A. S. Tissue-engineering approach to regenerating the intervertebral disc. *Tissue Eng.* **13**, 1927–1954 (2007).

105. Kalson, N. S., Richardson, S. & Hoyland, J. A. Strategies for regeneration of the intervertebral disc. *Regen Med* **3**, 717–729 (2008).

106. Leung, V. Y. L., Chan, D. & Cheung, K. M. C. Regeneration of intervertebral disc by mesenchymal stem cells: potentials, limitations, and future direction. *Eur Spine J* **15**, 406–413 (2006).

107. Bron, J. L., Helder, M. N., Meisel, H.-J., Royen, B. J. V. & Smit, T. H. Repair, regenerative and supportive therapies of the annulus fibrosus: achievements and challenges. *Eur Spine J* **18**, 301–313 (2009).

108. Guterl, C. C. *et al.* CHALLENGES AND STRATEGIES IN THE REPAIR OF RUPTURED ANNULUS FIBROSUS. *Eur Cell Mater* **25**, 1–21 (2013).

109. Liu, Z., Tang, M., Zhao, J., Chai, R. & Kang, J. Looking into the Future: Toward Advanced 3D Biomaterials for Stem-Cell-Based Regenerative Medicine. *Adv. Mater. Weinheim* (2018) doi:10.1002/adma.201705388.

110. Ringe, J., Kaps, C., Burmester, G.-R. & Sittinger, M. Stem cells for regenerative medicine: advances in the engineering of tissues and organs. *Naturwissenschaften* **89**, 338–351 (2002).

111. Yang, S., Leong, K.-F., Du, Z. & Chua, C.-K. The Design of Scaffolds for Use in Tissue Engineering. Part I. Traditional Factors. *Tissue Engineering* **7**, 679–689 (2001).

112. Hutmacher, D. W. Scaffolds in tissue engineering bone and cartilage. in *The Biomaterials: Silver Jubilee Compendium* (ed. Williams, D. F.) 175–189 (Elsevier Science, 2000). doi:10.1016/B978-008045154-1.50021-6.

113. Ghosh, K. & Ingber, D. E. Micromechanical control of cell and tissue development: Implications for tissue engineering. *Advanced Drug Delivery Reviews* **59**, 1306–1318 (2007).

114. McBeath, R., Pirone, D. M., Nelson, C. M., Bhadriraju, K. & Chen, C. S. Cell Shape, Cytoskeletal Tension, and RhoA Regulate Stem Cell Lineage Commitment. *Developmental Cell* **6**, 483–495 (2004).

115. Engler, A. J., Sen, S., Sweeney, H. L. & Discher, D. E. Matrix elasticity directs stem cell lineage specification. *Cell* **126**, 677–689 (2006).

116. Haudenschild, A. K., Hsieh, A. H., Kapila, S. & Lotz, J. C. Pressure and Distortion Regulate Human Mesenchymal Stem Cell Gene Expression. *Ann Biomed Eng* **37**, 492–502 (2009).

117. Agrawal, C. M. & Ray, R. B. Biodegradable polymeric scaffolds for musculoskeletal tissue engineering. *J. Biomed. Mater. Res.* **55**, 141–150 (2001).

118. Sánchez-González, S., Diban, N. & Urtiaga, A. Hydrolytic Degradation and Mechanical Stability of Poly(ε-Caprolactone)/Reduced Graphene Oxide Membranes as Scaffolds for In Vitro Neural Tissue Regeneration. *Membranes (Basel)* **8**, (2018).

119. Saad, B. & Suter, U. W. Biodegradable Polymeric Materials. in *Encyclopedia of Materials: Science and Technology* (eds. Buschow, K. H. J. et al.) 551–555 (Elsevier, 2001). doi:10.1016/B0-08-043152-6/00105-4.

120. Kang, R. *et al.* Engineered three-dimensional nanofibrous multi-lamellar structure for annulus fibrosus repair. *Journal of Materials Chemistry B* **1**, 5462–5468 (2013).

121. Koepsell, L. *et al.* Tissue engineering of annulus fibrosus using electrospun fibrous scaffolds with aligned polycaprolactone fibers. *J. Biomed. Mater. Res.* **99A**, 564–575 (2011).

122. McGuire, R., Borem, R. & Mercuri, J. The fabrication and characterization of a multi-laminate, angle-ply collagen patch for annulus fibrosus repair. *J Tissue Eng Regen Med* **11**, 3488–3493 (2017).

123. Nerurkar, N. L., Elliott, D. M. & Mauck, R. L. Mechanics of oriented electrospun nanofibrous scaffolds for annulus fibrosus tissue engineering. *J. Orthop. Res.* **25**, 1018–1028 (2007).

124. Gullbrand, S. E. *et al.* Long-term mechanical function and integration of an implanted tissue-engineered intervertebral disc. *Science Translational Medicine* **10**, (2018).

125. Bowles, R. D., Gebhard, H. H., Härtl, R. & Bonassar, L. J. Tissue-engineered intervertebral discs produce new matrix, maintain disc height, and restore biomechanical function to the rodent spine. *Proc. Natl. Acad. Sci. U.S.A.* **108**, 13106–13111 (2011).

126. Yang, F. *et al.* Fabrication of a novel whole tissue-engineered intervertebral disc for intervertebral disc regeneration in the porcine lumbar spine. *RSC Advances* **8**, 39013–39021 (2018).

127. Lotz, J. C. Animal Models of Intervertebral Disc Degeneration: Lessons Learned. *Spine* **29**, 2742–2750 (2004).

128. Alini, M. *et al.* Are animal models useful for studying human disc disorders/degeneration? *Eur Spine J* **17**, 2–19 (2008).

129. Ribitsch, I. *et al.* Large Animal Models in Regenerative Medicine and Tissue Engineering: To Do or Not to Do. *Front Bioeng Biotechnol* **8**, (2020).

130. Easley, N. E., Wang, M., McGrady, L. M. & Toth, J. M. Biomechanical and radiographic evaluation of an ovine model for the human lumbar spine. *Proc Inst Mech Eng H* **222**, 915–922 (2008).

131. Wilke, H. J., Kettler, A. & Claes, L. E. Are sheep spines a valid biomechanical model for human spines? *Spine (Phila Pa 1976)* **22**, 2365–2374 (1997).

132. Lindley, E. M. *et al.* An analysis of spine fusion outcomes in sheep pre-clinical models. *Eur Spine J* **26**, 228–239 (2017).

133. McGilvray, K. C. *et al.* Bony ingrowth potential of 3D-printed porous titanium alloy: a direct comparison of interbody cage materials in an in vivo ovine lumbar fusion model. *The Spine Journal* **18**, 1250–1260 (2018).

134. Pirvu, T. *et al.* A combined biomaterial and cellular approach for annulus fibrosus rupture repair. *Biomaterials* **42**, 11–19 (2015).

135. Park, S.-H. *et al.* Intervertebral Disk Tissue Engineering Using Biphasic Silk Composite Scaffolds. *Tissue Engineering Part A* **18**, 447–458 (2011).

136. Nesti, L. J. *et al.* Intervertebral disc tissue engineering using a novel hyaluronic acid-nanofibrous scaffold (HANFS) amalgam. *Tissue Eng Part A* **14**, 1527–1537 (2008).

137. Driscoll, T. P., Nakasone, R. H., Szczesny, S. E., Elliott, D. M. & Mauck, R. L. Biaxial mechanics and inter-lamellar shearing of stem-cell seeded electrospun angle-ply laminates for annulus fibrosus tissue engineering. *J. Orthop. Res.* **31**, 864–870 (2013).

138. Chan, B. P. & Leong, K. W. Scaffolding in tissue engineering: general approaches and tissue-specific considerations. *Eur Spine J* **17**, 467–479 (2008).

139. Melchels, F. P. W. *et al.* Additive manufacturing of tissues and organs. *Progress in Polymer Science* **37**, 1079–1104 (2012).

140. Strange, D. G. T., Tonsomboon, K. & Oyen, M. L. Mechanical behaviour of electrospun fibre-reinforced hydrogels. *J Mater Sci: Mater Med* **25**, 681–690 (2014).

141. Nerurkar, N. L. *et al.* Nanofibrous biologic laminates replicate the form and function of the annulus fibrosus. *Nat. Mater.* **8**, 986–992 (2009).

142. Woodfield, T. B. F. *et al.* Design of porous scaffolds for cartilage tissue engineering using a three-dimensional fiber-deposition technique. *Biomaterials* **25**, 4149–4161 (2004).

143. Moroni, L., de Wijn, J. R. & van Blitterswijk, C. A. 3D fiber-deposited scaffolds for tissue engineering: Influence of pores geometry and architecture on dynamic mechanical properties. *Biomaterials* **27**, 974–985 (2006).

144. Brown, T. D., Dalton, P. D. & Hutmacher, D. W. Melt electrospinning today: An opportune time for an emerging polymer process. *Progress in Polymer Science* **56**, 116–166 (2016).

145. Ushiki, T. Collagen Fibers, Reticular Fibers and Elastic Fibers. A Comprehensive Understanding from a Morphological Viewpoint. *Archives of Histology and Cytology* **65**, 109–126 (2002).

146. Hendrikson, Wim. J., van Blitterswijk, Clemens. A., Rouwkema, J. & Moroni, L. The Use of Finite Element Analyses to Design and Fabricate Three-Dimensional Scaffolds for Skeletal Tissue Engineering. *Front Bioeng Biotechnol* **5**, (2017).

147. Olivares, A. L., Marsal, È., Planell, J. A. & Lacroix, D. Finite element study of scaffold architecture design and culture conditions for tissue engineering. *Biomaterials* **30**, 6142–6149 (2009).

148. Miranda, P., Pajares, A. & Guiberteau, F. Finite element modeling as a tool for predicting the fracture behavior of robocast scaffolds. *Acta Biomaterialia* **4**, 1715–1724 (2008).

149. Moroni, L., Poort, G., Keulen, F. V., Wijn, J. R. de & Blitterswijk, C. A. van. Dynamic mechanical properties of 3D fiber-deposited PEOT/PBT scaffolds: An experimental and numerical analysis. *Journal of Biomedical Materials Research Part A* **78A**, 605–614 (2006).

150. Brown, T. D. *et al.* Design and Fabrication of Tubular Scaffolds via Direct Writing in a Melt Electrospinning Mode. *Biointerphases* **7**, 1–16 (2012).

151. Entezari, A. *et al.* Nondestructive characterization of bone tissue scaffolds for clinical scenarios. *J. Mech. Behav. Biomed.* **89**, 150–161 (2019).

152. Idaszek, J. *et al.* Investigation of mechanical properties of porous composite scaffolds with tailorable degradation kinetics after in vitro degradation using digital image correlation. *Polym. Compos.* **38**, 2402–2410 (2017).

153. Page, M. I. & Puttlitz, C. M. Biaxial Mechanics of 3D Fiber Deposited Ply-Laminate Scaffolds for Soft Tissue Engineering Part II: Finite Element Analyses. *J. Mech. Behav. Biomed.* **100**, 103395 (2019).

154. Zhu, Q., Jackson, A. R. & Gu, W. Y. Cell viability in intervertebral disc under various nutritional and dynamic loading conditions: 3d Finite element analysis. *J. Biomech.* **45**, 2769–2777 (2012).

155. Gadomski, B. C. *et al.* Computational characterization of fracture healing under reduced gravity loading conditions. *J. Orthop. Res.* **34**, 1206–1215 (2016).

156. Laurent, C. P., Durville, D., Mainard, D., Ganghoffer, J.-F. & Rahouadj, R. A multilayer braided scaffold for Anterior Cruciate Ligament: Mechanical modeling at the fiber scale. *J. Mech. Behav. Biomed.* **12**, 184–196 (2012).

157. Moroni, L. *et al.* Finite Element Analysis of Meniscal Anatomical 3D Scaffolds: Implications for Tissue Engineering. *Open Biomed. Eng. J.* **1**, 23–34 (2007).

158. Williams, J. M. *et al.* Bone tissue engineering using polycaprolactone scaffolds fabricated via selective laser sintering. *Biomaterials* **26**, 4817–4827 (2005).

159. Lacroix, D. & Prendergast, P. J. A mechano-regulation model for tissue differentiation during fracture healing: analysis of gap size and loading. *J. Biomech.* **35**, 1163–1171 (2002).

160. Olivares, A. L., Marsal, È., Planell, J. A. & Lacroix, D. Finite element study of scaffold architecture design and culture conditions for tissue engineering. *Biomaterials* **30**, 6142–6149 (2009).

161. Kelly, D. J. & Prendergast, P. J. Mechano-regulation of stem cell differentiation and tissue regeneration in osteochondral defects. *J. Biomech.* **38**, 1413–1422 (2005).

162. Ayturk, U. M. & Puttlitz, C. M. Parametric convergence sensitivity and validation of a finite element model of the human lumbar spine. *Computer Methods in Biomechanics and Biomedical Engineering* **14**, 695–705 (2011).

163. Makinde, A., Thibodeau, L. & Neale, K. W. Development of an apparatus for biaxial testing using cruciform specimens. *Experimental Mechanics* **32**, 138–144 (1992).

164. Loh, Q. L. & Choong, C. Three-Dimensional Scaffolds for Tissue Engineering Applications: Role of Porosity and Pore Size. *Tissue Eng Part B Rev* **19**, 485–502 (2013).

165. Pitt C. G., Chasalow F. I., Hibionada Y. M., Klimas D. M., & Schindler A. Aliphatic polyesters. I. The degradation of poly(ϵ-caprolactone) in vivo. *Journal of Applied Polymer Science* **26**, 3779–3787 (2003).

166. Uden, S. van, Silva-Correia, J., Correlo, V. M., Oliveira, J. M. & Reis, R. L. Custom-tailored tissue engineered polycaprolactone scaffolds for total disc replacement. *Biofabrication* **7**, 015008 (2015).

167. Labus, K. M. & Puttlitz, C. M. An anisotropic hyperelastic constitutive model of brain white matter in biaxial tension and structural–mechanical relationships. *Journal of the Mechanical Behavior of Biomedical Materials* **62**, 195–208 (2016).

168. Schmidt, H., Kettler, A., Rohlmann, A., Claes, L. & Wilke, H.-J. The risk of disc prolapses with complex loading in different degrees of disc degeneration - a finite element analysis. *Clin Biomech (Bristol, Avon)* **22**, 988–998 (2007).

169. Liu, C. *et al.* The effect of the fibre orientation of electrospun scaffolds on the matrix production of rabbit annulus fibrosus-derived stem cells. *Bone Research* **3**, 15012 (2015).

170. Chen, F. *et al.* Additive Manufacturing of a Photo-Cross-Linkable Polymer via Direct Melt Electrospinning Writing for Producing High Strength Structures. *Biomacromolecules* **17**, 208–214 (2016).

171. Michalek, A. J., Buckley, M. R., Bonassar, L. J., Cohen, I. & Iatridis, J. C. Measurement of Local Strains in Intervertebral Disc Anulus Fibrosus Tissue under Dynamic Shear: Contributions of Matrix Fiber Orientation and Elastin Content. *J Biomech* **42**, 2279–2285 (2009).

172. Waldman, S. D. & Lee, J. M. Effect of sample geometry on the apparent biaxial mechanical behaviour of planar connective tissues. *Biomaterials* **26**, 7504–7513 (2005).

173. Mekhileri, N. V. *et al.* Automated 3D bioassembly of micro-tissues for biofabrication of hybrid tissue engineered constructs. *Biofabrication* **10**, 024103 (2018).

174. Schuurman, W. *et al.* Bioprinting of hybrid tissue constructs with tailorable mechanical properties. *Biofabrication* **3**, 021001 (2011).

175. Iatridis, J. C., Nicoll, S. B., Michalek, A. J., Walter, B. A. & Gupta, M. S. Role of biomechanics on intervertebral disc degeneration and regenerative therapies: What needs repairing in the disc and what are promising biomaterials for its repair? *Spine J* **13**, 243–262 (2013).

176. Castilho, M. *et al.* Mechanical behavior of a soft hydrogel reinforced with three-dimensional printed microfibre scaffolds. *Scientific Reports* **8**, 1245 (2018).

177. Pei, B. *et al.* Fiber-reinforced scaffolds in soft tissue engineering. *Regen Biomater* **4**, 257–268 (2017).

178. Eshraghi, S. & Das, S. Mechanical and Microstructural Properties of Polycaprolactone Scaffolds with 1-D, 2-D, and 3-D Orthogonally Oriented Porous Architectures Produced by Selective Laser Sintering. *Acta Biomater* **6**, 2467–2476 (2010).

179. Liu, F. *et al.* Structural Evolution of PCL during Melt Extrusion 3D Printing. *Macromol. Mater. Eng.* **303**, n/a-n/a (2018).

180. Cohn, E. J., Oncley, J. L., Strong, L. E., Hughes, W. L. & Armstrong, S. H. Chemical, clinical, and immunological studies on the products of human plasma fractionation. I. The characterization of the protein fractions of human plasma. *J Clin. Invest.* **23**, 417–432 (1944).

181. Lam, C. X. F., Hutmacher, D. W., Schantz, J.-T., Woodruff, M. A. & Teoh, S. H. Evaluation of polycaprolactone scaffold degradation for 6 months in vitro and in vivo. *Journal of Biomedical Materials Research Part A* **90A**, 906–919 (2009).

182. Christensen, B. B. *et al.* A novel nano-structured porous polycaprolactone scaffold improves hyaline cartilage repair in a rabbit model compared to a collagen type I/III scaffold: in vitro and in vivo studies. *Knee Surg Sports Traumatol Arthrosc* **20**, 1192–1204 (2012).

183. Goh, B. T., Teh, L. Y., Tan, D. B. P., Zhang, Z. & Teoh, S. H. Novel 3D polycaprolactone scaffold for ridge preservation – a pilot randomised controlled clinical trial. *Clinical Oral Implants Research* **26**, 271–277 (2015).

184. Abbah, S. A., Lam, C. X. L., Hutmacher, D. W., Goh, J. C. H. & Wong, H.-K. Biological performance of a polycaprolactone-based scaffold used as fusion cage device in a large animal model of spinal reconstructive surgery. *Biomaterials* **30**, 5086–5093 (2009).

185. Bao, W. *et al.* Effect of 3D printed polycaprolactone scaffold with a bionic structure on the early stage of fat grafting. *Materials Science and Engineering: C* **123**, 111973 (2021).

186. Park, S. Y. *et al.* Tissue-engineered artificial oesophagus patch using three-dimensionally printed polycaprolactone with mesenchymal stem cells: a preliminary report. *Interactive CardioVascular and Thoracic Surgery* **22**, 712–717 (2016).

187. Xu, T., Miszuk, J. M., Zhao, Y., Sun, H. & Fong, H. Electrospun Polycaprolactone 3D Nanofibrous Scaffold with Interconnected and Hierarchically Structured Pores for Bone Tissue Engineering. *Advanced Healthcare Materials* **4**, 2238–2246 (2015).

188. Farrugia, B. L. *et al.* Dermal fibroblast infiltration of poly(ε-caprolactone) scaffolds fabricated by melt electrospinning in a direct writing mode. *Biofabrication* **5**, 025001 (2013).

189. Reddy, G. K. & Enwemeka, C. S. A simplified method for the analysis of hydroxyproline in biological tissues. *Clin Biochem* **29**, 225–229 (1996).

190. Junqueira, L. C. U., Bignolas, G. & Brentani, R. R. A simple and sensitive method for the quantitative estimation of collagen. *Analytical Biochemistry* **94**, 96–99 (1979).

191. Thomas, V. J. C.- & Gesteira, T. F. Dimethylmethylene Blue Assay (DMMB). *Bio-protocol* **4**, e1236–e1236 (2014).

192. Labarca, C. & Paigen, K. A simple, rapid, and sensitive DNA assay procedure. *Analytical Biochemistry* **102**, 344–352 (1980).

193. Molinos, M. *et al.* Inflammation in intervertebral disc degeneration and regeneration. *J R Soc Interface* **12**, (2015).

194. Miyamoto, H. *et al.* Effects of cyclic mechanical stress on the production of inflammatory agents by nucleus pulposus and anulus fibrosus derived cells in vitro. *Spine (Phila Pa 1976)* **31**, 4–9 (2006).

195. Cambria, E. *et al.* TRPV4 Inhibition and CRISPR-Cas9 Knockout Reduce Inflammation Induced by Hyperphysiological Stretching in Human Annulus Fibrosus Cells. *Cells* **9**, (2020).

196. Pratsinis, H. *et al.* Cyclic tensile stress of human annulus fibrosus cells induces MAPK activation: involvement in proinflammatory gene expression. *Osteoarthritis Cartilage* **24**, 679–687 (2016).

197. Page, M. I., Linde, P. E. & Puttlitz, C. M. Development of a Finite Element Model to Predict the Cellular Micromechanical Environment in Tissue Engineering Scaffolds. *J Biomech* **In review.**,.

198. Shirazi-Adl, S. A., Shrivastava, S. C. & Ahmed, A. M. Stress analysis of the lumbar disc-body unit in compression. A three-dimensional nonlinear finite element study. *Spine (Phila Pa 1976)* **9**, 120–134 (1984).

199. Desrochers, J. & Duncan, N. A. Strain transfer in the annulus fibrosus under applied flexion. *Journal of Biomechanics* **43**, 2141–2148 (2010).

200. Heuer, F., Schmidt, H. & Wilke, H.-J. Stepwise reduction of functional spinal structures increase disc bulge and surface strains. *Journal of Biomechanics* **41**, 1953–1960 (2008).

201. Hollingsworth, N. T. & Wagner, D. R. The stress and strain states of the posterior annulus under flexion. *Spine (Phila Pa 1976)* **37**, E1134-1139 (2012).

202. Lama, P., Kulkarni, J. P. & Tamang, B. K. The Role of Cell Clusters in Intervertebral Disc Degeneration and its Relevance behind Repair. *Spine Res.* **3**, 15 (2017).

203. Pattappa, G. *et al.* Diversity of intervertebral disc cells: phenotype and function. *J. Anat.* **221**, 480–496 (2012).

204. Sun, T. *et al.* Development of a 3D cell culture system for investigating cell interactions with electrospun fibers. *Biotechnol. Bioeng.* **97**, 1318–1328 (2007).

205. Shao, X. & Hunter, C. J. Developing an alginate/chitosan hybrid fiber scaffold for annulus fibrosus cells. *J. Biomed. Mater. Res. A* **82A**, 701–710 (2007).

206. Nerurkar, N. L., Sen, S., Baker, B. M., Elliott, D. M. & Mauck, R. L. Dynamic culture enhances stem cell infiltration and modulates extracellular matrix production on aligned electrospun nanofibrous scaffolds. *Acta Biomater.* **7**, 485–491 (2011).

207. Roughley, P. J. Biology of intervertebral disc aging and degeneration: involvement of the extracellular matrix. *Spine* **29**, 2691–2699 (2004).

208. Pérez-Garijo, A. & Steller, H. Spreading the word: non-autonomous effects of apoptosis during development, regeneration and disease. *Development* **142**, 3253–3262 (2015).

209. Driessen, N. J. B., Wilson, W., Bouten, C. V. C. & Baaijens, F. P. T. A computational model for collagen fibre remodelling in the arterial wall. *J. Theor. Biol.* **226**, 53–64 (2004).

210. Wilson, W., Driessen, N. J. B., van Donkelaar, C. C. & Ito, K. Prediction of collagen orientation in articular cartilage by a collagen remodeling algorithm. *Osteoarthr. Cartil.* **14**, 1196–1202 (2006).

211. Daniels, F., ter Haar Romeny, B. M., Rubbens, M. & van Assen, H. Quantification of Collagen Orientation in 3D Engineered Tissue. in *3rd Kuala Lumpur International Conference on Biomedical Engineering 2006* (eds. Ibrahim, F., Osman, N. A. A., Usman, J. & Kadri, N. A.) 282–286 (Springer, 2007). doi:10.1007/978-3-540-68017-8_73.

212. McNally, D. S. & Adams, M. A. Internal Intervertebral Disc Mechanics as Revealed by Stress Profilometry. *Spine* **17**, 66–73 (1992).

213. Lee, H., Yoo, J. J., Kang, H.-W. & Cho, D.-W. Investigation of thermal degradation with extrusion-based dispensing modules for 3D bioprinting technology. *Biofabrication* **8**, 015011 (2016).

214. Dalton, P. D. Melt electrowriting with additive manufacturing principles. *Curr. Opin. Biomed. Eng.* **2**, 49–57 (2017).

215. Vernengo, J., Fussell, G. W., Smith, N. G. & Lowman, A. M. Synthesis and characterization of injectable bioadhesive hydrogels for nucleus pulposus replacement and repair of the damaged intervertebral disc. *J. Biomed. Mater. Res. B* **93B**, 309–317 (2010).

216. Albrecht, F., Roessner, A. & Zimmermann, E. Closure of osteochondral lesions using chondral fragments and fibrin adhesive. *Arch. Orth. Traum. Surg.* **101**, 213–217 (1983).

217. McGilvray, K. C. *et al.* Bony ingrowth potential of 3D-printed porous titanium alloy: a direct comparison of interbody cage materials in an in vivo ovine lumbar fusion model. *The Spine Journal* **18**, 1250–1260 (2018).

218. Ayturk, U. M., Garcia, J. J. & Puttlitz, C. M. The Micromechanical Role of the Annulus Fibrosus Components Under Physiological Loading of the Lumbar Spine. *Journal of Biomechanical Engineering* **132**, (2010).

219. Wang, T. *et al.* A novel in vivo large animal model of lumbar spinal joint degeneration. *The Spine Journal* **18**, 1896–1909 (2018).

220. Katz, J. N. & Harris, M. B. Lumbar Spinal Stenosis. *New England Journal of Medicine* **358**, 818–825 (2008).

221. Kambin, P. Arthroscopic microdiscectomy. *Arthroscopy: The Journal of Arthroscopic & Related Surgery* **8**, 287–295 (1992).

222. Beckstein, J. C., Sen, S., Schaer, T. P., Vresilovic, E. J. & Elliott, D. M. Comparison of animal discs used in disc research to human lumbar disc: axial compression mechanics and glycosaminoglycan content. *Spine (Phila Pa 1976)* **33**, E166-173 (2008).

223. Sato, K., Kikuchi, S. & Yonezawa, T. In Vivo Intradiscal Pressure Measurement in Healthy Individuals and in Patients With Ongoing Back Problems. *Spine* **24**, 2468 (1999).

224. Cook, D. J., Yeager, M. S. & Cheng, B. C. Range of Motion of the Intact Lumbar Segment: A Multivariate Study of 42 Lumbar Spines. *Int J Spine Surg* **9**, 5 (2015).

225. Spenciner, D., Greene, D., Paiva, J., Palumbo, M. & Crisco, J. The multidirectional bending properties of the human lumbar intervertebral disc. *The Spine Journal* **6**, 248–257 (2006).

226. Busscher, I. *et al.* Biomechanical Characteristics of Different Regions of the Human Spine: An In Vitro Study on Multilevel Spinal Segments. *Spine* **34**, 2858–2864 (2009).

227. Michalek, A. J., Gardner-Morse, M. G. & Iatridis, J. C. Large residual strains are present in the intervertebral disc annulus fibrosus in the unloaded state. *Journal of Biomechanics* **45**, 1227–1231 (2012).

228. Mehdizadeh, M., Weng, H., Gyawali, D., Tang, L. & Yang, J. Injectable citrate-based mussel-inspired tissue bioadhesives with high wet strength for sutureless wound closure. *Biomaterials* **33**, 7972–7983 (2012).

229. Xu, Y., Liang, K., Ullah, W., Ji, Y. & Ma, J. Chitin nanocrystal enhanced wet adhesion performance of mussel-inspired citrate-based soft-tissue adhesive. *Carbohydrate Polymers* **190**, 324–330 (2018).

APPENDIX A – COMPARISON OF CIRCULAR AND RECTANGULAR FIBER CROSS-SECTIONS IN MODELLING ANGLE-PLY LAMINATE FIBER SCAFFOLDS

A.1 Introduction

To improve the performance of the high-throughput computational model of angle-ply laminate scaffolds, it is advantageous to simplify the extruded fibers with a rectangular cross-section, rather than the approximately circular cross-section observed in the prints. Specifically, rectangular sections: (1) reduce geometric complexity to enhance mesh quality, and (2) simplify contact mechanics by creating planar interfaces between adjacent lamellae to vary the size of the contact region independent of other geometric parameters. In this appendix, the mechanics of scaffolds with circular and rectangular section fibers were compared to assess if rectangular sections were viable for use in the scaffold model.

A.2 Methods

A model with circular cross-section fibers was generated equivalent to the base model with square cross-section fibers. Due to the complex intersections between fibers, a constant contact radius between adjacent fibers could not be modelled. Instead, the natural intersection of the fibers was defined as fully bonded. With a layer spacing (Z) of 0.24 mm, the circular intersection yielded a mean radius of 0.16 mm when approximated as an ellipse. This was most comparable to the lower bound contact radius of 0.18 mm in the study.

As compared to the square fiber model, the circular fiber model had more complex geometric features and could not be meshed with hex elements in Abaqus. Tetrahedral elements (C3D10) were used instead with the same validated seed size from the square fiber model (0.075

mm). An equibiaxial condition was conducted using the circular fiber model with the same materials, boundary conditions, and analyses as the square fiber model. The full analysis with cylindrical fibers (meshing, solving, and post-processing) took more than ten times longer than the corresponding square fiber analysis.

A.3 Results

Figure A3 shows the deformed state of both models and Table A1 compares the resultant mechanics of both models. The maximum error in the calculated mechanics between the two geometries was 1.05%.

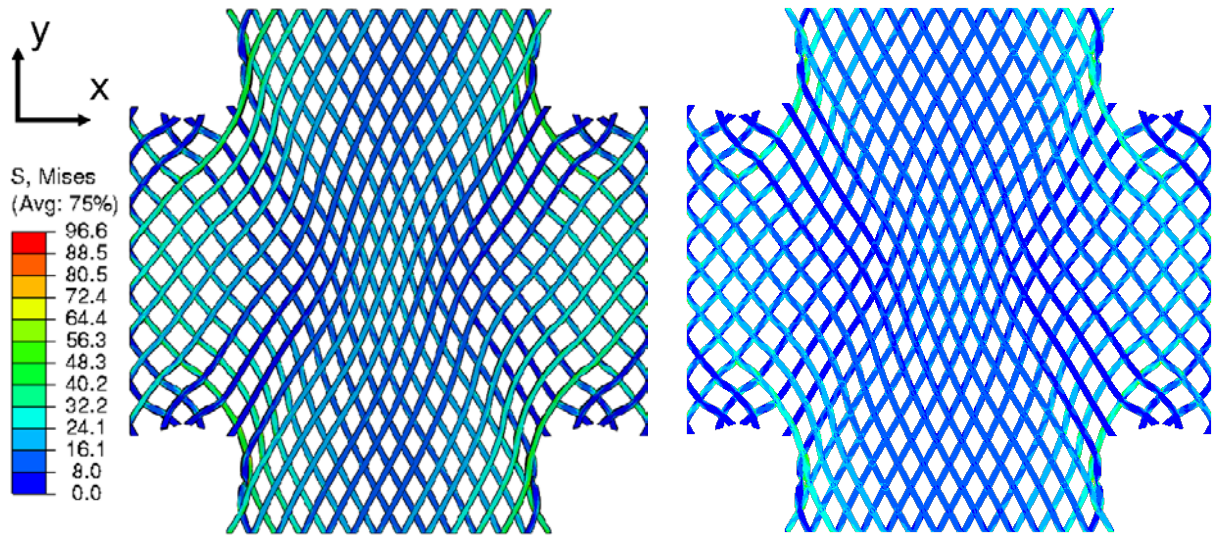

Figure A1. Comparison of (a) square cross-section fibers and (b) circular cross-section fibers subject to equibiaxial tension showing Mises equivalent stress contours (MPa).

Table A1. Resultant mechanics of square and circular cross-section fibers subject to equibiaxial tension showing error of square cross sections relative to circular cross sections.

	EE_x (MPa)	EE_y (MPa)	EE_r (MPa)
Circular Cross-Section	-9.88	32.8	-3.32
Square Cross-Section	-9.93	33.1	-3.33
% Error	0.58	1.05	0.46

A.4 Conclusion

Models with circular and rectangular fiber cross sections showed visually similar deformation, although local stresses may vary between the two geometries. The maximum error in the calculated effective elastic moduli was 1.05%, indicating a high level of agreement in the global scaffold mechanics. Therefore, simplifying the fiber cross-sections as rectangular appears to be a valid method to improve the computational performance of angle-ply laminate scaffold models.

APPENDIX B – DEVELOPMENT OF AN INCUBATOR TO DELIVER DYNAMIC BIAXIAL MECHANICAL LOADS TO TISSUE ENGINEERING SCAFFOLDS

B.1 Introduction

Mechanical loading is a known regulator of cell responses in TE strategies. Accordingly, *in vitro* methods are advantageous investigate the influence of physiological loading modalities on ECM production in cell laden scaffolds. Accordingly, there is a need to develop an apparatus to incubate tissue engineered scaffolds with specific and precise mechanical loading regimes. Specifically, this appendix details the development and validation of a custom incubator with two independent, orthogonal biaxial actuators.

B.2 Methods

The biaxial system was mounted on a portable x-shaped aluminum frame that could be removed from a thermal enclosure (Figure B1). Two orthogonal linear actuators (Zaber NA34C60-T4, Vancouver, BC, Canada) were used to generate precise biaxial displacements. The arms of the actuators were sealed in a polycarbonate chamber which contained a controlled environment for cell-culture. Specifically, the flow carbon dioxide into the environmental enclosure was controlled with a solenoid value, an electronic carbon dioxide sensor, and a Raspberry Pi (Raspberry Pi Foundation, Cambridge, England, UK) programmed with Python (Python Software Foundation, USA). The Raspberry Pi sensor system also measured the temperature and humidity within the environmental enclosure. A relative humidity greater than 80% was maintained in the environmental enclosure via a flask of deionized water. A sterile enclosure with two sets of orthogonal grips for biaxial stimulus was housed in the environmental enclosure and the grips were

mounted to the actuator arms (Figure B2). Opposite the actuator arms, the grips of the sterile incubator were mounted to support arms with load cells (Honeywell AL311CN, Charlotte, NC, USA) to measure the forces applied through the grips during cell culture. Both the actuator arms and the support arms contained transverse linear bearings to facilitate translation of the arm in the direction of orthogonal actuation and ensure a pure biaxial loading regime was delivered to the sterile enclosure. Additionally, the sterile enclosure was mounted on a translation table to prevent any support reaction forces in the plane of the actuators. The sterile enclosure consisted of a custom polycarbonate well with a lid vented with a standard culture flask cap. Two sets of orthogonal, custom polycarbonate grips were mounted through openings in the walls of the sterile enclosure well, and were sealed with rubber boots and aluminum clamps. Stainless steel screws were used to clamp the scaffold between the mating parts of each grip and the grips were shaped to fit around the well wall to ensure that the culture media was retained in the well and the gripped scaffold remained submerged in media. Each grip was coupled to the corresponding actuator arm and support arm via machine screws.

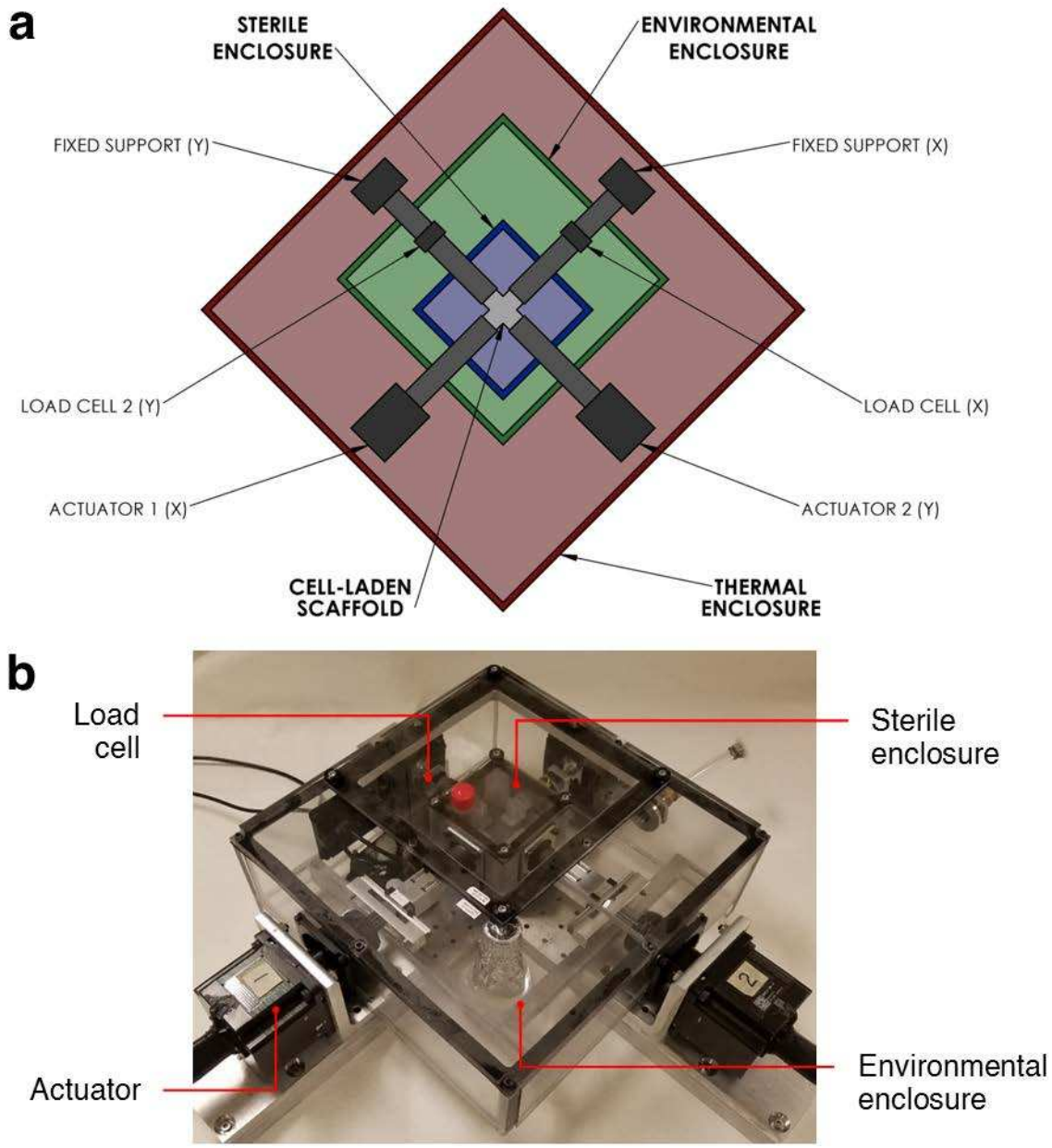

Figure B1. Custom biaxial incubator design: **(a)** schematic showing the incubator enclosures and critical features; and **(b)** digital photograph of the fabricated biaxial system and environment enclosure. The system was housed in a thermal enclosure (red are in the schematic) controlled at 37°C. An environment chamber (green area in the schematic was located around the center of the biaxial mechanical system and controlled the gas composition and humidity for the cell culture. A sterile enclosure (blue area in the schematic) was also located around the center of the biaxial system and within the environmental enclosure.

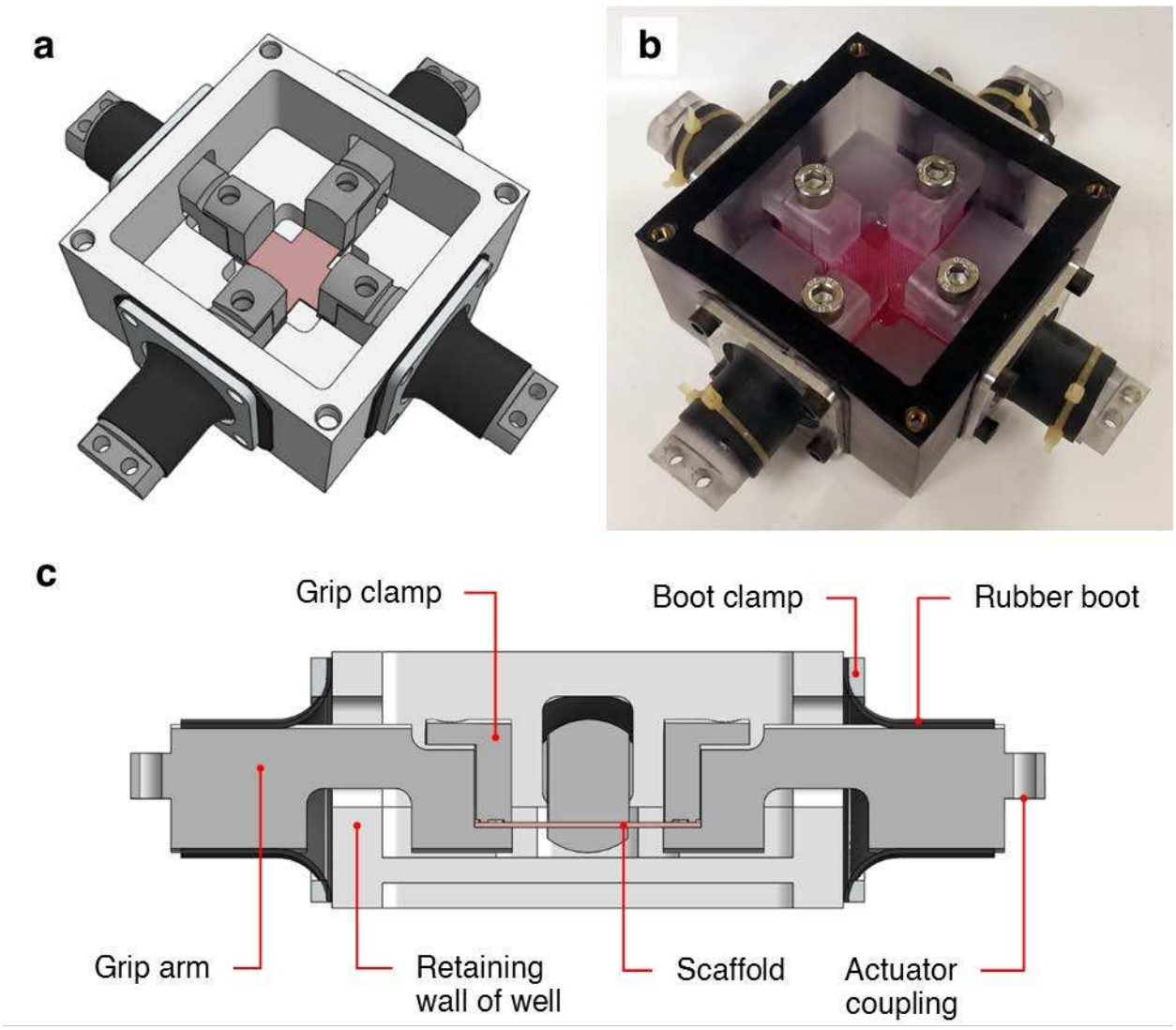

Figure B2. The sterile enclosure for the custom biaxial incubator: **(a)** digital rendering of the enclosure design; **(b)** digital photograph of the fabricated enclosure loaded with a scaffold and culture media; and **(c)** section view schematic of the sterile enclosure showing the critical features.

As described in Section 3.1.2.1, a cruciform scaffold was infused with a cell-laden hydrogel, placed in the sterile enclosure, clamped within the two sets of orthogonal grips, and submerged in culture media. The sterile enclosure was then sealed and transferred to the environmental chamber and fastened to the biaxial system. The incubator environment was allowed to equilibrate (temperature = 37 °C, relative humidity > 80%, CO_2 level = 5%) and the

scaffold was exposed to a sinusoidal, global equibiaxial strain protocol (amplitude = 5.0%, frequency = 1 Hz) for 8 hours a day. The tissue constructs were incubated under these prescribed conditions for seven days. Following the culture period, the scaffold was removed and scaffold sections adjacent to the ROI were flushed with phosphate-buffered saline to extract a solution containing the cell-laden hydrogel. Cell viability was assessed with a mammalian cell live/dead viability/cytotoxicity kit (Thermo Fisher Scientific, Waltham, MA, USA) using a standard protocol. Digital images were captured with a fluorescence microscope (Olympus IX70-S1F2, Tokyo, Japan).

B.3 Results

The custom biaxial incubator was observed to maintain the prescribed culture temperature, humidity, and CO_2 concentration for the duration of the study. Following the culture period, the tissue structure and culture media demonstrated no signs of infection when observed with the light microscope. The live/dead fluorescent microscopy demonstrated robust cell viability following the dynamic culture (Figure B3).

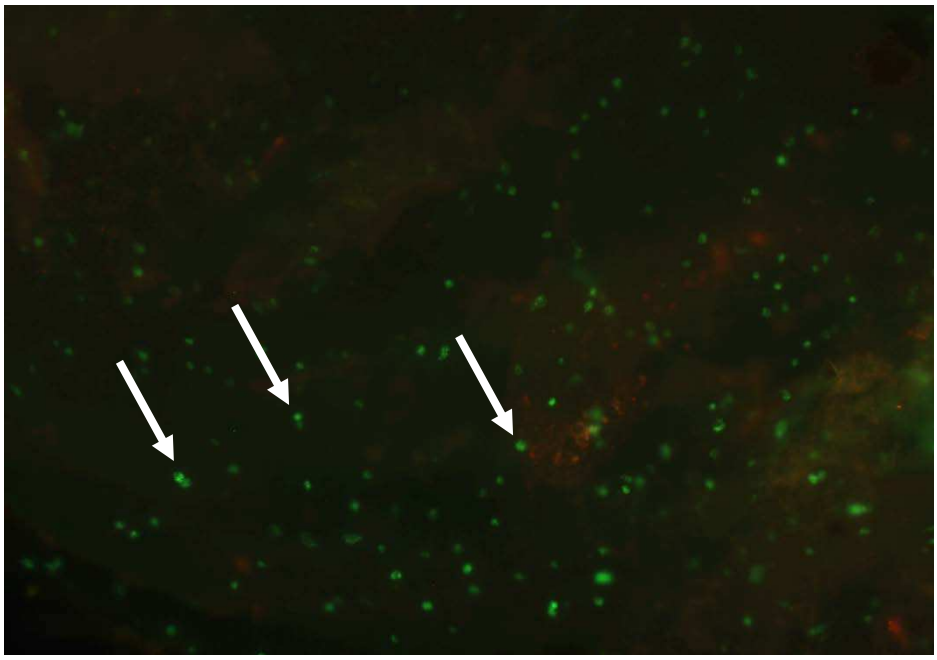

Figure B3. Fluorescent microscope image of mature ovine annulus fibrosus cells following seven days of dynamic culture in a custom incubator with dynamic biaxial loading. Green fluorescence indicates viable cells, red fluorescence indicates inviable cells, and a degree of background red and green fluorescence was observed. Examples of intense green fluorescence indicating live cells are identified with white arrows.

B.4 Discussion

The developed incubator system demonstrated the capacity to maintain the requisite environment for cell culture while containing the apparatus for precise, dynamic, biaxial mechanical loading of TE scaffolds. Accordingly, the biaxial incubator is sufficient to study the ECM production in a group of cell-laden TE scaffolds under a physiologically relevant loading regime.

APPENDIX C – RATIONALE FOR THE BIAXIAL STRAIN PROTOCOL FOR DYNAMIC CULTURING OF TISSUE ENGINEERED SCAFFOLDS

C.1 Introduction

Due to the material issues associated with cyclic loading of the PCL scaffolds in a physiological environment, a constraint was imposed on the magnitude of the global strain protocol for biaxial cell culture. Accordingly, there was a need to identify a global biaxial strain protocol for the cruciform scaffolds to elicit the greatest ECM. Because experimental methods are prohibitively challenging to characterize the cellular micromechanical environment (CME) that regulates ECM production, finite element methods were leveraged to provide a rationale for selecting the global biaxial strain protocol.

C.2 Methods

First, the unit cell model of CME in TE scaffolds (Section 3.2) was used to identify the most advantageous local ROI strains in the cruciform for an anabolic response of AF cells. The map of %PTE as a function of the biaxial strain combination presented in Figure 34 was used to inform the selection of the target local ROI strains. Specifically, tensile axial strain (i.e. x-direction strain > 0%) that is constrained in the circumferential direction (i.e. y-direction strain approximately 0%) would theoretically lead to the greatest increase in %PTE at low strains (Figure C1). Therefore, the target local ROI strains to theoretically optimize ECM production and prevent scaffold failure were 2.5% in the x-direction and 0.0% in the y-direction. Second, the developed model of angle-ply laminate scaffolds (Section 2.2) was used to predict the global strain protocol most likely to deliver the identified local ROI strains. The cruciform scaffold model with

parameters from the *in vitro* 3DF scaffold design (expected average fiber diameter of 338 µm from Section 2.1) was evaluated with various combinations of global biaxial strains until the target local ROI strains were met.

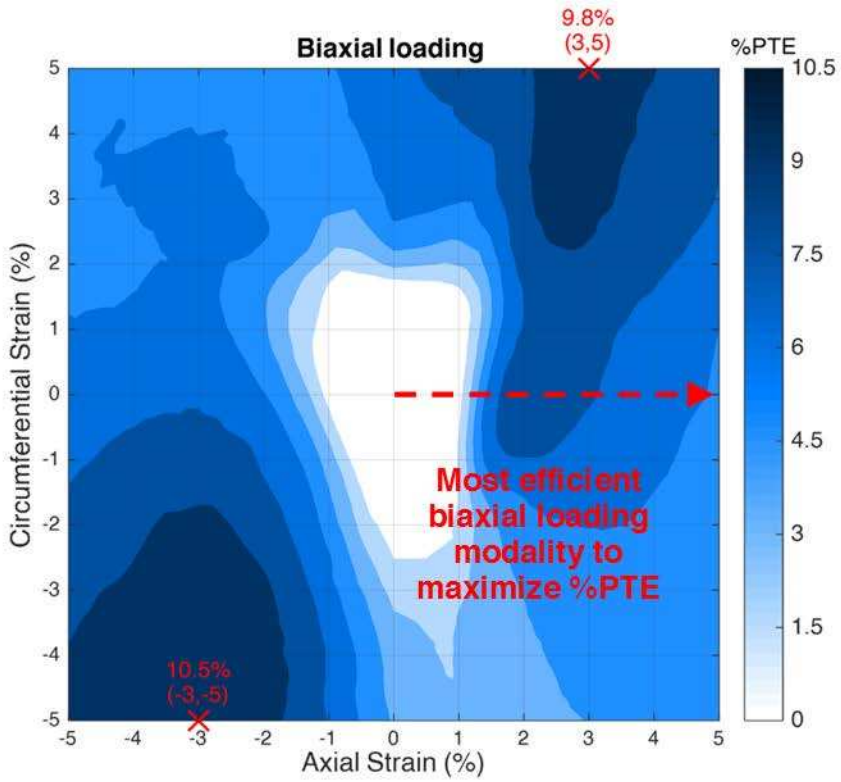

Figure C1. Map of %PTE as a function of biaxial strains (adapted from Figure 34b) showing the loading modality that would theoretically lead to the greatest %PTE at low magnitudes of local ROI strains.

C.3 Results

The global biaxial strains that met the target local biaxial strains (tensile x-direction strain with approximately 0% strain in the y-direction) were 2.5% and 0.5% in the x-direction and y-direction, respectively (local strains of 1.4% and 0.1%; Table C1). This target was also met with a lower magnitude global strains (2.0% and 0.4% in the x-direction and y-direction, respectively),

which generated local ROI strains of 1.1% and 0.0% in the x-direction and y-direction, respectively.

Table C1. Summary of the local, biaxial ROI strains in the cruciform scaffold as a function of the prescribed global biaxial strains. The final row shows the prescribed global strains that met the target local ROI strains.

Prescribed global strains (%)		**Local ROI strains (%)**	
x-direction	**y-direction**	**x-direction**	**y-direction**
2.0	2.0	-0.9	2.2
3.0	2.0	-0.1	1.9
2.0	0.0	1.6	-0.5
2.0	1.0	0.9	0.3
2.5	1.5	0.1	1.4
2.0	0.5	1.0	0.2
2.0	0.2	1.3	-0.2
2.0	0.3	1.2	-0.1
2.0	0.4	1.1	0.0
2.5	0.5	1.4	0.1

C.4 Discussion

Due to the limitations associated with characterizing the CME in TE scaffolds with experimental methods, a theoretical framework based on finite element analyses was utilized as a rationale for a biaxial loading protocol to elicit ECM production in TE scaffolds. Experimental validation of these results may be beneficial in future work. Nonetheless, the FE models afforded a rapid method to compare loading regimes for *in vitro* testing of TE scaffolds.

APPENDIX D – SUPPLEMENTARY FINITE ELEMENT ANALYSES OF 3DF, MEW, AND HYBRID SCAFFOLDS

D.1 Introduction

The developed finite element model of angle-ply laminate scaffolds and unit cells were used to generate additional finite element predictions to supplement experimental and computational studies. First, this appendix describes the validated angle-ply laminate scaffold model as a solid, orthotropic continuum of the measured 3DF and MEW scaffolds in the study. The orthotropic properties of 3DF scaffolds were utilized in a finite element model of the AF repair implant in a human lumbar spine (Section 4.2). Second, retrospective predictions of the scaffold mechanics are reported from the expected and fabricated measurements of 3DF scaffolds in the cell culture study (Section 3.1). Third, the orthotropic material properties and scaffold measurements were used to provide preliminary predictions for how the developed hybrid MEW/3DF architecture (Section 3.1) may influence the CME within a cell-laden interpenetrating hydrogel.

D.2 Methods

D.2.1 Continuum level material properties of angle play laminate scaffolds

Orthotropic material parameters were derived from FE simulations of a validated angle-ply fiber scaffold model (Section 542.2) in uniaxial tension and pure shear. Specifically, the model geometries used were: (1) the total length flange width of the previously developed cruciform scaffolds (22.5 mm by 15 mm for 3DF scaffolds and 2.25 by 0.15 mm for MEW scaffolds) and for evaluation in the x-y plane (3 bilayers thickness in the z-direction); and (2) the total length of

the previously developed cruciform scaffolds (22.5 mm for 3DF scaffolds and 2.25 mm for MEW scaffolds) and 24 bilayers thick in the z-direction for evaluation out of the x-y plane (two lattice units thick). These orthotropic parameters were then converted to elastic stiffness matrix terms to define and orthotropic material in ABAQUS:

$$\begin{Bmatrix}\sigma_{11}\\ \sigma_{22}\\ \sigma_{33}\\ \sigma_{12}\\ \sigma_{13}\\ \sigma_{23}\end{Bmatrix} = \begin{bmatrix} D_{1111} & D_{1122} & D_{1133} & 0 & 0 & 0 \\ & D_{2222} & D_{2233} & 0 & 0 & 0 \\ & & D_{3333} & 0 & 0 & 0 \\ & & & D_{1212} & 0 & 0 \\ & sym & & & D_{1313} & 0 \\ & & & & & D_{2323} \end{bmatrix} \begin{Bmatrix}\epsilon_{11}\\ \epsilon_{22}\\ \epsilon_{33}\\ \gamma_{12}\\ \gamma_{13}\\ \gamma_{23}\end{Bmatrix} \quad \text{(D1)}$$

where the σ terms are components of the Cauchy stress tensor, the D terms are elastic stiffness constants, the ϵ and γ terms are normal and shear strains, respectively, and the subscripts are the principal directions in Cartesian coordinates (1 = x/axial direction, 2 = y/ circumferential direction, and 3 = z/radial direction).

D.2.3 Additional predictions of the CME in cell-laden scaffolds

Predictions of the CME in the fibrin hydrogel of a pure 3DF scaffold were generated as a guide for the regenerative potential of the scaffold under the prescribed biaxial strain protocol in the *in vitro* experimental study. Specifically, the %PTE was evaluated for scaffolds with the average fiber diameter from mechanical testing of cruciform scaffolds (338 μm; Section 2.1) and for the measured average fiber diameter of the scaffolds in the *in vitro* study (230 μm; Section 3.1).

D.2.2 Additional predictions of cruciform scaffold mechanics

In the cell-culture study (Section 3.1), it was expected that the 3DF scaffolds would have fiber diameters similar to the average measured fiber in the biaxial characterization of the scaffolds (338 μm; Section 2.1). Although the fabricated scaffolds in the cell culture study matched the

designed fiber spacing, the fibers measured an average of 230 µm in diameter. Therefore, the mechanics of two cruciform models with identical architectures and these two fiber diameters were modelled with the angle-ply laminate scaffold model. The global scaffold reaction forces and ROI strains were compared for the global biaxial strain regime prescribed in the cell culture study (2.5% axial strain and 0.5% circumferential strain).

D.2.4 Modelling the CME within 3DF and hybrid scaffold architectures

The finite element model of hydrogel-infused, angle-ply scaffold unit cells (Section 3.2) considered only scaffolds with 3DF fibers. However, in the cell culture study (Section 3.1) a hybrid architecture was leveraged for a multiscale scaffold architecture. Therefore, solid continuum sheets of MEW were added to the developed unit cell model to reflect the hybrid scaffold architecture described in Section 3.1 (Figure D1). The MEW sheets were added to the 3DF model centered at the intersection of each bilayer and prescribed orthotropic material properties derived in this appendix. The MEW sheets were assumed to have a layer height of half the fiber diameter which was similar to the 3DF scaffolds. Therefore, the total thickness of the MEW sheets was 160 µm. Because the ROI in the unit cell model only encapsulated a single repeating unit within the scaffold, two configurations of the hybrid scaffold were considered with the MEW at the odd and even intersections of the lamellae (Figure D1c-d) to represent all possible regions the resident cells could occupy. The results from the ROIs of each configuration were totaled to characterize the overall %PTE of the hybrid scaffold. The unit cell was prescribed the expected and measured 3DF fiber diameters (338 µm and 230 µm, respectively) and predicted biaxial ROI strains in the experimental study (1.4% axial and 0.1% circumferential; Appendix C). Biaxial strains with double the magnitude of the experimental study were also considered. Equivalent pure 3DF

scaffolds were modelled to compare the predicted %PTE and biaxial reaction forces of the two scaffold architectures.

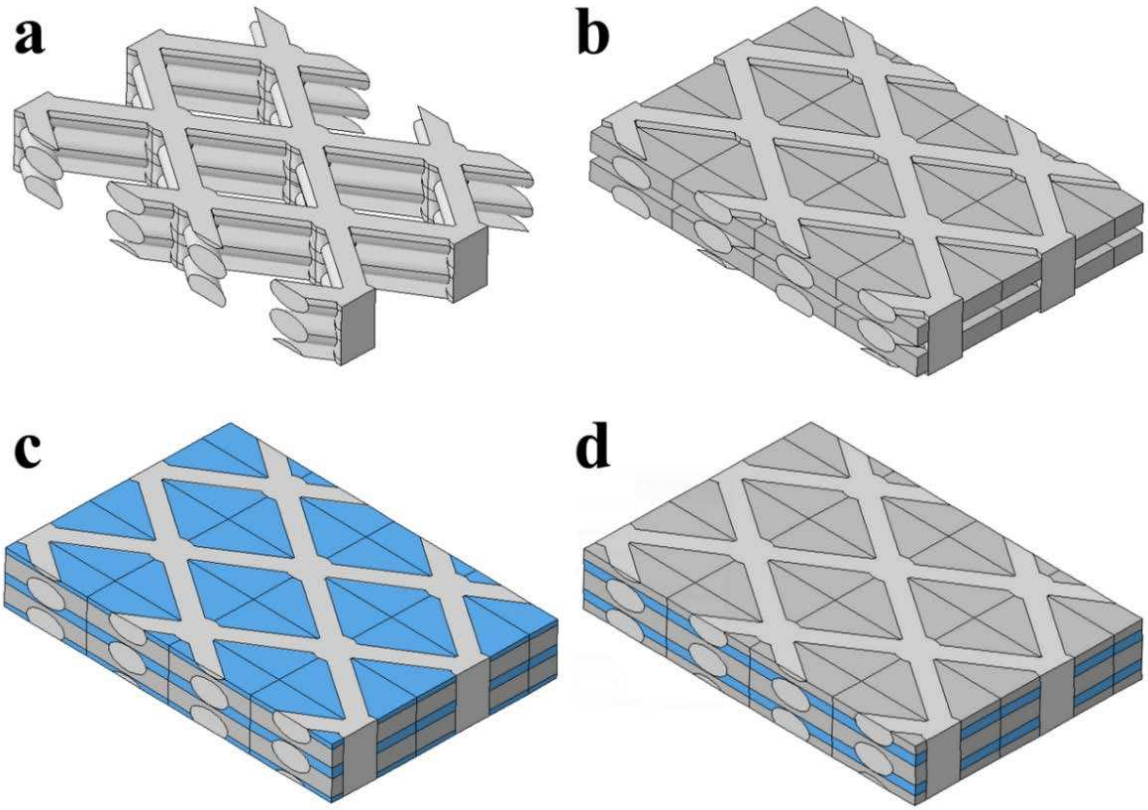

Figure D1. Unit cell model of the hybrid 3DF/MEW scaffold: **(a)** the 3DF fiber scaffold; **(b)** the hybrid scaffold with 3DF fibers (light grey) and MEW sheets modelled as a solid continuum (dark grey); **(c)** even configuration of the full hybrid scaffold unit cell model with hydrogel in the voids of the scaffold (blue); and **(d)** odd configuration of the full hybrid scaffold.

D.3 Results

D.3.1 Continuum level material properties of angle play laminate scaffolds

FE modelling of angle-ply laminate scaffolds predicted anisotropic continuum-level material properties for the 3DF and MEW architectures (Table D1). These material properties were converted to ABAQUS orthotropic definition and found to meet stability criteria.

Table D1. Orthotropic material parameters as derived from FE predictions of angle-ply laminate scaffolds and material stiffness matrix components used in the ABAQUS orthotropic material definition.

Orthotropic Material Parameters									
Scaffold	**E_{11} (MPa)**	**E_{22} (MPa)**	**E_{33} (MPa)**	**G_{12} (MPa)**	**G_{31} (MPa)**	**G_{23} (MPa)**	**ν_{12}**	**ν_{31}**	**ν_{23}**
3DF	3.72	15.4	43.2	1.70	2.97	1.98	0.357	0.305	0.109
MEW	0.124	0.608	8.57	0.780	0.034	0.056	0.430	0.392	0.002
ABAQUS Material Parameters									
Scaffold	**D_{1111} (MPa)**	**D_{3333} (MPa)**	**D_{2222} (MPa)**	**D_{1133} (MPa)**	**D_{1122} (MPa)**	**D_{2233} (MPa)**	**D_{1313} (MPa)**	**D_{1212} (MPa)**	**D_{2323} (MPa)**
3DF	8.84	50.1	37.6	6.92	13.8	15.7	2.97	3.73	2.95
MEW	1.36	8.87	6.66	0.634	2.87	1.36	0.034	0.780	0.056

D.3.4 Modelling the CME within hybrid scaffold architectures

For the same prescribed local strains, the model of CME in the TE scaffold unit cell demonstrated appreciably reduced %PTE for the smaller fiber diameter (Table D2).

Table D2. Summary of the %PTE in the fibrin hydrogel matrix of angle-ply laminate scaffolds with two different fiber diameter under the same local strain protocol.

Fiber diameter (μm)	**Prescribed local strains (%)**		**%PTE**
	x	**y**	
338	1.4	0.1	5.7
230	1.4	0.1	1.1

D.3.3 Additional predictions of cruciform scaffold mechanics

For the same global strain protocol, the scaffold with smaller diameter fibers demonstrated reduced reaction forces in both biaxial directions (Table D3). The scaffold with smaller diameter fibers also had notably different local ROI strains to the scaffold with larger diameter fibers.

Table D3. Summary of the global reaction forces and local ROI strains for angle-ply laminate cruciform scaffolds with two different fiber diameters under the same global biaxial strain protocol.

Fiber diameter (μm)	**Prescribed global strains (%)**		**Global reaction force (N)**		**Local ROI strains (%)**	
	x	**y**	**x**	**y**	**x**	**y**
338	2.5	0.5	11.3	16.6	1.4	0.1
230	2.5	0.5	4.2	6.6	0.4	0.3

D.3.4 Modelling the CME within 3DF and hybrid scaffold architectures

The addition of the MEW sheets generated an increase in the predicted scaffold stiffness or 12% in the x-direction and 18% in the y-direction (Table D4). As compared to the large fiber diameter, the smaller fiber diameter for the pure 3DF scaffold resulted in reduced scaffold stiffness consistent with the results in Table D3. The %PTE dramatically decreased due to the smaller fiber diameters, yet the hybrid scaffold demonstrated a marked increase in the overall %PTE due to the addition of the MEW sheets. Further, this increase in %PTE was driven solely by cell volumes in the hydrogel and none in the MEW sheets.

Table D4. Summary of the reaction forces and %PTE in pure 3DF and hybrid scaffolds. The same local strain protocol was used for all analyses and two 3DF fiber diameters were considered. For the hybrid scaffold, the %PTE is reported for the total matrix region (including the solid MEW sheets), only the MEW sheets, and only the hydrogel region (HG).

Model	3DF fiber diameter (μm)	Prescribed local strains (%)		Reaction forces (N)		%PTE		
		x	y	x	y	Overall	MEW	HG
3DF	338	1.4	0.1	0.93	0.76	5.7	-	-
	230	1.4	0.1	0.31	0.30	0.1	-	-
Hybrid	230	1.4	0.1	0.35	0.36	1.1	0.0	1.8

D.4 Discussion

The derived orthotropic material properties represent a rapid way to approximate the continuum level mechanics of TE scaffold designs. However, for broader application of the results, experimental validation will be advantageous. The cruciform and unit cell predictions of the sensitivity of scaffold mechanics to the fiber diameter are consistent with the results of Section 2.2. The fiber diameter also dramatically influenced the %PTE for the prescribed *in vitro* strain protocol which may have notable effects in the experimental results. These results demonstrate how discrepancies in print parameters can lead to large changes in the behavior of TE scaffolds.

The hybrid unit cell model predicted a greater %PTE than the corresponding pure 3DF scaffold in the prescribed biaxial loading regime. This is consistent with the rationale for the hybrid architecture; as compared to the 3DF fibers, the MEW fibers are closer in size to resident cells in the TE scaffold and provide a greater surface area, which is hypothesized to enhance the CME experienced by the cells under global scaffold loading. However, this preliminary model is currently limited because: (1) only one biaxial loading protocol was considered and modelling of

larger strains was unstable; and (2) the CME within the solid continuum MEW sheets was likely not modelled accurately. Nonetheless, the hybrid model demonstrated increased CME within the hydrogel sections alone. The MEW sheets were found to have a notable change to the biaxial reaction forces of the scaffold which are directly correlated with the scaffold stiffness. Accordingly, it may not be valid to assume that the influence of the MEW sheets on the overall scaffold mechanical is negligible.

APPENDIX E – DEVELOPMENT OF A FINITE ELEMENT MODEL TO PREDICT THE CELLULAR MICROMECHANICAL ENVIRONMENT IN TISSUE ENGINEERING SCAFFOLDS[d]

E.1 Introduction

Tissue engineering (TE) aims to restore the healthy function of organs by stimulating cells into a regenerative process. To this end, the fate of these cells is critical. In many tissues, the cellular micromechanical environment (CME) largely drives these cell fates.[1–4] However, it is prohibitively complex to prescribe and measure the inhomogeneous, three-dimensional CME in the hydrogel matrix of tissue engineering scaffolds. Accordingly, a fundamental understanding of how the loading, architecture, and materials of TE scaffolds influences the CME has not been comprehensively described.

Computational models, such as those that utilize the finite element (FE) method, hold the potential to increase our understanding of mechanobiological responses for a broad range of scaffold and target tissues.[5–7] A previously-developed FE model of a TE scaffold has replicated the physiologically-relevant (i.e. biaxial) mechanical properties of the intervertebral disc's annulus fibrosus.[8] However, the CME generated within this scaffold under physiological loading remains unclear. Accordingly, the aim of this work was to: (1) characterize the mechanical behavior of a

[d] The content of Appendix E has been published as a Short Communication in the Journal of Biomechanics (DOI: 10.1016/j.jbiomech.2021.110355). All content has been adapted with permission from Elsevier.

common fibrin hydrogel and (2) to implement this hydrogel as the composite matrix material within the previously-developed model.

E.2 Materials and Methods

E.2.1 Mechanical characterization of fibrin hydrogel

E.2.1.1 Fabrication of fibrin samples

Whole blood was collected from healthy, mature sheep and fibrinogen was isolated using the Cohn fractionation method.[9] Whole blood collection was performed under approval from the Institutional Animal Care and Use Committee at Colorado State University (protocol #: KP104). Fibrin hydrogel samples were cast into cylindrical molds (15.9 mm diameter) by pipetting 1.2 mL of fibrinogen into the mold, adding 4 mg of thrombin (bovine thrombin, MilliporeSigma, Burlington, MA, USA) and mixing the fibrin and thrombin by gently pipetting in and out of the mold. The fibrin samples were solidified at room temperature, maintained at 37°C for 24 hours, then gently removed from the molds (Figure E1a).

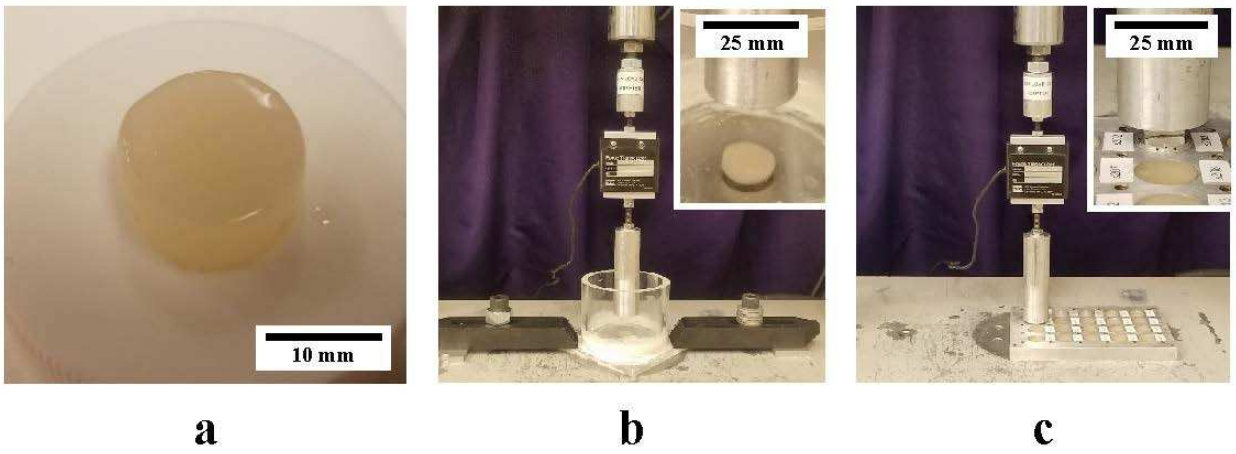

Figure E1. Mechanical testing of fibrin hydrogels: (a) cylindrical sample of fibrin hydrogel removed from mold, (b) experimental apparatus for unconfined compression, and (c) experimental apparatus for confined compression. Insets show close up images of the samples in the experimental configurations.

E.2.1.2 Material testing of fibrin

Hydrogel specimens were divided into two groups for unconfined compression (n = 9) and confined compression (n = 7) testing. Prior to testing, the diameter and height of each specimen was measured with digital calipers (CD-6”PSX, Mitutoyo, Kawasaki, Japan). Unconfined compression and confined compression tests were conducted using a servo-hydraulic materials testing system (858 MiniBionix; MTS Systems Corp., Eden Prairie, MN) with a 100 N force capacity tranducer (Model 661.09B-21, MTS Systems Corporation, Eden Prairie, MN, USA) and a custom designed testing apparatus (Figure E1b-c). For both testing regimes, samples were preconditioned with 10 compression cycles of 5% strain then compressed to 50% strain at a displacement rate of 0.1 mm/s. Force and displacement data were recorded at 100 Hz by the materials testing system and converted to the engineering stress and strain space following testing using the measured sample height and diameter.

E.2.1.3 Hyperelastic fitting of fibrin

In ABAQUS (Dassault Systèmes, Vélizy-Villacoublay, France), stress-strain data for uniaxial compression and volumetric compression were imported from the confined compression (data up to 5.0% strain) and unconfined compression (data up to 33% strain) regimes, respectively. ABAQUS determines material coefficients using a least-squares-fitting procedure to minimize the relative error in stress. The data were then fit to polynomial (first order to third order),[10] Ogden (first order to third order), [11] Van der Waals,[12] and reduced polynomial (first order to third order)[13] compressible hyperelastic models. For example, the following equation represents the second order reduced polynomial model used in this study:

$$U = C_{10}(I_1 - 3) + C_{20}(I_1 - 3)^2 + D_1(J - 1)^2 + D_2(J - 1)^4 \quad \text{(E1)}$$

where U is the strain energy potential, C_{10} and C_{20} are the fitted material elasticity constants, I_1 is the first invariant of the strain tensor, D_1 and D_2 are the fitted material compressibility constants, and J is the Jacobian determinant of the deformation gradient tensor. The most appropriate material model was selected based on: (1) fit to the experimental data as measured by a lack-of-fit test and (2) numerical stability (elastic and volumetric) when implemented in the FE method. The averaged material models (elasticity and compressibility independently) were compared to the experimental data resampled 0.1% strain increments with lack-of-fit F-tests ($\alpha = 0.05$ for all tests).

E.2.2 Scaffold unit cell model

In ABAQUS, a repeating unit of an angle-ply laminate scaffold geometry was generated based on a previously developed scaffold (Figure E2a-b).[8] This angle-ply fiber architeture has demonstrated similar anisotropic mechanical properties to native annulus fibrosus tissue. Polycaprolactone (PCL) fibers were assumed to be linear elastic ($E = 265$ MPa, $\nu = 0.3$) and idealized as straight cylinders. The geometry where two fibers intersect was simplified by

superimposing cylindrical columns of PCL material in the z-direction at the center of every fiber intersection (Figure E2b). A hydrogel matrix infill was modelled in the scaffold void spaces (Figure E2c) and prescribed compressible, hyperelastic material properties based on the described characterization of fibrin. The fiber and matrix geometries were merged, assuming perfect bonding between the two materials. At the center of the hydrogel geometry, a region of interest (ROI) of mesh elements was defined as a repeating unit that encompassed all possible positions of the hydrogel matrix relative to the fiber scaffold.

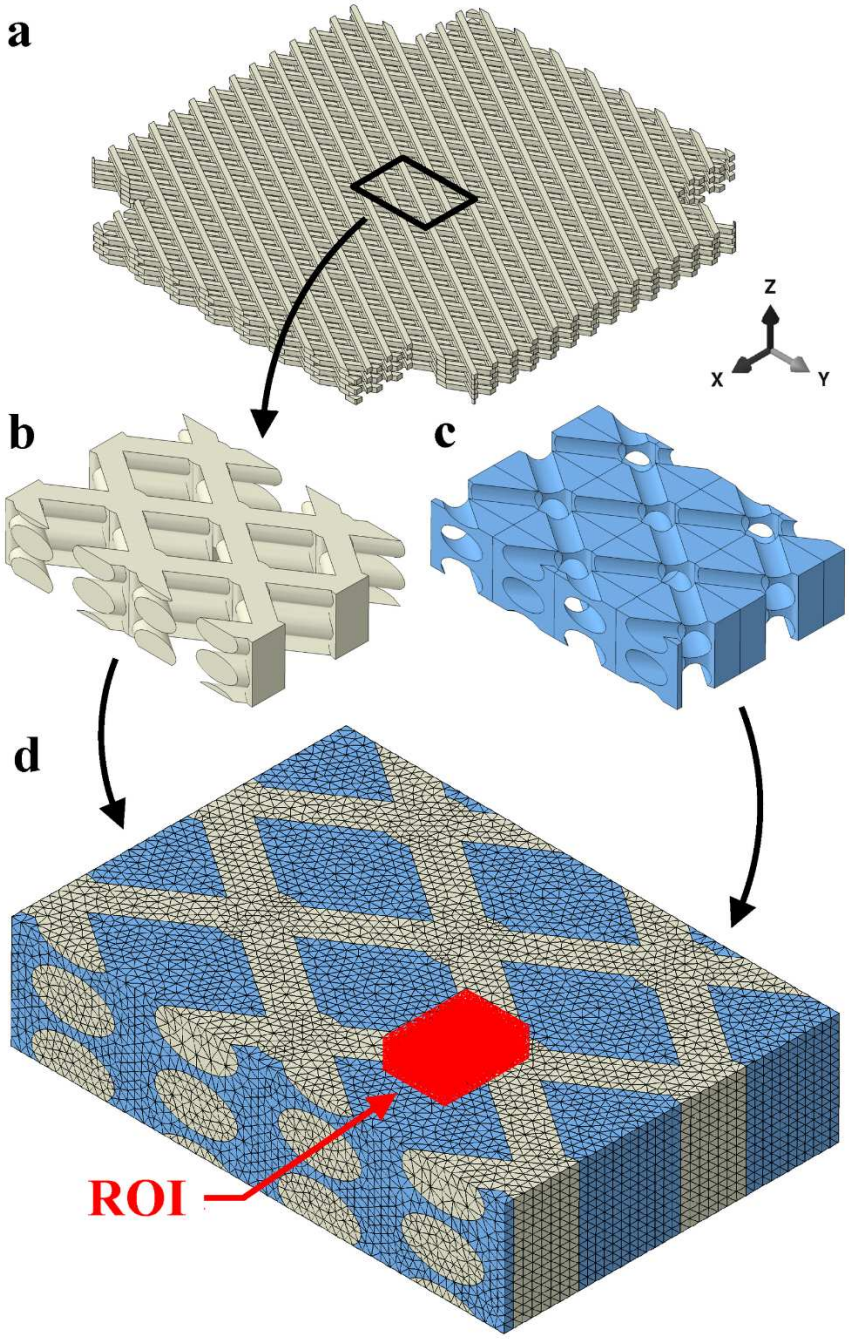

Figure E2. Scaffold model for the base geometry showing (a) the previously validated angle-ply fiber scaffold (Section 2.2), (b) the double unit cell of the fiber scaffold, (c) the hydrogel infill for the double unit cell, and (d) the final model with mesh and ROI for CME evaluation. The x-, y-, and z-directions represent the axial, circumferential, and radial directions of the intervertebral disc, respectively.

This particular model was based on a TE strategy for repair of the annulus fibrosus. Accordingly, to mimic the dominant *in vivo* loads experienced by the posterolateral annulus fibrosus, tensile strains were applied to the model in the x-direction (axial) and y-direction (circumferential).[14,15] For all model analyses, 5.0% equibiaxial strains were generated by prescribing displacements on the positive axial and circumferential faces. All ABAQUS jobs were computed on a Linux operating system (CentOS Linux 7) with 60 processor cores (Xeon E5 2683 v4, Intel Corporation, Santa Clara, CA) and 128 GB RAM.

E.2.3 Model analyses

E.2.3.1 Unit cell size

The influence of the idealized boundary conditions at the circumferential and axial faces (i.e., uniform normal displacement) on the ROI mechanics was investigated. The double (2-by-2) unit cell was compared to 1-by-1, 1.5-by-1.5, and 3-by-3 unit cells, representing both increases and reductions of the influence of boundary conditions on the ROI mechanics. Specifically, the ROI strain energy (SE) and total unit cell SE were used to measure the ROI mechanics and the central processing unit (CPU) time was used to measure the trade-off in solution time. Preliminary data indicated that a perfectly centered ROI produced unstable boundary conditions because the boundary coincided with small geometric features, leading to localized poor mesh quality. This instability was also exacerbated when architectural parameters were changed. Accordingly, the ROI was offset in the positive y-direction by 1/8 of a unit cell to provide more stable boundary geometries whilst minimizing the boundary influence on the ROI mechanics.

E.2.3.2 Mesh refinement

Analysis of the unit cell size was conducted prior to mesh refinement because preliminary data indicated that mesh convergence was dependent on the unit cell size. All unit cell analyses were performed with a uniform quadratic tetrahedral (C3D10) mesh with 40 µm seed size, which was subsequently validated. The selected unit cell size was then prescribed a series of mesh sizes to evaluate convergence of the mesh and ROI mechanics. Uniform meshes of 40 µm, 35 µm, and 30 µm seed size were considered. For more coarse meshes, a 40 µm seed size was maintained in the ROI to ensure cell-sized volumes were maintained for CME evaluation. The remaining unit cell was seeded with increasing size from 40 µm to 250 µm. For all meshes, the element growth rate within the ROI was set to 1.0 and the element growth rate outside of the ROI was set to 5%.

E.2.3.3 Boundary conditions

To further understand the influence of unit cell boundary conditions on the mechanics within the ROI, the base model was tested with numerous boundary conditions. In the radial (out-of-plane) direction, the following conditions were modified: (1) constraining all nodes on the positive and negative radial faces, (2) constraining all nodes on the positive radial face, (3) constraining all nodes on the negative radial face, and (4) changing the bilayer count (N) to N = 1, N = 3 and N = 4 to create scaffolds of different thicknesses. In the axial and circumferential directions, the following conditions were modified: (5) removing constraints from the hydrogel on all four in-plane faces, (6) removing constraints from the hydrogel on both axial direction faces, (7) removing constraints from the hydrogel on both circumferential direction faces.

E.3 Results and Discussion

E.3.1 Hyperelastic characterization of fibrin hydrogel

The only hyperelastic models with extensive elastic and volumetric stability were the first-order reduced polynomial (neo-Hookean; all data fits were stable) and second-order reduced polynomial (the elastic data from one sample was unstable and omitted, resulting in $n = 6$ for this model). Of these two models, both exhibited no statistically significant evidence for lack of fit to the volumetric data ($p = 0.99$ for both). Similarly, for the elastic data, there was no statistically significant evidence for lack of fit of the second-order model to the experimental data ($p = 0.99$). However, the first-order model had statistically significant evidence of lack of fit to the experimental data ($p < 0.001$). Based on the stability and accuracy measures, the second-order reduced polynomial model was selected for subsequent analyses (Equation E1; Figure E3). Average fitted coefficients for the second-order reduced polynomial model were obtained by averaging the coefficients from all samples (Table E1).

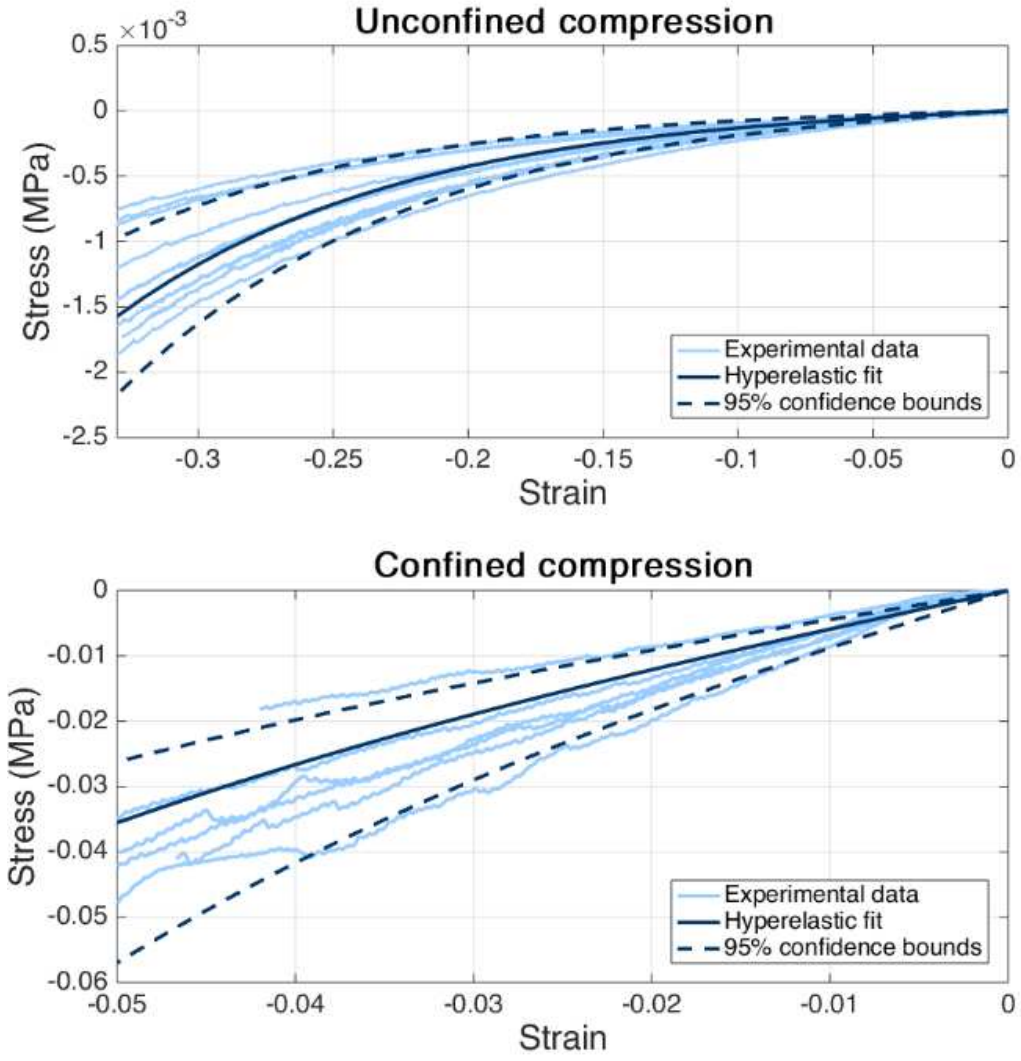

Figure E3. Unconfined and confined compression experimental data with hyperelastic model fits (second-order reduced polynomial). The 95% confidence bounds of the model coefficients (Table E1) are shown (dashed lines). One confined compression sample failed prior to 5% strain, however, was retained in the fitted data set.

Table E1. Summary of second-order fitted coefficients for fibrin hydrogel.

	C_{10} (MPa)	C_{20} (MPa)	D_1 (MPa)	D_2 (MPa)
Average	1.72×10^{-4}	3.83×10^{-4}	3.41	8.06×10^{-2}
Standard deviation	9.64×10^{-5}	1.76×10^{-4}	1.05	4.15×10^{-2}
Upper 95% confidence bound	2.46×10^{-4}	5.19×10^{-4}	4.51	1.24×10^{-1}
Lower 95% confidence bound	9.79×10^{-5}	2.48×10^{-4}	2.30	3.71×10^{-2}

E.3.2 Model analysis

The results of unit cell analyses demonstrated that cell sizes greater than 1.5-by-1.5 had ROI strain energy within 0.01% of the 3 by 3 unit cell (Figure E4). The ROI strain energies of the 1-by-1 unit cells with centered and offset ROI were 38% and 65% greater, respectively, than the 3-by-3 unit cell. Due to the observed influence of geometric boundary conditions on model stability in preliminary studies, the 2-by-2 unit cell was selected as the most suitable size for this study. All three of the reduced boundary conditions on the in-plane (x- and y-direction) faces resulted in changes to the ROI strain energy of 0.5% or less.

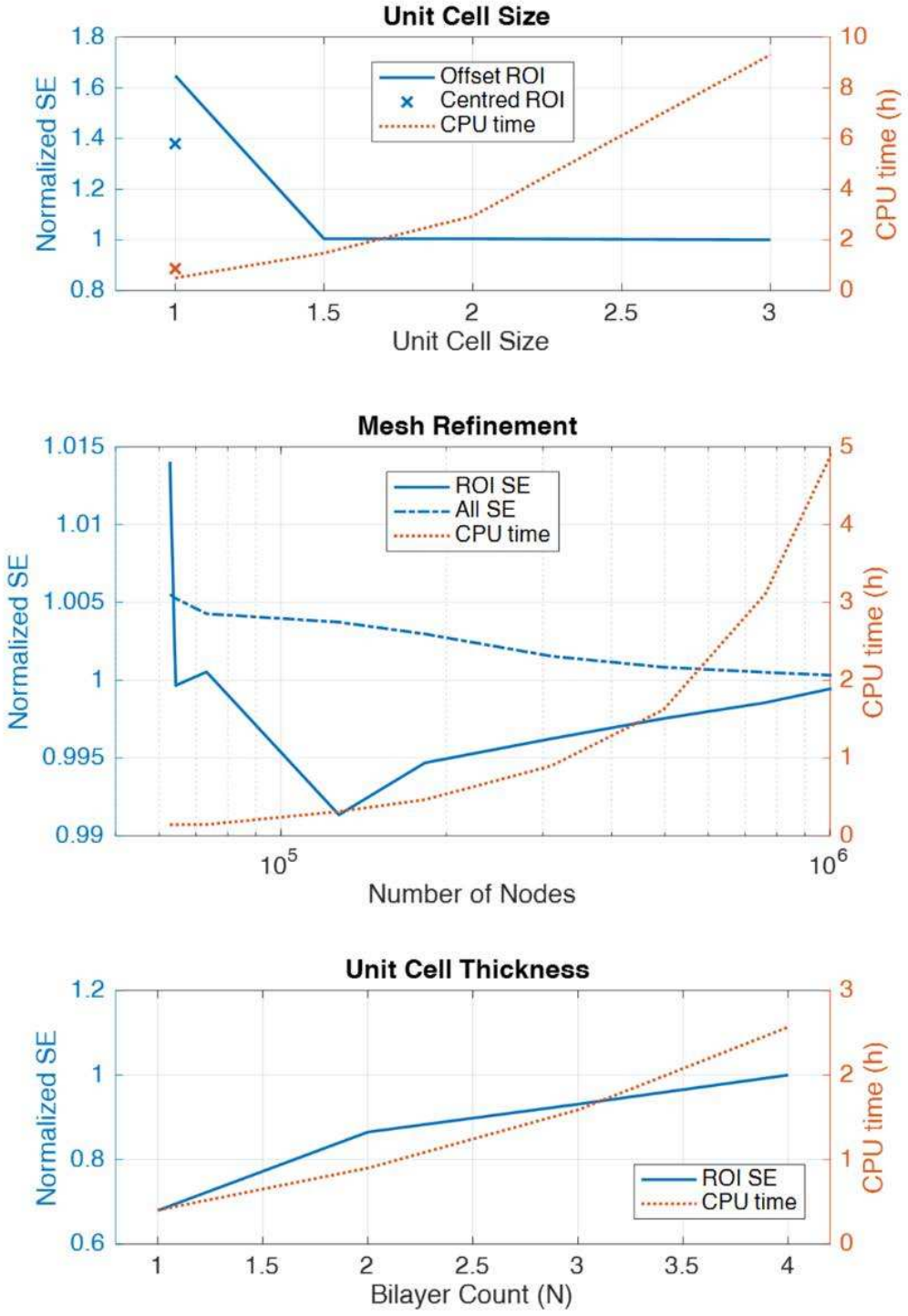

Figure E4. Analysis of the unit cell size, mesh refinement, and unit cell thickness for the scaffold CME model. For each analysis, the convergence of strain energy was weighed against CPU time. In the unit cell analysis, a centered ROI was shown to be similar to an ROI offset by 1/8 of a unit cell in order to improve boundary conditions.

The mesh refinement yielded total strain energies within 1% of the 30 µm mesh for all considered meshes. Similarly, the ROI strain energy was within 1% of the 30 µm mesh for all meshes and exhibited apparent convergence for meshes finer than 100 µm. Therefore, the uniform 40 µm mesh was deemed acceptable as compared to finer uniform meshes and the 40 µm ROI mesh was also accepted for all coarser meshes. To select the most appropriate mesh with a 40 µm ROI size, the ROI strain energy and computational time were considered. The 60 µm mesh (0.9 hours CPU time) had ROI strain energy within 0.5% of the uniform 30 µm mesh (10.6 hours CPU time). Therefore, the mesh with 60 µm general size and 40 µm ROI size was selected for all subsequent analyses.

The ROI SE demonstrated a monotonic increase as a function of bilayer count; the one-, two-, and three-bilayer scaffolds yielded SE of 68%, 87%, and 93%, respectively, of the four bilayer scaffold SE. Based on these results, the two bilayer (N = 2) was selected for all subsequent model analyses. The fully constrained boundary condition on both out-of-plane (z-direction) faces failed to converge. When considered independently, the fully constrained boundary condition on the top and bottom faces resulted in increases to the ROI strain energy of 179% and 196%, respectively. All of the modified boundary conditions in the out-of-plane direction (z-direction) yielded changes in the total model strain energy of 0.03% or less.

Based on the results of all considered boundary conditions, the out-of-plane (z-direction) boundary condition will likely have the greatest influence on the ROI CME. Careful consideration should be given to the context of these imposed constraints, for example, how these constraints relate to TE scaffolds both *in vitro* and *in vivo*. These constraints are also idealized as uniform planar deformation, which may not reflect the true boundary conditions in a physical scaffold. The

scaffold boundary conditions were constrained in this manner to balance ROI convergence, numerical stability, and computational time.

Overall, this study demonstrated the convergence of the ROI mechanics in a unit cell model as a function of the unit cell size and mesh refinement. This model will subsequently be used to elucidate the relative influence of the scaffold loading, materials, and architecture on the CME within this TE scaffold. Further, the developed model may also be adopted for numerous alternative TE scaffold preparations. For example, the new hydrogel material models could be easily implemented to investigate the CME sensitivity to alternate matrix materials or the measured variance of the fitted material parameters in this study. Ultimately, this model will be leveraged to predict cell local cell fate and guide the design of TE scaffolds for enhanced regeneration.

E.4 References

1. Altman, G. *et al.* Cell differentiation by mechanical stress. *FASEB J.* **16**, 270–272 (2001).

2. Haj, A. J. E., Minter, S. L., Rawlinson, S. C. F., Suswillo, R. & Lanyon, L. E. Cellular responses to mechanical loading in vitro. *J. Bone Miner. Res.* **5**, 923–932 (1990).

3. Aarabi, S. *et al.* Mechanical load initiates hypertrophic scar formation through decreased cellular apoptosis. *FASEB J.* **21**, 3250–3261 (2007).

4. Lotz, J. C. & Chin, J. R. Intervertebral Disc Cell Death Is Dependent on the Magnitude and Duration of Spinal Loading. *Spine* **25**, 1477–1483 (2000).

5. Lotz, J. C., Colliou, O. K., Chin, J. R., Duncan, N. A. & Liebenberg, E. Compression-induced degeneration of the intervertebral disc: an in vivo mouse model and finite-element study. *Spine* **23**, 2493–506 (1998).

6. Zhu, Q., Jackson, A. R. & Gu, W. Y. Cell viability in intervertebral disc under various nutritional and dynamic loading conditions: 3d Finite element analysis. *J. Biomech.* **45**, 2769–2777 (2012).

7. Gadomski, B. C. *et al.* Computational characterization of fracture healing under reduced gravity loading conditions. *J. Orthop. Res.* **34**, 1206–1215 (2016).

8. Page, M. I. & Puttlitz, C. M. Biaxial Mechanics of 3D Fiber Deposited Ply-Laminate Scaffolds for Soft Tissue Engineering Part II: Finite Element Analyses. *J. Mech. Behav. Biomed.* **100**, 103395 (2019).

9. Cohn, E. J., Oncley, J. L., Strong, L. E., Hughes, W. L. & Armstrong, S. H. Chemical, clinical, and immunological studies on the products of human plasma fractionation. I. The characterization of the protein fractions of human plasma. *J Clin. Invest.* **23**, 417–432 (1944).

10. Rivlin, R. S., Saunders, D. W. & Andrade, E. N. D. C. Large elastic deformations of isotropic materials VII. Experiments on the deformation of rubber. *Philosophical Transactions of the Royal Society of London. Series A, Mathematical and Physical Sciences* **243**, 251–288 (1951).

11. Ogden, R. W. & Hill, R. Large deformation isotropic elasticity – on the correlation of theory and experiment for incompressible rubberlike solids. *Proceedings of the Royal Society of London. A. Mathematical and Physical Sciences* **326**, 565–584 (1972).

12. Kilian, H.-G., Enderle, H. F. & Unseld, K. The use of the van der Waals model to elucidate universal aspects of structure-property relationships in simply extended dry and swollen rubbers. *Colloid & Polymer Sci* **264**, 866–876 (1986).

13. Yeoh, O. H. Some Forms of the Strain Energy Function for Rubber. *Rubber Chemistry and Technology* **66**, 754–771 (1993).

14. Stokes, I. A. Surface strain on human intervertebral discs. *J. Orthop. Res.* **5**, 348–355 (1987).

15. Cassidy, J. J., Hiltner, A. & Baer, E. Hierarchical Structure of the Intervertebral Disc. *Connect. Tissue Res.* **23**, 75–88 (1989).

APPENDIX F – DETAILED METHOD FOR EVALUATING THE CME IN FINITE ELEMENT ANALYSES OF TISSUE ENGINEERED SCAFFOLDS

F.1 Introduction

A post-processing algorithm was developed to predict the cellular micromechanical environment (CME) in a finite element model of cell-laden, tissue-engineered scaffolds. The algorithm facilitated the evaluation of a constant three-dimensional strain tensor for cell-sized volumes while maintaining the stability, accuracy, and efficiency of an FE model with larger and more complex elements (i.e. quadratic tetrahedral elements). Specifically, the deformation solution of each model with quadratic tetrahedral (C3D10H) elements was reverse-engineered to yield Green strain tensors for cell-sized linear tetrahedral elements (C3D4).

F.2 Methods

The following procedure was implemented in Python (Python Software Foundation, USA) with the Abaqus Scripting Interface (Dassault Systemes SIMULIA, Johnston, RI, USA) to process finite element results from a solution database. Specifically, each quadratic tetrahedral element (i.e. parent element) in a defined region of interest was divided into eight linear quadratic tetrahedral sub-elements (sub-tets; Figure F1). The elements in the ROI were prescribed a size such that the sub-tets represented cell-sized volumes. These sub-tetrahedral elements (sub-tets) were defined using the nodal indices of the parent element (Table F1).

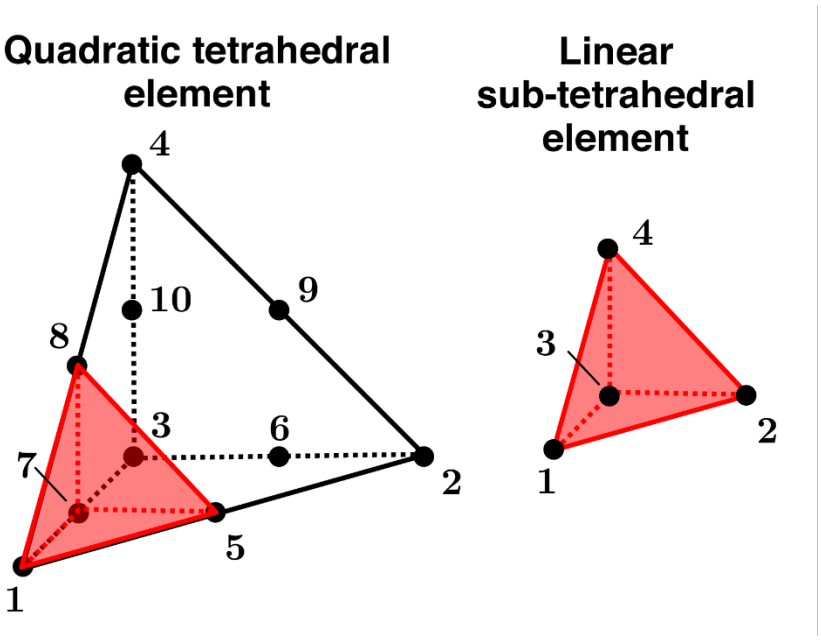

Figure F1. Diagrams of the quadratic tetrahedral element (black outlines) and linear sub-tetrahedral element (red). The example shown is sub-tet 1 as defined in Table F1.

Table F1. Definition of the four nodes of the linear sub-tetrahedral element (sub-tets) from the node numbers of the parent quadratic tetrahedral elements (as defined in Figure F1).

Subtet	Node 1	Node 2	Node 3	Node 4
Subtet 1	1	5	7	8
Subtet 2	2	5	6	9
Subtet 3	3	6	7	10
Subtet 4	4	8	9	10
Subtet 5	5	6	7	8
Subtet 6	5	6	8	9
Subtet 7	6	7	8	10
Subtet 8	6	8	9	10

The displacement vector of the each sub-tet was extracted from the finite element solution of the parent element. The finite element definition of the displacement field, $\vec{\boldsymbol{u}}$, for a linear tetrahedral element is shown in Equation F1:

$$\vec{\boldsymbol{u}} = \begin{bmatrix} u_x \\ u_y \\ u_z \end{bmatrix} = \begin{bmatrix} u_{x1} & u_{x2} & u_{x3} & u_{x4} \\ u_{y1} & u_{y2} & u_{y3} & u_{y4} \\ u_{z1} & u_{z2} & u_{z3} & u_{z4} \end{bmatrix} \begin{Bmatrix} \xi_1 \\ \xi_2 \\ \xi_3 \\ \xi_4 \end{Bmatrix} \tag{F1}$$

where u_x, u_y, and u_z are the displacement components in the x-, y-, and z-directions, respectively; the subscripts 1, 2, 3, and 4 refer to the node indices of the sub-tet; and ξ_1, ξ_2, ξ_3, and ξ_4 are the finite element shape functions for the respective node indices of the sub-tet. For example, the shape function for the index 1 node of the subtet is shown in Equations F2-F4:

$$\frac{\partial x}{\partial \xi_1} = x_1 \tag{E2}$$

$$\frac{\partial y}{\partial \xi_1} = y_1 \tag{E3}$$

$$\frac{\partial z}{\partial \xi_1} = z_1 \tag{E4}$$

where x, y, and z are the cartesian system coordinates and the subscript 1 represents the node index 1 of the sub-tet. By expressing the element displacement field, $\boldsymbol{u}^e$, as a vector (Equation F5), an alternative expression for the sub-tet displacement field was derived as per Equation F6.

$$\boldsymbol{u}^e = \{u_{x1} \quad u_{y1} \quad u_{z1} \quad u_{x2} \quad u_{y2} \quad u_{z2} \quad u_{x3} \quad u_{y3} \quad u_{z3} \quad u_{x4} \quad u_{y4} \quad u_{z4} 0\}^T \tag{F5}$$

$$\vec{\boldsymbol{u}} = \begin{bmatrix} u_x \\ u_y \\ u_z \end{bmatrix} = \begin{bmatrix} \xi_1 & 0 & 0 & \xi_2 & 0 & 0 & \xi_3 & 0 & 0 & \xi_4 & 0 & 0 \\ 0 & \xi_1 & 0 & 0 & \xi_2 & 0 & 0 & \xi_3 & 0 & 0 & \xi_4 & 0 \\ 0 & 0 & \xi_1 & 0 & 0 & \xi_2 & 0 & 0 & \xi_3 & 0 & 0 & \xi_4 \end{bmatrix} \begin{Bmatrix} u_{x1} \\ u_{y1} \\ u_{z1} \\ u_{x2} \\ u_{y2} \\ u_{z2} \\ u_{x3} \\ u_{y3} \\ u_{z3} \\ u_{x4} \\ u_{y4} \\ u_{z4} \end{Bmatrix} \tag{F6}$$

Next, the deforation gradient, **F** (or F_{ij} in indicial notation, as defined in Equation F7), was expressed with respect to the element displacement field (Equation F8).

$$F_{ij} = \delta_{ij} + u_{i,j} \tag{F7}$$

$$\boldsymbol{F} = \boldsymbol{I}^* + \boldsymbol{B}^* \boldsymbol{u}^e \tag{F8}$$

where the matrix $\boldsymbol{I}^*$ is defined as per Equation F9:

$$\boldsymbol{I}^* = \{1 \quad 0 \quad 0 \quad 0 \quad 1 \quad 0 \quad 0 \quad 0 \quad 1\}^T \tag{F9}$$

and the matrix $\boldsymbol{B}^*$ is defined as per Equation F10:

$$\boldsymbol{B}^* = \frac{1}{6V} \begin{bmatrix} a_1 & 0 & 0 & a_2 & 0 & 0 & a_3 & 0 & 0 & a_4 & 0 & 0 \\ b_1 & 0 & 0 & b_2 & 0 & 0 & b_3 & 0 & 0 & b_4 & 0 & 0 \\ c_1 & 0 & 0 & c_2 & 0 & 0 & c_3 & 0 & 0 & c_4 & 0 & 0 \\ 0 & a_1 & 0 & 0 & a_2 & 0 & 0 & a_3 & 0 & 0 & a_4 & 0 \\ 0 & b_1 & 0 & 0 & b_2 & 0 & 0 & b_3 & 0 & 0 & b_4 & 0 \\ 0 & c_1 & 0 & 0 & c_2 & 0 & 0 & c_3 & 0 & 0 & c_4 & 0 \\ 0 & 0 & a_1 & 0 & 0 & a_2 & 0 & 0 & a_3 & 0 & 0 & a_4 \\ 0 & 0 & b_1 & 0 & 0 & b_2 & 0 & 0 & b_3 & 0 & 0 & b_4 \\ 0 & 0 & c_1 & 0 & 0 & c_2 & 0 & 0 & c_3 & 0 & 0 & c_4 \end{bmatrix} \tag{F10}$$

where a_i, b_i, and c_i (for i = 1,2,3,4) are defined by Equations F11-F13:

$$6V\frac{\partial \xi_{\mathrm{i}}}{\partial x} = a_{\mathrm{i}} \tag{F11}$$

$$6V\frac{\partial \xi_{\mathrm{i}}}{\partial y} = b_{\mathrm{i}} \tag{F12}$$

$$6V\frac{\partial \xi_{\mathrm{i}}}{\partial z} = c_{\mathrm{i}} \tag{F13}$$

Also note that the Jacobian determinant, $J = 6V$. The deformation gradient of the sub-tet was validated by comparing the calculated linear sub-tet deformation gradients to the reported deformation gradient of the parent element. Finally, the Green-Lagrange strain tensor, $\boldsymbol{E}$, was calculated from the deformation tensor using Equation F14:

$$\boldsymbol{E} = \frac{1}{2}(\boldsymbol{F}^T \cdot \boldsymbol{F} - \boldsymbol{I}) \tag{F14}$$

where $\boldsymbol{I}$ is the identity matrix. Finally, from the green strain of each linear sub-tet element, the maximum principal strain component and hydrostatic strain component were extracted and compared to cell microenvironment criteria.

APPENDIX G – DETAILED DESIGN AND FABRICATION PROCESS FOR THE ANNULUS FIBROSUS REPAIR PATCH IMPLANT

F.1 Introduction

Additive manufactured materials have been developed for AF repair. However, to implement these materials in a surgical strategy, they need to be fabricated into an implantable geometry. Additionally, this geometry must be compatible with the fabrication process for the developed additive manufactured architecture. For example, in 3DF printing, the implant must be printed in layers of the deposited fiber. Accordingly, in this appendix, the process for the design and fabrication of the AF repair implant presented in Section 4.1 is described in detail.

F.2 Methods

Production of the proposed lumbar AF implant began with digital geometries of human and ovine lumbar spines. Solid models of the implant designs that conform to these spines were generated in Solidworks (2016 SP4.0, Dassault Systèmes, Vélizy-Villacoublay, France). However, the initial model could not be printed effectively due to the inherent curvature from conforming to the spine geometry. Accordingly, the initial implant model was split into the attachment plate model and the remaining model of the AF insert. The AF insert geometry was also simplified to reduce manufacturing complexity. The plate model was subsequently flattened using Solidworks and Meshmixer (Autodesk Inc, San Rafael, CA, USA) and merged with the AF insert model to form a printable implant model.

The printable implant model was then converted to g-code by applying the desired print parameters in BioCAD software (RegenHU, Villaz-Saint-Pierre, Switzerland). To generate the desired angle-

ply 3DF architecture with varied shell thickness, four separate g-codes were created for the model with different fiber orientations. A custom splicing algorithm (Python 2.7, Python Software Foundation, USA) subsequently extracted select 3DF layers from the g-code files to produce a single g-code file with the desired angle-ply architecture and varied shell thickness. The splicing algorithm also inserted pauses between the 3DF layers to facilitate the manual insertion of MEW layers to yield a hybrid 3DF/MEW construct. MEW layers were pre-fabricated and manually inserted because direct deposition of MEW layers onto a 3DF scaffold does not generate planar layers with straight fibers because of the void spaced between the 3DF fibers.

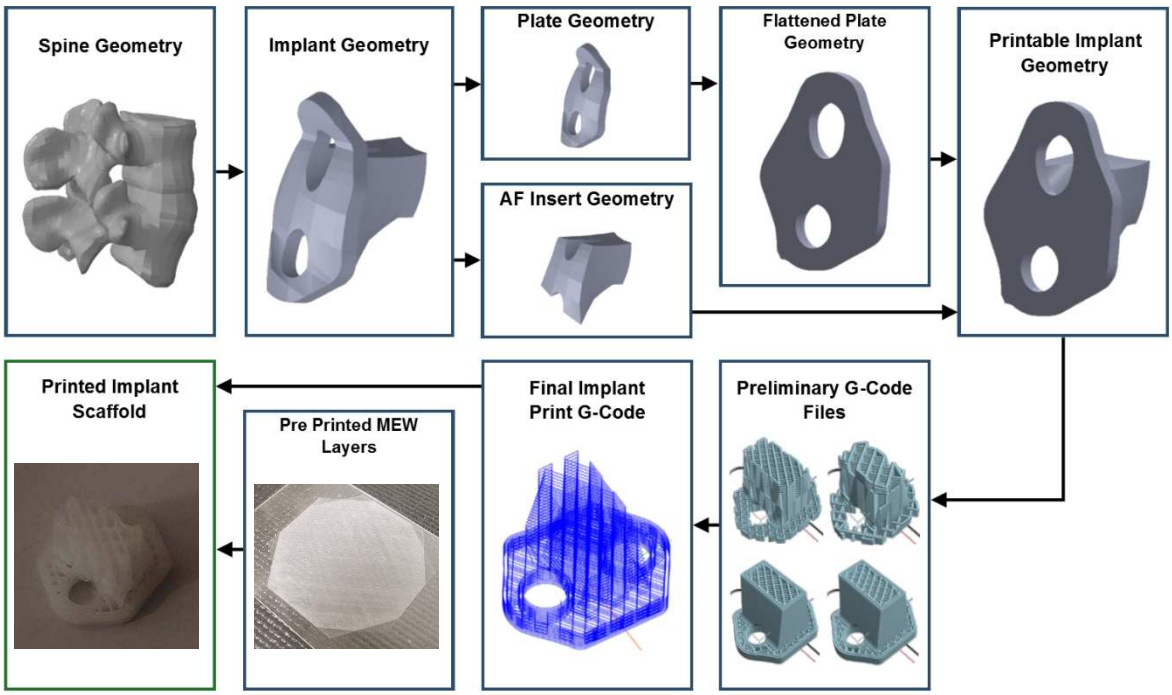

Figure G1. Process flow diagram summarizing the production of a human lumbar AF repair implant. The process began with a spine geometry and resulted in a fabricated implant design. Representative images are shown for each production step.